Large-scale crack propagation in heterogeneous materials : an insight into the homogenization of brittle fracture properties

Mathias Lebihain

THÈSE DE DOCTORAT

SORBONNE UNIVERSITÉ
Spécialité: Mécanique
École Doctorale de Sciences Mécaniques, Acoustique, Electronique et Robotique de Paris
(ED SMAER 391)

Présentée par
Mathias Lebihain

Pour obtenir le grade de
DOCTEUR DE SORBONNE UNIVERSITÉ

Large-scale crack propagation in heterogeneous materials : an insight into the homogenization of brittle fracture properties

---

Réalisée sous la direction de
Jean-Baptiste Leblond, Laurent Ponson et Michel Bornert
entre l'Institut Jean le Rond ∂'Alembert et le Laboratoire Navier

Soutenance tenue le 10 Décembre 2019 devant le jury composé de

Alan Needleman	Professeur, Texas A&M	Président du jury
Daniel Bonamy	Expert senior, CEA	Rapporteur
Véronique Lazarus	Professeure, ENSTA ParisTech	Rapporteure
Corrado Maurini	Professeur, Sorbonne Université	Examinateur
Karam Sab	Directeur de recherche, ENPC	Examinateur
Damien Vandembroucq	Directeur de recherche, ESPCI	Examinateur
Jean-Baptiste Leblond	Professeur, Sorbonne Université	Directeur de thèse
Michel Bornert	ICPEF, ENPC	Co-directeur
Laurent Ponson	Chargé de recherche, Sorbonne Université	Co-directeur

"T'allonges le bras, tu pars du Nord-Ouest,
pour arriver au Sud-Est, sans toucher la Corse.
Et tu casses, et tu casses, et tu casses."
Brice de Nice

Abstract

Being able to predict the macroscopic response of a material from the knowledge of its constituent at a microscopic or mesoscopic scale has always been the Holy Grail pursued by material science, for it provides building bricks for the understanding of complex structures as well as for the development of tailor-made optimized materials. The homogenization theory constitutes nowadays a well-established theoretical framework to estimate the overall response of composite materials for a broad range of mechanical behaviors. Such a framework is still lacking for brittle fracture, which is a dissipative evolution problem that (ii) localizes at the crack tip and (iii) is related to a structural one. In this work, we propose a theoretical framework based on a perturbative approach of Linear Elastic Fracture Mechanics to model (i) crack propagation in large-scale disordered materials as well (ii) the dissipative processes involved at the crack tip during the interaction of a crack with material heterogeneities. Their ultimate contribution to the macroscopic toughness of the composite is (iii) estimated from the resolution of the structural problem using an approach inspired by statistical physics. The theoretical and numerical inputs presented in the thesis are finally compared to experimental measurements of crack propagation in 3D-printed heterogeneous polymers obtained through digital image correlation.

Résumé

La compréhension du comportement macroscopique d'un matériau à partir de la donnée de ses constituants à l'échelle microscopique a toujours été le Saint Graal en science des matériaux dans la mesure où elle fournit les éléments essentiels à la prédiction de la résistance d'une structure et au développement de matériaux aux propriétés innovantes. Si la théorie de l'homogénéisation constitue un cadre théorique établi pour prédire la réponse effective d'une vaste classe de comportements matériaux, elle ne permet pas à l'heure actuelle de prédire les propriétés effectives en rupture fragile. S'attaquer à cette question suppose de tirer profit des caractéristiques uniques de la rupture fragile qui est (i) un problème d'évolution dissipatif, (ii) localisé en pointe de fissure et (iii) relié à un problème de structure. Dans ce travail, nous proposons un formalisme théorique fondé sur une approche perturbative de la mécanique de la rupture afin de (i) modéliser la propagation de fissure dans les milieux désordonnés de grande taille. L'implémentation numérique de ce modèle nous permet (ii) d'étudier en détail les mécanismes dissipatifs mis en jeu en pointe de fissure lorsqu'une fissure interagit avec des hétérogénéités. Leur contribution au renforcement du matériau à l'échelle macroscopique est finalement (iii) estimée à partir de la résolution du problème de structure à l'aide d'outils empruntés à la physique statistique. Les apports théoriques et numériques de la thèse sont finalement confrontés aux résultats d'expériences de fissuration de polymères hétérogènes imprimés 3D, extraits d'outils de corrélation d'image.

Table of contents

1

Introduction

Contents

Whether of a material or structural nature, failure constitutes a major threat to population safety, environmental protection and economic growth. From the collapse of the Bouzey dam in 1895, the failure of the Liberty ships in 1943, the crash of the Comet commercial airplanes in 1953 to the latest collapse of the Genoa bridge in 2018, catastrophic failures of man-made structures have occurred in recent human history. Associated with dramatic human cost, notable environmental pollution and significant economic losses, these spectacular accidents have also driven substantial progress in the understanding of the underlying failure mechanisms. For a long time, engineers had been focused on preventing the appearance of cracks in anthropogenic structures. Yet progresses in monitoring techniques showed that cracks were somewhat bound to nucleate in highly loaded structures, so that one has rather to learn how to live with them. It motivated the development of Linear Elastic Fracture Mechanics (LEFM), a comprehensive theory based on the works of Griffith [1921] and Irwin [1957], which allows for the quantitative description of the conditions under which preexisting cracks propagate.

Recent developments in additive manufacturing techniques as well as the emergence of bio-source and recycled composite materials driven by environmental concerns have increased further the need to rationalize the failure behavior of microstructured solids. If LEFM constitutes nowadays a well-established theory for the study of crack propagation in homogeneous materials, it does not currently provide an appropriate theoretical framework to assess the impact of small-scale microstructural heterogeneities of materials on their macroscopic failure properties. If significant progress has been made recently on the homogenization of linear and non-linear mechanical behavior, a comprehensive homoge-

nization theory in fracture is still missing. Such a framework is nonetheless a prerequisite to the optimization of the performance and the reduction of both the environmental and economical costs of future man-made structures, which will be built in what may be a resource-constrained world.

This introduction chapter highlights the current challenges in heterogeneous fracture mechanics. First are recalled in Section 1.1 some basic concepts on which is built the homogeneous Linear Elastic Fracture Mechanics theory. In Section 1.2, we investigate the impact of heterogeneities on crack propagation in composite materials. The interaction between a crack and heterogeneities often involves multiple and complex mechanisms, which are difficult to isolate during experiments. It has driven the need for powerful computational methods that allow for the quantitative description of individual mechanisms and their subsequent impact on crack trajectory and effective fracture properties. Such computational methods are detailed in Section 1.3. This brief review of the current state of knowledge in fracture mechanics allows us to stress out in Section 1.4 the two main challenges we address in this work : (i) how do microstructural heterogeneities affect the loading conditions under which crack propagate ? In other words, what is the *effective toughness* of a heterogeneous solid, and how does it relate to its microstructural features ? (ii) What traces reminiscent of this interaction are left on the fracture surface through the *surface roughness* and which information can be inferred from the statistical analysis of their topographic map ? The strategy we adopt to tackle these ambitious challenges is finally outlined in Section 1.5.

1.1 Basic concepts of Linear Elastic Fracture Mechanics

Based on an energetic approach developed all over the twentieth century, Linear Elastic Fracture Mechanics (LEFM) brings nowadays a tried and tested theoretical framework to predict how and when cracks propagate in homogeneous media. We briefly summarize the history of fracture mechanics along with its core elements on which the subsequent chapters heavily rely.

Brittle fracture, a process governed by material flaws

Quantum-mechanical calculations performed by Marder and Fineberg [1996] showed that when the atom spacing exceeds 20% of its value at equilibrium, the bond breaks. The critical stress to failure, or brittle material *strength* σ_c, is thus expected to be of the order of $\sigma_c \sim E/5$, where E is the Young's modulus. When compared to experimental results of fracture tests on glass, this theoretical prediction appears to be three orders of magnitude larger than experimental measurements, leading Marder and Fineberg [1996] to stress out the central role played by material flaws in brittle fracture. Inglis [1913] was the first to study the distribution of stress in an infinite plate containing a single elliptical defect of semi-axes a in the x-direction and b in the y-direction (see Fig. 1.1.a). He showed that, when the plate is subjected to some uniform applied tension σ, the opening stress σ_{yy}^P acting locally on the point P, where the curvature is maximal, is amplified by a geometrical factor :

$$\sigma_{yy}^P = \left(1 + 2\frac{a}{b}\right)\sigma \tag{1.1}$$

The *stress concentrations* at the vicinity of material flaws may account for the discrepancy between the theoretical and experimental strengths mentioned above. In particular, when the defect is sharp $b \ll a$, the local stresses becomes singular. Westergaard [1939] derived the evolution of the stress field in the neighborhood of a slit crack of length $2a$ embedded in an infinite plate loaded in tension σ (see Fig. 1.1.b) :

$$\sigma_{yy}(x) = \begin{cases} \dfrac{\sigma}{\sqrt{1-\left(\frac{a}{x}\right)^2}}, \text{ when } |x| > a \\ 0, \text{ when } |x| \leq a \end{cases} \tag{1.2}$$

which yields a characteristic square-root singularity.

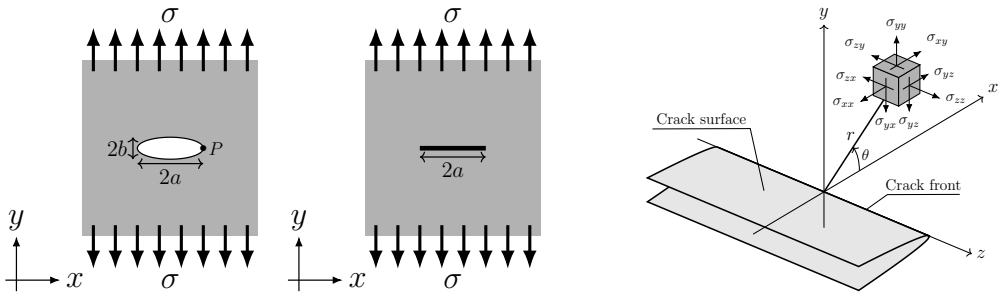

Figure 1.1: Flaws in infinite media : infinite plate subjected to uniform applied tension σ with an elliptical defect of semi-axes a and b (a) or a slit crack of length $2a$ (b). Semi-infinite plane crack inducing stresses $(\sigma_{i,j})$ on a point (r, θ) located in its vicinity (c).

Westegaard's work triggered a wide range of studies of stress singularity in elasticity. In particular, following the asymptotic expansion proposed by Williams [1952], Irwin [1957] introduced the notion of *stress intensity factors* (K_p) (SIFs) to express the singular elastic fields at the crack tip :

$$\sigma_{ij} = \sum_{p \in \{\mathrm{I,II,III}\}} \frac{K_p}{\sqrt{2\pi r}} f_{ij}^p(\theta) \tag{1.3}$$

where f_{ij}^p are universal functions and (r, θ) are the polar coordinates of a point located ahead of the crack tip where the stresses are evaluated (see Fig. 1.1.c). The stress intensity factors (K_p) depict the contributions of the tensile Mode I, plane shear Mode II and anti-plane shear Mode III, respectively (Fig. 1.2). They depend only on the geometry of the system and the external loading.

A quantitative description of the stress state in the neighborhood of a crack was a prerequisite to derive phenomenological criteria describing the conditions under which propagation occurs. Given that the stresses are singular in the vicinity of the crack tip, a propagation criterion cannot rest upon the existence of a critical opening stress. To circumvent this limitation, Irwin [1958] proposed a propagation criterion in tensile Mode I based on the associated SIF K_I :

$$\text{Propagation occurs when } K_\mathrm{I} = K_\mathrm{Ic} \tag{1.4}$$

where K_Ic is an intrinsic material property called *toughness*.

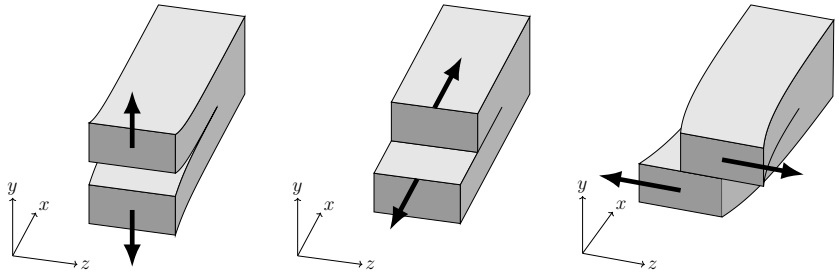

Figure 1.2: The three modes of fracture : *tensile* Mode I (a), plane shear or *plane shearing* Mode II (b) and anti-plane shear or *anti-plane shearing* Mode III (c).

Crack propagation, a phenomenon ruled by an energy-balance principle

Irwin's approach gave nonetheless predominant importance to the stress singularity at the crack tip, which is not physically acceptable since no real material can withstand infinite stresses. It motivated the construction of a theoretical approach based on energy balance rather than on the crack tip stresses. The early work of Griffith [1921] proposed an energy-based criterion stating that a crack propagates only if the decrease in total potential energy $\mathcal{P}$ compensates the energy 2γ required to create new surfaces :

$$\begin{cases} G = -\dfrac{d\mathcal{P}}{d\mathcal{A}} \leq 2\gamma \\ (G - 2\gamma)\,\dot{l} = 0 \end{cases} \tag{1.5}$$

where the total potential energy $\mathcal{P} = W - \phi$ is the sum of the elastic energy W and the potential energy of the external loads ϕ. $d\mathcal{A}$ denotes an infinitesimal extension of the crack surface and $\dot{l}$ is the crack velocity. Finally, G is the *elastic energy release rate* (ERR), which is a finite quantity contrary to the crack tip stresses.

Irwin [1962] major contribution consisted in proving that the ERR G is entirely determined by the near-tip stresses and consequently by the SIFs (K_p) following the equation :

$$G = \frac{1-\nu^2}{E}\left(K_{\mathrm{I}}^2 + K_{\mathrm{II}}^2\right) + \frac{1+\nu}{E}K_{\mathrm{III}}^2 \tag{1.6}$$

where E is the material Young's modulus and ν its Poisson's ratio. Irwin's formula connects Griffith's energy balance to the square-root singular stress fields existing at the tip of a crack embedded in an elastic material :

$$\text{Propagation occurs in Mode I when } G = G_{\mathrm{c}} = \frac{1-\nu^2}{E}K_{\mathrm{Ic}}^2 \tag{1.7}$$

where G_{c} is called the *fracture energy*. With some abuse of terminology, we will refer to G_{c} as the toughness of the material.

Equations (1.6) and (1.7) constitute the core of the modern framework of Linear Elastic Fracture Mechanics. Additional criteria have been since developed to predict the path that the crack follows during propagation under mixed mode loading (e.g. the Maximal

Tangential Stress criterion [Erdogan and Sih, 1963], the Maximal Energy Release Rate criterion [Hussain et al., 1974], the Principle of Local Symmetry [Gol'dstein and Salganik, 1974]) or the loading level at which crack nucleation occurs in a sound material (e.g. the coupled criterion [Leguillon, 2002]).

Linear Elastic Fracture Mechanics, a question of lengthscale

If the energetic approach allows to circumvent difficulties arising from the singular elastic fields in the vicinity of the crack tip, the divergence of the stress field remains nonetheless physically unacceptable. Most materials develop plastic strains or damage when local stresses exceed the material yield stress σ_s. These dissipative processes take place in a region surrounding the crack tip called the *fracture process zone* (FPZ). Barenblatt [1962] predicted the size ℓ_{FPZ} of the fracture process zone from a cohesive zone model with constant strength σ_c. This size reads :

$$\ell_{FPZ} = \frac{\pi}{8}\left(\frac{K_{Ic}}{\sigma_c}\right)^2 \tag{1.8}$$

We can thus distinguish three regimes of behavior for the stress field in the crack tip neighborhood (Fig. 1.3):

- in the process zone, stress is released by dissipative mechanisms ;
- outside of but close to the process zone, the near elastic fields are dominated by the square-root singular terms and their intensity is prescribed by the SIFs (K_p) ;
- far away from the crack tip, higher-order terms in William's expansion, such as the T-stresses (T_{ij}) (constant terms in the asymptotic expansion of the crack tip stresses) and A-stresses (A_p),($\sqrt{r}$ terms in the asymptotic expansion of the crack tip stresses), play a significant role in the estimation of the far-field values.

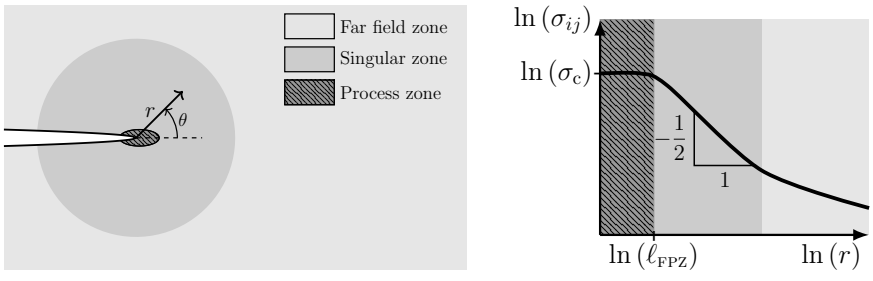

Figure 1.3: (a) Stress field regimes in vicinity of the crack tip; (b) stress released by dissipative processes within the process zone, square-root singular stress near the crack tip and stress dominated by higher-order terms in the William's expansion further away.

In brittle materials such as ceramics, rocks or glass, the size ℓ_{FPZ} of the fracture process zone is generally smaller than any structural length related to the specimen or structure size. With this so-called *small scale yielding assumption* [Rice, 1987], LEFM allows for an accurate prediction of the physical mechanisms occurring in the vicinity of the crack tip. For ductile (e.g. metallic alloys) or quasi-brittle (e.g. mortar, clay) materials, the process

zone may be of the order of the specimen size and some other theoretical framework may account for a better prediction of crack nucleation and propagation if the specimen size does not permit to apply the small scale yielding assumption.

To summarize, Linear Elastic Fracture Mechanics provides an energy-based framework to predict crack behavior in homogeneous materials, as long as the dissipative processes are confined in a small region surrounding the crack tip. It has been successfully applied in the past sixty years to predict both material and structural failure for a wide range of engineering and physical systems. It is thus natural to try extending these powerful concepts to the description of fracture in heterogeneous materials, that is the impact of microstructural heterogeneities on the macroscopic behavior of composite materials. This will lead to the development of a heterogeneous LEFM.

1.2 Material toughening by heterogeneities

Heterogeneous brittle materials are ubiquitous in our modern world, be they natural (e.g. rocks) or artificial (e.g. composite ceramics, mortar). Because of the stress concentration occurring at the crack tip, the presence of micro-scale heterogeneities may have a substantial impact on the failure behavior of heterogeneous materials on a structural scale. This section is devoted to the experimental investigation of the influence of small-scale heterogeneities on crack trajectory and the subsequent fracture properties of brittle composites.

Modern materials are increasingly designed for specific applications. The design of tailored materials, even sometimes called *meta-materials*, is steered by the need to achieve greater strengths (sensitivity to crack nucleation) as well as higher toughness levels (sensitivity to crack propagation), two properties which are often mutually exclusive [Ritchie, 2011]. Brittle materials such as ceramics and glass are rarely *stress challenged* so that material science has been pursuing the Holy Grail of achieving higher toughness levels for decades [Launey and Ritchie, 2009]. Evans [1990] distinguished two main classes of toughening mechanisms in brittle ceramics : *crack-wake* processes, which occur in the wake of a propagating crack and influence propagation through mechanisms acting on the crack lips/surfaces, and *crack-tip* processes, which happen in the vicinity of the crack tip.

Crack-wake processes have been shown to toughen efficiently brittle materials by reducing the crack-driving force ($G - G_c$) acting locally in the crack tip. Among those processes, *crack bridging* occupies a central place in the literature. It occurs when grain or fibers are left unbroken in the wake of the crack, pinning the crack front (see Fig. 1.4). The pinning forces hinder the opening of the crack lips, thus reduce the SIFs at the crack tip and higher loading levels are consequently required to fracture the specimen. Such a mechanism can be promoted for example by weak interfaces (Fig. 1.4.a), crack nucleation ahead of the crack tip (Fig. 1.4.b) or by the merging of the crack lips around a tough defect (Fig. 1.4.c). When *crack bridging* occurs, the effective fracture properties of the composite are no more governed by the toughness of the surrounding material but only by the mechanical and geometrical properties of the bridging heterogeneities. The energy can be dissipated either through frictional pulling or by fracturing bridging elements (see Fig. 1.4.a). Krstic et al.

[1981] showed that fractural bridging can increase the toughness of ceramics by a factor of 10 when the bridging particles are ductile. Recent experimental studies on bio-inspired materials [Mirkhalaf et al., 2014; Malik and Barthelat, 2016] suggest that frictional bridging can lead to similar levels of toughening.

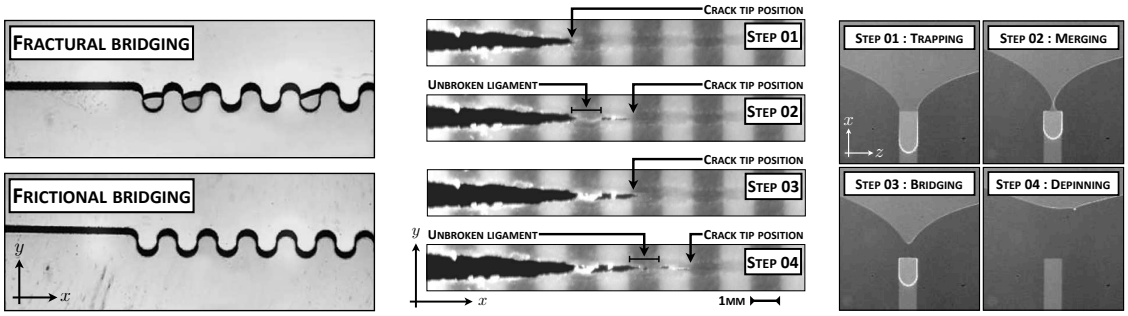

(a) (b) (c)

Figure 1.4: Experimental observations of the *crack bridging* mechanism : frictional and fractural bridging along a weak interface in a laser-engraved glass (after [Mirkhalaf et al., 2014]) (a), crack bridging due to nucleation ahead of the crack tip in 3D printed polymers with elastic heterogeneities (after [Avellar, 2018]) (b), crack bridging during the peeling experiment of an elastomer block from a patterned glass substrate containing a tougher central defect (after [Chopin, 2010]) (c).

Crack-tip mechanisms act quite differently since they directly change the intrinsic fracture properties of the composite material. They often involve dissipative processes confined within the process zone (e.g. crack shielding by micro-cracking [Evans and Faber, 1981; Ortiz, 1987; Ritchie, 1988] or by phase-transformation [Pohanka et al., 1978; McMeeking and Evans, 1982; Evans and Cannon, 1986; Hannink and Swain, 1994; Guazzato et al., 2004]), which cannot be grasped within the LEFM framework. Yet, some mechanisms such as *crack trapping* and *crack deflection* have been shown to be quantitatively predicted by LEFM. In the case of *crack trapping*, the crack tip is locally pinned by inclusions and the loading has to increase to ensure further propagation of the crack (Fig. 1.5.a). While the loading is increasing, the crack front deforms in-plane (Fig. 1.5.b), until the crack crosses the inclusion and keeps propagating (Fig. 1.5.c). Toughness heterogeneities [Dalmas et al., 2009; Chopin et al., 2011; Patinet et al., 2013a; Vasoya et al., 2016b], elastic inclusions [Xia et al., 2013; Wang and Xia, 2017; Hsueh et al., 2018] or residual stresses [Bower and Ortiz, 1993; Lacondemine, 2019] have been shown to induce trapping mechanisms. The ultimate material reinforcement depends on how long the crack remains pinned by the inclusion so that the properties of the heterogeneity strongly influence the subsequent toughening. *Crack trapping* has been shown experimentally to produce toughening increases up to 50% [Vasoya et al., 2016b; Wang and Xia, 2017].

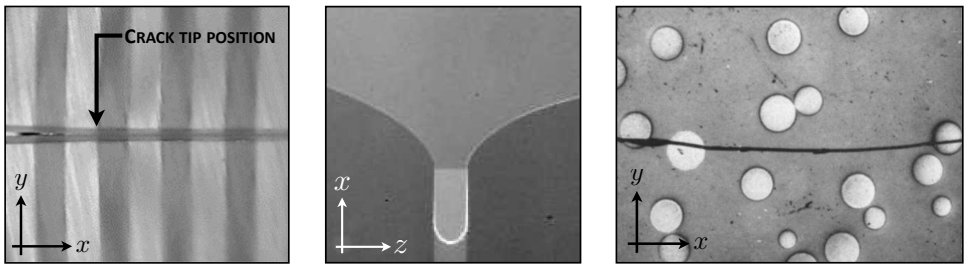

(a) (b) (c)

Figure 1.5: Experimental observations of the *crack trapping* mechanism : crack pinned at an interface between a weak/tough 3D printed materials (after [Wang and Xia, 2017]) (a), crack front in-plane deformation during the peeling experiment of an elastomer block from a patterned glass substrate with a tougher layer at the center (after [Chopin, 2010]) (b), crossing of tough inclusions in a ThO_2 soda-lime glass (after [Lacondemine, 2019]) (c).

While crack trapping is an inherently coplanar mechanism, *crack deflection* makes the crack kink around the inclusions (see Fig. 1.6). The properties of the inclusion are no more involved in the toughening process and material reinforcement is dictated by the mechanical properties of the interface and the geometry of the inclusions. Weak interfaces [Mirkhalaf et al., 2014], high inclusion toughness [He and Hutchinson, 1989], elastic properties mismatch [Lacondemine et al., 2017] and residual stresses [Lacondemine, 2019] have been shown to promote crack deflection at the matrix/inclusion interface. The subsequent material reinforcement can reach 30-50% [Faber and Evans, 1983b; Mirkhalaf et al., 2014].

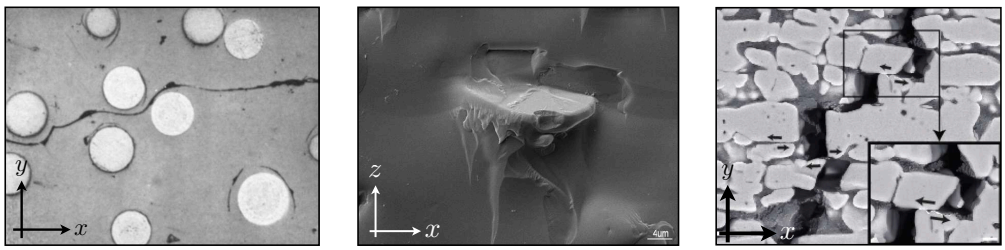

(a) (b) (c)

Figure 1.6: Experimental observations of the *crack deflection* mechanism : crack deflected around ThO_2 inclusions in a borosilicate glass due to residual stresses (after [Lacondemine, 2019]) (a), out-of-plane deviation of the crack front around an alumina platelet in a composite glass (after [Kotoul et al., 2008]) (b), crack deflection at the interface of a bioinspired synthetic alumina–PMMA made by freeze-casting (after [Munch et al., 2008]) (c).

In practice, the reinforcement induced by each toughening mechanisms taken individually is nonetheless very difficult to estimate experimentally given the interplay between all of them [Steinbrech, 1992]. A weak interface promotes *crack deflection*, which does not induce a substantial toughening of the material and can even be detrimental to the overall toughness of the composite if the interface is too weak [Ma et al., 2004; Mirkhalaf et al., 2014]. Yet it can simultaneously lead to frictional bridging of the unbroken particles left in the wake of the crack (see Fig. 1.6.c), which toughens the material very efficiently [Munch

et al., 2008; Mirkhalaf et al., 2014]. In the same manner, during *crack trapping* on very tough inclusions, the crack lips may merge in front of the crack and make way for *crack bridging* [Chopin, 2010]. Alternatively, a crack is often pinned on the matrix/inclusion interface before kinking and being deflected along it. One can observe a transition between *crack trapping* and *crack deflection* if the inclusion is tough enough. In order to design materials with tailored fracture properties, one must first identify which mechanisms are liable to take place during crack propagation, estimate the conditions (e.g. inclusion/matrix mechanical properties, inclusion geometry) under which one mechanism prevails over the others and finally quantify the toughening induced by the dominant mechanism.

Theoretical analyses of brittle fracture, among which the seminal work of He and Hutchinson [1989] plays a central role, have tried to extend LEFM to the heterogeneous case and estimate the conditions of occurrence of the interaction mechanisms between a crack and heterogeneities. Yet the complexity of such mechanisms as well as their coupling motivates their preliminary observation on model systems to stress out the parameters relevant in their competition. The development of computational methods for brittle fracture during the last decade provides now mandatory tools to perform numerical experiments and investigate the mechanisms involved during the interaction between a crack and heterogeneities, their coupling as well as the toughening they induce.

1.3 Computational modeling of crack propagation in heterogeneous materials

Many powerful computational methods have been developed in the last decades to study brittle fracture. In this section, we describe how these methods can be used to model crack propagation in heterogeneous materials and the underlying interaction mechanisms, with particular emphasis on three-dimensional situations. This short review ultimately allows for a better appreciation of the strengths and limitations of the LEFM-based perturbative approach that will be developed and detailed in the manuscript.

Early works of Newman and Raju [1984] and Ingraffea and Saouma [1985] marked the beginning of computational simulation of crack propagation. Cracks were modeled as sharp interfaces in Finite Element Method (FEM) and their propagation was studied through LEFM classical theory (see Section 1.1). Given the stress concentration induced by the sharp crack, a fine mesh is required in the region surrounding the crack tip. In the more complex context of heterogeneous materials, crack propagation requires powerful remeshing algorithms which are hardly tractable in three-dimensions [Branco et al., 2015], even if FEM-based innovating techniques allow to circumvent those difficulties [Kikuchi et al., 2014].

This motivated the development of enriched FEM discretizations to model specificities associated with fracture mechanics. In the eXtended Finite Element Method (XFEM) [Belytschko and Black, 1999; Moës et al., 1999], the finite element discretization is enriched with additional nodal degrees of freedom, which involve local discontinuous functions along the crack lips as well as singular terms at the crack tip (see Fig. 1.7.a). Crack propagation

can be modeled at a lower computational cost without continuously updating the mesh through the means of level set functions. This allows to compute efficiently crack propagation in heterogeneous media [Huynh and Belytschko, 2009; Gao et al., 2018b] (Fig. 1.7.b) even in a three-dimensional setting [Moës et al., 2002; Gravouil et al., 2002] and/or in a multi-physics context [Gupta and Duarte, 2014; Paul et al., 2018]. Yet one must rely on analytical ad-hoc criteria to predict both crack initiation and crack trajectory. If not experimentally assessed, these criteria may not reproduce the physical mechanisms at play during the propagation of the crack.

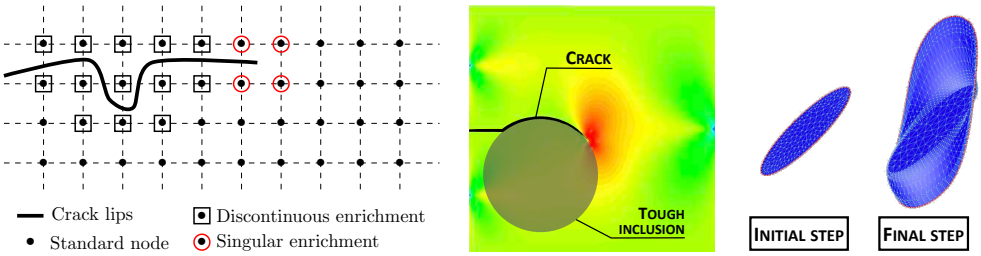

(a) (b) (c)

Figure 1.7: XFEM nodal enrichment for sharp cracks modeling (a) and applications to crack propagation : two-dimensional interaction of a single crack with a tougher spherical defect (after [Gao et al., 2018b]) (b), three-dimensional propagation of a penny-shape crack (after [Gupta and Duarte, 2014]) (c)

In contrast, cohesive zone modeling allows to predict both crack propagation and crack initiation in heterogeneous materials. The cohesive-zone model was introduced by Barenblatt [1962] and Dugdale [1960] to solve the issue of the stress singularity at the crack tip. In these models, the crack tip is smeared through the progressive decrease of the interface strength of a cohesive zone located ahead of the crack tip. All the dissipative processes, that occur within the cohesive zone, are modeled through a *cohesive law*. Yet, cohesive zone elements cannot be inserted in the bulk material without inducing a mesh sensitivity of the numerical results [Xu and Needleman, 1994]. Thus, cohesive zone models are mostly used in the case of prescribed crack trajectory to predict the loading levels at which initiation and propagation occur [Raous and Monerie, 2002]. Otherwise, cohesive elements can be inserted gradually [Camacho and Ortiz, 1996; Ortiz and Pandolfi, 1999] at a higher computational cost, since a remeshing procedure is then required. This allows for the study of crack propagation in heterogeneous materials both in two-dimensional [Perales et al., 2008; Li and Zhou, 2013a; Snozzi et al., 2012] and three-dimensional settings [Yilmaz and Molinari, 2017].

Recently, a variational approach to brittle fracture has been developed starting from the pioneering work of Francfort and Marigo [1998]. In this model, the crack is no more considered as a sharp discontinuity but is rather described by an ancillary variable α, which can be interpreted as a phase-field or a damage variable and is smeared over a distance ℓ. Both crack initiation and crack propagation result from a variational-based energy minimization problem, whose solution has been proved to $\Gamma-$ converge towards the brittle one when $\ell \to 0$ by Ambrosio and Tortorelli [1990], who studied the Mumford and

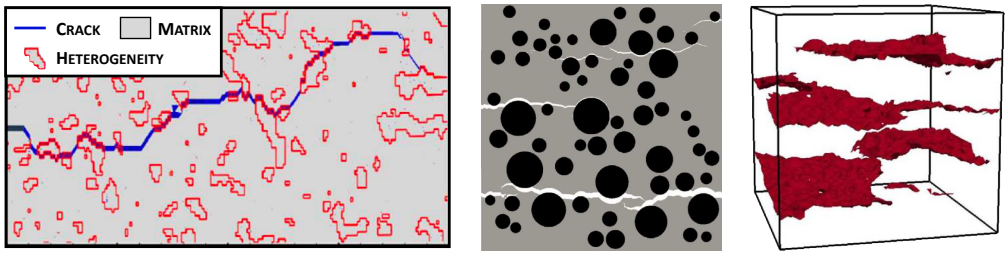

(a) (b) (c)

Figure 1.8: Application of cohesive zone models to crack propagation in heterogeneous materials : crack interacting with elastic heterogeneities (after [Li and Zhou, 2013a]), dynamic propagation in a heterogeneous medium containing two-dimensional spherical heterogeneities (b) and three-dimensional spherical ones (c) (after [Yilmaz and Molinari, 2017]).

Shah [1989] functional. Since no assumption is made on crack trajectory, it constitutes a powerful tool to investigate how a crack interacts with material heterogeneities. It has been intensively applied to study crack propagation in heterogeneous materials displaying anisotropic toughness [Hakim and Karma, 2005, 2009; Bleyer and Alessi, 2018; Li and Maurini, 2019] as well as crack interaction with material heterogeneities in 2D [Hossain et al., 2014; Nguyen et al., 2015; Da et al., 2018; Brach et al., 2019a] and 3D [Clayton and Knap, 2014; Nguyen et al., 2017b,a], taking into account interface debonding [Nguyen et al., 2016] or inertial effects [Ylmaz et al., 2018]. Moreover, this approach is not restricted to the brittle case since it can be coupled to plasticity [Alessi et al., 2018; Brach et al., 2019b] or cohesive-zone models [Verhoosel and Borst, 2013]. The phase-field approach offers one of the most promising computational frameworks to tackle numerically the question of heterogeneous brittle fracture. Nonetheless, its computational cost remains high so that one can only model the interaction of a crack with a small number of inclusions.

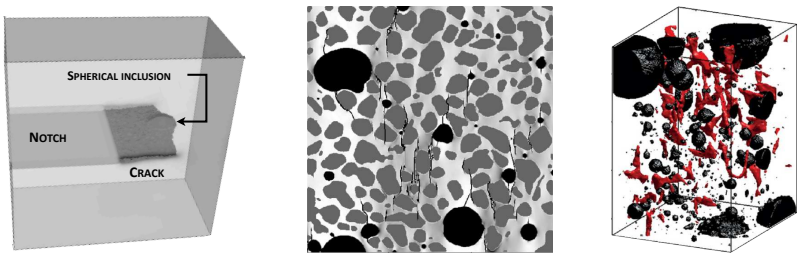

(a) (b) (c)

Figure 1.9: Application of phase-field models to crack propagation in heterogeneous materials : crack interacting with a single elastic spherical heterogeneity (after [Clayton and Knap, 2014]), crack propagation in concrete under compressive loading in two-dimensions (after [Nguyen et al., 2016]) (b) and three-dimensions (after [Nguyen et al., 2017b]) (c).

Last but not least, a new approach, the Thick Level-Set (TLS) method, has been recently introduced by Moës et al. [2011] to model three-dimensional crack propagation and initiation at a lower computational cost by constraining the non-local interactions within a damaged zone of prescribed size. Contrary to phase-field models, the TLS method models

the crack as a discontinuity to which are associated level-set functions as was the case in the XFEM framework. The sharp crack is surrounded by a damaged zone, in which all the dissipative processes are confined and whose size is a parameter of the model. Crack initiation is governed by damage evolution, which is a function of the level-set functions. The sharp crack description might allow for a better description of mechanisms associated to crack lips/surfaces (e.g. contact, friction, fluid exchange in hydraulic fracture), while the localization of the damage within the damaged zone allows for a coarse mesh away for the crack and results in a gain in computational efficiency. Moreover, the fact that the size of the damaged zone is a parameter of the model might allow to study its influence during the interplay between a crack and material defects. The TLS method has been used to model crack propagation in heterogeneous material in both two- and three-dimensions (see examples from Salzman et al. [2016] in Fig. 1.10) and has recently been coupled with a cohesive zone approach [Lé et al., 2018].

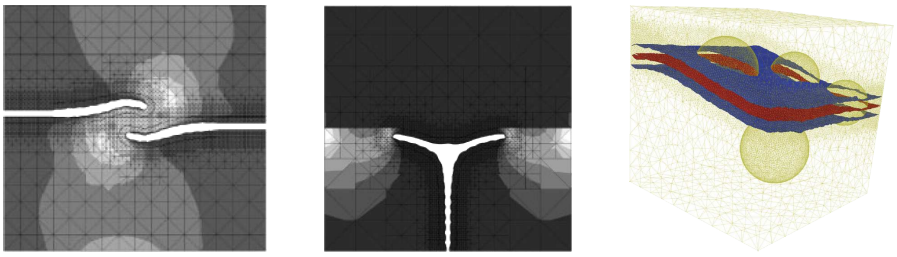

(a) (b) (c)

Figure 1.10: Application of thick-level-set (TLS) models to crack propagation in heterogeneous materials : two-dimensional multi-cracking with en-passant crack-pairs (a) and crack deflection at a bi-material interface (after [Moës et al., 2011])(b) and three-dimensional crack propagation in a porous medium (after [Salzman et al., 2016]) (c).

The last two numerical approaches yield very promising results that reveal the strong impact of material heterogeneities on the mechanisms of propagation, and the ensuing increase of fracture properties. They are nonetheless computationally expensive and do not currently allow to simulate crack propagation in a disordered medium containing thousands or millions of heterogeneities. As pointed out by Chambolle et al. [2009], one must envisage all possible geometric configurations of the crack before selecting the path it will follow during the subsequent propagation event. This specific condition gives a prominent position to perturbative approaches in fracture mechanics [Leblond, 2003]. Based on Bueckner-Rice weight function theory [Bueckner, 1970, 1987], these approaches allow to compute local stress intensity factor variations arising from any small crack front geometrical perturbation from a reference crack without solving the whole elasticity problem. The SIF calculation can then be coupled to *ad hoc* criteria to describe crack propagation in large-scale disordered materials. It has been implemented numerically to investigate the impact of *crack trapping* mechanisms on the effective toughness by Bower and Ortiz [1990] and Lazarus [2003], as well as its coupling with *crack bridging* by Bower and Ortiz [1991]. First-order studies have allowed to investigate numerically crack dynamics resulting from the interaction between a semi-infinite crack and systems disordered on a large-scale [Bonamy et al., 2008; Laurson

et al., 2010; Barès et al., 2014; Ponson and Pindra, 2017]. They have been shown to quantitatively describe non-trivial features observed experimentally in crack propagation experiments in disordered materials, despite the crudeness of the first-order approximation [Delaplace et al., 1999; Ponson and Bonamy, 2010; Chopin et al., 2011, 2018]. The numerical performance offered by the perturbative approach is a prerequisite to study the impact of material disorder on the effective fracture properties and the statistical properties of the fracture surface, the two main challenges taken up during the PhD thesis and described in the next section.

1.4 Challenges in heterogeneous brittle fracture

Linear Elastic Fracture Mechanics is currently facing many challenges when it comes to the question of heterogeneous materials. In particular, a LEFM-based theory that would relate microstructural properties to its effective toughness is still lacking. Being able to predict the macroscopic response of a material from the knowledge of its constituent at a microscopic or mesoscopic scale has always been the Holy Grail pursued by material science [Torquato, 2002], for it provides building bricks for the understanding of complex structures as well as for the development of tailor-made optimized materials. A well-established theoretical framework has been developed within the mechanics community to estimate the overall response of composite materials from their microstructure, for linear static behavior such as elasticity [Hashin and Shtrikman, 1963; Hill, 1965; Herve and Zaoui, 1993; Ponte-Castañeda and Willis, 1995] by concentrating on the average strain energy. Such approaches cannot be directly adapted to brittle fracture, which is an inherently dissipative evolution process. The homogenization theory usually handles dissipative processes such as plasticity within the limit analysis framework, by considering the volume average of the dissipation [Hill, 1967; Gurson, 1977; Monchiet et al., 2008; Madou and Leblond, 2012; Morin et al., 2015]. It has also been extended to tackle the case of non-linear behavior [Ponte-Castañeda, 1991; Ponte-Castañeda and Suquet, 1997; Lahellec and Suquet, 2007; Agoras et al., 2016; Lucchetta et al., 2019], through the introduction of some linear comparison composite eventually combined with an incremental variational problem, focusing once again on the volume dissipation. Yet fracture processes are not distributed within the bulk volume but localized in the crack neighborhood. Moreover, the stress singularity at the crack tip enhances the impact of microstructural heterogeneities so that rare but tough heterogeneities can substantially modify the effective fracture properties. Take for example a very simple two-dimensional dual-phase composite, composed of a matrix material of toughness G_c^{mat} and tougher stripe inclusions $G_c^{\mathrm{inc}} \geq G_c^{\mathrm{mat}}$ (see Fig. 1.11.a-c). When the stripes are aligned with the propagation direction, the effective toughness G_c^{eff} is equal to that of the matrix G_c^{mat} (Fig. 1.11.a). The situation is quite the opposite when the crack is facing stripes oriented in the direction perpendicular to the propagation direction : the effective toughness of the material is determined by the toughness of the tough inclusions G_c^{inc} (Fig. 1.11.b). The problem appears to be even more complex since it seems to be independent of the inclusion density, an infinitely thin single layer toughening the material in the same way as multiple thicker layers (Fig. 1.11.b-c); so that averaging the dissipation does

not produce appropriate results. Yet, all this concerns only *two-dimensional* case where the crack only interacts through a *trapping mechanism* with *toughness heterogeneities*, whereas the crack often propagates in the bulk of *three-dimensional* structures, interacting with the microstructure displaying *different elastic, strength and toughness properties* through *various complex mechanisms* (see Section 1.2). Moreover, Griffith's criterion of Eq. (1.7) states that, when the crack propagates, the elastic energy release rate G, which is inferred from a structural problem with a growing crack, equals the material toughness G_c. Recent numerical investigations suggest that the effective fracture properties of heterogeneous materials may depend on the loading conditions [Hun et al., 2019]. One may even wonder if the problem of homogenizing brittle fracture properties of heterogeneous materials can be separated from the influence of the global structure in which the crack propagates, thus defining the intrinsic material properties.

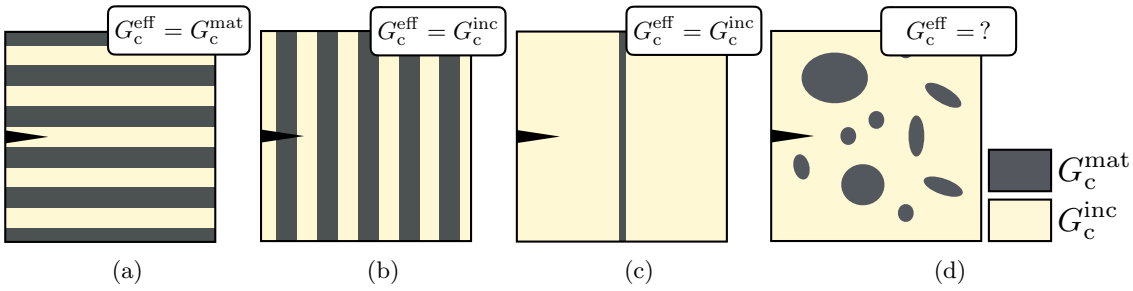

Figure 1.11: Bi-phase composite constituted by a matrix material of toughness G_c^{mat} and tougher inclusions $G_c^{inc} \geq G_c^{mat}$, characterized by its effective toughness G_c^{eff}.

Homogenization of brittle fracture properties appears to represent a particular conundrum the solid mechanics scientific community is currently struggling with. Salvation could come from statistical and condensed matter physics. In the physics community, brittle fracture has been linked to the depinning transition theory through the framework of the perturbative LEFM initially proposed by Rice [1985]. Approaches and concepts borrowed from this theory have been consequently adapted to fracture problems with remarkable successes [Bonamy and Bouchaud, 2011; Ponson, 2016]. Recent works of Patinet et al. [2013b], Démery et al. [2014b] and Démery et al. [2014a] renewed the interest in applying tools borrowed from statistical physics to predict effective fracture properties, an approach already implemented by Roux et al. [2003]. Yet, these works are restricted to the case of coplanar crack propagation where the crack can only interact with tough heterogeneities by a crossing mechanism. An extended framework needs to be developed to grasp the impact of the various mechanisms of interaction on the reinforcement of composite materials.

Physics of condensed matter also provided clues for considering fracture as a critical transition. Among them, the remarkable scaling properties of fracture surfaces have attracted a lot of attention in the last two decades. Since the pioneering work of Mandelbrot et al. [1984], fracture surfaces have been proven to display a unique scaling behavior referred to as *self-affinity*. If one looks at the height difference Δh between two points located at a

distance Δr (see Fig. 1.12), one observes that on average :

$$\Delta h \propto \Delta r^{\zeta} \tag{1.9}$$

where ζ is the roughness exponent. After a decade dedicated to the experimental characterization of the self-affinity of fracture surfaces for a wide range of materials [Mecholsky et al., 1989; Bouchaud et al., 1990; Dauskardt et al., 1990; Engøy et al., 1994; Schmittbuhl et al., 1995; Lôpez and Schmittbuhl, 1998; Morel et al., 1998; Boffa and Allain, 1998], studies have been focused on extracting quantitative information on the material properties or the loading failure conditions from the fracture surface through the investigation of its scaling properties [Ponson et al., 2006b; Ponson, 2007; Vernède et al., 2015]. Indeed, fracture surfaces, as persistent traces of crack propagation, can be viewed as crime scenes, which contain information on both the victim, i.e. the fractured material and its mechanical properties, the criminal, i.e. the loading which lead to structural failure, and the modus operandi, i.e. the history of crack propagation and dynamics. A true forensic science for fracture mechanics called *quantitative fractography* has been developed to extract information on the propagation direction [Ponson et al., 2006b; Ponson, 2007], the failure processes [Hansen and Schmittbuhl, 2003; Bonamy et al., 2006; Morel et al., 2008] and even the fracture properties of the material inferred from the measurement of the process zone size [Vernède et al., 2015; Osovski et al., 2015; Barak et al., 2019]. Yet the surface roughness of brittle materials remains puzzling since a self-affine behavior with $\zeta = 0.4$ has been observed on porous brittle materials such as sandstone [Boffa and Allain, 1998; Ponson et al., 2007] or sintered glass/polysterene beads material [Ponson et al., 2006a; Cambonie et al., 2015] while phase-separated [Dalmas et al., 2008] or oxide brittle glass [Pallares et al., 2018] display a logarithmic scaling behavior ($\Delta h \propto \ln(\Delta r)$). If LEFM-based models can predict both behaviors theoretically [Ramanathan et al., 1997; Bonamy et al., 2006], direct simulations of crack growth in disordered brittle solids only capture logarithmically rough surfaces [Ramanathan et al., 1997; Barès et al., 2014]. Without a deep understanding of the underlying physical mechanisms, quantitative fractographic tools for brittle materials are currently out of reach.

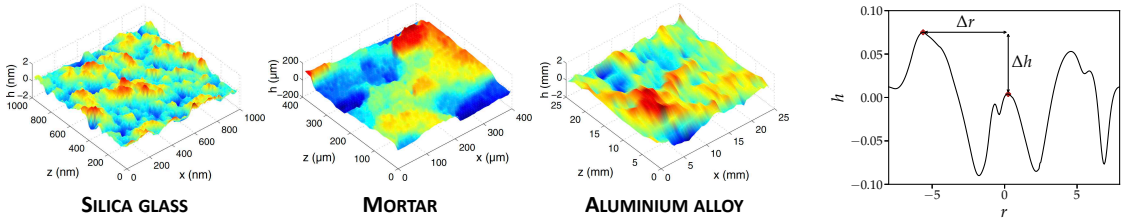

(a) (b) (c) (d)

Figure 1.12: Topograhic images of rough surfaces of brittle silica glass (a), quasi-brittle mortar (b) and ductile aluminium alloy (c) (after [Ponson, 2007]) and 1D height profile along the front direction (Oz) for the computation of the height-height correlation function (d).

1.5 Outline of the PhD thesis

The challenges exposed above motivates the development of reliable models that capture three-dimensional crack propagation from the microscopic scale up to the macroscopic one, and quantify the impact of material heterogeneities on the effective fracture properties and the scaling properties of brittle fracture surfaces. The present work addresses this challenge, building on the specificities of brittle fracture. Brittle fracture is (i) an *evolution problem*, which (ii) involves *dissipative processes localized at the crack tip* and (iii) is related to a *structural problem*. Crack evolution is described here by a powerful semi-analytical method, modeling *crack propagation* in heterogeneous materials based on the perturbative approach of Linear Elastic Fracture Mechanics [Gao and Rice, 1986; Movchan et al., 1998]. Our main objective is to go beyond the previous works of Gao and Rice [1989], Patinet et al. [2013b] and Démery et al. [2014b], which were restricted to coplanar crack propagation, by *enriching the dissipative processes* occurring at the crack tip through the modeling of a by-pass mechanism, which triggers excursions of the crack out of the mean fracture plane. The ultimate contribution of each mechanism to material toughening is inferred from the *evolution of the Energy Release Rate G*. Numerical results are compared to theoretical predictions, derived from a three-step homogenization scheme inspired by micromechanics and statistical physics. The PhD manuscript is structured as follow :

Chapter 2 - Crack propagation in heterogeneous materials

This chapter is dedicated to the construction of a powerful perturbative LEFM-based theoretical framework to model crack propagation in large-scale composite materials made of toughness heterogeneities embedded in a homogeneous matrix. Two interaction mechanisms are modeled : inclusion crossing, wherein the crack penetrates the tough inclusion, and inclusion by-pass, where the crack goes around the inclusion and propagates along the matrix/inclusion interface. We also detail the key points of the numerical implementation and the unprecedented computational performance offered by the method.

Chapter 3 - Mechanisms of interaction between a crack and tough inclusions

Interaction mechanisms control both the crack dynamics and the material reinforcement induced by toughness heterogeneities. In this chapter, we focus on periodic geometries to deeply investigate some fundamental aspects of the crack interaction problem in model situations. Our work reveals the subtle three-dimensional coupling between the in-plane and out-of-plane deformation modes of a crack front during its interaction with a microstructural heterogeneity. The conditions under which one mechanism prevails over the other and its ultimate contributions to toughening are thoroughly investigated for a broad range of inclusion shapes and fracture properties.

Chapter 4 - Homogenization of brittle fracture properties for large-scale composites

This chapter is dedicated to the question of the effective fracture properties of large-scale disordered materials. After questioning the definition of the effective toughness, we develop a theoretical framework for the homogenization of brittle fracture properties, which takes into account the various contribution of crack-tip interaction mechanisms. The predictions of the effective toughness resulting from the homogenization procedure are compared to numerical simulations modeling the competing influence of the crossing and by-pass mechanisms for a wide range of microstructural parameters.

Chapter 5 - Deciphering fracture surfaces of brittle materials

The chapter investigates the impact of material disorder on the scaling properties of brittle fracture surfaces. A theoretical study allows for the determination of a structure function for the two-points correlation function of the height of the fracture surface. Analytic predictions are then compared to the roughness of numerically generated large-scale fracture surfaces in order to quantify the impact of microstructural parameters on the surface statistical properties. Finally, we describe which quantities can be extracted from the surface roughness using statistical fractographic tools.

Chapter 6 - Experimental study of crack propagation in 3D printed heterogeneous polymers

This chapter closes the loop and proposes an experimental study of dynamic crack propagation in 3D-printed polymers. Tensile fracture tests of 3D-printed striped polymers are performed. The test results are analyzed through the means of advanced digital image correlation methods and provide quantitative measurements of the effective toughness of composite materials in the most simple case of one-dimensional heterogeneities.

Chapter 7 - Conclusion and perspectives

Finally, some conclusions are drawn by summarizing the main results of the combined theoretical, numerical and experimental approaches. Future prospects are also evoked, by furnishing indications towards more advanced development of heterogeneous brittle fracture.

Results of Chapters 2 & 3, Chapter 4 and Chapter 6 are submitted for publication ([Lebihain et al., 2020a], [Lebihain et al., 2020b] and [Albertini et al., 2020]). Additional publications related to Chapter 4 and Chapter 5 are currently in preparation ([Lebihain et al., 2020d] and [Lebihain et al., 2020c]).

2

Crack propagation in heterogeneous materials : a perturbative approach

Contents

2.1 Introduction

The development of a microstructure-sensitive theory of fracture has been a query for decades in solids mechanics. Today, the boom of additive manufacturing techniques and the emergence of bio-source and recycled composite materials driven by environmental concerns has increased further the need to rationalize the failure behavior of micro-structured solids [Reis, 2006; Jo et al., 2008; Dimas et al., 2013; Wang and Xia, 2017]. Yet, a theoretical framework that allows to predict the toughness of materials from their microstructural features is still missing.

Since Griffith [1921]'s energy-balance concept put crack advance at the core of the notion of material toughness G_c, the construction of a theoretical framework for toughness homogenization properties should undoubtedly be based on an accurate description of crack propagation in presence of material heterogeneities. If recent approaches such as the energetic variational minimization approach to fracture [Francfort and Marigo, 1998] has displayed substantial advantages in taking into account material disorder, traditional LEFM

approach, based on the stress intensity factors (SIF) $(K_{\mathrm{I}}, K_{\mathrm{II}}, K_{\mathrm{III}})$ or the elastic energy release rate G (ERR), still finds a prominent place in the fracture community due to the maturity acquired by its long history. This approach allows to describe crack propagation through appropriate propagation criteria. Those criteria link local stress intensity factors (K_p) or energy release rate G to material toughness K_{Ic} or its fracture energy G_{c} to describe under which loading conditions [Griffith, 1921; Irwin, 1962] and in which direction [Erdogan and Sih, 1963; Hussain et al., 1974; Gol'dstein and Salganik, 1974] the crack will extend. The construction of a LEFM based theoretical framework requires thus three main ingredients : (i) the access to local SIF (K_p) or ERR G in the presence of material disorder, (ii) an accurate description of the local toughness field,G_{c}, (iii) the development of adequate propagation criteria taking into account the mechanical anisotropy induced by material heterogeneities.

Theoretical developments, among which the J-integral method [Rice, 1968], have allowed the analytical determination of local stress intensity factors for various crack geometries in two-dimensional and three-dimensional settings. Yet, the presence of heterogeneities distorts the crack front and surface, which cannot be modeled by standard configurations any further. It has driven the development of a perturbative LEFM approach pioneered by Rice [1985] to circumvent those limitations. Based on Bueckner-Rice weight functions theory [Bueckner, 1970, 1987], this method allows to compute local stress intensity factors variations (δK_p) from any small crack front geometrical perturbations from a reference crack without resolving the whole elasticity problem. Initially developed for coplanar perturbations of an half-plane crack under tensile loading [Rice, 1985], it has been then extended to coplanar cracks in mixed mode [Gao and Rice, 1986], various crack geometries (internal and external circular crack [Gao and Rice, 1987b,a], single and double tunnel crack [Leblond et al., 1996; Lazarus and Leblond, 2002b; Pindra et al., 2010; Legrand and Leblond, 2010]), dynamic propagation [Rice et al., 1994; Willis and Movchan, 1995] and even to second-order in the perturbation [Leblond et al., 2012; Vasoya et al., 2013]. This theory has been implemented numerically to model coplanar crack propagation in heterogeneous materials displaying weak toughness discontinuities. It allowed to predict, at first-order, the influence of crack trapping [Gao and Rice, 1989] microstructural disorder [Roux et al., 2003; Roux and Hild, 2008; Patinet et al., 2013b; Démery et al., 2014b,a] or inclusion shape [Xia et al., 2012; Hsueh and Bhattacharya, 2018] on the effective fracture properties of such materials. For larger perturbations arising from higher heterogeneity toughness contrast, numerical methods have been developed [Bower and Ortiz, 1990; Lazarus, 2003] to highlight various toughening mechanisms such as crack bridging [Bower and Ortiz, 1991] or crack fingering [Vasoya et al., 2016a] and their respective impact of the effective toughness. This perturbative framework has also been successfully compared to experiments of interfacial fracture set-up [Delaplace et al., 1999; Dalmas et al., 2009; Chopin et al., 2011], especially when finite-size effects [Legrand et al., 2011; Patinet et al., 2013a] or second-order terms [Vasoya et al., 2016b] are taken into account.

Movchan et al. [1998] extended Rice's coplanar perturbative approach to the fully three-dimensional problem by estimating the first-order perturbated stress intensity factors, (δK_p) induced by an out-of-plane perturbation of the crack front and crack surface. Explicit formulæ have been derived in the case of the half-plane crack under mixed mode I+II+III. Theoretical and numerical studies are thus no more constrained to coplanar propagation, paving the way for the study of the in-plane and out-of-plane coupling of both deformation modes on crack trajectory. Yet, up to this day, studies dealing with the full three-dimensional perturbative framework remain scarce. It has mainly been used to study the nucleation of facets in mode I+III from an instability [Leblond et al., 2011; Leblond and Ponson, 2016; Leblond et al., 2019]. Among those studies, only Leblond and Ponson [2016] consider a heterogeneous material, being a single inclusion invariant in the direction of crack propagation. Other studies relying on Gao and Rice [1986] and Movchan et al. [1998]'s formulæ chose as main hypothesis a complete decoupling of the in-plane and out-of-plane problem [Ramanathan et al., 1997; Bonamy et al., 2006; Barès et al., 2014], the in-plane perturbation controlling crack dynamics whereas the out-of-plane perturbation dictates crack trajectory. Thus, they fail into predicting the effect of the coupling between the in-plane and out-of-plane perturbations during the interaction of a crack and given inclusions, that will be shown to play an important role. Moreover, these works do not introduce an accurate description of the material microstructure and its mechanical properties since microstructural effects are heuristically embedded in the set of perturbative equations as stochastic noises. We will show that in a three-dimensional non-coplanar setting crack-inclusion interaction and their occurrence conditions cannot be captured by such an approach as it was the case for coplanar mechanisms.

As in any micro-mechanical approach, introducing realistic microstructures requires local mechanical properties and especially a local toughness field G_c. Combined with the estimation of the local stress intensity factors ($K_p + \delta K_p$) along the crack front, computed from the perturbative approach [Gao and Rice, 1986; Movchan et al., 1998], such theoretical framework would still miss a propagation criterion to be complete. In the coplanar case, the propagation criterion reduces to a kinetic law, linking G and G_c (or equivalently K_I and K_{Ic}) to the local speed of the crack front. It can be derived from a viscous regularization of Griffith's criterion [Gao and Rice, 1989] in brittle fracture or a Paris' law [Paris and Erdogan, 1963; Bower and Ortiz, 1990; Lazarus, 2003] in fatigue. In the three-dimensional case, the kinetic law has to be combined with a direction criterion, since the propagation is no more constrained in a plane. In homogeneous media, criteria such as the principle of local symmetry (PLS) [Gol'dstein and Salganik, 1974], the maximum tangential stress criterion (MTS) [Erdogan and Sih, 1963] or the maximum energy release rate criterion (MERR) [Hussain et al., 1974], have been shown to describe accurately the direction taken by the crack in mixed mode I+II observed in experiments. In the case of heterogeneous materials, many of these criteria break down due to the introduction of local toughness anisotropy. A new direction criterion has to be proposed to address the heterogeneous case and the generalized energy release rate criterion (GMERR) appears to be the most promising candidate. Initially introduced by He and Hutchinson [1989] for the problem of

crack deflection at the interface between two materials with dissimilar elastic properties, it states that the crack propagates in the first direction where $G = G_c$ is achieved, as a direct extension of Griffith's and MERR criteria to the anisotropic case. Theorized by Gurtin and Podio-Guidugli [1998], it has then been validated numerically through phase field simulations [Hakim and Karma, 2005, 2009] and in the variational approach of fracture [Chambolle et al., 2009; Bleyer and Alessi, 2018; Li and Maurini, 2019]. Recent experiments on the tearing of weakly [Ibarra et al., 2016] and strongly [Takei et al., 2013] heterogeneous sheets tend to confirm the validity of such criterion in the heterogeneous case.

Following this line, the present chapter aims at proposing a perturbative framework allowing to model crack propagation in three-dimensional heterogeneous brittle materials exhibiting toughness discontinuities. The proposed approach combines a detailed description of a microstructure constituted by tougher inclusions, a perturbative approach for SIF evaluation and finally an energetic propagation criterion, to link them together. It allows us to model two interaction mechanisms : inclusion crossing, when the crack goes through the defect [Gao and Rice, 1989; Bower and Ortiz, 1990], and inclusion by-pass, where the crack goes out-of-plane and propagates along the inclusion interface [Clayton and Knap, 2014; Gao et al., 2018a], both observed experimentally for example in fracture tests on clay (Fig. 2.1). In Section 2.2, fundamental elements and hypotheses of the theoretical framework will be presented : our microstructure and its geometrical and mechanical properties, the perturbative approach based on the combination of the works of Gao and Rice [1986] and Movchan et al. [1998] to compute local stress intensity factors for any crack configuration and finally the propagation criterion, which consists in the combination of a viscous regularization of Griffith criterion with the GMERR [Gurtin and Podio-Guidugli, 1998], applied via Amestoy-Leblond's formulæ in three dimensions [Leblond, 1999]. Section 2.3 is devoted to the numerical implementation of the model in language C. Its numerical performances, relying on the execution of fast Fourier transforms, are presented. An acceleration procedure is then proposed to speed up computations and model the interaction of a crack with millions of inclusions, making its performances impossible to match with equivalent finite element simulations. Finally, the potential of the perturbative approach developed in is illustrated in Section 2.4.

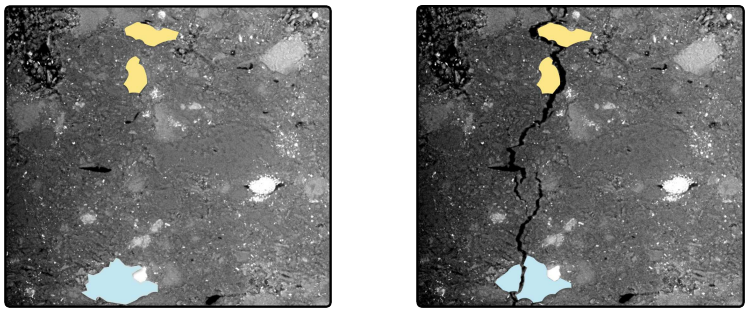

(a) Sane clay (b) Fractured clay

Figure 2.1: Fracture experiments on clay with by-passed inclusion (in beige) and crossed one (in blue) (courtesy of M. Bornert)

2.2 Theoretical modeling

In contrast to variational approaches [Francfort and Marigo, 1998; Nguyen et al., 2017b; Bleyer and Alessi, 2018; Li and Maurini, 2019] and phase field models [Hakim and Karma, 2005, 2009], where both questions of crack initiation and propagation are addressed within a "global" approach at the scale of the entire structure, the traditional approach of LEFM, as used in this chapter, relies on local propagation criteria using the Stress Intensity Factors $(K_{\mathrm{I}}, K_{\mathrm{II}}, K_{\mathrm{III}})$ (SIFs) and/or the elastic Energy-Release-Rate G (ERR) in combination with the material toughness G_{c}, to predict the crack path and the loading conditions actually leading to fracture. Any predictive method of crack propagation based on this classical framework thus requires three main ingredients, be it in the homogeneous or heterogeneous case, for a mode I loading or mixed-mode conditions :

1. the definition of a given microstructure, which provides, in our specific case, the field $G_{\mathrm{c}}(\underline{x})$ of fracture energy experienced by the crack when propagating. Note that with some abuse of terminology, we shall refer to the fracture energy $G_{\mathrm{c}} \equiv \dfrac{1-\nu^2}{E} K_{\mathrm{Ic}}^2$ as the "toughness" of the material;

2. some way of calculating the SIFs $(K_p)_{p\in\{\mathrm{I,II,III}\}}$ and the ERR G along the crack front $\mathcal{F}$, for any crack configuration differing slightly from a planar crack with a straight front;

3. some propagation criteria, combining a prediction of the future direction of propagation and a kinetic law for the crack front advance, based on the previous elements.

The following sections describe how each of these ingredients is accounted for, and how they are connected to each other. In Section 2.2.1, we describe the microstructures considered and explain how they are generated, including a discussion of the simplifying hypotheses made. Section 2.2.2 expounds the perturbative three-dimensional LEFM approach used, focusing on the sole case of a semi-infinite crack subjected to some tensile loading. The combination of these two ingredients within a Generalized Maximum Energy Release Rate (GMERR) criterion and a kinetic law is explained in Section 2.2.3.

2.2.1 Heterogeneous microstructure and toughness field

2.2.1.a Microstructural properties of the cracked composite

We consider a semi-infinite crack embedded in an infinite periodic body. We adopt the usual convention of LEFM and thus denote x the direction of crack propagation, y the direction orthogonal to the crack plane, and z the direction parallel to the crack front $\mathcal{F}$. Also, the period in the z-direction is denoted L_z. The associated unit vectors are denoted $(\underline{e}_p)$. At a given time t, the position of the crack front within the crack plane is noted $x(t)$, the origin O being chosen arbitrarily within this plane (Fig. 2.2.a).

The fracture specimen is made of a heterogeneous material constituted by two phases : a homogeneous matrix and spherical inclusions. The inclusion distribution $\mathcal{D}$ is defined by the inclusion position $(x^s, y^s, z^s)_{s\in[\![1;N]\!]}$ and their geometry $(\mathcal{G}^s)_{s\in[\![1;N]\!]}$, which can be either

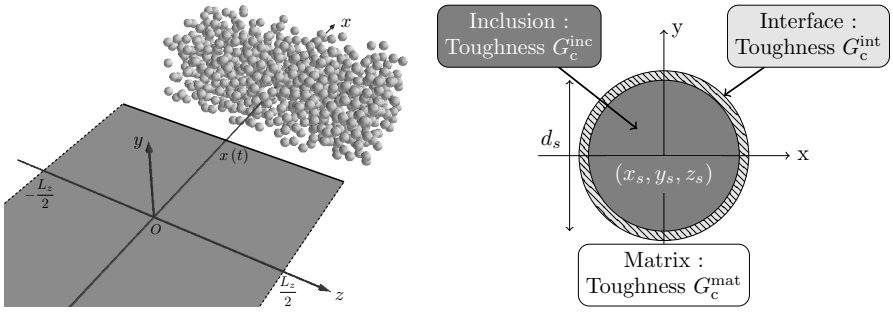

(a) 3D heterogeneous cracked material

(b) Inclusion properties definition

Figure 2.2: (a) Semi-infinite crack facing a polydisperse inclusion distribution with varying toughness; (b) Fracture properties of the inclusion, the matrix and their interface.

spherical, cubical or ellipsoidal as depicted in Fig. 2.3. These inclusions are characterized by their typical size d, which is for example the inclusion diameter in the case of spherical inclusions (mean diameter for polydisperse distribution) or its edge length in the case of cubical ones (mean edge length for polydisperse distribution). In the following, the spherical geometry is taken as a reference case.

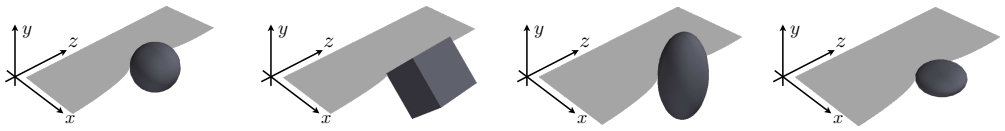

(a) (b) (c) (d)

Figure 2.3: Various geometries considered in the following manuscript : spherical (a), cubical (b), ellipsoidal prolate (c) or oblate (d) inclusions

Two main assumptions are made regarding the mechanical behavior of each phase. First, the matrix and the inclusions are assumed to be isotropically and linearly elastic and share the same Young modulus E and Poisson ratio ν. Second, the phases are assumed to be brittle but differ in their fracture properties: the inclusions may be tougher and/or weakly bonded to the matrix. These properties are characterized by an inclusion toughness G_c^{inc} and an interfacial toughness G_c^{int} as depicted in Fig. 2.2.b.These fracture properties may vary from one inclusion to another. They are defined as :

$$\begin{cases} G_c^{inc} = G_c^{mat}\left(1 + c_{inc}\right), \; c_{inc} > 0 \\ G_c^{int} = G_c^{mat}\left(1 + c_{int}\right), \; c_{int} < 0 \end{cases} \tag{2.1}$$

where $G_c^{mat} = \dfrac{1-\nu^2}{E} K_{Ic}^{mat\,2}$ is the matrix toughness.

Limiting our study to toughness heterogeneities, without considering the impact of spatial variations of elastic properties on crack propagation, is a severe restricting hypothesis of this work. The impact of elastic heterogeneities on crack propagation have been underlined in many studies, both on crack trajectory [He and Hutchinson, 1989; Leguillon and Martin,

2013] and effective fracture properties [Li and Zhou, 2013a,b; Hossain et al., 2014; Wang and Xia, 2017; Brach et al., 2019b]. Possible extensions of our study incorporating elastic heterogeneities based on the work of Gao [1991] and Muju [2000] are discussed at the end of this chapter in Section 2.5.

2.2.1.b Toughness discontinuities : a matter of lengthscale

As explained in the introduction chapter, the question of lengthscales is at the core of the LEFM framework. Because of the description of a crack as displacement discontinuity, the crack tip stresses become singular [Williams, 1952]. Yet, this stress singularity is physically unacceptable so that dissipative processes are present in the vicinity of the crack tip, thus releasing stresses. All these processes are confined in a zone called *process zone*, or alternatively *fracture process zone* (Fig. 2.4.b). An estimation based on a cohesive zone approach with constant material strength σ_c has been proposed by Barenblatt [1962] :

$$\ell_{\text{FPZ}} = \frac{\pi}{8}\left(\frac{K_{Ic}}{\sigma_c}\right)^2 \tag{2.2}$$

Considering the case of brittle failure, we assume that the process zone size ℓ_{FPZ} is far smaller than the typical size d of the heterogeneities. Otherwise the interaction from a crack with inclusion can result in inclusion debonding and microcracking, as numerically predicted and experimentally observed in quasi-brittle materials such as concrete [Nguyen et al., 2017b]. Those phenomena are not modeled in our study.

Aside from the brittle failure hypothesis, we seek to model the impact of toughness discontinuities. It supposes that the crack is not able to detect the continuous variation of G_{c} between its value in the matrix, $G_{\text{c}}^{\text{mat}}$, on the interface $G_{\text{c}}^{\text{int}}$ and in the inclusion $G_{\text{c}}^{\text{inc}}$. If we note ℓ_Δ the typical lengthscale on which those properties vary (Fig. 2.4.c), ℓ_Δ has to be far smaller than the process zone size ℓ_{FPZ}. Otherwise, the crack will see a continuous variation of G_{c}, which can have tremendous impact on crack-inclusion interaction since the crack no longer by-passes the inclusion (Chapter 6).

Finally, our assumptions require than we can model fairly well crack propagation in our material by considering a semi-infinite crack. We thus suppose that the heterogeneity size d is far small that the size of the structure L_{struct}. Otherwise, finite-size effect as reported in Legrand et al. [2011] could be observed. In the end, we assume that :

$$\ell_\Delta \ll \ell_{\text{FPZ}} \ll d \ll L_{\text{struct}} \tag{2.3}$$

These assumptions are mandatory if one wants to use Gao and Rice [1986]'s and Movchan et al. [1998]'s perturbative formulæ. They are compatible with a large range of brittle materials including ceramics, glasses or brittle rocks like limestone.

The proposed description of a typical microstructure of a heterogeneous brittle solid leads to a three-dimensional toughness field $G_{\text{c}}(z, x, y)$. This field markedly differs from those considered in previous three-dimensional perturbative studies [Ramanathan et al., 1997;

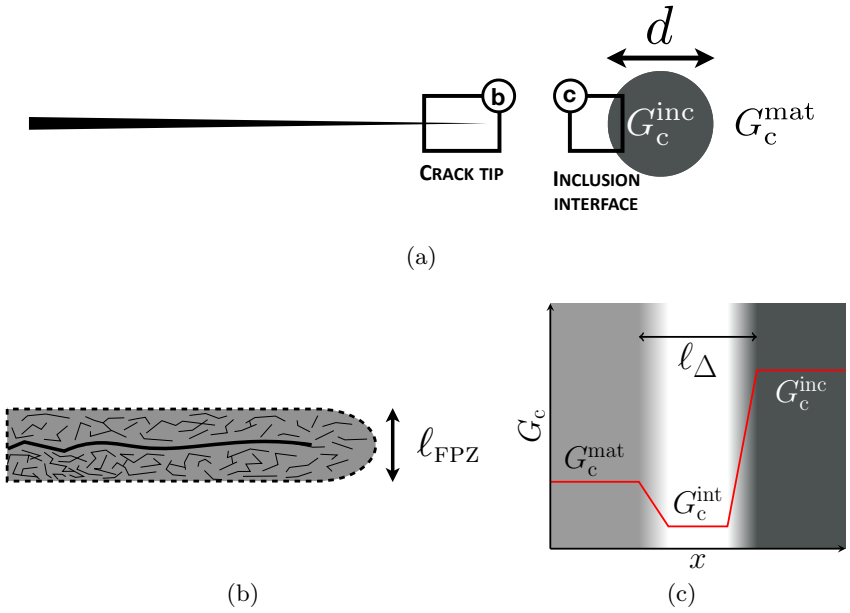

Figure 2.4: Illustration of the different lengthscales involved during the interaction of a crack with an inclusion : the inclusion size d (a), the size ℓ_{FPZ} of the process zone, within which all inelastic processes are confined, (b) and the interface width ℓ_Δ, characterizing the size of the transition region between the fracture toughness of the matrix and the one of the inclusion (c).

Barès et al., 2014] which used a stochastic field of fracture energy deriving from a statistical distribution, since we consider here actual microstructures resulting from inclusions with given shape and fracture properties. Also, the perturbations introduced in the set of LEFM equations will not be imposed heuristically but deduced from the actual interaction between the crack and the inclusions. It is worth noticing that the methodology proposed may be applied to any defect geometry provided that the defect boundary and in particular the normal vector to this boundary are unambiguously defined, which may be achieved for instance using level set methods.

2.2.2 Perturbative approach for three-dimensional cracks

2.2.2.a Macroscopic loading

We consider a semi-infinite plane crack in a fracture specimen loaded under tension (Mode I) with a loading parameter λ. To comply with the experimental set-up used in Chapter 6, this parameter can be taken as a prescribed displacement. The effect of the loading conditions and the sample geometry are included in our model via the evolution of the macroscopic elastic energy release rate G^∞ with the crack position x (Fig. 2.2.a) :

$$G^\infty(\lambda, x) = \lambda^2 g(x) \tag{2.4}$$

where the geometrical contribution g of the ERR derives either from analytical solutions or from FE simulations. We assume $g'(x) < 0, \forall x$ that ensures stable crack propagation, *i.e.* crack arrest under constant loading $\dot{\lambda} = 0$.

Yet, we want to study the effect of loading conditions and sample geometry through as

few parameters as possible. So, following Ponson and Bonamy [2010], we limit our analysis to short propagation distance $x(t) \ll \mathcal{L}$, where $\mathcal{L}$ is a structural length that emerges from the variations of g with crack length. Considering a constant loading rate $\dot{\lambda}$, we can write at the first order :

$$G^{\infty}(\lambda, x) = G^{\infty}(\lambda_0, 0) + \left.\frac{\partial G^{\infty}}{\partial \lambda}\right|_{\lambda_0,0} \dot{\lambda} t + \left.\frac{\partial G^{\infty}}{\partial x}\right|_{\lambda_0,0} x \tag{2.5}$$

which can be put in the form :

$$G^{\infty}(t) = G_0 \left(1 + \frac{v_{\mathrm{m}} t - x(t)}{\mathcal{L}}\right) \tag{2.6}$$

where $G_0 = G^{\infty}(\lambda_0, x_0 = 0)$ is the initial loading. The structural length $\mathcal{L}$ and the average crack front velocity v_{m} imposed by the loading rate are defined by:

$$\mathcal{L} = -G_0 / \left.\frac{\partial G^{\infty}}{\partial x}\right|_{\lambda_0,0}, \; v_{\mathrm{m}} = -\dot{\lambda} \left.\frac{\partial G^{\infty}}{\partial \lambda}\right|_{\lambda_0,0} / \left.\frac{\partial G^{\infty}}{\partial x}\right|_{\lambda_0,0}. \tag{2.7}$$

These parameters are of particular interest and have the following physical meanings:

- v_{m} is the crack velocity for a semi-infinite plane crack propagating in a homogeneous medium. Indeed, in the stationary regime $G(x,t) = G_{\mathrm{c}}^{\mathrm{mat}}$ according to Griffith's criterion. If we differentiate this relation in time, it gives us $\dot{x}(t) = v_{\mathrm{m}}$, which shows that v_{m} characterizes both a loading and a structural effect : it corresponds to the mean crack advance for a given sample geometry and a given loading rate ;
- $\mathcal{L}$ is a characteristic distance of G^{∞} variations for a straight front. This characteristic length allows to model the impact of sample geometry and has implications on the growth of the in-plane perturbations. If $\mathcal{L}$ is low, any planar perturbation δx around the mean position $v_{\mathrm{m}} t$ of the crack is shutdown immediately whereas if $\mathcal{L}$ is large enough, such perturbation can persist during the propagation allowing non-local interactions along the front [Ponson and Pindra, 2017].

Note that we assume that the macroscopic ERR G^{∞} is constant along z for the reference straight plane crack. As noted by Gao and Rice [1989], this means that the crack perturbation wavelengths are small in comparison to any structural length.

2.2.2.b Perturbative approach for local SIF evaluation

In a homogeneous material, the semi-infinite crack would undergo stable coplanar propagation at the speed v_{m}, and the crack front $\mathcal{F}$ would remain straight at the instantaneous position $x(t) = v_{\mathrm{m}} t$. But material heterogeneities distort the crack front both within the mean fracture plane (crack trapping) and out of it (crack deflection) (Fig. 2.2). In this case, the ERR $G(z,t)$ along the crack front differs locally from $G^{\infty}(t)$ and needs to be computed in order to predict crack propagation through a propagation criterion. As stated in the chapter introduction, the perturbative LEFM approach can be a powerful theoretical framework to address this question.

Bueckner-Rice weight functions theory

Based on Bueckner [1970]'s and Bueckner [1987]'s work on weight functions theory, Rice [1985] developed a perturbative method, which allows to compute at first-order local stress intensity factors variations (δK_p) from any coplanar crack front perturbations. We present here shortly the core elements of Rice's approach revisited in a broader context by Leblond et al. [1999]. Readers are invited to see Lazarus [2011] for an extensive review.

Following Favier et al. [2006a], we consider a planar crack of arbitrary shape embedded in an isotropic elastic medium Ω subjected to arbitrary loading : given forces $\underline{T}^0$ on $\partial\Omega_T$ and given displacements $\underline{u}^0$ on $\partial\Omega_u$. We define $k_{pj}\left(\mathcal{F}, M, \tau, \tau'\right)$ the p-th SIF for a given linear position τ' along the crack front $\mathcal{F}$ resulting from application at point M, located at a distance r from τ, of a pair of opposite unit point forces equal to $\pm\underline{e}_j\left(\tau\right)$ on the upper (+) and lower (-) crack surfaces. The applied loading is zero elsewhere ($\underline{T}^0 = \underline{0}$ on $\partial\Omega_T$ and $\underline{u}^0 = \underline{0}$ on $\partial\Omega_u$). Those functions are called *crack face weight functions* (CFWFs) and depend only on the crack geometry and the definition of the partition $\partial\Omega_T \cup \partial\Omega_u$ of Ω frontier $\partial\Omega$. The situation is illustrated in Fig. 2.5.

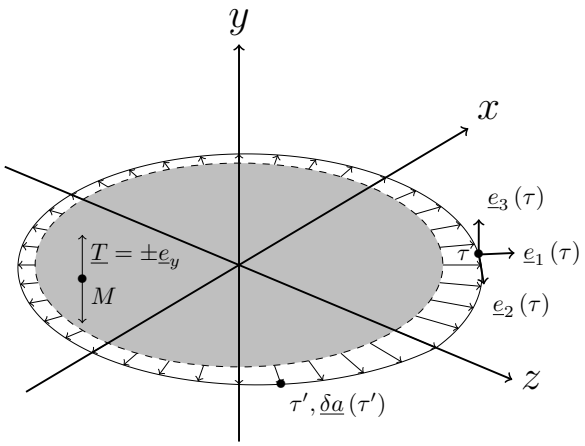

Figure 2.5: Arbitrary coplanar crack perturbed in its plane by $\underline{\delta a}$

Let us now consider a small in-plane extension $\delta a\left(\tau\right)\underline{e}_x\left(\tau\right)$ of the crack front $\mathcal{F}$ in the direction perpendicular to its front, under fixed loading condition. An ingenious reasoning based on an energy balance gives the variation of the crack opening displacement at point $M\left(z, x, y = \pm 0\right)$. It reads at first order :

$$\delta[\![u_y]\!]\left(M,\tau\right) = 2\frac{1-\nu^2}{E}\int_{\mathcal{F}} k_{Iy}\left(\mathcal{F}, M, \tau, \tau'\right) K_{\mathrm{I}}\left(\tau'\right)\delta a\left(\tau'\right) d\tau' \tag{2.8}$$

We can link this perturbed opening to local variations of Mode I SIF :

$$\delta K_{\mathrm{I}}\left(\tau\right) = \frac{E}{8\left(1-\nu^2\right)}\lim_{r\to 0}\sqrt{\frac{2\pi}{r}}\delta[\![u_y]\!]\left(M,\tau\right) \tag{2.9}$$

Leblond [1999] proved in a broader case that this limit is well-defined in the case where

$\delta a(\tau) = 0$, and gives :

$$\delta K_{\mathrm{I}}(\tau) = \frac{1}{2\pi} \int_{\mathcal{F}} \frac{W_{Iy}(\tau, \tau')}{D^2(\tau, \tau')} K_{\mathrm{I}}(\tau') \, \delta a(\tau') \, d\tau' \tag{2.10}$$

where $D(\tau, \tau')$ is the cartesian distance between the two points τ and τ' of the crack front $\mathcal{F}$, and W_{Iy} is called the *fundamental kernel* for Mode I in the y-direction.

The restriction $\delta a(\tau) = 0$ is then removed using a trick of Rice [1989] decomposed in two steps :

- for a given point determined by the linear abscissa τ_0, we subject the whole front $\mathcal{F}$ to a translatory motion $\delta a(\tau_0) \, \underline{e}_x(\tau_0)$. This motion brings the point τ_0 to its final position and the crack advance at some arbitrary point τ is $\delta a^*(\tau) = \delta a(\tau_0) \, \underline{e}_x(\tau_0) \cdot \underline{e}_x(\tau)$. The corresponding variation of K_{I} is denoted $\delta K_{\mathrm{I}}^*(\tau)$.
- a motion with normal advance $\delta a(\tau) - \delta a^*(\tau)$ so that the advance is null at τ_0 and the corresponding variation of K_{I} is given by Eq. (2.10).

Finally :

$$\delta K_{\mathrm{I}}(\tau) = \delta K_{\mathrm{I}}^*(\tau) + \frac{1}{2\pi} \int_{\mathcal{F}} \frac{W_{Iy}(\tau, \tau')}{D^2(\tau, \tau')} K_{\mathrm{I}}(\tau') \left[\delta a(\tau') - \delta a^*(\tau') \right] d\tau' \tag{2.11}$$

In the case of an half-plane crack parametrized by $\tau = z$ and loaded in macroscopic tensile mode, we have :

$$\begin{aligned} &K_{\mathrm{I}}(z) = K_{\mathrm{I}}^{\infty} \text{ and } \delta K_{\mathrm{I}}^*(z) = \frac{\partial K_{\mathrm{I}}^{\infty}}{\partial x} \delta a(z) = -\frac{1}{2\mathcal{L}} \delta a(z) \\ &\frac{W_{Iy}(\tau, \tau')}{D^2(z, z')} = \frac{1}{(z - z')^2} \end{aligned} \tag{2.12}$$

which finally leads to :

$$\frac{\delta K_{\mathrm{I}}}{K_{\mathrm{I}}^{\infty}}(z) = -\frac{1}{2\mathcal{L}} \delta a(z) - \frac{1}{2\pi} \int_{z'} \frac{\delta a(z) - \delta a(z')}{(z - z')^2} dz' \tag{2.13}$$

Initially derived by Rice [1985] for the half-plane crack under tensile loading, this result has latter been extended to mixed mode loading [Gao and Rice, 1986] and various geometries such as circular cracks [Gao and Rice, 1987b,a], and tunnel cracks [Leblond et al., 1996; Lazarus and Leblond, 2002b; Pindra et al., 2010; Legrand and Leblond, 2010]. Favier et al. [2006a] described the approach in the general case thanks to the introduction of the fundamental kernels W. The perturbative framework has been extensively used to study the questions of crack stability [Rice, 1985; Gao and Rice, 1986, 1987b, 1989; Lazarus and Leblond, 2002b,a; Favier et al., 2006a] , where is investigated whether a given perturbation vanishes (stability) or instead increases (instability) in time, and bifurcation [Rice, 1985; Gao and Rice, 1986, 1987b; Leblond et al., 1996; Nguyen, 2000; Lazarus and Leblond, 2002a], where solutions satisfying $G = G_{\mathrm{c}}$ for non-straight configurations are explored.

In light of our problem, the perturbative framework paved the way for numerical simulations of coplanar crack propagation in materials displaying toughness discontinuities. Gao and Rice [1989] shed light on the mechanism of *crack trapping*, where weakly tough inclusions block the crack front, making it bow between them. Bower and Ortiz [1990] extended this numerical method by updating the fundamental kernels during propagation and make the crack propagate with an implicit scheme. Lazarus [2003] later simplified the procedure with an explicit scheme. It allowed to illustrate the case of crack interaction with tougher inclusions, where the crack bows so much around the particle that it leaves it behind unbroken. The crack surfaces are thus pinned by those intact particles, leading to *crack bridging* which was quantitatively described by Bower and Ortiz [1991]. Vasoya et al. [2016a] described similar mechanism of crack fingering, where large bowing happens in-between very tough obstacles. These papers highlight rich crack-inclusion interaction mechanisms and their implications on fracture properties but in the sole coplanar case. We aim now at investigating the impact of out-of-plane excursions on crack propagation and the effective toughness of three-dimensional composites.

Three-dimensional perturbative approach

Movchan et al. [1998] extended Rice's coplanar first-order approach to the fully three-dimensional problem by estimating the perturbed SIF induced by an out-of-plane perturbation of the crack front and crack surface.

In the following, we note $f_x(z,t)$ the in-plane perturbation of the crack front, and $f_y(z,t)$ its out-of-plane perturbation. The in-plane perturbation is defined from the reference crack position $x(t)$ (see Fig. 2.6) chosen to satisfy the condition $\langle f_x(z,t)\rangle_z = 0$. With these notations, the coordinates of a point M along the crack front are given by $(z_M, x_M, y_M) = (z, x(t) + f_x(z,t), f_y(z,t))$.

Combining the respective work of Gao and Rice [1986] for the in-plane situation and Movchan et al. [1998] for the out-of-plane problem , we can link those perturbations f_x and f_y and the local SIF variations $(\delta K_p)_{p\in\{\mathrm{I,II,III}\}}$. Complete formulæ are given in Section 8.B for mixed loading (Mode I+II+III) considering (K_p) but also the T-stresses (T_{ij}) (constant terms in the asymptotic development of the crack tip stresses) and A-stresses (A_p),($\sqrt{r}$ terms in the asymptotic development of the crack tip stresses).

Here, we make the following assumptions :

- the propagation is quasi-static, so as any time t we can define the local crack front position (z_M, x_M, y_M) and the associated reference crack located at $x(t)$. This assumption is mandatory to use the quasi-static perturbative approach of Gao and Rice [1986] and Movchan et al. [1998];
- the crack is loaded in pure Mode I macroscopically : $K_{\mathrm{I}}^{\infty} = \sqrt{\frac{E}{1-\nu^2}\,G^{\infty}}$, $K_{\mathrm{II}}^{\infty} = 0$, $K_{\mathrm{III}}^{\infty} = 0$. Under this hypothesis, we can put aside all the terms related to macroscopic K_{II} and K_{III} in the expressions of (δK_p);
- L_z, period in the z-direction but also the size of the biggest wavelength of the geo-

metrical crack front perturbations, is far smaller than the structural lengths $\left(\frac{K_{\mathrm{I}}^{\infty}}{T_{ij}}\right)^2$ and $\left(\frac{K_{\mathrm{I}}^{\infty}}{A_p}\right)$. Under these hypotheses, we can neglect the terms related to T-stresses and A-stresses in (δK_p) [Leblond and Ponson, 2016].

The last two assumptions are noncompulsory and are only made to address the difficult question of the homogenization of fracture properties in a "simpler" setting.

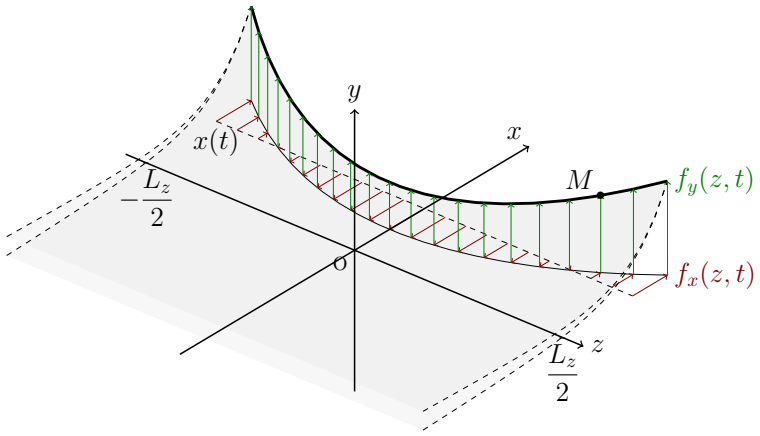

Figure 2.6: Perturbed crack with $f_x(z,t)$, in-plane perturbations along the crack front (in thick black), and $f_y(z,t)$, out-of-plane one, around a semi-infinite reference plane crack in $x(t)$

Under these assumptions, the SIF perturbations read at first-order :

$$\begin{cases} \dfrac{\delta K_{\mathrm{I}}(z,t)}{K_{\mathrm{I}}^{\infty}(t)} = -\dfrac{1}{2\mathcal{L}} f_x(z,t) - \dfrac{1}{2\pi}\,\mathrm{PV}\int_{-\infty}^{+\infty} \dfrac{f_x(z,t) - f_x(z',t)}{(z-z')^2}\,dz' \\ \dfrac{\delta K_{\mathrm{II}}(z,t)}{K_{\mathrm{I}}^{\infty}(t)} = \dfrac{1}{2}\dfrac{\partial f_y}{\partial x}(z,t) + \dfrac{2-3\nu}{2-\nu}\dfrac{1}{2\pi}\,\mathrm{PV}\int_{-\infty}^{+\infty} \dfrac{f_y(z,t) - f_y(z',t)}{(z-z')^2}\,dz' \\ \dfrac{\delta K_{\mathrm{III}}(z,t)}{K_{\mathrm{I}}^{\infty}(t)} = -\dfrac{2(1-\nu)^2}{2-\nu}\dfrac{\partial f_y}{\partial z}(z,t) \end{cases} \tag{2.14}$$

where ν is the Poisson ratio of the material and (PV) denotes the Cauchy principal value of the integral.

Simple comments can be made :

- even though the crack is loaded macroscopically in Mode I, local Mode II and Mode III components can arise from out-of-plane distortions of the crack;
- long-range elastic interactions exist along the crack front through the integral terms. This may lead to a collective response of the crack during its propagation in a three-dimensional medium as the behavior of a given point along the front is affected by the evolution of all the other ones;
- there are no terms proportional to f_y in the expression of δK_{I}, and no terms proportional to f_x in the expressions of δK_{II} and δK_{III}, a consequence of the various symmetries of the problem.

Formulæ (2.14) permit to compute the SIFs $\left(K_{\mathrm{I}}^{M}, K_{\mathrm{II}}^{M}, K_{\mathrm{III}}^{M}\right)$, and thus the ERR G at any location M along the crack front. Since the toughness values along the front and in its vicinity are determined from the position $\left(z, x\left(t\right) + f_x\left(z,t\right), f_y\left(z,t\right)\right)$, there remains only one missing piece in the puzzle, the propagation criterion, which is detailed hereafter.

2.2.3 Propagation criterion in heterogeneous LEFM

In homogeneous LEFM, standard propagation criteria are composed of a direction criterion, which states in which direction the crack extends, and a kinetic law, which tells along which distance it propagates. In the following subsection, we develop how to connect local stress intensity factors $\left(K_p\right) = \left(K_p^{\infty} + \delta K_p\right)$ with the toughness field data $G_{\mathrm{c}}\left(z,x,y\right)$ to determine in the heterogeneous case, the path the crack follows.

2.2.3.a Propagation states

During the propagation, the points along the crack front can be in four different states depicted in Fig. 2.7 through views in the $(x0z)$ and $(x0y)$ planes :

- State I : the point is propagating inside the matrix and may encounter an inclusion (Fig. 2.7.a and Fig. 2.7.b);
- State II : the point has just "landed" on a tough inclusion and is now trapped at its interface with the matrix (Fig. 2.7.c and Fig. 2.7.d);
- State III : after depinning from the matrix-inclusion interface, the crack crosses the inclusion (Fig. 2.7.e and Fig. 2.7.f);
- State IV : after depinning from the matrix-inclusion interface, the crack by-passes the inclusion, thus leaving the original fracture plane (Fig. 2.7.g and Fig. 2.7.h);.

One may distinguish between two types of propagation states. In State I and State III the point M is in a homogeneous phase; whereas in State II and State IV, it lies on an interface between two materials having different toughnesses. The local angular distribution of toughness is here anisotropic.

In homogeneous materials, standard direction criteria have been derived in mixed Mode I+II to determine in which direction the crack extends. The maximum tangential stress criterion (MTS) [Erdogan and Sih, 1963] states that the crack propagates in the direction where $\sigma_{\theta\theta}$, the local opening stress, is maximal. The maximum energy release rate (MERR) [Hussain et al., 1974] predicts that the crack goes in the direction where the ERR G is maximal. The principle of local symmetry (PLS) [Gol'dstein and Salganik, 1974; Cotterell and Rice, 1980], based on symmetry considerations, tells us that the crack kinks to make the Mode II vanish. The discrepancy between those criteria has been theoretically discussed by Amestoy and Leblond [1992]. Differences are so small that experiments may not allow to choose one over the other, especially between the MERR (energetic criterion) and the PLS (geometric criterion) whose expansions are identical up the third order in the kink angle.

The PLS being based on isotropy considerations, it is bound to fail in the heterogeneous

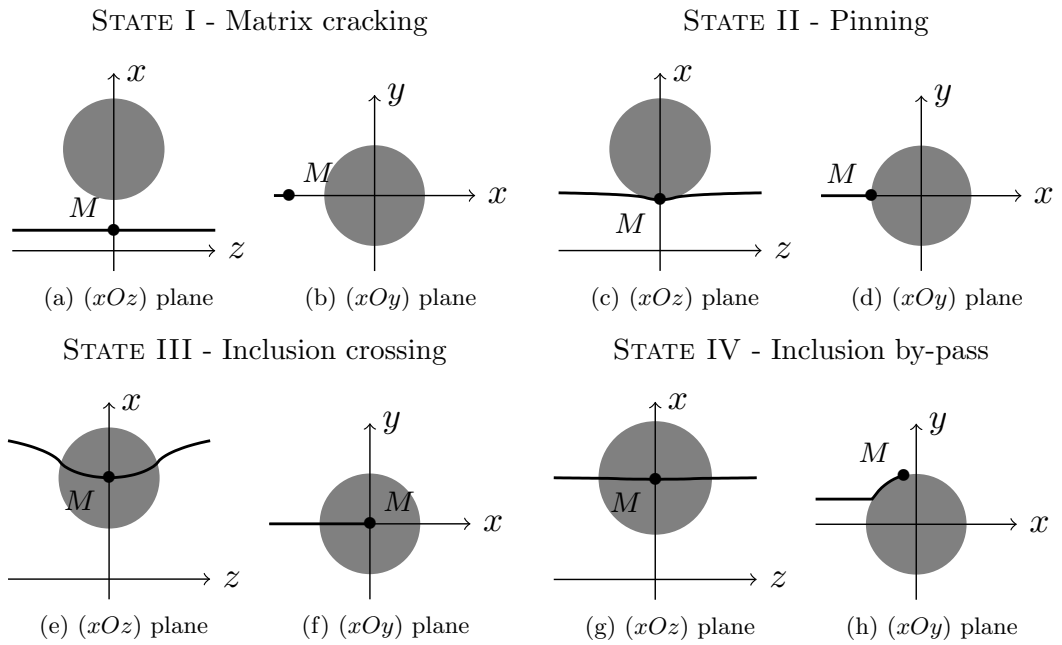

Figure 2.7: Four different possible states of a point M along the crack front during the propagation of a crack in our heterogeneous medium (front configurations extracted from simulations).

case. The three criteria being practically indistinguishable, they are thus all invalid in the heterogeneous case. Another direction criterion has to be applied to handle toughness anisotropy.

2.2.3.b A Generalized Maximum Energy Release Rate (GMERR) criterion for crack direction selection in anisotropic media

Generally, a point along the front is assumed to propagate within the plane orthogonal to the local tangent to the crack front, as depicted in Fig. 2.8. Here, we consider instead that each point M on the crack front propagates within the (xMy) plane. This approximation, that greatly simplifies the numerical computation by avoiding remeshing strategies like the one used in Bower and Ortiz [1990], Lazarus [2003] and Favier et al. [2006a], amounts to simplify second-order terms that thus can be neglected in our first-order perturbation model.

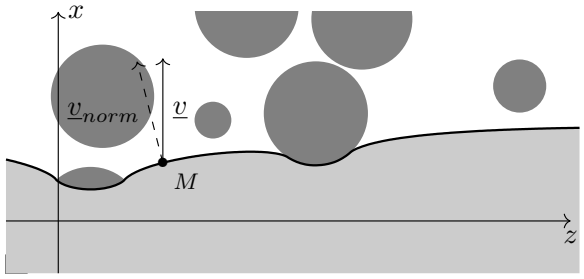

Figure 2.8: Propagation imposed for the point M in the plane (xMy) following $\underline{v}$ instead of the standard normal direction $\underline{v}_{norm}$

For pedagogical reasons, we shall now comment on the application of the criterion first

to State II and State IV, then to State I and State III.

Pinning on an interface (State II)

Let us consider the general case where a crack which just has just landed in M on an inclusion with an attack angle θ_{ini} at a landing height $y_{\text{landing}} = (y_p - y_s)$. It faces a discontinuity with a tangent angle θ_{tan} as depicted in Fig. 2.9.

Our direction criterion should tell us at which subsequent propagation direction, noted θ, the propagation occurs. Even if the MERR does not take into account this heterogeneous distribution of toughness, it can naturally be extended into the following condition [He and Hutchinson, 1989; Gurtin and Podio-Guidugli, 1998; Hakim and Karma, 2005; Chambolle et al., 2009] :

Propagation occurs in the direction θ such that $(G - G_c)(\theta)$ be globally maximal. (2.15)

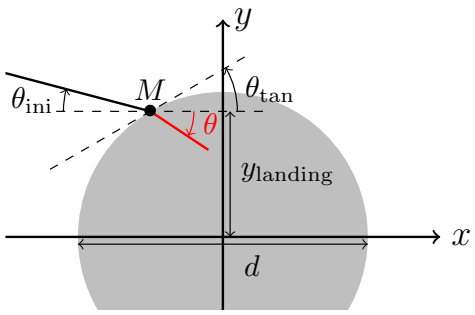

Figure 2.9: Crack landing on an inclusion with an attack angle θ_{ini} at a landing height y_{landing} corresponding to a local tangent angle θ_{tan}

This criterion complies with the theoretical framework developed Francfort and Marigo [1998] for the variational formulation of brittle fracture. Indeed maximizing $(G - G_c)$ is equivalent to minimizing the sum of the elastic energy and fracture surface energy :

$$W(\ell + \delta\ell) - W(\ell) + G_c \delta\ell \sim -(G - G_c)\,\delta\ell \tag{2.16}$$

where W is the elastic energy and $\delta\ell$ a small elongation of a crack of length ℓ.

This criterion is often found in the literature in a fractional way $(G/G_c)_{\max}$ since the seminal work of He and Hutchinson [1989]. The substractive form $(G/G_c)_{\max}$ and fractional form $(G/G_c)_{\max}$ are nonetheless strictly equivalent since the positions of the extrema verify in both cases $G'(\theta) - G_c'(\theta) = 0$ and that Griffith's formalism of brittle fracture states that propagation occurs at $G = G_c$. We here prefer the substractive form $(G/G_c)_{\max}$, which has a physical meaning as presented above.

This energetic criterion has been verified experimentally very recently in the tearing test of brittle polymeric thin sheets [Takei et al., 2013; Ibarra et al., 2016]. It has also been confirmed numerically through anisotropic phase field simulations [Hakim and Karma, 2005, 2009; Bleyer and Alessi, 2018; Li and Maurini, 2019].

In our case, the anisotropic distribution $G_c(\theta)$ is given by the microstructure geometrical

and fracture properties :

$$\begin{cases} G_{\mathrm{c}}(\theta) = G_{\mathrm{c}}^{\mathrm{mat}}, \text{ if } \theta \in [-\pi, -\pi + \theta_{\tan}[\cup]\theta_{\tan}, \pi] \\ G_{\mathrm{c}}(\theta) = G_{\mathrm{c}}^{\mathrm{inc}}, \text{ if } \theta \in]-\pi + \theta_{\tan}, \theta_{\tan}[\\ G_{\mathrm{c}}(\theta) = G_{\mathrm{c}}^{\mathrm{int}}, \text{ if } \theta = -\pi + \theta_{\tan} \text{ or } \theta = \theta_{\tan} \end{cases} \tag{2.17}$$

The variations of $G_{\mathrm{c}}(\theta)$ are depicted in Fig. 2.11.a for $\theta_{\tan} = 45°$, $G_{\mathrm{c}}^{\mathrm{inc}} = 1.4\, G_{\mathrm{c}}^{\mathrm{mat}}$ and $G_{\mathrm{c}}^{\mathrm{int}} = 0.8\, G_{\mathrm{c}}^{\mathrm{mat}}$.

Since the point M lies on the interface between two materials with identical elastic properties, one may apply the so-called Amestoy-Leblond formulæ (see for instance Leblond [1999]). These formulæ link the local SIFs, $\underline{\mathbf{K}}^*$, just after an arbitrary kink to those, $\underline{\mathbf{K}}$, just before it (see Fig. 2.10). They read :

$$\underline{\mathbf{K}}^* = \underline{\underline{\mathbf{F}}}(\alpha) . \underline{\mathbf{K}} \tag{2.18}$$

where $\underline{\underline{\mathbf{F}}} = (F_{i,j})$ is a universal operator depending only on the (arbitrary) kink angle α. These formulæ show that whatever the geometry and the loading, the SIFs right after a kink depend only on those before the kink and the angle defining this kink. It is also worth noting that $F_{\mathrm{I,III}} = F_{\mathrm{III,I}} = 0$, which evidences the decoupling of the plane and anti-plane loading modes.

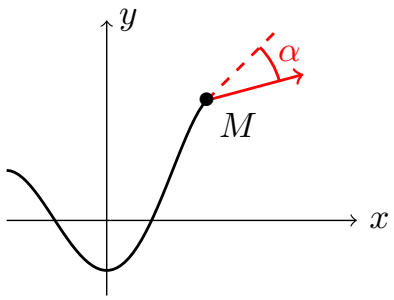

Figure 2.10: Schematics of a crack kinking situation where an initial crack suddenly propagates with an arbitrary large kink α

We use these formulæ to obtain the angular distribution of the SIFs at the tip of an infinitesimal extension in the direction defined by the angle θ from the values of the SIFs K_{I}^M, K_{II}^M and K_{III}^M before the kink :

$$\begin{cases} K_{\mathrm{I}}(\theta) = F_{I,I}(\theta - \theta_{\mathrm{ini}})\, K_{\mathrm{I}}^M + F_{I,II}(\theta - \theta_{\mathrm{ini}})\, K_{\mathrm{II}}^M \\ K_{\mathrm{II}}(\theta) = F_{II,I}(\theta - \theta_{\mathrm{ini}})\, K_{\mathrm{I}}^M + F_{II,II}(\theta - \theta_{\mathrm{ini}})\, K_{\mathrm{II}}^M \\ K_{\mathrm{III}}(\theta) = F_{III,III}(\theta - \theta_{\mathrm{ini}})\, K_{\mathrm{III}}^M \end{cases} \tag{2.19}$$

The values of the SIFs K_{I}^M, K_{II}^M and K_{III}^M are provided by the perturbative framework presented above.

By combining Eq. (2.19) with Irwin's formula, we obtain (Fig. 2.11.b) :

$$G(\theta) = \frac{1-\nu^2}{E}\left(K_{\mathrm{I}}^2(\theta) + K_{\mathrm{II}}^2(\theta)\right) + \frac{1+\nu}{E} K_{\mathrm{III}}^2(\theta) \tag{2.20}$$

where we have eliminated the Mode III contribution, which is of second order in the perturbation since $K_{\mathrm{III}}(\theta)$ is itself of first order.

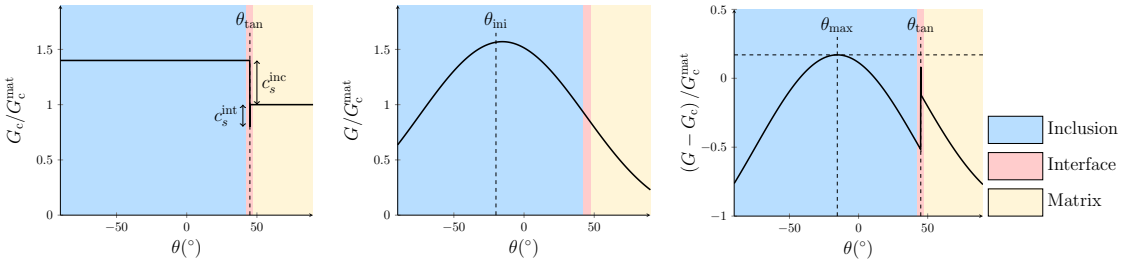

(a) (b) (c)

Figure 2.11: Application of the GMERR direction criterion: (a) variations of the toughness G_{c}, (b) the ERR G and (c) their difference $G - G_{\mathrm{c}}$ with the potential propagation direction θ, for the parameter values $\theta_{\mathrm{tan}} = 45°$, $\theta_{\mathrm{ini}} = -20°$, $G_{\mathrm{c}}^{\mathrm{inc}} = 1.4\,G_{\mathrm{c}}^{\mathrm{mat}}$ and $G_{\mathrm{c}}^{\mathrm{int}} = 0.8\,G_{\mathrm{c}}^{\mathrm{mat}}$, $K_{\mathrm{I}}^{M} = 1.25 K_{Ic}^{\mathrm{mat}}$ and $K_{\mathrm{II}}^{M} = -0.05 K_{Ic}^{\mathrm{mat}}$.

We then obtain the difference $G - G_{\mathrm{c}}$ as a function of the angle θ defining the propagation direction that is shown in Fig. 2.11.c. We clearly see that some preferential directions emerge from the interaction between the crack and an inclusion. The energetic competition behind the direction choice is illustrated in Section 3.3.

An interesting point is that we do not need to check every single direction θ, which would be costly numerically, but only in two directions : the tangent one θ_{tan} and the one where G is maximal, θ_{max}. Indeed, under the following assumptions :

1. the inclusions are tougher than the matrix $G_{\mathrm{c}}^{\mathrm{inc}} \geq G_{\mathrm{c}}^{\mathrm{mat}}$ and their interface weaker $G_{\mathrm{c}}^{\mathrm{int}} \leq G_{\mathrm{c}}^{\mathrm{mat}}$;
2. for small enough $K_{\mathrm{II}}/K_{\mathrm{I}}$, as in our case, G increases until $\theta_{\mathrm{max}} = \theta_{\mathrm{ini}} - 2\dfrac{K_{\mathrm{II}}^{M}}{K_{\mathrm{I}}^{M}}$ and decreases after ;
3. we consider angles $\theta \in \left[-\frac{\pi}{2}, \frac{\pi}{2}\right]$;

$G - G_{\mathrm{c}}$ can only be maximal either inside the interval where G is maximum and G_{c} is constant (i.e. matrix or inclusion) or on the edges of this interval (i.e. along the interface). Thus we only have to check the maximum value between $(G - G_{\mathrm{c}})()$ and $(G - G_{\mathrm{c}})(\theta_{\mathrm{max}})$.

The GMERR criterion finally boils down to :

$$\text{Propagation occurs in the direction } \theta \in \{\theta_{\mathrm{tan}}, \theta_{\mathrm{max}}\}, \text{ where } (G - G_{\mathrm{c}}) \text{ is maximal} \quad (2.21)$$

where θ_{tan} is the local tangent angle at the landing point on the inclusion and θ_{max} is the angle where G is maximal.

Propagation along the interface (State IV)

When the point M is propagating along an interface between the matrix and the inclusion, we apply the same criterion as before with the sole difference that $\theta_{\mathrm{ini}} = \theta_{\mathrm{tan}}$ since kinking has already occurred. Note that the crack can remain on the interface, stop by-passing the inclusion and cross it, or leave the interface and go back to the matrix.

Propagation in a homogeneous phase (State I & III)
When a point M is either in the matrix or crossing an inclusion, the angular distribution of toughness $G_c(\theta)$ is isotropic so that the PLS is applicable. However, since the MERR and the PLS are in practice almost equivalent for the small kink angles encountered in the homogeneous phases [Amestoy and Leblond, 1992], we retain the GMERR criterion.

2.2.3.c Viscous regularization of Griffith's propagation law for brittle fracture

The last missing ingredient of our model is a kinetic law, which links G , the ERR, and G_c, the local toughness, to v, the local front velocity. Kinetic laws may be derived from Griffith's criterion [Gao and Rice, 1989; Patinet et al., 2013b; Démery et al., 2014b; Ponson and Pindra, 2017] or Paris's law in fatigue [Bower and Ortiz, 1990, 1991; Lazarus, 2003; Favier et al., 2006a; Vasoya et al., 2016a]. The brittle case can be found back in the limit of large Paris exponents [Lazarus, 2003]. The kinetic law used here falls into the first category and derives from two key relationships : the Griffith criterion and the variation of toughness with crack speed.

First, all the points along the crack front are assumed to follow Griffith's condition [Griffith, 1921]:

$$G = G_c(v) \tag{2.22}$$

where G does not depend on v under the quasi-static propagation hypothesis. We thus assume that the crack velocity $v \ll c_R$, where c_R is the Rayleigh wave speed.

We then postulate that the toughness is a given function of the crack speed, $G_c = G_c(v)$. Depending on the material, the function $G_c(v)$ may take different forms. Its linearization around the mean crack velocity v_m provides a linear kinetic law:

$$G = G_c(v) = G_c(v_m)\left(1 + \frac{v - v_m}{v_0}\right) \Leftrightarrow \quad v = \left[v_m + v_0 \frac{G - G_c(v_m)}{G_c(v_m)}\right]^+ \tag{2.23}$$

where $v_0 = G_c(v_m) \,/\, \frac{\partial G_c}{\partial v}\big|_{v_m}$ is a characteristic velocity of the material emerging from the rate-dependency of its toughness and $[\cdot]^+$ the positive part function.

This equation of motion has been largely used in the literature (see for example Gao and Rice [1989]; Ramanathan et al. [1997]; Ponson and Bonamy [2010]) and was recently shown to capture quantitatively the relaxation dynamics of a crack depinning from a single obstacle [Chopin et al., 2018]. More complex kinetic laws extracted from experiments can be used in order to grasp finer effects [Ponson, 2009; Scheibert et al., 2010; Vasudevan et al., 2019], for instance :

$$G = G_c(v) = G_c^0\left(1 + \frac{v}{v_c}\right)^\gamma \Leftrightarrow v = v_c\left[\left(\frac{G}{G_c^0}\right)^{\frac{1}{\gamma}} - 1\right]^+ \tag{2.24}$$

where v_c is a material characteristic velocity. It can be linked to v_0 since for such kinetic law $v_0 = G_c(v_m) \,/\, \left.\dfrac{\partial G_c}{\partial v}\right|_{v_m} = \dfrac{v_c + v_m}{\gamma}$ and $G_c^0 = \lim\limits_{v \to 0} G_c(v)$.

Subcritical or fatigue propagation has not been considered in this study. It is a natural extension of our work and may have implications on crack propagation since "memory"

effects have been highlighted for fatigue cracks in heterogeneous materials for the case of coplanar propagation [Pindra et al., 2008].

2.2.4 Validity range of the perturbative approach

The perturbative procedure used requires $\left|\frac{\partial f_x}{\partial z}\right| \ll 1$, $\left|\frac{\partial f_y}{\partial z}\right| \ll 1$, $\left|\frac{\partial f_y}{\partial x}\right| \ll 1$, which raises the issue of the validity range of our approach. Gao and Rice [1989] studied the validity range of the first-order perturbation for coplanar crack propagation. They showed that for inclusions with $G_c^{inc} \simeq 4\,G_c^{mat}$, the perturbative approach gives accurate results when compared to boundary elements simulations. Above this toughness level, the results of the perturbative framework are no more quantitatively correct and can even be qualitatively wrong. We thus limit our study to such toughness levels, ensuring the condition $\left|\frac{\partial f_x}{\partial z}\right| \ll 1$.

Regarding the out-of-plane perturbations of the crack, Eq. (2.14) provides a good estimate of the SIFs even for large values of the slope $\theta = \arctan\left(\frac{\partial f_y}{\partial x}\right)$, *provided* it is corrected through the use of Amestoy-Leblond's formulæ [Amestoy and Leblond, 1992; Leblond, 1999] that provide the SIFs just after an abrupt, arbitrary change of direction of the crack. The necessary procedure of correction is described in Section 8.A. This procedure permits to handle the large slope which may arise during the by-pass of inclusions. It is also explained in the same appendix that even with the procedure of correction, the mode III contribution is of second-order in the expression of the ERR G, due to the decoupling of the anti-plane shear mode with respect to the tensile and plane shear modes in Amestoy-Leblond's formulæ. Neglect of this contribution implies that the derivative $\frac{\partial f_y}{\partial z}$ plays no role in the model.

2.3 Numerical implementation

Our LEFM-based theoretical model has to be numerically implemented. As in 2.2, this numerical implementation shall allow us to get efficiently the data of G_c and G at all simulation time-steps. Large-scale microstructure generation is presented in Section 2.3.1 for considered inclusion geometries (Fig. 2.3). In Section 2.3.2, we describe how to make the crack propagate through an efficient explicit scheme based on the fast Fourier transform computation of the local SIF (K_p). Section 2.3.3 is devoted to the development of an acceleration procedure based on the physics of depinning transition to increase both robustness and efficiency of the proposed numerical method.

2.3.1 Microstructure generation

We have to keep in mind that we want to model crack propagation in large-scale heterogeneous materials where the numerical performances offered by the perturbative approach are unreachable with other numerical methods such as cohesive zone models or phase-field simulations. Thus microstructure generation procedure has to be efficient and must generate, in reasonable computing time, microstructures containing millions of inclusions for a broad range of inclusion density, size disorder and various geometries.

2.3.1.a Spherical inclusions

First let us tackle the case of spherical inclusions, which are the reference geometry in our study. In the following, we are considering only non-overlapping inclusions, the only case our model can currently handle.

Random isotropic non-overlapping microstructures have been built using a simple RSA algorithm, which consists in placing randomly and sequentially non-overlapping spheres into a fixed volume [Widom, 1966]. For each new spherical inclusion added in the volume, random coordinates are drawn from a uniform distribution. The intersection between the inclusion and those surrounding it is then tested. If the inclusion does not overlap with any previously generated one, it is added to the distribution and a new inclusion addition is considered. This algorithm allows to produce large-scale distributions ($L_z \times L_x \times L_y = 1024d \times 1024d \times 20d$) at low densities (up to 25%) (Fig. 2.12.a), or highly polydisperse microstructures (Fig. 2.12.c). At higher densities of monodisperse microstructures, the algorithm does not converge and other generation procedures have to be implemented.

For higher densities (up to 50%) at low size dispersion levels (Fig. 2.12.b), we used the procedure developed by Delarue and Jeulin [2011], which starts from a dense ordered microstructure as CFC (cubic face centered) and introduce disorder by deleting some spheres at random or by randomly moving some of the remaining spheres. These efficient methods allow us to generate isotropic disordered microstructures on large scales in relatively short computation times.

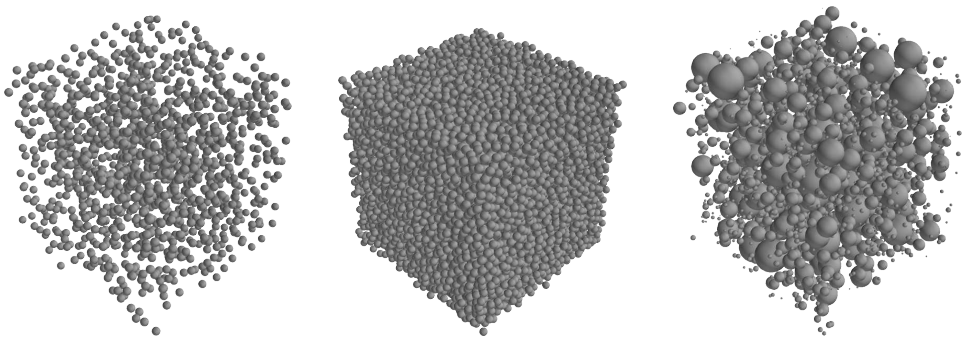

(a) (b) (c)

Figure 2.12: Spherical microstructures generated for our simulations : monodisperse spherical distribution at 5% density (a), monodisperse spherical distribution at 50% density (b) and polydisperse spherical distribution at 25% density (c)

Polydisperse microstructures, as displayed in Fig. 2.12.c, are generated following a log-normal distribution for inclusion diameters. We ensure that the mean diameter is the same as in the case of mono-disperse microstructure but we vary the diameter dispersion, thus fixing the log-normal distribution characteristics.

2.3.1.b Cubical and ellipsoidal distributions

Aside from spherical distributions, we are considering random arrangements of cubical and ellipsoidal inclusions. In the case of cubical inclusion, we are considering cubes of mean edge length d which are rotated by an angle β around the z-axis. It considerably simplifies the inclusion-inclusion overlapping test required by generation procedure. Consecutively, as in the spherical case, RSA algorithm is used at low densities (up to 20%) or high size dispersion and the procedure presented by Delarue and Jeulin [2011] is used for higher densities (up to 35%).

For ellipsoidal inclusions, the inclusion-inclusion overlapping test is significantly more complicated than in the spherical and cubical cases since it involves a minimization procedure [Anoukou et al., 2018]. Thus generation of large-scale random isotropic arrangements of ellipsoidal inclusions proves to be numerically costly. If the implementation of such a procedure can be accelerated through GPU parallelization, it is out of the scope of our study and a compromise must be found to investigate textural effects on crack trajectory and effective fracture properties of heterogeneous materials. Starting from an isotropic distribution of spherical inclusions, we perform on each inclusion a composition of three dilations in the main directions $\underline{e}_z, \underline{e}_x, \underline{e}_y$, to give to the inclusion the shape we want, and a rotation, whose center is the position of the inclusion, to give to the distribution the texture we aim at. The isotropy of the distribution is lost but large-scale textured distribution of ellipsoidal inclusions are generated in a small computed time. Examples of such distributions is given in Fig. 2.13.b and Fig. 2.13.c.

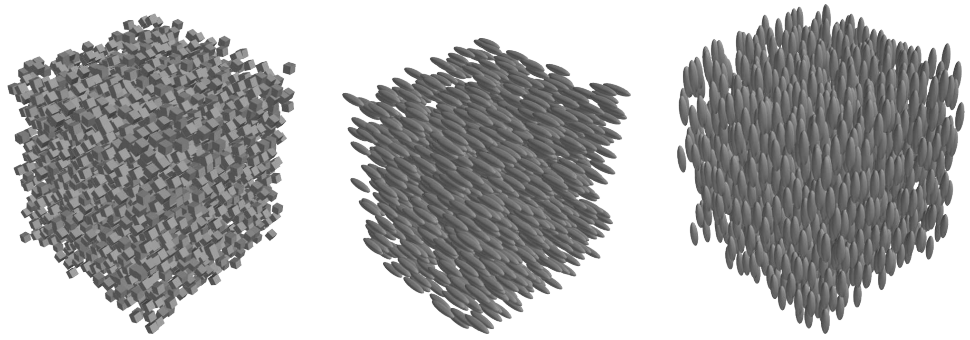

(a) Monodisperse cubical distribution at 25% density

(b) Monodisperse ellipsoidal distribution textured at 25% density

(c) Monodisperse ellipsoidal distribution textured in the x-direction at 25% density

Figure 2.13: Isotropic microstructures with cubical inclusions (a) and textured microstructures of ellipsoidal prolate inclusions oriented in the x-direction (b) or in the y-direction (c)

2.3.2 Explicit scheme for crack propagation

2.3.2.a Crack front meshing

One of the main advantages of the perturbative approach in tensile Mode I loading with toughness heterogeneities is that we only have to mesh the crack front. Note that in the presence of macroscopic Mode II or Mode III [Leblond and Ponson, 2016] or in the case where the influence of T-stresses are considered, non-local terms over the whole crack surface appear in the perturbed SIF formulæ. The crack surface has then to be meshed, increasing the numerical cost of the procedure. In the case of elastic heterogeneities [Gao, 1991; Muju, 2000], the inclusions have a volume effect on the SIF and therefore on crack propagation and the whole domain has to be meshed, leading to a large increase in the computational cost of the perturbative approach. In the case considered here of toughness heterogeneities with uniform elastic properties, the crack only "sees" an inclusion when it interacts with it, decreasing by a large amount the complexity of our algorithm.

The crack front is discretized in N equidistant points $(M_i)_{i\in[1,N]}$, separated by a distance $\Delta z = \frac{L_z}{N}$ (Fig. 2.14). Their position $\left(f_x^i, f_y^i, z_i\right)$ is tracked at each time step, the subsequent position being inferred from the instantaneous speed vector $\underline{v}^i$ that points along the direction $\theta^i = \arctan\left(\frac{\partial f_y^i}{\partial x}\right)$ in the plane (xM_iy) thanks to the criterion presented in Eq. (2.21) and Eq. (2.23).

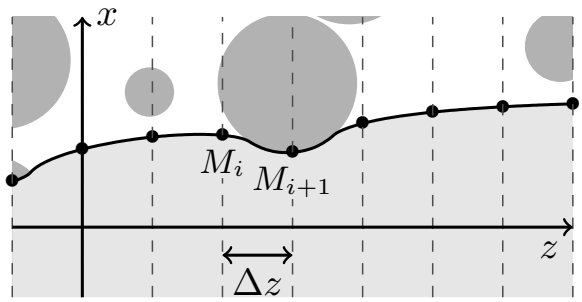

Figure 2.14: Crack front discretization with a spatial step Δz

2.3.2.b Perturbed stress intensity factors computation

The core of our computational model is the fast computation of the local SIF along the front through explicit formulæ. These equations relate the geometrical perturbations of the front to the distribution of SIF, and involve integrals along the whole crack front (2.14). Such integrals are computationally costly as their computational time grows as $O\left(N^2\right)$, where N is the number of discretization points along the front. However, by considering a periodic medium along the crack front direction, these non-local terms take the following *local* form in the Fourier space.

Indeed, if we define $\hat{\phi}$ the z-Fourier transform of real function ϕ by the equivalent formulæ :

$$\hat{\phi}\left(k,t\right) = \int_{-\infty}^{+\infty} \phi\left(z,t\right) e^{-ikz} dz \Leftrightarrow \phi\left(z,t\right) = \frac{1}{2\pi} \int_{-\infty}^{+\infty} \hat{\phi}\left(k,t\right) e^{+ikz} dk \tag{2.25}$$

then the long-range operator reads in the Fourier space :

$$\mathcal{L}f\,(z,t) = \mathrm{PV}\int_{-\infty}^{+\infty} \frac{f\,(z,t) - f\,(z',t)}{(z-z')^2}\,dz' \Leftrightarrow \widehat{\mathcal{L}f}\,(k,t) = |k|\pi\hat{f}\,(k,t) \tag{2.26}$$

This property allows us to compute efficiently the long-range parts of the SIF perturbations through direct and inverse fast Fourier transforms (FFTs), reducing the computational cost from $O\left(N^2\right)$ to $O\,(N\,log(N))$. To take optimum advantage of the FFT algorithm, we try to keep the number of crack front points as a power of 2, $N = 2^p$.

2.3.2.c Detailed procedure for the execution of a single propagation step

The computation of the crack evolution employs an explicit scheme that predicts the configuration of the front at time $t + \Delta t$ from its configuration at time t. Each point along the crack is characterized by the parameters $x\,(t)$, $f_x\,(z,t)$, $f_y\,(z,t)$ and $\theta\,(z,t)$, from which the subsequent position is inferred.

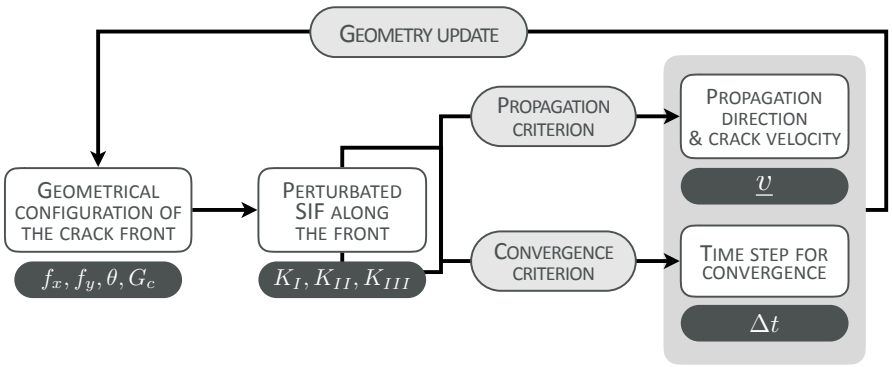

Figure 2.15: Schematics of the explicit numerical scheme implemented in our simulations.

In the following, the term *local* means that we are looking at a given point M of the crack front. At each time step t :

1. we get the geometrical configuration $x\,(t)$, $f_x\,(z,t)$, $f_y\,(z,t)$, $\theta\,(z,t)$ at each point of the crack front ;

2. from it, we compute the local SIF perturbations (K_p) using Eq. (2.14) ;

3. those local SIF and the data of the macroscopic current loading $G^{\infty}\,(t)$ are used to get the local angular distribution of G from Eq. (8.6). The local angular distribution toughness G_{c} is given by the position of each point related to the microstructure. The local propagation direction $\theta\,(z,t) + \delta\theta\,(z,t)$ is computed from the GMERR criterion of 2.21 and the local crack velocity $v\,(z,t)$ is given by the kinetic law (Eq. (2.23)). The procedure gives us the local velocity vector $\underline{v}\,(z,t)$;

4. convergence criteria and an acceleration procedure set a propagation time-step Δt, which ensure robustness and is described in Section 2.3.3 ;

5. the geometrical configuration of the front is updated by making each point of the crack front propagate by the distance $\underline{v}(z,t)\,\Delta t$ according to an explicit numerical scheme.

The procedure goes on until the whole domain is cracked.

2.3.3 Accelerating procedure for large-scale simulations

Explicit numerical schemes are often preferred to implicit schemes since they are easier to implement. One of their major drawbacks is that they require a small time step Δt to ensure numerical stability and control numerical errors. Acceleration procedures are usually developed to circumvent those limitations and speed up simulations. In this regard, we here detail the possible source of numerical instabilities and derive a convergence criterion adapted from a Courant-Friedrichs-Lewy condition. This criterion proves too restrictive since it does not take into account the physics of crack propagation and its intermittent dynamics, thus spoiling badly numerical performances. An acceleration procedure based on the physics of depinning is then developed, allowing unprecedented performances for large-scale simulations.

2.3.3.a Absolute convergence criterion

In the following, all results have been derived for coplanar propagation and have been shown to work numerically in the non-coplanar case.

As explained before, the use of an explicit scheme to make the crack propagate is expected to trigger numerical instabilities, namely spatial oscillations on the long-range interactions in the SIF perturbations. These oscillations appear as soon as the crack encounters a toughness discontinuity at some point (Fig. 2.16.a) : when a point lands on an inclusion, the toughness it sees suddenly increases. Thus the point stops moving whereas its neighbors keep propagating (Fig. 2.16.b), inducing oscillations in the non-local part of the perturbed SIFs and subsequently on G (Fig. 2.16.c). For a given time step Δt, we want to ensure that those oscillations decay in time (stability).

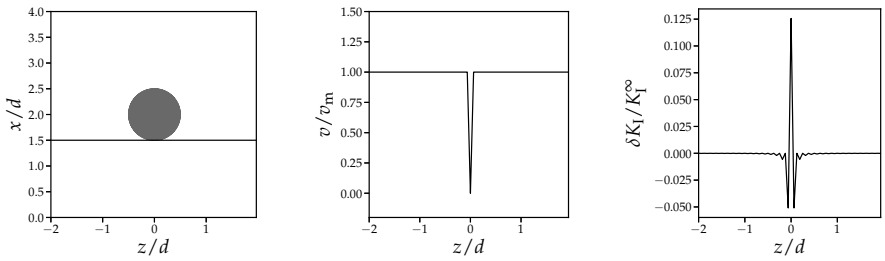

(a) (b) (c)

Figure 2.16: Numerical oscillations induced on the long-range interactions during the pinning on an inclusion (a) : when the crack meets the inclusion, the local velocity becomes zero (b), triggering oscillations on the long-range interactions when the crack propagates further (c).

Standard numerical schemes for crack propagation in a perturbative approach try to avoid such numerical errors by introducing a maximum advance criterion, which bounds the

amplitude of the oscillations [Bower and Ortiz, 1990; Lazarus, 2003; Patinet et al., 2013b; Ponson and Pindra, 2017]. In our evolution problem, we chose to introduce a maximum time-step criterion designed to prevent the occurrence of such errors. This time-step is based on the analysis of the coplanar model which follows :

$$\frac{1}{v_0}\frac{\partial f_x}{\partial t}(z,t) = -\frac{1}{\pi}\,\mathrm{PV}\int_{-\infty}^{+\infty}\frac{f(z,t)-f(z',t)}{(z-z')^2}\,dz' + \eta_c\left(z, x+f_x(z,t)\right) \tag{2.27}$$

where η_c describes the variations of toughness in the propagation plane.

After discretization along the z-axis with a step Δz, the integral follows :

$$-\frac{1}{\pi}\,\mathrm{PV}\int_{-\infty}^{+\infty}\frac{f(z,t)-f(z',t)}{(z-z')^2}\,dz' \sim -\frac{1}{\pi}\left(\int_{-\infty}^{z-\Delta z}+\int_{z+\Delta z}^{+\infty}\right)\frac{f(z,t)-f(z',t)}{(z-z')^2}\,dz' + \frac{\Delta z}{\pi}\frac{\partial^2 f}{\partial z^2}(z,t) \tag{2.28}$$

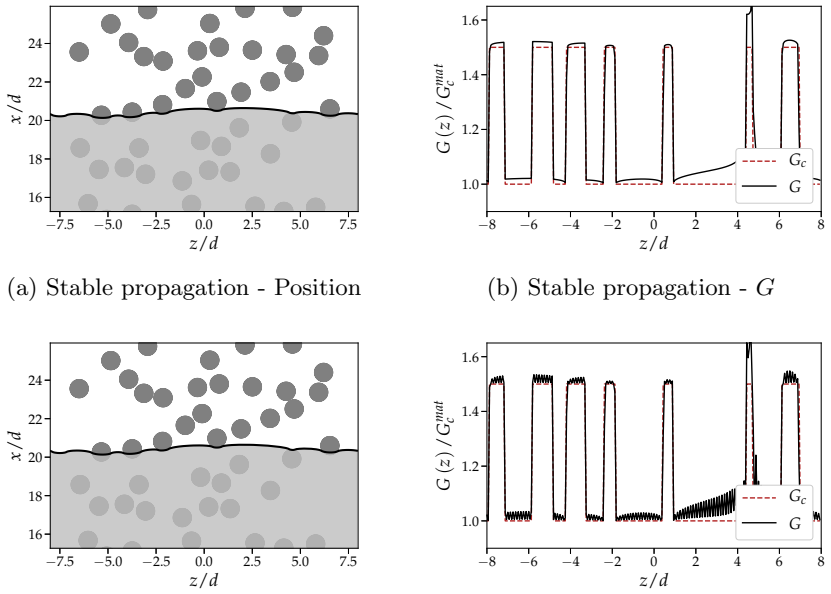

(a) Stable propagation - Position

(b) Stable propagation - G

(c) Unstable propagation - Position

(d) Unstable propagation - G

Figure 2.17: (a) & (b) Non-oscillatory behavior for $\Delta t_{\text{step}} = \Delta t_{\text{conv}}$; (c) & (d) oscillatory behavior for $\Delta t_{\text{step}} > \Delta t_{\text{conv}}$.

As the curvature term is responsible for the numerical instabilities, a Courant-Friedrichs-Lewy convergence condition. :

$$\Delta t_{\text{conv}} = \alpha\, v_0\, \Delta z \tag{2.29}$$

largely used in diffusion problems turns out to ensure convergence where the constant α is set here to 0.2.

Examples of propagation with $\Delta t_{step} = \Delta t_{\text{conv}}$ and $\Delta t_{step} > \Delta t_{\text{conv}}$ are given in Fig. 2.17. From our experience, one of the advantages of a time-step based convergence criterion over

a maximum advance one [Bower and Ortiz, 1990; Lazarus, 2003; Patinet et al., 2013b; Ponson and Pindra, 2017] is that convergence does not depend on inclusion properties.

2.3.3.b Other restraining conditions

Other conditions are imposed to the numerical scheme to ensure realistic and accurate modeling of the crack evolution:

- **Interaction with microstructure** – We make sure that no point on the crack front crosses a toughness discontinuity during a time-interval, as its behavior at such interfaces largely controls the interaction mechanism between the crack and the inclusion. As a result, the time step may be adjusted to a value Δt_{inter} to ensure that the crack lands exactly on the interface;
- **Maximum advance** – We introduce a maximum value $\Delta x_{\max} = \Delta z/5$ of the incremental crack advance to avoid sudden variations of the non-local contributions to the SIFs perturbations (see Section 2.3.3.a). This introduces a maximum time step $\Delta t_{\text{advance}} = \frac{\Delta x_{\max}}{\max_{\mathcal{F}} v}$ which is generally much larger than Δt_{conv};
- **Maximum load variations** – A maximum value $\Delta G_{\max}$ of the load variation between subsequent time steps is introduced to avoid sudden drops of G^{∞} during the depinning phases. According to Eq. (2.6), this leads to an additional time scale $\Delta t_{\text{loading}} = \Delta G_{\max}/G_{\text{c}}^{\text{mat}}\,\mathcal{L}/v_{\text{m}}$.

During each time interval, the time-step Δt is chosen as the smallest of those defined previously:

$$\Delta t_{step} = \min\left(\Delta t_{\text{conv}}, \Delta t_{\text{inter}}, \Delta t_{\text{advance}}, \Delta t_{\text{loading}}\right) \tag{2.30}$$

2.3.3.c Accelerating procedure

We saw that a time-step based convergence criterion ensures convergence no matter the inclusion fracture properties. What constitutes an asset in regards to numerical stability is actually detrimental to numerical performances.

Indeed inclusion properties naturally influence the macroscopic loading to be applied to induce material failure. In the limit of weak inclusions, the loading required to break a matrix of toughness $G_{\text{c}}^{\text{mat}}$ reinforced by a periodic array of tougher inclusions of density ρ and toughness $G_{\text{c}}^{\text{inc}}$. The required loading to fracture this media reads [Gao and Rice, 1989] :

$$G_{\text{frac}}^{\infty} = G_{\text{c}}^{\text{mat}}\left(1 + \rho\frac{G_{\text{c}}^{\text{inc}} - G_{\text{c}}^{\text{mat}}}{G_{\text{c}}^{\text{mat}}}\right) = G_{\text{c}}^{\text{mat}}\left(1 + \rho c_{inc}\right) \tag{2.31}$$

Starting with $G_{\infty} = G_{\text{c}}^{\text{mat}}$, the loading has to be increase up to G_{frac}^{∞}. This loading variations happens with a characteristic time :

$$\Delta t_{\text{incr}} = \frac{\mathcal{L}}{v_{\text{m}}}\rho\, c_{inc} \tag{2.32}$$

Since we often work in the limit where $v_{\text{m}} \to 0$ (typically $v_{\text{m}} \sim 10^{-8} v_0$) and large $\mathcal{L} \gg d$ to suppress the impact of the structural problem (typically $\mathcal{L} \sim 10^3 - 10^6 d$), several order of

magnitude separates Δt_{conv} from Δt_{incr}.

Moreover, crack propagation in heterogeneous brittle materials is highly intermittent [Bonamy et al., 2008; Barès et al., 2014] and can be viewed as a depinning transition. At a given stable crack position, the loading increases until the crack jumps from its stable position to the next stable one. Crack propagation is thus a succession of long pinned configurations separated by short depinning events called *avalanches*. If we consider a constant time-step Δt_{conv}, all the time-steps calculated during pinned configurations are useless. Fig. 2.18 illustrates the intermittent dynamics in coplanar propagation, which are also found in the non-coplanar case.

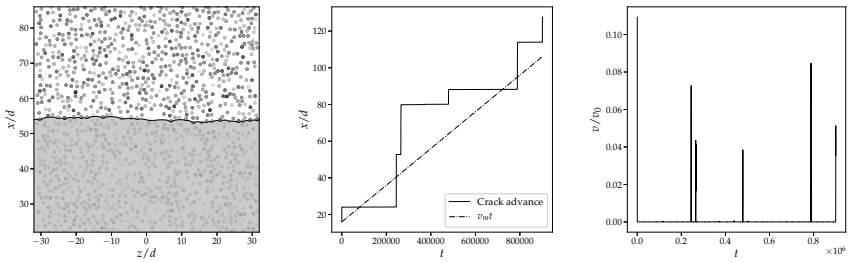

(a) Crack propagation (b) Crack advance (c) Crack velocity

Figure 2.18: Coplanar propagation (a) in heterogeneous brittle materials displaying crack jumps (b), signature of the intermittent dynamics (c)

Finally, it all comes down to the question : how does one compute efficiently the pinned configurations where the crack does not propagate but the loading has to increase ? With a constant time-step, determined to ensure convergence, the numerical cost is prohibitive since nothing happens during most of the time steps as illustrated in Fig. 2.19.b. An acceleration procedure is mandatory to overcome the limitations imposed by the intermittent dynamics of crack propagation in disordered systems.

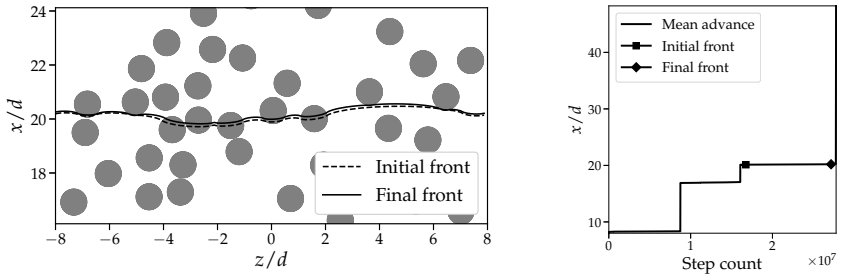

(a) (b)

Figure 2.19: Crack front propagation during a pinned configuration (a) with the associated number of numerical steps computed to model such small crack advance (b)

A naive solution would be to increase the time-step during those phases. Yet, as pictured in Fig. 2.19.a, pinned configurations often correspond to configurations where part of the front is blocked on a toughness discontinuity, where $G < G_c$. As explained before, increasing the time-step above Δt_{conv} would induce numerical oscillations in the SIF computation

(Fig. 2.17.c). The key component is to either make the crack propagate or increase brutally the loading, but never do it simultaneously. The conditions under which such brutal loading increase should occur has to be described.

Our acceleration procedure is constructed on the following scheme, summarized in Fig. 2.20. Let us consider two fronts $\mathcal{F}_1$ and $\mathcal{F}_2$, separated by N_{acce} simulation steps (typically $N_{\text{acce}} = 20$). $\mathcal{F}_1$ at time t_1 was at x_1. $\mathcal{F}_2$ at time t_2 is now at x_2. At $t = t_2$:

1. if no points along the crack front has been blocked (null velocity) during the whole last N_{acce} steps, nothing happens ;
2. else, at least a point has been blocked the whole last N_{acce} steps. We then look at the mean crack velocity during those steps i.e. $\langle v \rangle = (x_2 - x_1) / (t_2 - t_1)$:
   (a) if $\langle v \rangle \geq v_{crit}$, we can consider that the crack front progresses efficiently enough to allow good numerical performances ;
   (b) else we make a sudden loading increase by a value ΔG_{acce} by jumping in time by an amount $\Delta t_{\text{acce}} = \frac{\mathcal{L}}{v_{\text{m}}} \frac{\Delta G_{\text{acce}}}{G_0}$. We then re-estimate all local SIFs and make the crack propagate following the standard procedure.

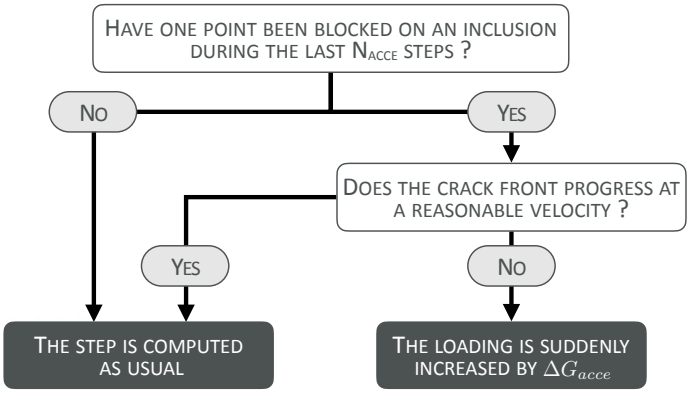

Figure 2.20: Schematics of the accelerating procedure implemented in our simulations

We take, $v_{crit} = \frac{\Delta G_{\max}}{2G_0} v_0$ and $\Delta G_{\text{acce}} = \frac{\Delta G_{\max}}{2}$. In that case, the global error we make on the value of the macroscopic loading at the depinning transition is at most $\Delta G_{\max}$. It also means that, during pinning events, in the part which is propagating at $G = G_{\text{c}}$, the acceleration procedure ensures that $|G - G_{\text{c}}| \leq \Delta G_{\max}$. Our procedure makes thus Griffith's criterion locally satisfied at a precision $\Delta G_{\max}/G_{\text{c}}^{\text{mat}}$, allowing us then to bound our numerical errors.

Finally, we also allow the crack to ignore the convergence condition in Eq. (2.29) when the crack front is almost flat i.e. when the crack velocity is almost constant along the crack front. This situation might happen at low inclusion density and in this case, the crack might propagate at a speed $v_{\text{m}} \ll v_0$, which would be costly. Under the flat velocity profile condition, we can ascribe the mean speed to all crack points, and thus do not propagate any numerical errors, while substantially increasing the numerical performances. This condition

reads :

$$\text{if } \forall z,\ |v(z) - \langle v \rangle_z| \leq p_v \langle v \rangle_z \text{ , then } \forall z,\ v(z) = \langle v \rangle_z \tag{2.33}$$

where p_v is a numerical convergence parameter which is typically taken as $p_v = 10^{-2}$, which constitutes a very strong condition.

Fig. 2.21 illustrate the performance of our global acceleration procedure on the coplanar propagation presented in Fig. 2.19 for a precision $\varepsilon = \Delta G_{\max}/G_{\mathrm{c}}^{\mathrm{mat}} = 10^{-3}$. The number of steps performed to make the crack propagate is tremendously reduced (from 10^7 to 10^4 steps for $v_{\mathrm{m}} = 10^{-4} v_0$ and $\mathcal{L} = 10^2 d$, which are much looser loading conditions as in our real simulations) and the computation time is diminished accordingly. Moreover, our acceleration procedure allows to decouple the computation time from those loading conditions v_{m} and $\mathcal{L}$. A study of the algorithm complexity of the proposed computational method is conducted in 8.C.

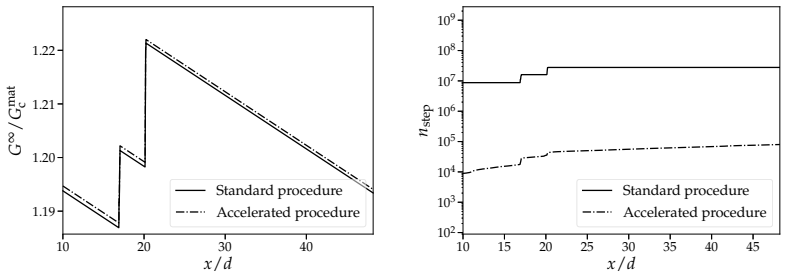

(a) Macroscopic loading (b) Total steps count

Figure 2.21: Macroscopic loading (a) and simulation steps count (b) for reference simulation and accelerated one with $\Delta G_{\max}/G_{\mathrm{c}}^{\mathrm{mat}} = 10^{-3}$

2.4 Crack propagation in large-scale disordered systems : a unique feature backed up by unprecedented numerical performances

The newly developed numerical method builds on analytical expressions of the SIFs, thus allowing an efficient computation of quantities of interest like the ERR from the discretization of the front only. As a result, crack propagation in heterogeneous media including as many as one million inclusions can be computed in only a few hours using a single core computer, a feature that FEM-based methods cannot currently emulate. It allows to describe the interaction of a crack through two possible interaction mechanisms : inclusion crossing where the crack penetrates the inclusion and inclusion by-pass where the crack goes out-of-plane and propagates along the interface matrix/inclusion. Such interaction on medium-scale microstructure is illustrated in Fig. 2.22 at various stages of the propagation of the crack.

Large-scale simulations, where the crack interacts with millions of inclusions, allow us to produce fracture surfaces with a size similar to the one that can be observed experimentally. An example of a numerically produced fracture surface is given in Fig. 2.23.

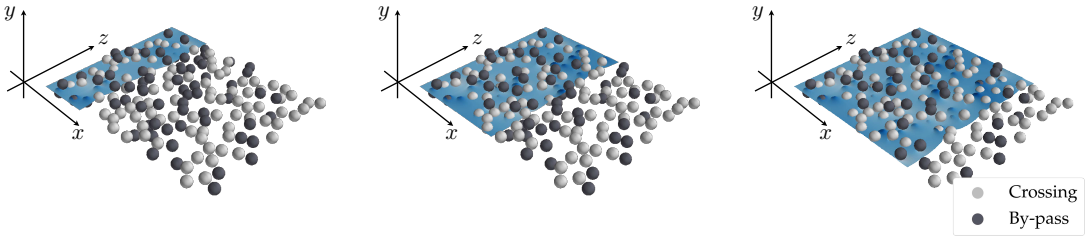

(a) (b) (c)

Figure 2.22: 3D fracture simulations of medium-sized specimens illustrating the interaction mechanisms modeled in the newly developed numerical method : crack surface after propagation through a matrix with randomly distributed tough inclusions, that have either been by-passed (dark grey) or crossed (light grey).

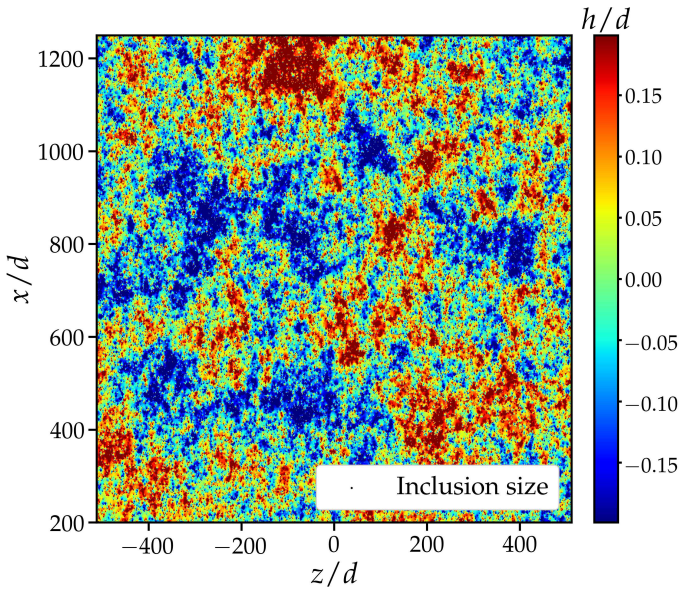

Figure 2.23: 3D fracture simulations of large-scale specimens with disordered microstructures illustrating the computational performance of the newly developed numerical method. This fracture surface topography characterized by its height map $h(x, y)$, normalized by the inclusion diameter d, results from the interaction of the crack with about 10^6 tough inclusions. The computation takes less than one hour on a single core computer.

2.5 Concluding remarks

A semi-analytical method for crack propagation displaying unprecedented performances

In this chapter, we described a new LEFM-based theoretical framework allowing to model crack propagation in three-dimensional heterogeneous brittle materials. The considered microstructures are constituted of a homogeneous matrix populated by spheroidal, ellipsoidal or cubical inclusions. Both constituents share the same elastic properties but the inclusions may be tougher than the matrix and the interface separating the inclusion from the matrix can be weaker. The proposed approach predicts the propagation of a semi-infinite crack loaded in tensile Mode I and in particular the front distortion both within and out of the initial crack plane as it interacts with the inclusions. The tougher inclusions hinder the propagation of the crack, making it bow in-plane (crack trapping) and wander out-of-plane due to inclusion by-pass (crack deflection). The geometrical perturbations of the crack front can ultimately be linked with local SIF variations within the perturbative LEFM approach developed by Gao and Rice [1986] for the in-plane deformation mode and Movchan et al. [1998] for the out-of-plane mode. A propagation criterion, resulting in the combination of a viscous regularization of Griffith's criterion and the generalized maximum energy release rate (GMERR) criterion, allows us to describe the interaction between a crack and an inclusion through two mechanisms : inclusion crossing, where the crack penetrates the inclusion, and inclusion by-pass, where the crack goes out-of-plane and propagates along the weaker interface.

This model is implemented numerically with an explicit scheme in language C. Considering the case of a crack loaded in tensile mode interacting with toughness heterogeneities, the first-order perturbative approach allows us to mesh only the crack front, which results in a major decrease in computational time as compared to other simulation techniques (FEM, X-FEM, cohesive zone or phase field models). Those remarkable performances are increased even further thanks to the convenient form of the interaction kernels in the Fourier space, allowing a computation of the local SIF with a FFT algorithm. An acceleration procedure has been developed to make the simulations even faster. Based on the physics of crack depinning, it allows us the reduce significantly the computational time of our simulations while controlling at the same time the order of magnitude of the computational errors. The current implementation allows us to describe the interaction of a crack with millions of tougher inclusions in only a few hours on a laptop computer for a monocore simulation. Such performances are unprecedented and pave the way for addressing the difficult questions of fracture properties homogenization, crack dynamics and fracture surface roughness.

Current limitations of the method and potential extensions

Our model displays remarkable advantages, yet it relies on strong hypotheses that impose many limits on our approach. Those limitations can be sorted into three main categories :

1. **Nature of the microstructural heterogeneities :** one of the strongest hypotheses consists in assuming that both the matrix and the inclusions share the same elastic properties and only differ in their fracture properties. It presents the advan-

tage that the crack only sees a defect when it lands on the inclusion since toughness heterogeneities do not have any long-range effect, in contrast with elastic heterogeneities. Yet elastic heterogeneities have been shown to impact crack trajectory [He and Hutchinson, 1989; Leguillon and Martin, 2013] and effective fracture properties [Li and Zhou, 2013a,b; Hossain et al., 2014; Wang and Xia, 2017; Brach et al., 2019a]. For example, stiffer heterogeneities have been shown to repel the crack while more compliant ones attract it. Elastic discontinuities can trigger not only crack deflection but also crack arrest through denucleation-renucleation processes. The perturbative approach developed in our model, which allows the estimation of SIF perturbations from geometrical crack perturbations, could be coupled at first-order to the formulæ of Gao [1991] extended by Muju [2000], which provide SIF perturbations induced by elastic heterogeneities. In that case, only continuous variations of elastic and fracture properties could be considered since neither the current perturbative framework nor Amestoy-Leblond's formulæ can deal with elastic discontinuities. Such formalism would also be extended to weakly anisotropic materials and homogeneous media displaying residual stresses. The computational cost would be thus increased but remarkable performances could still be reached through hardware-based optimization such as GPU parallelism ;

2. **Crack-inclusion interaction mechanisms :** crack trapping by tougher inclusions and crack deflection by inclusion by-pass are the only two mechanisms considered in this study. Bridging mechanism [Bower and Ortiz, 1991], where two separate regions of the crack coalesce around the particle and leave it unbroken in its wake, is out of reach of our first-order approach. Crack nucleation and inclusion debonding in the vicinity of the crack tip are also out of the study's range. Nucleation processes could be addressed within LEFM through the Leguillon and Martin [2013]'s double criterion. However, dealing with the interaction between two cracks is not possible yet within the current perturbative approach. Crack branching, which can happen at the interface with an inclusion [Xu et al., 1998], cannot be modeled either in our perturbative approach. For those mechanisms exhibiting more complex topological crack configurations, the pertubative approach may not be the appropriated tool and phase field modeling seems to be a more suitable framework [Nguyen et al., 2015, 2016, 2017b] ;

3. **Loading type :** this study only considers macroscopic tensile loading. It can be however extended to plane (Mode II) and anti-plane shear (Mode III) loading since Gao and Rice [1986] and Movchan et al. [1998] already provide the suitable formulæ for the half-plane crack. In that case, the crack surface has also to be meshed and SIF perturbations involve integral over the whole crack surfaces. It may be Future developments may provide rich insights on crack fragmentation in Mode I+III in presence of disorder as suggested by the preliminary results of Leblond and Ponson [2016]. The same remarks can be made for the T-stresses and A-stresses on the behavior of cracks.

3

Mechanisms of interaction between a crack and tough inclusions : a decisive factor in material toughening

Contents

3.1 Introduction

Predicting at which loading levels does crack propagation start and the path the crack will follow during the subsequent propagation is of utmost importance in materials science since the design and reliability of macroscopic structures often depend on it. Understanding how material heterogeneities impact crack trajectory and effective fracture properties is a first but mandatory step to construct a theoretical framework rationalizing the failure behavior of heterogeneous solids. It also paves the way for the development of tailored micro-structured materials where the main features of crack propagation, its trajectory (propagation along a chosen path) or its dynamics (sudden propagation or progressive crack advance) can be controlled. Engineers would thus have at their disposal a vast range of *meta-materials* with either increased fracture resistance, where cracks would only propagate at high loading levels, or a better crack tolerance, where cracks would not propagate suddenly through the whole sample but rather step by step with a controlled dynamic.

The impact of heterogeneities on crack trajectory has been extensively studied since the seminal works of He and Hutchinson [1989] and Hutchinson and Suo [1991], who studied two-dimensional crack kinking at the interface between materials with different elastic and fracture properties. A wide range of materials displays toughness anisotropy from experimental measurements : geological materials as granites [Nasseri and Mohanty, 2008; Kataoka et al., 2015], shales [Chandler et al., 2016; Li et al., 2019], single crystals [Ebrahimi and Kalwani, 1999; Li et al., 2005], piezoelectric ceramics [Pisarenko et al., 1985], foams [Gomez-Monterde et al., 2016] or extruded polymers [Takei et al., 2013; Ibarra et al., 2016]. This anisotropy happens to substantially modify the crack path. Recent phase-field studies investigate the question of crack propagation in the presence of such anisotropic toughness via the introduction of an angular toughness distribution $G_c(\theta)$ [Hakim and Karma, 2005, 2009; Nguyen et al., 2017a; Li and Maurini, 2019], without mentioning how such a distribution emerges from the microstructure. In contrast, other numerical studies investigate the way a crack interacts with a single material heterogeneity, thus focusing on *the interaction mechanisms*. Gao et al. [2018a] explored via X-FEM simulations the two-dimensional scenario where a crack interacts with a tougher circular inclusion for various toughness ratios, either through a by-pass or a crossing mechanism. Clayton and Knap [2014] looked at the same mechanisms with three-dimensional phase-field simulations. They identified the conditions of toughness properties and elastic properties under which one mechanism, by-pass or crossing, prevails over the other. Nguyen et al. [2017b] considered crack interaction with microstructures directly extracted from computed micro-tomography. They modeled various phenomena including inclusion by-pass, interface debonding, micro-fracturing and successfully compared numerical simulations with experimental observations of the crack trajectory.

The *interaction mechanisms*, which take place during the interplay between a crack and heterogeneities, set the local toughness values the crack visits during propagation which subsequently control the *effective fracture properties* of the material. For a one-dimensional layered material, where the defects are invariant along the direction (Oz) of the crack

front and along the direction (Oy) orthogonal to the crack plane, Hossain et al. [2014] showed through numerical phase field simulations that the crack is *trapped* by tougher layers. The effective toughness, defined as the maximum ERR imposed by the loading, is then determined by the maximum toughness among all layers. In the two-dimensional case, where the heterogeneities are only invariant in the z-direction, they showed that tougher defects could be by-passed by the crack and that toughness increases do not emerge from the sole crack tortuosity. Li and Zhou [2013a] modeled crossing and by-pass mechanisms in a two-dimensional setting through cohesive zone model simulations, supported by an analytical model [Li and Zhou, 2013b]. They investigated the impact of inclusion shape and properties on the reinforcement induced by the two mechanisms. Xia et al. [2018] and Da et al. [2018] combined heterogeneous phase-field models to topological optimization to increase peak loading at the onset of fracture by promoting inclusion debonding over inclusion by-pass (see Fig. 3.1).

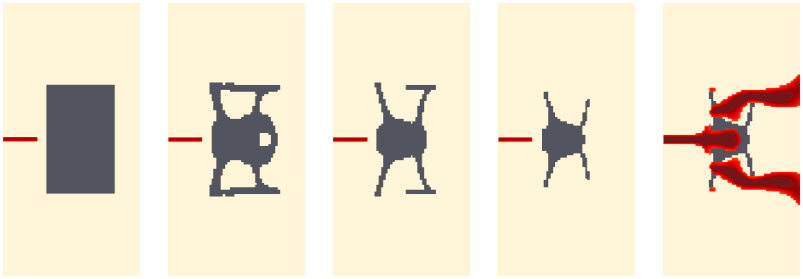

(a) Iteration 0 (b) Iteration 13 (c) Iteration 24 (d) Iteration 39 (e) Crack propagation

Figure 3.1: Defect geometry at various iterations of the iteration process (a)-(d) for a 20% inclusion density and crack propagation under tensile loading (e) (after [Xia et al., 2018])

However, quantitative three-dimensional studies on the interaction between a crack and tougher inclusions within the perturbative approach have been up to now restricted to the sole coplanar crossing mechanism. In particular, the interaction of a crack with a single defect has been studied in details, comparing theoretical results derived from the LEFM-based perturbative framework to experimental observations for the stationary shape of the crack front during the crossing of the tough inclusion [Dalmas et al., 2009; Chopin et al., 2011; Patinet et al., 2013a; Vasoya et al., 2016b] and the subsequent relaxation of this front out of the defect [Chopin et al., 2018]. It brought to light the decisive link between the local toughness, crack front deformations and propagation dynamics. Gao and Rice [1989] investigated theoretically and numerically the impact of this coplanar *crack trapping* on the effective fracture properties, where the crack bows between periodic arrays of pinning obstacles. They showed that the effective toughness increases linearly with the inclusion toughness when "regular" crossing occurs during the interaction of the crack with the inclusion, while "irregular" processes resulting from an instability are detrimental to the material reinforcement. They highlighted how the regularity of the crossing mechanism is related to both the inclusion geometry and its mechanical properties. Xia et al. [2013] and Xia et al. [2015] exploited those features to design materials displaying anisotropic tough-

ness. Recently, Hsueh and Bhattacharya [2018] combined this approach with topological optimization to find the optimal inclusion shape for the trapping mechanism and maximize either the effective toughness or the toughness anisotropy. Bower and Ortiz [1991] considered the competing influence of *crack trapping* and *crack bridging*, where inclusions are left unbroken in the wake of the crack and pin the crack surface. This mechanism has been proved to toughen brittle composites in a very efficient way [Krstic et al., 1981; Malik and Barthelat, 2016]. Recently, Vasoya et al. [2016a] evidenced a fingering mechanism in strongly heterogeneous materials. In that case, the crack only propagates in the weaker parts of the materials so that the effective toughness may reach the smallest value of the local toughness field.

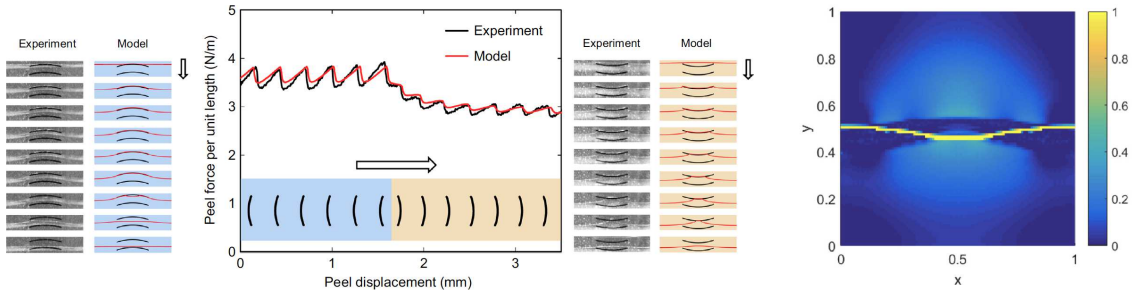

(a) Anisotropic toughness (b) Optimized defect

Figure 3.2: Toughness anisotropy induced by inclusion shape (after [Xia et al., 2015]) (a) and optimized defect for toughness anisotropy (after [Hsueh and Bhattacharya, 2018]) (b)

When it comes to non-coplanar propagation, studies lying within the perturbative framework are scarce and only concern the disordered case, where the fundamental interactions between a crack and tougher inclusions have not been modeled *per se* [Ramanathan et al., 1997; Barès et al., 2014]. Consequently, they cannot study the interaction mechanisms happening at the crack tip and their ultimate impact on the reinforcement of brittle composite materials. The study presented in this chapter aims at filling this gap by investigating how the coupling of the in-plane and out-of-plane modes of deformation of the crack front may impact crack trajectory, its dynamics, and the final effective fracture properties. Our theoretical framework allows to account for two competing interaction mechanisms happening at the crack tip : inclusion crossing and by-pass, which respectively activate material toughening by *crack trapping* or *crack deflection*. Section 3.2 is devoted to an illustrated review of the coplanar interaction of a crack and tough inclusions by inclusion crossing and the subsequent toughening by crack trapping. In Section 3.3, we introduce a second interaction mechanism, inclusion by-pass. The conditions under which one mechanism prevails over the other are thoroughly investigated in the case of spherical inclusions, as well as their respective impact on effective fracture properties. Section 3.4 highlights how inclusion shape can modify the conditions under which the crossing to by-pass transition occurs through three-dimensional collective effects along the crack front. We show how it facilitates inclusion by-pass in the case of ellipsoidal inclusion elongated along the front direction. This early transition from inclusion crossing to inclusion by-pass is shown to limit further material toughening. Section 3.5 details how a cubical inclusion shape can

on the contrary delay inclusion by-pass by the activation of a third mechanism, inclusion repenetration, where the crack goes back in the inclusion after an initial phase of by-pass. Not only does it extend material reinforcement by crack trapping but it also improves the toughening potential of crack deflection. Section 3.6 is dedicated to the coupling of crack trapping, crack deflection and crack bridging. Based on the results of Bower and Ortiz [1991], our study shows that the by-pass mechanism can not only limit crack trapping but also prevent crack bridging from happening if the inclusion is not elongated enough in the direction perpendicular to the crack surface. Finally, Section 3.7 is devoted to the influence of the interface toughness on the effective fracture properties. In general, a weaker interface promotes inclusion by-pass and thus has a negative impact upon the effective fracture properties. Yet, under some specific conditions, it can toughen the material, highlighting the complexity of material design for increased fracture properties.

3.2 Inclusion crossing : an efficient material toughening by coplanar crack trapping

When a crack interacts with a tough inclusion in a three-dimensional setting, the crack front distorts both within the crack plane (crack trapping) and out of it (crack deflection). The resulting crack trajectory and dynamics strongly depends on the mechanical and geometrical properties of the inclusion. It ultimately determines the effective fracture properties of the heterogeneous medium.

We start here by investigating the *crossing interaction* where a *coplanar* crack is pinned by periodic arrangements of tough inclusions through a *crack trapping* mechanism. Coplanar crack trapping has been thoroughly investigated in previous works [Gao and Rice, 1989; Bower and Ortiz, 1991; Chopin et al., 2011; Vasoya et al., 2016b; Chopin et al., 2018]. In this section, we propose to revisit the main results of those coplanar studies and illustrate them on the various inclusion geometries (spherical, cubical, ellipsoidal) considered in this manuscript. In Section 3.2.1, we investigate how a coplanar crack behaves when facing a tough inclusion. Section 3.2.2 is dedicated to the impact of the coplanar interaction mechanisms on the effective fracture properties of periodic arrangements of tough inclusions.

3.2.1 In-plane perturbations and their dynamics : a reflection of the local material toughness

In this section, we describe the crack front configuration and its evolution when a coplanar crack interacts with a tougher inclusion. In particular, we show that crack front in-plane distortions and their dynamics are in fact mirror images of the local toughness field : the intensity of the in-plane perturbations are directly linked to the inclusion toughness, as well as its spatial distribution, while their dynamics is closely connected to the local variations of the toughness field $G_c(z, x)$.

3.2.1.a Equation of motion for a coplanar crack

When the crack cannot wander out-of-plane i.e. $f_y(z, t) = 0$ and $\theta(z, t) = 0$, Mode II contributions are null $\delta K_{\mathrm{II}} = 0$ i.e. it propagates in pure Mode I. Crack propagation is

therefore planar and can be described by the sole kinetic law of Eq. (2.23) linking the local ERR G to the material toughness G_{c}. The ERR G along the crack front can be expressed at first-order in the perturbation f_x as :

$$\begin{aligned} G\left(z,t\right) &= \frac{1-\nu^2}{E} K_{\mathrm{I}}^2\left(z,t\right) = G^{\infty}\left(t\right)\left(1+\frac{\delta K_{\mathrm{I}}}{K_{\mathrm{I}}^{\infty}}\left(z,t\right)\right)^2 = G^{\infty}\left(t\right)\left(1+2\frac{\delta K_{\mathrm{I}}}{K_{\mathrm{I}}^{\infty}}\left(z,t\right)\right) \\ &= G^{\infty}\left(t\right)\left(1-\frac{1}{\mathcal{L}} f_x\left(z,t\right) - \frac{1}{\pi}\,\mathrm{PV}\int_{-\infty}^{+\infty} \frac{f_x\left(z,t\right)-f_x\left(z',t\right)}{\left(z-z'\right)^2}\,dz'\right) \end{aligned} \tag{3.1}$$

The equation of motion thus reads :

$$\begin{aligned} \frac{1}{v_0}\frac{\partial f_x}{\partial t}\left(z,t\right) =& \frac{v_{\mathrm{m}}}{v_0} + \frac{G\left(z,t\right) - G_{\mathrm{c}}\left(z, x=f_x\left(z,t\right)\right)}{G_{\mathrm{c}}^{\mathrm{mat}}} \\ =& \frac{v_{\mathrm{m}}}{v_0} + \frac{G^{\infty}\left(t\right)}{G_{\mathrm{c}}^{\mathrm{mat}}}\left(1-\frac{f_x\left(z,t\right)}{\mathcal{L}} - \frac{1}{\pi}\,\mathrm{PV}\int_{-\infty}^{+\infty}\frac{f_x\left(z,t\right)-f_x\left(z',t\right)}{\left(z-z'\right)^2}\,dz'\right) \\ & - \frac{G_{\mathrm{c}}\left(z, x=f_x\left(z,t\right)\right)}{G_{\mathrm{c}}^{\mathrm{mat}}} \end{aligned}$$

This equation is highly non-linear due to the dependence in f_x of the toughness field but analytical results can be derived in simple cases.

3.2.1.b Interaction of a crack with a single obstacle : stationary shape of the crack front and relaxation dynamics out of the defect

In this section, we study the interaction of a crack with a single obstacle invariant in the propagation direction (Ox). We thus revisit the analytical results of Chopin et al. [2011] for the stationary shape of a crack interaction with a single defect and Chopin et al. [2018] for the relaxation of the in-plane perturbations of the crack front out of the defect. Analytical solutions are finally compared to numerical results derived from the computational method described in Section 2.3, assessing its validity on model situations.

Problem statement

We consider a half-plane crack propagating in a matrix of toughness $G_{\mathrm{c}}^{\mathrm{mat}}$. The crack is interacting with a defect of toughness $G_{\mathrm{c}}^{\mathrm{inc}}$. The defect has a finite width d in the z-direction while it is invariant in the x-direction so that the local toughness field reads :

$$G_{\mathrm{c}}\left(z,x\right) = G_{\mathrm{c}}\left(z\right) = \begin{cases} G_{\mathrm{c}}^{\mathrm{inc}} = G_{\mathrm{c}}^{\mathrm{mat}}\left(1+c_{\mathrm{inc}}\right), \text{ if } x \in \left[-\dfrac{d}{2},\dfrac{d}{2}\right] \\ G_{\mathrm{c}}^{\mathrm{mat}}, \text{ otherwise} \end{cases} \tag{3.2}$$

We can thus write :

$$G_{\mathrm{c}}\left(z,x\right) = G_{\mathrm{c}}\left(z\right) = G_{\mathrm{c}}^{\mathrm{mat}} + c_{\mathrm{inc}}\,\mathcal{H}\left(z\right) \tag{3.3}$$

where $\mathcal{H}$ is the indicator function of the interval $\left[-\frac{d}{2},\frac{d}{2}\right]$.

Stationary shape of the crack front interacting with the single obstacle

We first investigate how the crack front distorts when it is interacting with the single obstacle. This problem has been studied by Chopin et al. [2011], whose results are summarized below.

Let us consider the case where the crack front reaches its stationary configuration so that $\frac{\partial f_x}{\partial t}(z,t) = 0$. The in-plane perturbation of the crack front in the limit where $\mathcal{L} \to \infty$ and $v_\mathrm{m} \to 0$. Eq. (3.2) satisfies :

$$G^\infty \left(1 - \frac{1}{\pi}\,\mathrm{PV}\int_{-\infty}^{+\infty} \frac{f_x(z,t) - f_x(z',t)}{(z-z')^2}\,dz'\right) = G_\mathrm{c}(z,) = G_\mathrm{c}^\mathrm{mat} + c_\mathrm{inc}\,\mathcal{H}(z) \tag{3.4}$$

At zero-order in the perturbation, we get :

$$G^\infty = G_\mathrm{c}^\mathrm{mat} \tag{3.5}$$

Using Eq. (2.26), Eq. (3.4) reads at first-order in the perturbation :

$$-\frac{1}{\pi}\,\mathrm{PV}\int_{-\infty}^{+\infty} \frac{f_x(z) - f_x(z')}{(z-z')^2}\,dz' = c_\mathrm{inc}\mathcal{H}(z) \tag{3.6}$$

$$\Rightarrow \hat{f}_x(k) = -\frac{1}{|k|}\hat{\mathcal{H}}(k) = -\frac{c_\mathrm{inc} d}{|k|}\mathrm{sinc}\left(\frac{kd}{2}\right) \tag{3.7}$$

where $\mathrm{sinc}(x) = \frac{\sin(x)}{x}$ is the cardinal sine function.

As noted by Chopin et al. [2011], the absolute position of the crack front cannot be derived from this equation when $\mathcal{L} \to \infty$ and $v_\mathrm{m} \to 0$. This difficulty can be circumvented by estimating the crack front deviation from the position $f_x(0)$, that gives, using Eq. (2.25) :

$$f_x(z) = f_x(0) + \frac{2c_\mathrm{inc}}{\pi}\int_0^{+\infty} \frac{1}{k^2}\sin\left(\frac{kd}{2}\right)\left[1 - \cos(kz)\right]dk \tag{3.8}$$

which finally leads to (see for instance [Gradshteyn and Ryzhik, 2014]) :

$$f_x(z) = f_x(0) + \frac{c_\mathrm{inc} d}{2\pi}\left[\left(1 + \frac{2z}{d}\right)\ln\left|1 + \frac{2z}{d}\right| + \left(1 - \frac{2z}{d}\right)\ln\left|1 - \frac{2z}{d}\right|\right] \tag{3.9}$$

The crack front is thus pinned by the tougher defect while it crosses it. This mechanism is called *crack trapping*. Crack front deformations are plotted in Fig. 3.3.a for various inclusion toughnesses. Analytical predictions from Eq. (3.9) are compared to numerical results in Fig. 3.3.a. The infinite medium cannot be modeled in our numerical framework and the small discrepancy between the analytical and numerical front shape emerges from the finite inclusion spacing $L_z = 1024\,d$ considered in the numerical simulations.

These results illustrate that the in-plane front deformation mirrors the local toughness field. Indeed, the *characteristic size of the defect* d as well as the *inclusion contrast* $c_\mathrm{inc} = \left(G_\mathrm{c}^\mathrm{inc} - G_\mathrm{c}^\mathrm{mat}\right)/G_\mathrm{c}^\mathrm{mat}$, are embedded in the perturbation. This quantitative information on the toughness field can thus be entirely extracted from the crack front in-plane perturbation.

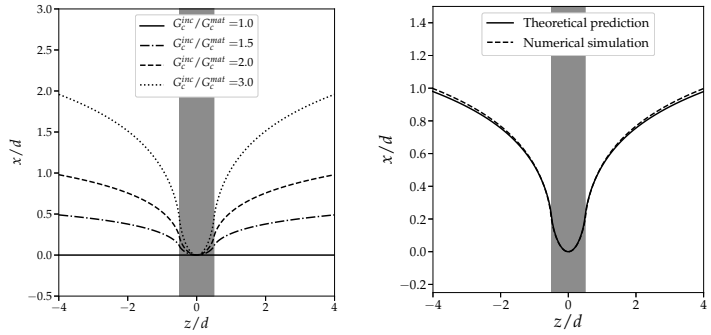

(a) (b)

Figure 3.3: Impact of a tough inclusions on crack front in-plane distortions : in-plane configuration for a crack-front interacting with a single inclusion of size d invariant in the z-direction for multiple values of inclusion toughness ratio G_c^{inc}/G_c^{mat} (a) and comparison between theoretical predictions and numerical simulations on a medium of finite size $L_z/d = 1024$ for an inclusion contrast $G_c^{inc}/G_c^{mat} = 1$ (b)

Relaxation dynamics of the perturbations of the front leaving the defect

We explore the question of the relaxation of the in-plane perturbation out of the defect. As studied by Chopin et al. [2018], let us then consider that at a time $t = 0$, the crack front leaves the defect as illustrated in Fig. 3.4.a. It now propagates in a homogeneous medium of toughness G_c^{mat}. The following evolution equation can be derived in the limit where $\mathcal{L} \to \infty$ and $v_m \to 0$:

$$\frac{1}{v_0}\frac{\partial f_x}{\partial t}(z,t) = -\frac{1}{\pi}\,\mathrm{PV}\int_{-\infty}^{+\infty}\frac{f_x(z,t) - f_x(z',t)}{(z-z')^2}\,dz' \tag{3.10}$$

Taking Eq. (3.10) in the Fourier space :

$$\begin{aligned}
&\frac{1}{v_0}\frac{\partial \hat{f}_x}{\partial t}(k,t) = -|k|\,\hat{f}_x(k,t)\\
&\Rightarrow\ \hat{f}_x(k,t) = e^{-|k|v_0 t}\hat{f}_x(k,0) = c_{inc} d\,\mathrm{sinc}\left(\frac{kd}{2}\right)\frac{e^{-|k|v_0 t}}{|k|}\\
&\Rightarrow\ \frac{\partial \hat{f}_x}{\partial t}(k,t) = e^{-|k|v_0 t}\hat{f}_x(k,t) = c_{inc} d v_0\,\mathrm{sinc}\left(\frac{kd}{2}\right)e^{-|k|v_0 t}
\end{aligned} \tag{3.11}$$

Going back to the real space, the crack velocity reads :

$$\frac{\partial f_x}{\partial t}(z,t) = \frac{2c_{inc}v_0}{\pi}\int_0^{+\infty}\sin\left(\frac{kd}{2}\right)\cos(kz)\,\frac{e^{-|k|v_0 t}}{|k|}dk \tag{3.12}$$

This integral can be calculated thanks to Gradshteyn and Ryzhik [2014] formula (3.947.3) :

$$\frac{\partial f_x}{\partial t}(z,t) = \frac{2c_{inc}v_0}{\pi}\left[\arctan\left(\frac{d/2+z}{v_0 t}\right) - \arctan\left(\frac{-d/2+z}{v_0 t}\right)\right] \tag{3.13}$$

We finally integrate Eq. (3.13) to find the crack dynamics during relaxation :

$$\begin{aligned} f_x(z,t) =& f_x(0,0) + \frac{c_{\text{inc}} d}{2\pi}\left[\left(1+\frac{2z}{d}\right)\ln\left|1+\frac{2z}{d}\right| + \left(1-\frac{2z}{d}\right)\ln\left|1-\frac{2z}{d}\right|\right] \\ &+ \frac{c_{\text{inc}} d}{4\pi}\left[\left(1+\frac{2z}{d}\right)\ln\left[1+\left(\frac{v_0 t}{d/2+z}\right)^2\right] + \left(1-\frac{2z}{d}\right)\ln\left[1+\left(\frac{v_0 t}{-d/2+z}\right)^2\right]\right] \\ &+ \frac{c_{\text{inc}}}{\pi} v_0 t\left[\arctan\left(\frac{d/2+z}{v_0 t}\right) - \arctan\left(\frac{-d/2+z}{v_0 t}\right)\right] \end{aligned} \tag{3.14}$$

Such a dynamic is plotted in Fig. 3.4. We see that when the toughness suddenly decreases, the crack relaxes until it finds back its straight configuration. By comparing theoretical predictions and our simulation results, we see that the numerical method grasps fairly well the depinning dynamics on a single inclusion. The geometry of the defect is nonetheless slightly different (see Fig. 3.4.a-b) so that the crack is pinned for a longer duration in the numerical simulations. This explains the slight discrepancy between theoretical predictions and numerical simulations for small wavelength components at small depinning time ($c_{\text{inc}} v_0 t/d = 0.5$) in Fig. 3.4.b).

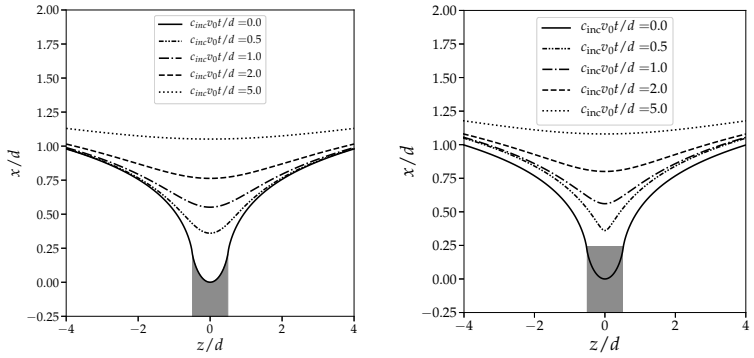

(a) (b)

Figure 3.4: In-plane relaxation of a crack front previously pinned by an inclusion : theoretical predictions (a) and numerical results on a medium of size $L_z/d = 1024$ with a slightly different defect geometry (b) for an inclusion contrast $G_{\text{c}}^{\text{inc}}/G_{\text{c}}^{\text{mat}} = 1$

If Eq. (3.9) told us that information on the toughness field can be deduced from in-plane front perturbation, Eq. (3.14) shows that information on the local variations of the toughness field is embedded as well in the crack dynamics, since the relaxation of a crack from a single defect happens at a characteristic velocity $c_{\text{inc}} v_0$.

3.2.1.c From the single obstacle to periodic arrangements of tougher inclusions : impact of particles inter-spacing on the crack front perturbation

We now consider a case in which the crack is pinned by an array of inclusions invariant in the z-direction of width d. The inclusions are spaced by a length L_z. Such microstructure

is depicted in Fig. 3.5.a. The toughness field reads :

$$G_{\mathrm{c}}(z,x) = G_{\mathrm{c}}(z) = \begin{cases} G_{\mathrm{c}}^{\mathrm{inc}} = G_{\mathrm{c}}^{\mathrm{mat}}(1+c_{\mathrm{inc}}), \text{ if } x \in \left[n\pi - \dfrac{d}{2}, n\pi + \dfrac{d}{2}\right] \\ G_{\mathrm{c}}^{\mathrm{mat}}, \text{ otherwise} \end{cases} \tag{3.15}$$

If we assume that the crack front reaches its stationary shape, the in-plane perturbation f_x satisfies Eq. (3.4). We get at zero-order in f_x :

$$G^{\infty} = G_{\mathrm{c}}^{\mathrm{mat}}\left(1 + \frac{d}{L_z}c_{\mathrm{inc}}\right) = \langle G_{\mathrm{c}}\rangle_z \tag{3.16}$$

At first-order on the perturbation :

$$-\frac{\langle G_{\mathrm{c}}\rangle_z}{\pi}\,\mathrm{PV}\int_{-\infty}^{+\infty}\frac{f_x(z)-f_x(z')}{(z-z')^2}\,dz' = G_{\mathrm{c}}(z) \tag{3.17}$$

Following the reasoning developed in Section 3.2.1.b, it is possible to show that :

$$\begin{aligned} f_x(z) - f_x(0) &= -\frac{G_{\mathrm{c}}^{\mathrm{inc}} - G_{\mathrm{c}}^{\mathrm{mat}}}{\langle G_{\mathrm{c}}\rangle_z}\frac{L_z}{\pi^2}\sum_{1}^{+\infty}\frac{\sin\left(n\pi\frac{d}{L_z}\right)}{n^2}\left[1-\cos\left(\frac{2\pi}{L_z}nz\right)\right] \\ \Leftrightarrow f_x(z) - f_x(0) &= \frac{G_{\mathrm{c}}^{\mathrm{inc}} - G_{\mathrm{c}}^{\mathrm{mat}}}{\langle G_{\mathrm{c}}\rangle_z}\frac{2}{\pi}\int_0^z \ln\left[\frac{\sin\left(\frac{\pi}{L_z}\left(\frac{d}{2}+z'\right)\right)}{\sin\left(\frac{\pi}{L_z}\left(\frac{d}{2}-z'\right)\right)}\right]dz' \end{aligned} \tag{3.18}$$

We plot the in-plane perturbation for such microstructure for various inclusion spacing L_z in Fig. 3.5.b for an inclusion twice as tough as the matrix.

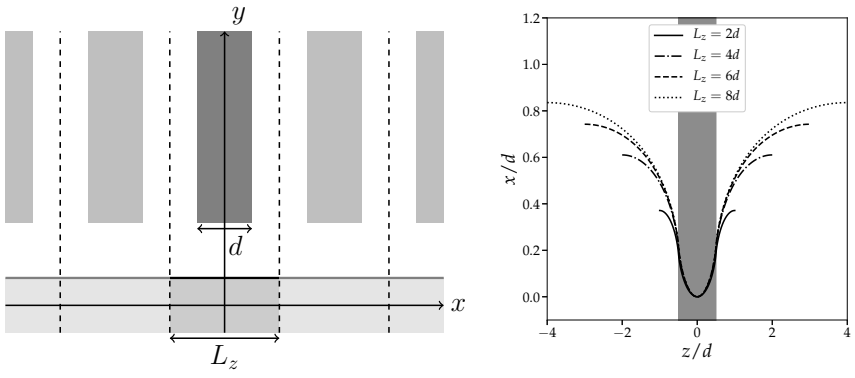

(a) (b)

Figure 3.5: Impact of the inclusion spacing L_z on crack front in-plane distortions : crack interacting with periodic arrangement of tougher defects of size d invariant the x-direction, whose centers are separated by a length L_z (a). Crack front configuration for $G_{\mathrm{c}}^{\mathrm{inc}} = 2\,G_{\mathrm{c}}^{\mathrm{mat}}$ for various inclusion spacing L_z, based on Eq. (3.18) (b)

We notice that the larger the inclusion spacing, the more the crack bows in the unpinned regions where $G_c(z) = G_c^{mat}$. It explains quantitatively the discrepancy between theoretical predictions on the front shape resulting from the interaction of a coplanar crack and a single defect and the associated numerical simulations for $L_z = 1024\,d$, which was discussed in Section 3.2.1.b. We finally conclude that the crack front in-plane distortion ultimately contains information on the toughness spatial distribution, as does their dynamics.

3.2.2 Coplanar crack trapping : an efficient toughening mechanism related to inclusion crossing

We have seen how tougher inclusions affect crack trajectory and dynamics. The tough inclusion makes the crack front distort within the crack plane through a *crack trapping mechanism*. It is now time to investigate how this mechanism impacts the effective fracture properties of the composite material.

3.2.2.a Effective toughness : a preliminary definition

We need first to define how effective fracture properties can be measured. In agreement with previous works [Gao and Rice, 1989; Bower and Ortiz, 1991; Hossain et al., 2014; Vasoya et al., 2016a; Brach et al., 2019a], we define the *effective toughness* as the maximal macroscopic elastic release rate G^∞ (resulting from the external loading) encountered during *cracking of the whole sample*: :

$$G_c^{eff} = \max_{x\in[0,L_x]} G^\infty(x) \tag{3.19}$$

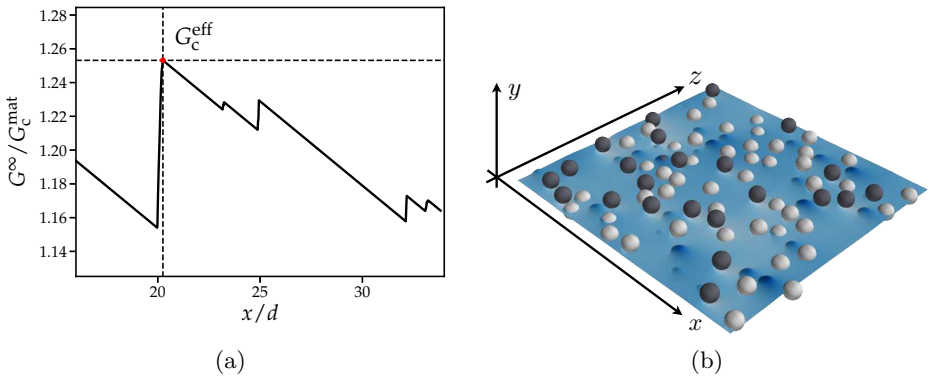

(a) (b)

Figure 3.6: Effective toughness G_c^{eff} defined as the maximum ERR imposed by the macroscopic loading G^∞ during crack propagation : evolution of G^∞ during crack propagation (a) for a medium-sized disordered system (b). The macroscopic ERR G^∞ increases while the front is pinned and decreases when the crack propagates according to Eq. (2.6).

This definition embraces Griffith's theoretical idea since total fracture of the composite happens for $G^\infty = G_c^{eff}$. Yet, up to this date, no consensus has emerged for the definition of the effective toughness. This question will be thoroughly discussed for disordered systems in Section 4.3.1. An example of G^∞ evolution and associated G_c^{eff} estimation is given in Fig. 3.6 for the three-dimensional propagation of a crack interacting with a disordered arrangement of inclusions whose toughnesses are $G_c^{inc} = 1.75\,G_c^{mat}$ and $G_c^{int} = G_c^{mat}$.

3.2.2.b Toughening induced by crack trapping : a theoretical analysis

Gao and Rice [1989] investigated in depth the impact of coplanar inclusion crossing on the effective toughness. They highlighted that effective fracture properties are controlled by what they call the "regularity" of the crossing processes. The following section is dedicated to the description and the illustration of this concept with numerical results extracted from our perturbative approach.

Effective toughness for periodic arrays of inclusions invariant in the propagation direction

The analysis of the stationary shape of a crack interacting with a periodic array of inclusions invariant in the propagation direction, for a width d and inclusion spacing L_z gave quantitative results on the effective properties of such composite. Indeed, we saw in Eq. (3.16) that the macroscopic ERR imposed by the loading follows a *mixture rule* [Gao and Rice, 1989] :

$$G^{\infty} = G_{\mathrm{c}}^{\mathrm{mat}} \left(1 + \frac{d}{L_z} c_{\mathrm{inc}}\right) \tag{3.20}$$

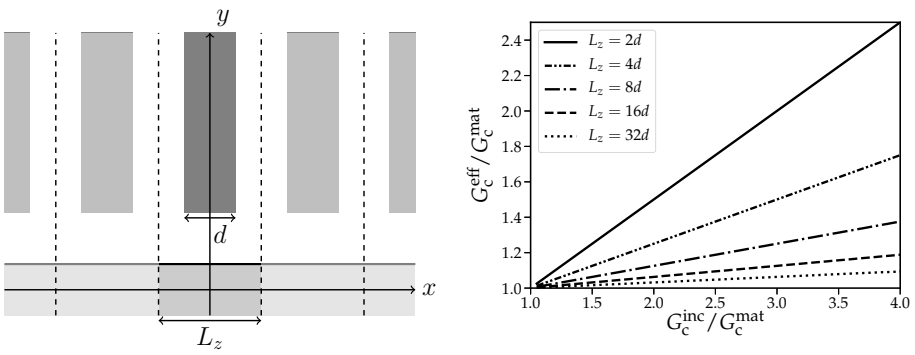

(a) (b)

Figure 3.7: Periodic arrangement of tougher inclusions of width d and inter-spacing L_z (a) and the associated effective toughness for various inclusion toughness ratio $G_{\mathrm{c}}^{\mathrm{inc}}/G_{\mathrm{c}}^{\mathrm{mat}}$ and inclusion spacing L_z, which follows a mixture rule in Eq. (3.20) (b)

The effective toughness happens to increase linearly with the inclusion width ratio d/L_z as well as the inclusion contrast $c_{\mathrm{inc}} = \left(G_{\mathrm{c}}^{\mathrm{inc}} - G_{\mathrm{c}}^{\mathrm{mat}}\right)/G_{\mathrm{c}}^{\mathrm{mat}}$. The impact of the inclusion width ratio and the inclusion contrast is plotted in Fig. 3.7. We propose a qualitative explanation for those results : when the inclusion spacing is low, the crack does not bow sufficiently between the inclusions (see Fig. 3.5) to ensure $G = G_c$ inside the inclusion through an increase of Mode I SIF perturbation δK_{I} (see Eq. (3.2)). One has then to increase the macroscopic ERR imposed loading G^{∞} to ensure further crack propagation.

Regularity of the crossing mechanism influences material toughening

For finite-sized inclusions in the propagation direction, Gao and Rice [1989] distinguished two cases : a first one where inclusion crossing is regular and the effective toughness follows a mixture rule in Eq. (3.20) and a second one where inclusion crossing is irregular and the mixture rule constitutes an upper bound for the effective toughness.

Let us consider a periodic arrangement of inclusions, characterized by their toughness G_c^{inc}, their size d in the front direction (Oz) spaced by a length L_z (see Fig. 3.9.a for the circular case or Fig. 3.9.b for the square one). Predicting the effective toughness of such heterogeneous materials consists in evaluating the maximum macroscopic ERR G^∞ imposed by the loading. If we average Eq. (3.2) along the z-direction in the limit where $\mathcal{L} \to \infty$ and $v_m \to 0$, we get :

$$G^\infty(t) = \langle G_c(z, x = f_x(z,t)) \rangle_z \tag{3.21}$$

where $\langle \cdot \rangle_z$ is the spatial average in the z-direction.

Given that the inclusion size in the z-direction is d, Eq. (3.21) proves that the mixture rule constitutes an upper bound of $G^\infty(t)$. It also implies that if the crossing process is regular i.e. the effective toughness G_c^{eff} follows Eq. (3.20), it is possible to find a stable configuration during crack propagation verifying the condition $G(z) = G_c^{inc}$ inside the inclusion and $G(z) = G_c^{mat}$ outside of it. A configuration verifying this condition has been found earlier in Eq. (3.18). The bifurcation analysis conducted by Rice [1985] for the half-plane crack states that this solution is unique given that $\frac{\partial G^\infty}{\partial x} \leq 0$, as it is assumed in our study.

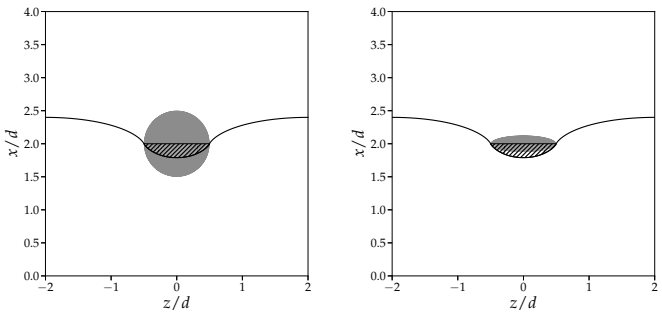

(a) Regular process (b) Irregular process

Figure 3.8: Visual method to assess the regularity of the crossing process : a regular process for a circular inclusion (a) and an irregular one for an elliptic inclusion elongated in the front direction (b) for $G_c^{inc} = 2.5\, G_c^{mat}$

It provides a visual method to assess whether the inclusion crossing is a regular process or an irregular one. Indeed if crack propagation verifies Eq. (3.20), the part of the front shape between $\left[-\frac{d}{2}, \frac{d}{2}\right]$ described by Eq. (3.18) has to be contained within the obstacle. For a circular inclusion of toughness $G_c^{inc} = 2.5\, G_c^{mat}$, the penetration process is regular as depicted in Fig. 3.8.a. On the contrary, if the crack front described by Eq. (3.18) cannot be fully contained in the inclusion, the crossing process is irregular. An example of such an

irregular process is given in Fig. 3.8.b with the example of an elliptic inclusion elongated in the z-direction of the crack front.

The regularity of the crossing mechanism is thus dictated by the shape of the inclusion, the ratio between its size d and the inclusion spacing L_z as well as its toughness G_c^{inc} with respect to the one of the matrix G_c^{mat} (see Eq. (3.18)). Therefore, even if an array of inclusions is crossed in a regular manner for a given set of material properties (shape, toughness, spacing), the process might become irregular if the inclusion toughness or the inclusion spacing increases.

3.2.2.c Impact of the inclusion shape on the effective fracture properties : a numerical study

To illustrate the impact of the regularity of the crossing mechanism on the effective fracture properties, we estimate the effective toughness of heterogeneous composites for various inclusion shapes through numerical simulations computed with the method exposed in Section 2.3.

Periodic arrangements of circular inclusions

We first consider the case of the interaction between a coplanar half-plane crack with arrays of tougher circular inclusions (Fig. 3.9a). The effective toughness is calculated following Eq. (3.19) by tracking the macroscopic ERR G^∞ during crack propagation. Simulation parameters are summarized in Table 8.2. The results are plotted in Fig. 3.9 for various inclusion toughness G_c^{inc} and inclusion spacing L_z.

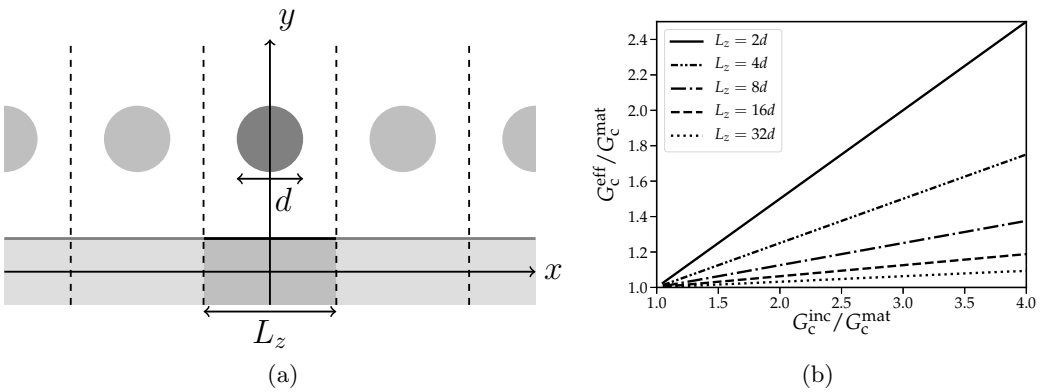

(a) (b)

Figure 3.9: Periodic arrangement of tougher circular inclusions of diameter d and spacing L_z (a) and the associated effective toughness G_c^{eff} for various inclusion toughness ratio G_c^{inc}/G_c^{mat} and inclusion spacing L_z (b). The effective toughness G_c^{eff} computed numerically fromEq. (3.19) follows the mixture rule in Eq. (3.19)

The visual method presented above confirms that the penetration process is regular for the circular inclusion in the range of inclusion toughness ($G_c^{inc}/G_c^{mat} \in [1, 4]$) and inclusion spacing ($L_z \in [2\,d, 32\,d]$) considered in our study . Thus, the effective toughness of such heterogeneous materials is expected to follow the mixture rule of Eq. (3.20), as confirmed in Fig. 3.9b.

Periodic arrangements of square inclusions

We then consider the case of periodic arrangements of square inclusions as depicted in Fig. 3.10.a. Simulation parameters are the same as in Table 8.2. Numerical results plotted in Fig. 3.10.b show once again that the effective toughness of such composite follows a mixture rule in the range of considered inclusion toughness and inclusion spacing. It is noticeable that, in the case of coplanar propagation, circular and square inclusions have the same toughening effect on the composite since they trigger the same interaction mechanism i.e. regular inclusion crossing.

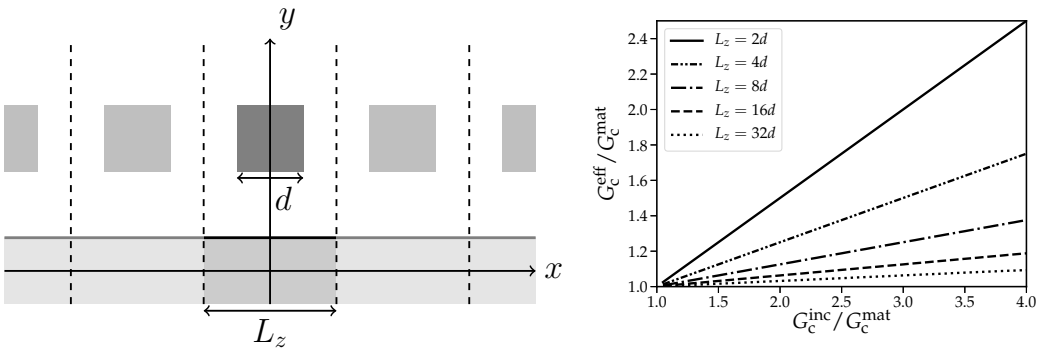

(a) (b)

Figure 3.10: Periodic arrangement of tougher square inclusions of diameter d and spacing L_z (a) and the associated effective toughness G_c^{eff} for various inclusion toughness ratio $G_c^{\text{inc}}/G_c^{\text{mat}}$ and inclusion spacing L_z (b). The effective toughness G_c^{eff} computed numerically fromEq. (3.19) follows the mixture rule in Eq. (3.19)

Periodic arrangements of ellipsoidal inclusions

But this observation cannot be repeated for every inclusion shape. If both circular and square inclusions proved to display regular penetration processes, it is not the case for elliptic inclusions as shown in Fig. 3.8.b.

To investigate the effect of process irregularity, we simulate the interaction between a coplanar half-plane crack and periodic arrangements of elliptic inclusions, elongated in the front direction (Oz). We consider elongation from $d_z/d_x = 1$ to $d_z/d_x = 8$ and inclusion toughness varying from $G_c^{\text{inc}}/G_c^{\text{mat}} \in [1 : 0.1 : 4]$. Simulation parameters are the same as in Table 8.2.

Crack front profiles are plotted during propagation in Fig. 3.11 for $G_c^{\text{inc}} = 2.5\, G_c^{\text{mat}}$. It illustrates why the crossing process for elongated elliptic inclusions is irregular. Indeed, we see in Fig. 3.11.a-b, that, for moderately elongated inclusions, it exists a configuration where a part of the crack front is contained in the whole width d of the obstacle, allowing the mixture rule to apply. On the contrary, we see in Fig. 3.11.c-d that, for highly elongated inclusions, lateral regions of the crack front $z = \pm\frac{d_z}{2}$ have already crossed the inclusion, when the central region penetrates in the obstacle. From Eq. (3.21), we understand that there is no crack front configuration satisfying the mixture rule and the effective toughness thus decreases $G_c^{\text{eff}} \leq G_c^{\text{mat}} \left(1 + \frac{d_z}{L_z} c_{\text{inc}}\right)$.

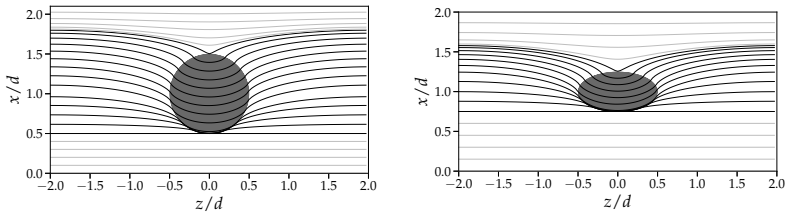

(a) $d_z/d_x = 1$ (b) $d_z/d_x = 2$

(c) $d_z/d_x = 4$ (d) $d_z/d_x = 8$

Figure 3.11: In-plane crack front at various loading time for the four different elliptic shapes used in the study for $G_c^{inc} = 2.5\, G_c^{mat}$

We observe that the effective toughness of periodic arrangements of elongated elliptic inclusions in the z-direction decreases with the inclusion elongation d_z/d_x. Numerical results are plotted in Fig. 3.11. The more elongated the inclusion, the earlier the penetration process becomes irregular and the smaller the effective toughness. To the best of our knowledge, no analytical results have been derived up to this date to quantitatively describe the impact of process irregularity. Bower and Ortiz [1991] proposes that one should rely on numerical simulations to estimate the effective toughness in this case.

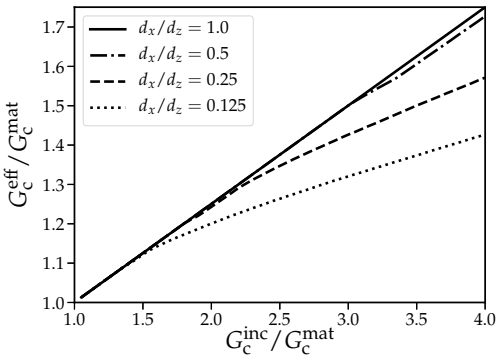

Figure 3.12: Impact of process irregularity on the effective toughness for various inclusion toughness and inclusion shape

Nonetheless, these planar situations illustrate that the effective toughness is controlled by the dynamics of the interaction between the crack and tougher inclusions, here regular or irregular crossing processes. Inclusion design is thus a key question for material toughening by tougher heterogeneities since it markedly affects the interaction dynamics.

3.3 Inclusion by-pass : a substantial loss of toughening induced by crack deflection

In our simulations, crack propagation is not bound to propagate within the crack plane and out-of-plane excursions of the crack front are triggered by by-pass events. Our theoretical framework provides a way to enrich the interaction between a crack and tough inclusions by modeling both *in-plane crack trapping* and *out-of-plane crack deflection*. In Section 3.3.1, we study the geometrical and mechanical conditions under which the by-pass mechanism or the crossing one prevails over one another. While inclusion crossing activates the crack trapping as we saw in Section 3.2, inclusion by-pass toughens composite materials with crack deflection. The respective impact of both mechanisms is discussed in Section 3.3.2.

3.3.1 Crack trajectory : a competition between by-pass and crossing mechanisms

As evidenced on Fig. 2.22 and Fig. 2.23, the competition between the crossing of an inclusion and its by-pass by an out-of-plane excursion of the front controls the crack trajectory, and ultimately the effective fracture properties of the heterogeneous medium. We start here by investigating which mechanism is selected by the crack front when it interacts with a periodic array of tough spherical inclusions. We consider periodic arrangements of spherical inclusions for an inclusion spacing $L_z = 4\,d$ and a spatial numerical discretization of $\Delta z = d/32$. We build our analysis on the GMERR criterion of Eq. (2.21) that compares the rate G of elastic energy released with the rate of energy G_c dissipated during fracture along the different possible propagation directions.

As the crack lands on a spherical inclusion, two possible propagation mechanisms are at play : either the crack by-passes the inclusion by propagating along the interface (Fig. 3.13.a) or it crosses the inclusion by remaining within the mean fracture plane (Fig. 3.14.a). To by-pass the obstacle, the crack must kink from its initial direction of propagation. This kink is detrimental as far as the ERR G is concerned since G is maximal along the mean fracture plane, and decreases when the kink angle increases (see Fig. 3.13.c). Yet, as far as the fracture energy G_c is concerned, kinking allows the crack to select a more favorable path since $G_c^{\text{int}} \leq G_c^{\text{mat}} \leq G_c^{\text{inc}}$ (see Fig. 3.13.c).

We choose three simple examples to illustrate qualitatively the competition under the hypothesis $G_c^{\text{int}} = G_c^{\text{mat}}$, which will be relaxed in Section 3.7 :

1. in the first example, the crack lands halfway between the equatorial plane and the top of an inclusion twice tougher than the matrix, $G_c^{\text{inc}} = 2\,G_c^{\text{mat}}$ (Fig. 3.13.a). We note θ_{tan} the angle between the current propagation direction and the matrix-inclusion interface for the central region of the front. By-passing the inclusion to pursue propagation within the matrix requires then a maximum kink angle $\theta_{\text{tan}} \simeq 60°$. As represented in Fig. 3.13.c where the normalized net driving force $(G - G_c)/G_c^{\text{mat}}$ is represented as a function of the kink angle θ at the onset of propagation, the drop

of G in that direction is sufficiently small so that it does not overcome the gain $G_c^{mat} - G_c^{inc} = G_c^{mat}$ in fracture energy. As a result, the *by-pass mechanism* is here selected.

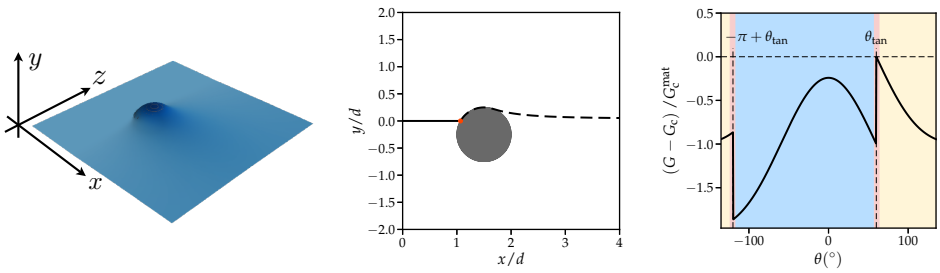

(a) (b) (c)

Figure 3.13: (a) By-pass mechanism during the trapping of a crack front by a tough spherical inclusion with $G_c^{inc} = 2\,G_c^{mat}$; (b) trajectory of the point of the crack front located in $z = L_z/2$; (c) application of the GMERR criterion of Eq. (2.21) in $z = L_z/2$; the normalized net driving force is represented as a function of the kink angle at the onset of depinning.

2. Consider now that the crack lands on the equatorial plane (xOz) of the same inclusion, as shown in Fig. 3.14.b. The kink angle required to by-pass the inclusion is then $\theta_{tan} = 90°$, so that the associated drop of G is significantly larger than in the previous case (Fig. 3.14.b); this explains here why the crack crosses the tough inclusion rather than by-passes it.

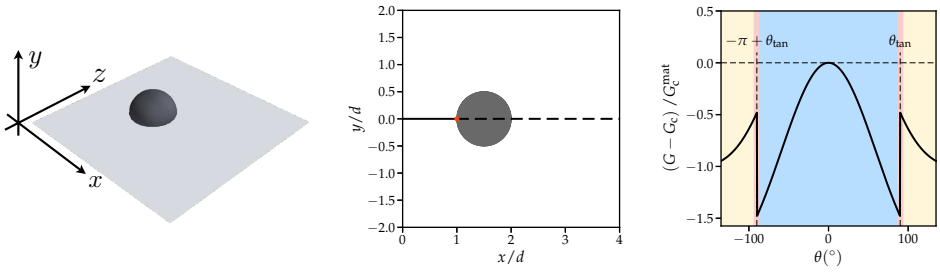

(a) (b) (c)

Figure 3.14: (a) Crossing mechanism during the trapping of a crack front by a tough spherical inclusion with $G_c^{inc} = 2\,G_c^{mat}$; (b) trajectory of the point of the crack front located at $z = L_z/2$; (c) application of the GMERR criterion of Eq. (2.21) in $z = L_z/2$; the normalized net driving force is represented as a function of the kink angle at the onset of depinning.

3. In the limit case of an infinitely tough inclusion, it is clear that the crack cannot remain trapped as the external loading is increased further and further, so the inclusion *must* be by-passed, whatever the landing position of the crack front. Thus we expect the existence of a critical toughness above which *all* inclusions are by-passed. In Fig. 3.15, we can see that this condition is already reached for a toughness $G_c^{inc} = 4\,G_c^{mat}$, an inclusion only four times tougher than the matrix.

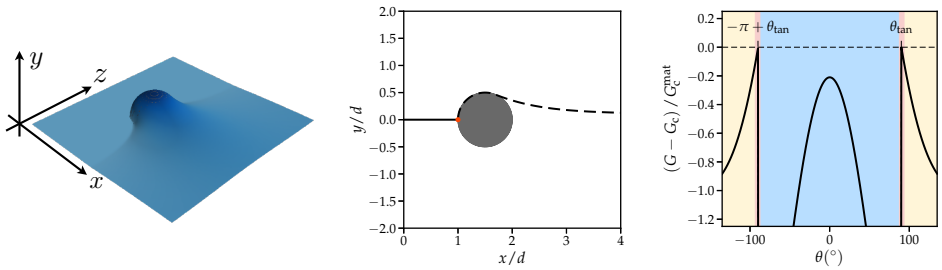

(a) 3D view (b) (x0y) plane (c) $(G - G_c)_{\max}$

Figure 3.15: (a) By-pass mechanism during the trapping of a crack by a very tough spherical inclusion with $G_c^{inc} = 4\,G_c^{mat}$; (b) trajectory of the point of the crack front located at $z = L_z/2$; (c) application of the GMERR criterion of Eq. (2.21) in $z = L_z/2$; the normalized net driving force is represented as a function of the kink angle at the onset of depinning.

3.3.1.a A two-dimensional analysis of the GMERR criterion for a cylindrical inclusion

In general, the competition between crossing and by-pass of a given inclusion is governed by the GMERR criterion that can be expressed explicitly thanks to Amestoy-Leblond's formulæ of Eq. (2.19) which provide the value of G after the kink as a function of the SIFs prior to kinking and the kink angle. In our simulations, the SIFs before the kink are computed from the pertubative LEFM formulæ of Eq. (2.14), which take into account three-dimensional effects due to interactions between different regions of the crack front. Overall, the ability of a tough inclusion to trap efficiently a crack results from the complex coupling between the in-plane bowing mode of deformation and the subsequent (potential) out-of-plane deviation of the front during by-pass.

To rationalize this mechanism, we start by neglecting these three-dimensional effects due to the variations of f_x and f_y along the crack front, and compare our numerical simulations with a two-dimensional theoretical analysis in which the SIFs are constant along the front. It amounts to consider a semi-infinite crack landing on an infinite cylindrical inclusion, as illustrated in Fig. 3.16.

Let us assume that the inclusion toughness is noted G_c^{inc} and the interface toughness G_c^{int}. The initially straight crack lands on the inclusion with an angle θ_{ini}, at a height $y_{landing}$, at some point on the interface where the tangent angle to the inclusion boundary is θ_{tan}. This tangent angle is linked to the other parameters through the relation:

$$\theta_{tan} = \arctan\left(\frac{\sqrt{\left(\frac{d}{2}\right)^2 - y_{landing}^2}}{y_{landing}}\right) \tag{3.22}$$

In order to capture the effect of a mode II component that may result from out-of-plane perturbations of the crack line, we assume that the crack is loaded under mixed mode I+II and we note $\rho_{II} = K_{II}/K_I$. As shown in Section 2.2.3.b, two directions of crack propagation only need to be considered : the direction θ_{max} lying within the inclusion and maximizing

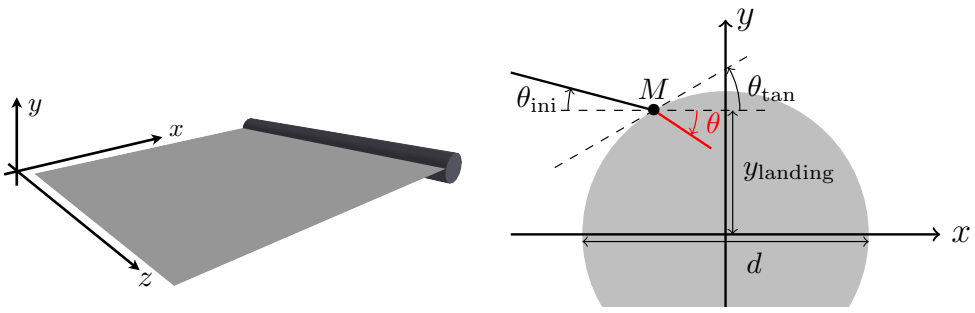

(a) 3D view (b) Plane (xOy)

Figure 3.16: Two-dimensional analysis of the by-pass to crossing transition: (a) the 2D aproximation consists in replacing the spherical inclusion by a cylindrical obstacles invariant along the crack front direction; (b) the crack lands with an angle θ_{ini} at a height y_{landing} and may by-pass the inclusion either upward or downward.

G, and the by-pass direction θ_{tan}. According to Amestoy-Leblond's formulæ, the ERR in the direction θ_{max} is given by :

$$G_{\text{cross}} = \frac{1-\nu^2}{E} K_{\text{I}}^2 \left[\left(F_{\text{I,I}}\left(\alpha_{\text{max}}\right) + F_{\text{I,II}}\left(\alpha_{\text{max}}\right) \rho_{\text{II}} \right)^2 + \left(F_{\text{II,I}}\left(\alpha_{\text{max}}\right) + F_{\text{II,II}}\left(\alpha_{\text{max}}\right) \rho_{\text{II}} \right)^2 \right] \tag{3.23}$$

where $\alpha_{\text{max}} = \theta_{\text{max}} - \theta_{\text{ini}}$ is the kink angle in the direction that maximizes G. Similarly, the ERR for the by-pass scenario is provided by :

$$G_{\text{tan}} = \frac{1-\nu^2}{E} K_{\text{I}}^2 \left[\left(F_{\text{I,I}}\left(\alpha_{\text{tan}}\right) + F_{\text{I,II}}\left(\alpha_{\text{tan}}\right) \rho_{\text{II}} \right)^2 + \left(F_{\text{II,I}}\left(\alpha_{\text{tan}}\right) + F_{\text{II,II}}\left(\alpha_{\text{tan}}\right) \rho_{\text{II}} \right)^2 \right] \tag{3.24}$$

Now gradually lower the inclusion toughness from infinity to the matrix toughness. At the crossing/by-pass transition, the following equalities must hold:

$$G_{\text{c}}^{\text{inc}} = G_{\text{cross}} = G_{\text{tan}} = G_{\text{c}}^{\text{int}} \tag{3.25}$$

Leading to :

$$\frac{G_{\text{c}}^{\text{inc}}}{G_{\text{c}}^{\text{int}}} = \frac{\left(F_{\text{I,I}}\left(\alpha_{\text{max}}\right) + F_{\text{I,II}}\left(\alpha_{\text{max}}\right) \rho_{\text{II}} \right)^2 + \left(F_{\text{II,I}}\left(\alpha_{\text{max}}\right) + F_{\text{II,II}}\left(\alpha_{\text{max}}\right) \rho_{\text{II}} \right)^2}{\left(F_{\text{I,I}}\left(\alpha_{\text{tan}}\right) + F_{\text{I,II}}\left(\alpha_{\text{tan}}\right) \rho_{\text{II}} \right)^2 + \left(F_{\text{II,I}}\left(\alpha_{\text{tan}}\right) + F_{\text{II,II}}\left(\alpha_{\text{tan}}\right) \rho_{\text{II}} \right)^2} \tag{3.26}$$

Specializing this equation to the simpler situation where $G_{\text{c}}^{\text{int}} = G_{\text{c}}^{\text{mat}}$, $\theta_{\text{ini}} = 0$ and $\rho_{\text{II}} = 0$, we obtain the critical toughness ratio at the crossing/by-pass transition :

$$\left[\frac{G_{\text{c}}^{\text{inc}}}{G_{\text{c}}^{\text{int}}} \right]_{\text{crit}} = \frac{1}{F_{\text{I,I}}\left(\theta_{\text{tan}}\right)^2 + F_{\text{II,I}}\left(\theta_{\text{tan}}\right)^2} \tag{3.27}$$

Together with Eq. (3.22), the former equation allows us to represent phase diagrams like the one of Fig. 3.17 where the depinning mechanism (crossing versus by-pass) is easily identified from the value of the toughness ratio $G_{\text{c}}^{\text{inc}}/G_{\text{c}}^{\text{mat}}$ and the relative landing height y_{landing}/d. Several comments are in order here :

- an energetic competition takes place between crossing and by-pass, governed by the inclusion toughness and the magnitude of the kink angle required for by-pass. The theory of LEFM can quantitatively predict this competition thanks to Amestoy-Leblond's formulæ;
- in the absence of mode II ($K_{\mathrm{II}} = 0$) and for an attack angle $\theta_{\mathrm{ini}} = 0$, the theoretically predicted upward and downward by-pass regions are symmetric with respect to the horizontal axis $y_{\mathrm{landing}} = 0$. This is because the depinning mechanisms are identical upwards and downwards for a given value of $|y_{\mathrm{landing}}|/d$. Note also if the crack lands on the upper (resp. lower) half of the inclusion, only an upward (resp. downward) by-pass is possible ;
- the critical toughness ratio beyond which the inclusion is systematically by-passed can be deduced from consideration of the particular case $y_{\mathrm{landing}} = 0$ that corresponds to a kink angle $\theta_{\mathrm{tan}} = 90°$. One thus gets $\left[G_{\mathrm{c}}^{\mathrm{inc}}/G_{\mathrm{c}}^{\mathrm{mat}}\right]_{crit} \sim 3.854$. This value is in close agreement with the simulation results of Fig. 3.15 where inclusion by-pass was systematically observed for $G_{\mathrm{c}}^{\mathrm{inc}}/G_{\mathrm{c}}^{\mathrm{mat}} = 4$, in spite of the different inclusion geometries considered (spherical in Fig. 3.15, cylindrical here)

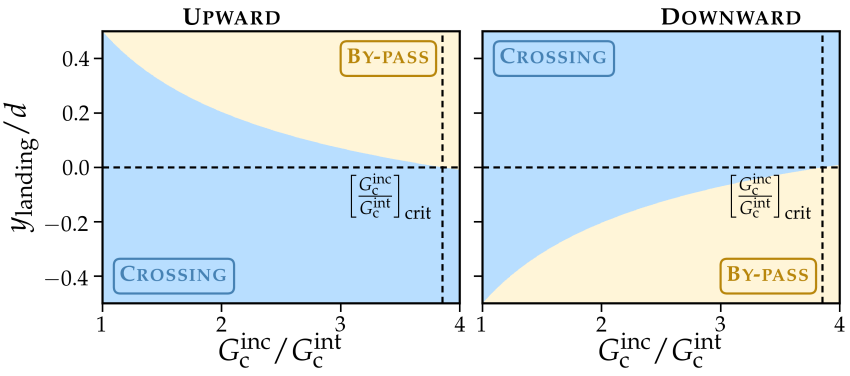

Figure 3.17: Theoretical phase diagram providing the depinning mechanism (crossing vs by-pass) of a crack pinned by a cylindrical inclusion (see Fig. 3.16) as a function of the toughness ratio $G_{\mathrm{c}}^{\mathrm{inc}}/G_{\mathrm{c}}^{\mathrm{int}}$ and the relative landing height y_{landing}/d. Note that the critical toughness ratio $\left[G_{\mathrm{c}}^{\mathrm{inc}}/G_{\mathrm{c}}^{\mathrm{inc}}\right]_{\mathrm{crit}} \sim 3.854$ beyond which the obstacle is systematically by-pass corresponds to the landing height $y_{\mathrm{landing}} = 0$, and so a normal kink angle $\theta_{\mathrm{tan}} = 90°$.

3.3.1.b Comparison of the two-dimensional theoretical model with three-dimensional numerical simulations on spherical inclusions

The transition diagram of Fig. 3.17 being derived from a simplified two-dimensional theory considering cylindrical inclusions, it is interesting to compare it to the results of fully three-dimensional simulations considering spherical inclusions, as the 3D case is more complex: when depinning (crossing or by-pass) occurs, the local SIFs are already perturbed by the deformations of the crack. The determination of the region of the front that triggers depinning is then not an easy task, and we shall resort to numerical simulations.

The numerical efficiency of our method allows to run several thousands of simulations with GNU Parallel [Tange, 2011], to investigate the impacts of both the toughness ratio between the inclusion and the matrix and the landing height. Since we consider the values $\theta_{\text{ini}} = 0$ and $\rho_{\text{II}} = 0$, the region $y_{\text{landing}}/d \in]-0.5, 0[$ of the phase diagram is deduced by symmetry from the region $y_{\text{landing}}/d \in [0, 0.5[$. Simulation parameters are listed in Table 8.3.

In practice, the depinning mechanism is determined from the evolution of the point of the front located in $z = L_z/2$ where θ_{tan} is maximal. In other words, we consider that the crack should get around the entire inclusion to consider that by-passing took place. Interestingly, the two-dimensional and three-dimensional theoretical diagrams are almost identical, as seen in Fig. 3.18, a behavior that is reminiscent of the absence of collective effects in the by-pass of inclusions. Moreover, these results seem to be in accordance with the ones presented in Clayton and Knap [2014] for similar elastic properties between the matrix and the inclusion, which is hit by the crack on its equatorial plane. Yet, we shall see in Section 3.4 that this coincidence breaks down for other shapes of inclusion.

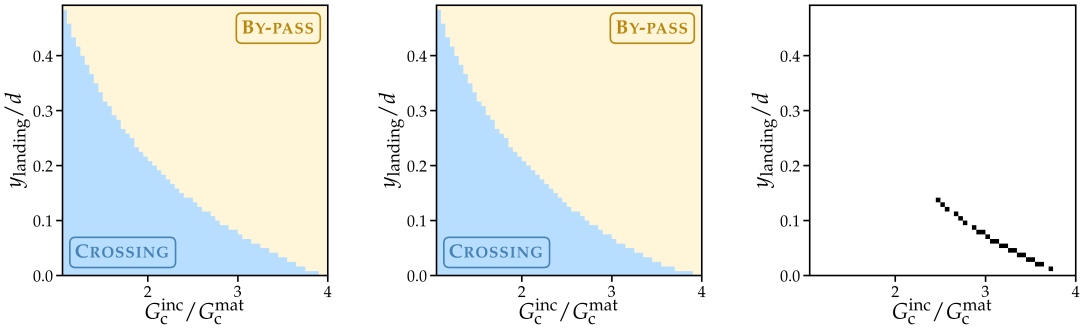

(a) (b) (c)

Figure 3.18: Comparison of the prediction of the two-dimensional theoretical model of Fig. 3.17 (a) with the results of the three-dimensional numerical simulations in case of spherical inclusions: (b) Phase diagram obtained from 1600 simulations with various toughness ratios $G_c^{\text{inc}}/G_c^{\text{mat}}$ and landing heights y_{landing}/d ; (c) Difference between the theoretical phase diagram of panel (a) and the numerically computed one of panel (b), where black regions indicate different behaviors.

3.3.2 Impact of the by-pass mechanism on the effective fracture properties

We investigated in Section 3.2.2 how crack trapping triggered by inclusion crossing toughens composite materials. The by-pass mechanism, introduced in this section, induces a toughening by crack deflection. Crack deflection has often been viewed as a toughening mechanism [Faber and Evans, 1983a; Suresh, 1985; Steinbrech, 1992], although quite weak in comparison to crack wake processes such as crack bridging [Bower and Ortiz, 1991]. We want here to highlight the idea that in the presence of toughness discontinuities, crack deflection must be considered more as a severely limiting factor of material toughening, than as a toughening process *per se*.

3.3.2.a Inclusion by-pass limits material toughness by crack trapping

In order to prove it, we estimate numerically the effective toughness of periodic arrangements $L_z = 4d$ of spherical inclusions, whose diameter is d. As we saw in Section 3.3, the landing height y_{landing} is an important parameter for the spherical inclusion since it controls, with the inclusion toughness G_c^{inc} and the interface toughness G_c^{int}, the way the crack interacts with the inclusion (see Eq. (3.27)). We thus consider multiple cases with varying landing height $y_{\text{landing}} \in [0., 0.5[$ ($]-0.5, 0[$ is covered by symmetry) and inclusion toughness $G_c^{\text{inc}} \in \left[G_c^{\text{mat}}, 4\,G_c^{\text{mat}}\right]$. We assume that the interface and the matrix share the same fracture properties $G_c^{\text{int}} = G_c^{\text{mat}}$, a hypothesis which is relaxed in Section 3.7. Simulation parameters are shared with those reported in Table 8.3.

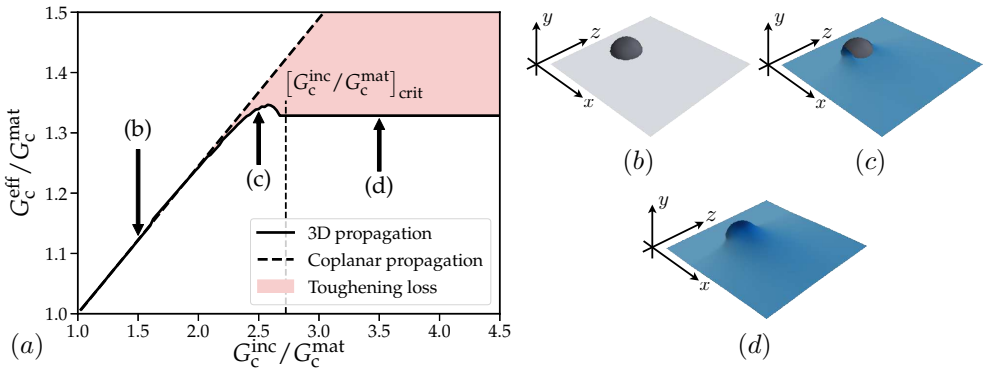

Figure 3.19: Impact of the inclusion toughness ratio $G_c^{\text{inc}}/G_c^{\text{mat}}$ on the effective toughness G_c^{eff} : the effective toughness increases linearly with the inclusion toughness while the inclusion is crossed (b). After the crossing to by-pass transition described by Eq. (3.27) (c), the effective toughness reaches a plateau and an increase of the inclusion toughness does not toughen the composite further (d).

We plot in Fig. 3.19 the effective toughness of the heterogeneous composite for various inclusion toughnesses for a given landing height $y_{\text{landing}}/d = 0.1$. Three regimes may be distinguished here:

1. for low values of the inclusion toughness, up to $G_c^{\text{inc}} = 2\,G_c^{\text{mat}}$, the effective toughness increases linearly with the inclusion toughness;
2. for medium values of the inclusion toughness, up to $G_c^{\text{inc}} = 2.5\,G_c^{\text{mat}}$, the "toughening rate" $\frac{\partial G_c^{\text{eff}}}{\partial G_c^{\text{inc}}}$ gradually decreases and the effective toughness reaches a peak;
3. for high values of the inclusion toughness, above $G_c^{\text{inc}} = 2.75\,G_c^{\text{mat}}$, the effective toughness reaches a plateau $G_c^{\text{eff}} \simeq 1.395\,G_c^{\text{mat}}$.

The first regime is characterized by the crossing of the inclusion as depicted in Fig. 3.19.b. The situation is thus equivalent to the coplanar propagation of a crack encountering a periodic array of circular inclusions. (see Section 3.2.2.c). The dynamic of such a mechanism is illustrated in Fig. 3.20, where is plotted the propagation of the central point of the crack front in the (xOy) plane along with macroscopic loading G^∞ in Fig. 3.20.a. The in-plane perturbations dynamics in the (zOx) plane are given in Fig. 3.20.b. The crack is initially

pinned by the inclusion. The macroscopic loading has to increase in order to make the crack propagates. The more the crack penetrates the inclusion, the larger the apparent inclusion width becomes and the loading needs to increase accordingly to allow stable propagation. Parts of the crack front finally go back in the matrix and the in-plane perturbations relax. Since, at such toughness levels and inclusion spacing the penetration process is regular for a circular inclusion, the effective toughness follows a mixture rule of Eq. (3.20) and the effective toughness G_c^{eff} increases linearly with the toughness ratio $G_c^{\text{inc}}/G_c^{\text{mat}}$.

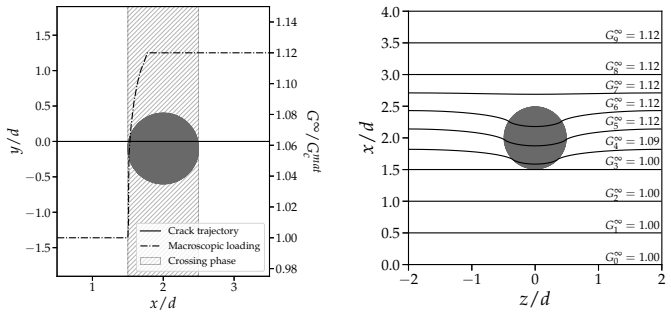

(a) (xOy) plane (b) (zOx) plane

Figure 3.20: Crossing of spherical inclusions with $G_c^{\text{inc}} = 1.5\, G_c^{\text{mat}}$, by a crack landing at $y_{\text{landing}} = 0.1\, d$. Trajectory in the plane (xOy) and macroscopic loading evolution for the center point in $z = 0$ (a). In-plane profiles in the (zOx) plane at various loading states (b)

Close but below the critical toughness at the crossing to by-pass transition $\left[G_c^{\text{inc}}\right]_{\text{crit}} \simeq 2.75\, G_c^{\text{mat}}$ for $y_{\text{landing}} = 0.1\, d$ (Eq. (3.27)), we observe a transient regime in which the region of the crack front close to the center of the inclusion crosses it whereas those closer to the edges by-pass it (Fig. 3.19.c). This phenomenon results from the variations along the front of the tangent angle θ_{tan} that is larger near the inclusion center. Indeed, the local tangent angle reads in the case of spherical inclusions :

$$\theta_{\text{tan}} = \arctan\left(\frac{\sqrt{\left(\frac{d}{2}\right)^2 - \left(y_{\text{landing}}\right)^2 - \left(z - z_s\right)^2}}{y_{\text{landing}}}\right) \tag{3.28}$$

where z_s is the abscissa of the center of the inclusion and z the one along the crack front. Since the depinning mechanism (crossing versus by-pass) is ruled by a local criterion that consists in maximizing $G - G_c$ at every location along the front and at every time step, lateral points may prefer to by-pass the inclusion. These numerical observations match the experimental findings of Takei et al. [2013] , who indeed observed that the choice of crack trajectory corresponded better to a local maximization of $G - G_c$ than some global maximization. This means that the crack propagates following the *locally* weakest path, and can thus globally dissipate more energy than it would by trying to achieve some global minimization. This interesting feature definitely needs to be exploited to design tougher materials.

Above the critical toughness $\left[G_c^{inc}\right]_{crit} \sim 2.75\, G_c^{mat}$, the crack interacts with the inclusion through a by-pass mechanism (Fig. 3.19.d).. Its dynamic is illustrated in Fig. 3.21. We see from the macroscopic loading in Fig. 3.21.a that the effective toughness is attained when the crack kinks and unpins. During the by-pass, in-plane perturbations relax, which confirms that the initial kink requires the largest loading to make the crack propagate. When the crack by-passes the inclusion, it propagates along the interface so that the inclusion toughness ceases to play any role. This is why a further increase of the inclusion toughness leaves the effective toughness unchanged.

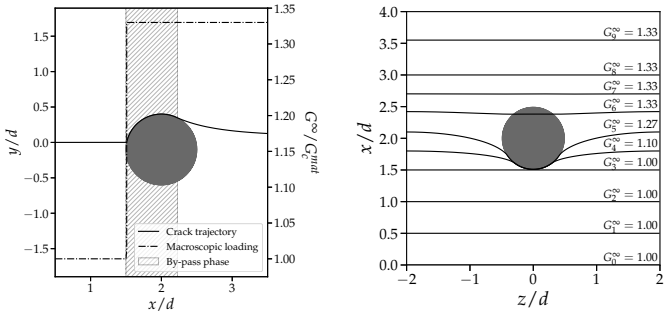

(a) (xOy) plane (b) (zOx) plane

Figure 3.21: By-pass of spherical inclusions with $G_c^{inc} = 3.5\, G_c^{mat}$, by a crack landing at $y_{landing} = 0.1\, d$. Trajectory in the plane (xOy) and macroscopic loading evolution for the center point in $z = 0$ (a). In-plane profiles in the (zOx) plane at various loading states (b)

To conclude, as the inclusion toughness is increased, we observe a rather sharp (though not instantaneous) transition from a regime where the inclusion is crossed and the effective toughness of the composite is increased by *crack trapping*, to a second one characterized by the by-pass of the inclusion, which activates a less efficient toughening mechanism, *crack deflection*.

3.3.2.b Effect of the landing height and the inclusion spacing on the effective toughness

As the landing height $y_{landing}$ increases, the tangent angle θ_{tan} decreases (see Eq. (3.28)), facilitating by-pass that happens for smaller values of the inclusion toughness. As a result, the plateau regime is reached earlier, and corresponds to a smaller effective toughness, as shown in Fig. 3.22.a. Predicting G_c^{eff} analytically when crack deflection occurs is nonetheless difficult since the toughness the front experiences varies in the z-direction (varying deflection angle) as well as in the x-direction (realignement with the loading). Such local variations of the local toughness trigger what Gao and Rice [1989] called "irregular processes", so that only numerical simulations may allow for an estimation of the effective toughness [Bower and Ortiz, 1991]. However, it is clear that below some critical toughness ratio $\left[G_c^{inc}/G_c^{mat}\right]_{crit}$, the inclusion is crossed and the effective toughness follows Eq. (3.20), while it reaches a plateau above $\left[G_c^{inc}/G_c^{mat}\right]_{crit}$. Using then Eq. (3.27) even though it strictly applies to 2D situations (cylindrical inclusions), and combining it with Eq. (3.20), one gets the following

estimate of the effective toughness :

$$\frac{G_c^{\text{eff}}}{G_c^{\text{mat}}} = 1 + \frac{d}{L_z}\sqrt{1 - 4\left(\frac{y_{\text{landing}}}{d}\right)^2}\left[\min\left(\frac{G_c^{\text{inc}}}{G_c^{\text{mat}}}, \left[\frac{G_c^{\text{inc}}}{G_c^{\text{mat}}}\right]_{\text{crit}}\right) - 1\right] \tag{3.29}$$

The comparison between the results of numerical simulations and the theoretical predictions of Eq. (3.29) is plotted in Fig. 3.22.a. One observes that Eq. (3.29) quantitatively describes the effective toughness in the crossing phase while it only provides an upper-bound prediction in the by-pass one.

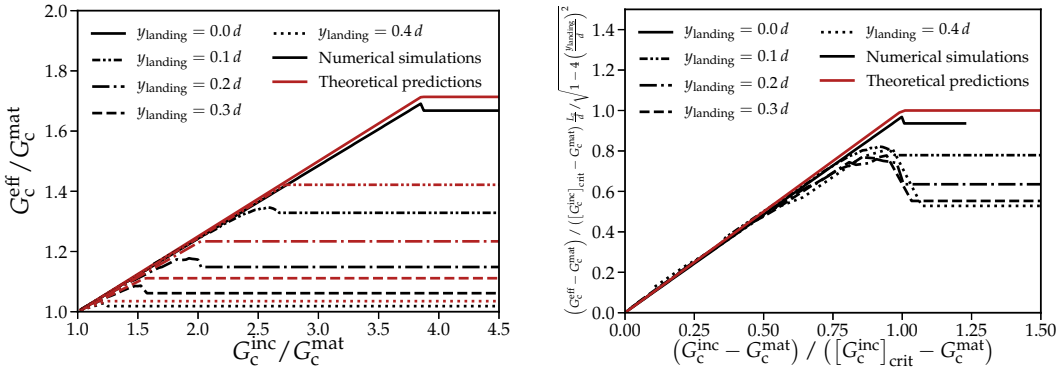

(a) (b)

Figure 3.22: Impact of the landing height y_{landing} on the effective toughness G_c^{eff} : the crossing/by-pass transition occurs at smaller inclusion toughness levels as the landing height increases, making the plateau value decrease accordingly; comparison of numerical simulations (in black) and theoretical predictions of 3.29 (in red) for the effective toughness (a); renormalization from 3.29 (b).

In the same manner, as the spacing L_z between neighboring inclusions increases, the "toughening rate" $\frac{\partial G_c^{\text{eff}}}{\partial G_c^{\text{inc}}}$ decreases in the linear regime corresponding to crossing of the inclusion (see Fig. 3.23.a). Yet, the critical toughness ratio $\left[G_c^{\text{inc}}/G_c^{\text{mat}}\right]_{\text{crit}}$ does not depend on the inclusion spacing but only on the inclusion mechanical and geometrical properties (see Eq. (3.27)). Thus the effective toughness reaches a plateau for a well-defined, constant critical toughness ratio $\left[G_c^{\text{inc}}/G_c^{\text{mat}}\right]_{\text{crit}}$, but its height decreases when the inclusion spacing increases as predicted Eq. (3.29) (Fig. 3.23.a). The constant value of the critical toughness ratio $\left[G_c^{\text{inc}}/G_c^{\text{mat}}\right]_{\text{crit}}$, irrespective of the value of L_z, is reminiscent of the absence of collective effects in the by-pass of inclusions. In other words, the interaction mechanism between the crack and a single inclusion is not affected by the presence of neighboring inclusions. Note however the smaller value of G_c^{eff} in the by-pass regime for the denser arrangement of inclusions ($L_z = 2\,d$). This is signature of collective by-pass of neighboring inclusions, explained by the fact that a lesser portion of the crack drags the front back in the mean fracture plane by long-range elastic effects (see Eq. (2.14)). Its impact on G_c^{eff} remains nonetheless small when compared to the overall impact of the by-pass mechanism.

In conclusion, the by-pass mechanism offers a more energetically favorable trajectory for crack propagation. It hinders toughening by limiting crack trapping. In order to toughen brittle materials, one should design inclusion geometries preventing inclusion by-pass; a

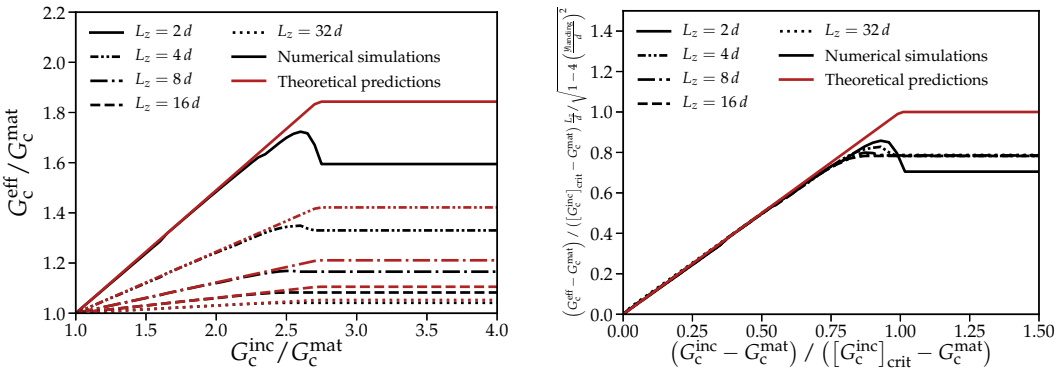

(a) (b)

Figure 3.23: Impact of the inclusion spacing L_z upon the effective toughness G_c^{eff}: both the slope in the linear regime and the plateau value decrease when the density of tough inclusions decreases; comparison of numerical simulations (in black) and theoretical predictions of 3.29 (in red) for the effective toughness (a) ; renormalization from 3.29 (b).

good example consists of inclusions with a concave interface, for which by-passing becomes more and more difficult as the crack progresses along it. This remark is compatible with the results of topological optimization studies of two-dimensional crack propagation [Da et al., 2018]. The results of topological optimization processes starting from an initial square inclusion are pictured in Fig. 3.24 Concave interfaces emerge from the optimization process, with the consequence of preventing inclusion by-pass and promoting crack nucleation on the other side of the inclusion. This phenomenon ultimately leads to crack bridging, which has been identified as a particularly efficient toughening mechanism as we will see in Section 3.6

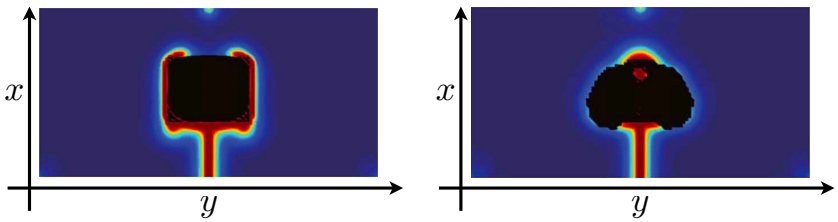

(a) (b)

Figure 3.24: Topological optimization processes to increase fracture properties : initial square inclusion (a) and optimized shape (b) (after Da et al. [2018])

The toughening reduction results from the three-dimensional coupling of the in-plane and out-of-plane deformation modes of the crack front, which modifies the interactions of the crack and the inclusions, and consequently the effective toughness of the composite. This coupling was disregarded in previous three-dimensional perturbative studies [Ramanathan et al., 1997; Barès et al., 2014], where only the question of crack trajectory was addressed; yet what precedes unambiguously shows that it must be accounted for in studies of effective fracture properties of three-dimensional heterogeneous materials. The following sections aim at exploring further the impact of this coupling on periodical arrangements of tougher inclusions with different geometries and interface properties.

3.4 Three-dimensional collective effects in the by-pass of tough inclusion : a further limitation on toughening processes

All previous results have been obtained for spherical inclusions. For such an inclusion shape, the interaction mechanisms are fairly well predicted by a simple two-dimensional theoretical analysis considering cylindrical inclusions, the explanation being that the difference between the macroscopic and local SIFs is small. We will see here that the three-dimensional coupling of the in-plane and out-of-plane deformation modes of the crack front can be enhanced by the inclusion shape and modify the conditions under which inclusion crossing and by-pass occurs. This phenomenon, which relies on collective effects triggered by the ellipsoidal shape of the inclusions, is described in Section 3.4.1. It ultimately impacts the effective toughness of three-dimensional heterogeneous materials, as discussed in Section 3.4.2.

3.4.1 The collective by-pass of ellipsoidal prolate inclusion : a three-dimensional effect induced by the coupling of the in-plane and out-of-plane modes of deformation

3.4.1.a Crossing to by-pass transition diagrams for ellipsoidal inclusion elongated in the front direction

We begin to understand that effective fracture properties are closely linked by the interaction mechanisms triggered during crack propagation. An interesting point would be to see how inclusion shape influences the crossing to by-pass transition highlighted on the cylindrical and spherical cases. We thus consider prolate ellipsoidal inclusions elongated in the z-direction of the crack front. (d_i) denotes the length of the principal axis (e_i). We take $d_z = d$, $d_x = d_y = d/2$ for the first geometry and $d_z = d$, $d_x = d_y = d/4$ for the second one, as depicted in Fig. 3.25.

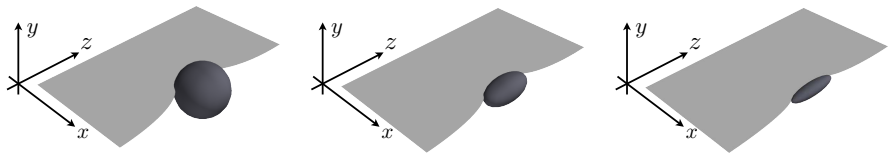

(a) (b) (c)

Figure 3.25: Interaction of a crack with ellipsoidal inclusions elongated in the front direction : the inclusion is either spherical (a) or ellipsoidal prolate with various elongation $d_z = d_x = 2\,d_y$ (b) and $d_z = 4\,d_x = 4\,d_y$ (c)

For both geometries, we construct their crossing to by-pass transition diagram with the procedure used for the spherical case in Section 3.3.1.b. Results are plotted in Fig. 3.26 and Fig. 3.27. One immediately notices that the new diagrams fundamentally differ from that obtained for spherical inclusions in Fig. 3.18. In the case of ellipsoidal prolate inclusions elongated in the z-direction, the by-pass mechanism happens at smaller inclusion toughness levels than for the cylindrical (2D) and spherical geometries. This phenomenon results from a strong coupling of the in-plane and out-of-plane deformation modes which is enhanced by

inclusion geometry. The following sections aim at describing the fundamental mechanisms behind the early by-pass inclusion of tough ellipsoidal inclusions.

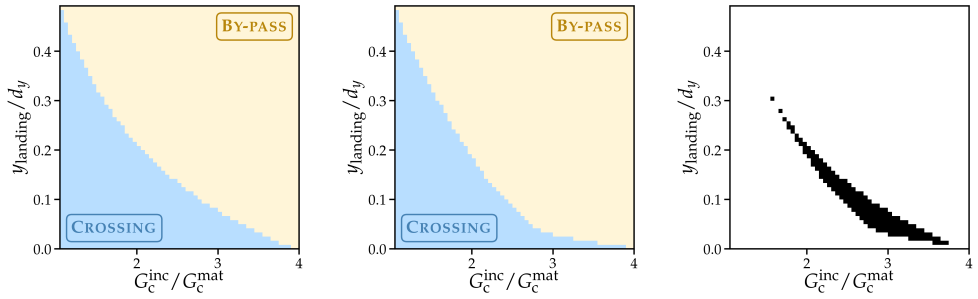

(a) (b) (c)

Figure 3.26: Comparison of two- and three-dimensional transition diagrams for prolate ellipsoidal inclusions with $d_z = 2\,d_x$: (a) Two-dimensional diagram for cylindrical inclusions; (b) three-dimensional transition diagram for spheroidal inclusions obtained from 1200 simulations with various toughness ratios $G_c^{\text{inc}}/G_c^{\text{mat}}$ and landing heights y_{landing}/d; (c) difference between the two diagrams - the black regions indicate different behaviors.

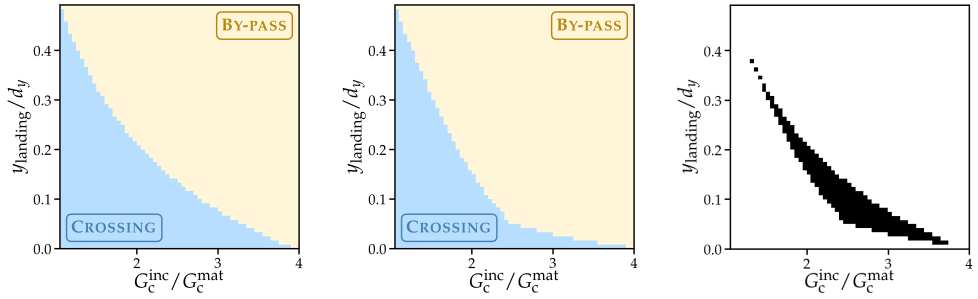

(a) (b) (c)

Figure 3.27: Comparison of two- and three-dimensional transition diagrams for prolate ellipsoidal inclusions with $d_z = 4\,d_x$: (a) Two-dimensional diagram for cylindrical inclusions; (b) three-dimensional transition diagram for spheroidal inclusions obtained from 1200 simulations with various toughness ratios $G_c^{\text{inc}}/G_c^{\text{mat}}$ and landing heights y_{landing}/d; (c) difference between the two diagrams - the black regions indicate different behaviors.

3.4.1.b In-plane defect geometry controls the depinning dynamics

As we saw in Section 3.2.1, the in-plane perturbation controls the dynamics of crack propagation. In particular, in-plane dynamics are influenced by inclusion shape as it was evidenced in Fig. 3.11 on the case of the coplanar propagation of a crack interacting with elliptic inclusions. Regions of the crack front located on the edges of the inclusion happen to propagate earlier than regions located near the center of the inclusion. It is due to the fact that the long-range elastic interaction term of the perturbed SIFs is sensitive to the local crack front curvature as underlined in Eq. (2.28).

In Fig. 3.28, we plot the perturbation of the Mode I SIF along the crack front, when

pinned by the three geometrically different inclusions considered. In the spherical case, the perturbation of the SIF is maximal at the center of the crack front (see Fig. 3.28.a & d); therefore unpinning occurs there first. For ellipsoidal inclusions, the SIF perturbations are lowered on the center part of the crack front due to a large in-plane curvature (Fig. 3.28.b & e); therefore unpinning occurs near the edges of the inclusion first.

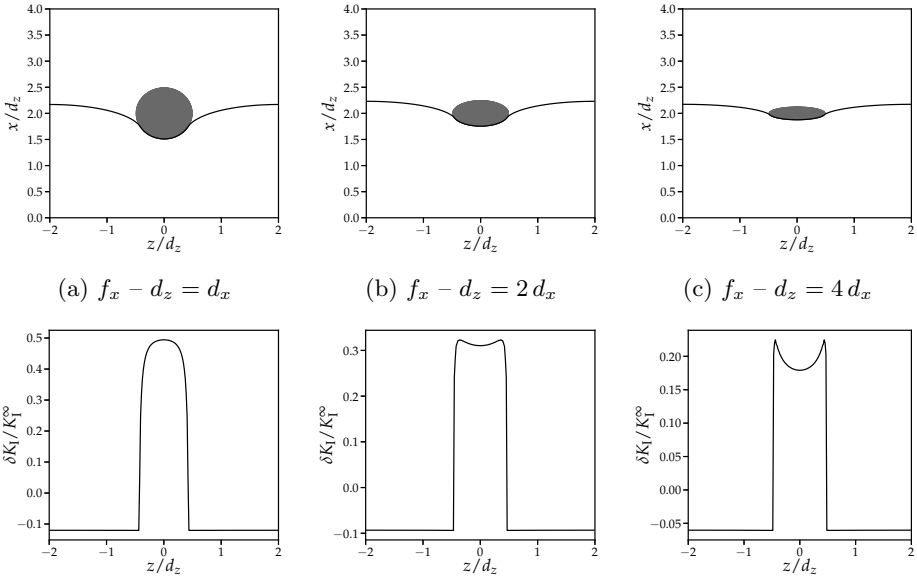

(a) $f_x - d_z = d_x$ (b) $f_x - d_z = 2\,d_x$ (c) $f_x - d_z = 4\,d_x$

(d) $\delta K_\mathrm{I} - d_z = d_x$ (e) $\delta K_\mathrm{I} - d_z = 4\,d_x$ (f) $\delta K_\mathrm{I} - d_z = 2\,d_x$

Figure 3.28: Impact of the in-plane perturbation of the crack front on crack depinning dynamics: the in-plane perturbation f_x is plotted just before depinning of the central point of the front, for a spherical inclusion (a), and two different prolate ellipsoidal inclusions (b) and (c). The associated perturbations of the Mode I SIF δK_I are plotted in (d-f); unpinning occurs first at the central point of the front for a spherical inclusion, but near the edges of the obstacle for prolate ellipsoidal inclusions.

3.4.1.c Out-of-plane defect geometry triggers a collective by-pass of the inclusion

This shift in depinning dynamics has a decisive impact on out-of-plane deviations of the crack. When crack front points unpin, they have to choose whether they kink and by-pass the inclusion or they go straight and cross it. Since all the points pinned on an inclusion see the same inclusion toughness $G_\mathrm{c}^\mathrm{inc}$, this choice is only dependent of the local tangent angle θ_tan. For a spheroidal inclusion of major axis e_z, the tangent angle reads :

$$\theta_\mathrm{tan} = \arctan\left(\frac{\sqrt{d_y^2 - (y_\mathrm{landing} - y_s)^2 - \left(\frac{d_y}{d_x}\right)^2 (z - z_s)^2}}{(y_\mathrm{landing} - y_s)}\right) \tag{3.30}$$

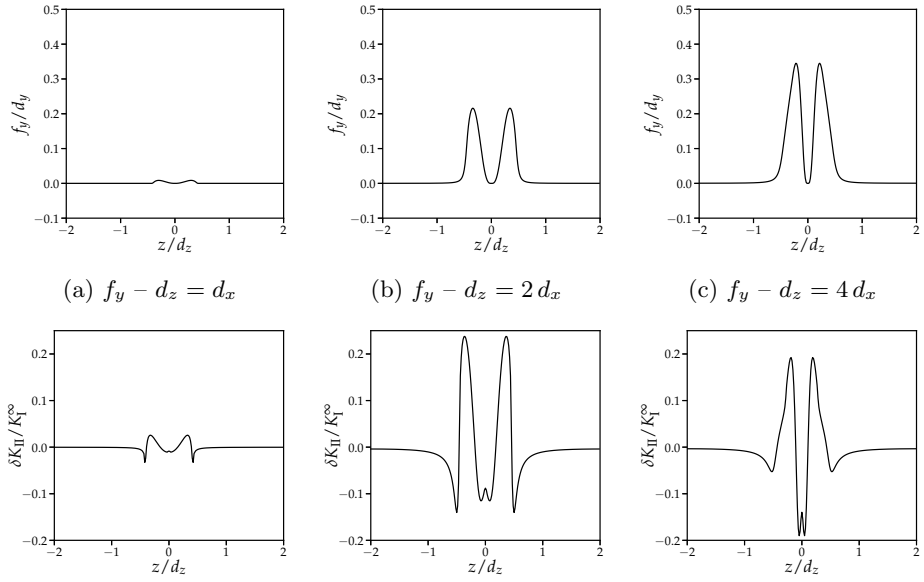

(a) $f_y - d_z = d_x$ (b) $f_y - d_z = 2\,d_x$ (c) $f_y - d_z = 4\,d_x$

(d) $\delta K_{\mathrm{II}} - d_z = d_x$ (e) $\delta K_{\mathrm{II}} - d_z = 2\,d_x$ (f) $\delta K_{\mathrm{II}} - d_z = 4\,d_x$

Figure 3.29: Impact of out-of-plane perturbations on crack path : the out-of-plane perturbation f_y is plotted just before the depinning of the central point of the inclusion for a spherical shape (a) and ellipsoidal one with different aspect ratio (b) and (c). The associated Mode II SIF perturbation δK_{II} are plotted in (d-f). Lateral points exerts a pulling force on the central one in the case of ellipsoidal shapes, where as the central point is loaded in pure Mode I in the spherical case.

Due to in-plane considerations, the lateral points unpin first for the ellipsoidal case. Since those points see a smaller tangent angle $\theta_{\tan}$, they are more likely to by-pass the inclusion. When the central points unpin, the out-of-plane configuration of the crack front is expected to be different for ellipsoidal inclusion than for the spherical case. Such out-of-plane configuration is plotted in Fig. 3.29.a-c for the three geometries considered in this study. We see that for the ellipsoidal inclusions, lateral points have begun to by-pass the inclusion when the central points are ready to unpin. The out-of-plane deformations induce then a negative δK_{II} on those points (Fig. 3.29.d-f). As we will see below, this facilitates the by-pass of the inclusion.

The impact of a local mode mixity on the crossing to by-pass transition can be analyzed within the two-dimensional framework where a planar crack lands on a cylindrical inclusion invariant in the z-direction, as exposed in Section 3.3.1.a. The inclusion toughness $G_{\mathrm{c}}^{\mathrm{inc}}$ is higher than the one of the matrix and while its interface shares the matrix properties $G_{\mathrm{c}}^{\mathrm{int}} = G_{\mathrm{c}}^{\mathrm{mat}}$. The crack is loaded in mixed Mode I+II with $\rho_{\mathrm{II}} = K_{\mathrm{II}}/K_{\mathrm{I}}$. As in Section 3.3.1.a, one can compute the two-dimensional transition diagram in mixed mode loading conditions from Eq. (3.26). Such two-dimensional diagram is plotted in Fig. 3.30 for $\rho_{\mathrm{II}} = 0.1$.

This diagram shows that a local positive Mode II contribution favors the crossing of the inclusion for a crack landing on its upper part and its by-pass on its lower portion. Considering the case where the inclusion toughness equals $G_{\mathrm{c}}^{\mathrm{inc}} = 1.8\,G_{\mathrm{c}}^{\mathrm{mat}}$ and the cracks lands at a height $y_{\mathrm{landing}}/d = 0.3$, we see in Fig. 3.31 that the local mode mixity shifts

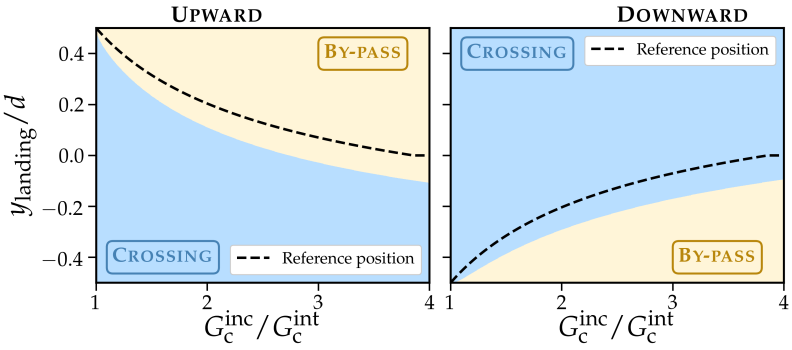

Figure 3.30: Two-dimensional analysis of the by-pass to crossing transition in mixed Mode I+II: the crack loaded in mixed mode with $\rho_{\text{II}} = 0.1$ lands a height y_{landing} on a cylindrical inclusion characterized by the toughness ratio $G_c^{\text{inc}}/G_c^{\text{int}}$. The reference transition limit in pure Mode I from Fig. 3.16 is plotted in black dashed line

the direction where the ERR G is maximal ($\theta_{\max} = -2\rho_{\text{II}}$ at first-order). In the case of a negative Mode II contribution $\rho_{\text{II}} < 0.$, it brings the natural kinking direction $\theta_{\max}$ closer to the by-pass direction $\theta_{\tan}$ (Fig. 3.31.a). The crack is thus able to develop a greater ERR G in the tangent direction to break the interface and by-pass the inclusion (Fig. 3.31.c).

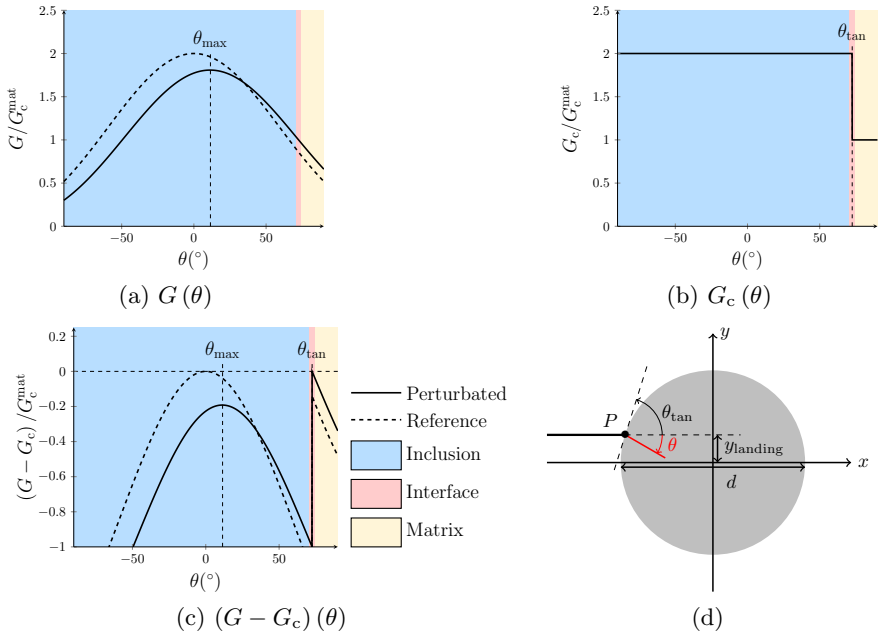

Figure 3.31: Generalized Maximum Energy Release Rate criterion in local mode mixity : angle distribution of G (a), G_c (b) and $(G - G_c)$ (c) for a crack locally loading in Mode I+II $\rho_{\text{II}} = -0.1$, landing at a height $y_{\text{landing}}/d = 0.15$ on a inclusion of toughness $G_c^{\text{inc}} = 2\,G_c^{\text{mat}}$ (d) at the onset of depinning

Coming back on the case of ellipsoidal inclusions, the out-of-plane deformations triggered by the inclusion shape at the onset of inclusion crossing/by-pass induce a negative δK_{II} on the points located at the center of the inclusion. It makes their by-pass easier as explained

by the two-dimensional model. In the spherical case of Fig. 3.29.a & d, the front is almost flat when the central region begins to by-pass the inclusion. It is thus loaded in pure Mode I and follows the theoretical two-dimensional predictions derived in Eq. (3.27). This phenomenon accounts for the discrepancy on the crossing to by-pass transition observed in Fig. 3.26 and Fig. 3.27.

3.4.2 Impact of collective three-dimensional behavior on the effective toughness

Three-dimensional effects triggered by inclusion geometry can thus drastically lower the inclusion toughness levels at which the by-pass mechanism prevails over inclusion crossing. Those effects are inherently collective since they are triggered by long-range elastic interactions along the crack front, both in-plane for the propagation dynamics (which point unpins first) and out-of-plane for the crack trajectory (which path is chosen under local mixed mode loading). They are expected to have a subsequent impact on the effective toughness of periodic arrangements of tougher inclusions.

To address this issue, we consider a crack interacting with inclusion, whose geometry is among the three considered above, for an inclusion spacing $L_z = 4\,d$, where inclusion size is $d = d_z$. Thus we keep constant the ratio $L_z/d_z = 4$ in order to get the same effective toughness for inclusion crossing if it followed a mixture rule (see Eq. (3.20)). Inclusion toughness ranges between $G_c^{\text{inc}} = G_c^{\text{mat}}$ and $G_c^{\text{inc}} = 4\,G_c^{\text{mat}}$ while interface toughness equals $G_c^{\text{int}} = G_c^{\text{mat}}$. The crack is landing at $y_{\text{landing}} = 0.1\,d_y$ so that the central point of the crack front, where the kink angle is the largest, sees the same tangent angle $\theta_{\tan}$ (see Eq. (3.30)). Simulation properties are summarized in Table 8.4. Results are plotted in Fig. 3.32.

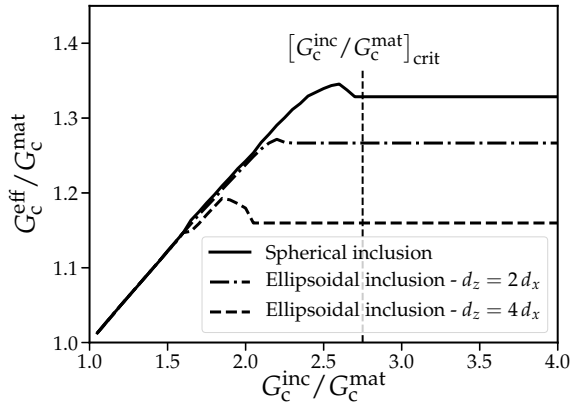

Figure 3.32: Impact of the aspect ratio of the inclusions upon the effective toughness G_c^{eff} : prolate spheroidal inclusions elongated in the direction of the crack front are by-passed by the crack at smaller toughness levels because of three-dimensional collective effects, resulting in a lowering of the plateau value of the effective toughness.

As expected from the trajectory analysis, a smaller toughness threshold for crossing to by-pass transition induces a dramatic loss of toughening in the case of ellipsoidal inclusions. The critical toughness at which the inclusion is always by-passed for $y_{\text{landing}}/d = 0.1$ is

$\left[G_c^{inc}/G_c^{mat}\right]_{crit} \sim 2.25$ for $d_z = 2\,d_x$ and $\left[G_c^{inc}/G_c^{mat}\right]_{crit} \sim 2.05$ for $d_z = 4\,d_x$ instead of the two-dimensional theoretical value $\left[G_c^{inc}/G_c^{mat}\right]_{crit} \sim 2.75\,G_c^{mat}$, which is valid for the spherical inclusion $d_z = d_x$. This smaller critical value of the inclusion toughness for the crossing to by-pass transition logically impacts the plateau value of the effective toughness for such inclusion geometry. If the effective toughness reach a plateau value of $G_c^{eff} = 1.328\,G_c^{mat}$ in the spherical case, it falls to $G_c^{eff} = 1.267, G_c^{mat}$ for $d_z = 2\,d_x$ and even to $G_c^{eff} = 1.160, G_c^{mat}$ for $d_z = 4\,d_x$.

The effective toughness for ellipsoidal geometries interacting with a crack landing at various heights $y_{landing}$ are given in Fig. 3.33. As for the spherical case, the effective toughness plateau is lowered for an increasing landing height because of the earlier crossing to by-pass transition. Naturally, due to three-dimensional collective effects, the more elongated the inclusion, the lower the plateau value for a similar landing height.

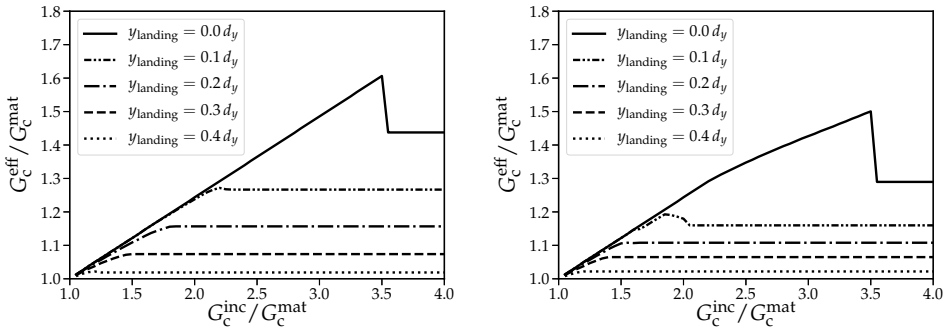

(a) $d_z = 2\,d_x = 2\,d_y$ (b) $d_z = 4\,d_x = 4\,d_y$

Figure 3.33: Impact of the landing height $y_{landing}$ on the effective toughness G_c^{eff} : numerical results for ellipsoidal inclusions with $d_z = 2\,d_x = 2\,d_y$ (a) and $d_z = 4\,d_x = 4\,d_y$ (b)

Again, such an effect on toughness emerges from the coupling between in-plane and out-of-plane deformation modes of the crack front. It affects crack trajectory in three-dimensions and subsequently the effective toughness of those materials. It stresses the importance of inclusion design in the development of composite materials with increased fracture properties.

3.5 Towards an improved toughening for crack deflection : the example of cubical inclusions

As we saw in the last section, playing on the inclusion shape might change the conditions under which one interaction mechanism (inclusion by-pass) prevails over one another (inclusion crossing) and so might decrease the potential reinforcement induced by tough inclusions. We show in this section that playing on inclusion geometry can, on the contrary, make inclusion by-pass less detrimental either by delaying its occurrence through inclusion repenetration or by increasing the toughening potential of the deflection mechanism. It is illustrated here with the interaction of a crack with cubical inclusions. As before, we first have to investigate the mechanisms involved during the interaction between a crack

and periodic arrangements of tougher cubical inclusions in Section 3.5.1. Their toughening contribution is then explored in Section 3.5.2 and compared to the results derived for the spherical shape.

3.5.1 Interaction between a crack and cubical inclusions : repenetration processes triggered by the inclusion shape

3.5.1.a Description of the cubical geometry

As described in Section 2.3.1, we consider the restricted case of cubical inclusions of edge length d, which are rotated by an angle β_{inc} in a clockwise direction around the z-axis. Such inclusion geometry is depicted in Fig. 3.34.with a cut in the (xPy) plane. The resulting intersection is a square of vertices $\{A, B, C, D\}$. The local tangent angle at the inclusion reads :

$$\begin{cases} \theta_{\tan}(z, y) = -\beta_{\text{inc}}, \text{ if } y \in [y_D, y_A) \\ \theta_{\tan}(z, y) = \dfrac{\pi}{2} - \beta_{\text{inc}}, \text{ if } y \in (y_A, y_B] \end{cases} \tag{3.31}$$

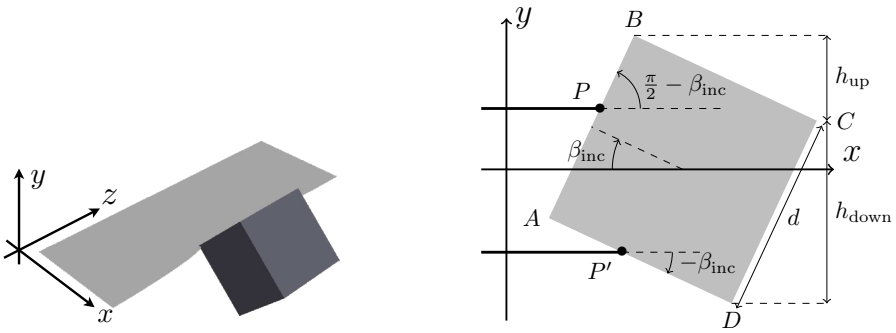

(a) 3D view (b) Plane (xPy)

Figure 3.34: Cubical inclusion of edge length d and inclination β_{inc} : three-dimensional view (a) and cut in the (xPy) plane (b)

The cubical geometry presents four main interesting properties with respect to the spherical inclusion :

1. the tangent angle to by-pass the inclusion is constant along the crack front. All the points interacting with the inclusion see the same tangent angle $\theta_{\tan}$ (Eq. (3.31)). In the spherical case, the tangent angle depended on the position of the point in the z direction (Eq. (3.28)) ;

2. the local slope is constant during the by-pass. In the spherical case, the slope rapidly vanishes, which allowed the crack to realign with the (Ox)-direction imposed by the macroscopic loading. In the cubical case, the crack is making an angle $\theta_{\tan}$ with the x-direction during the by-pass. It allows us to explore in details the impact of a stable out-of-plane deviation slope on the effective toughness ;

3. the questions of the tangent angle and the landing height are decoupled. The interaction mechanism (crossing or by-pass) selected by the crack does not depend on

the position where it lands on the inclusion. Moreover, the landing height controls the maximal height reached during inclusion by-pass. Thus the cubical geometry allows us to investigate the impact of the height of the out-of-plane deviation on crack trajectory and material toughening ;

4. the interaction mechanisms resulting from the phenomena evoked above are much richer. In the case of cubical inclusions, the out-of-plane propagation of the crack triggers a new interaction mechanism : inclusion repenetration, where the crack begins to by-pass the inclusion before going in the inclusion and crossing it. Crack propagation thus combines episodes of inclusion by-pass and inclusion crossing, which were decoupled in the spherical case.

3.5.1.b From crossing to by-pass mechanism : a soft transition for cubical inclusions characterized by inclusion repenetration

Inclusion by-pass : crack propagation in mixed Mode I+II

One major difference of crack propagation in anisotropic materials with the homogeneous situation is that the crack can propagate in local mixed mode. Indeed, in the heterogeneous case, the crack follows the path where $(G - G_c)$ is maximum, which may not correspond $K_{II}^* = 0$. This fact is illustrated with the by-pass of a tougher cubical inclusion in Fig. 3.35).

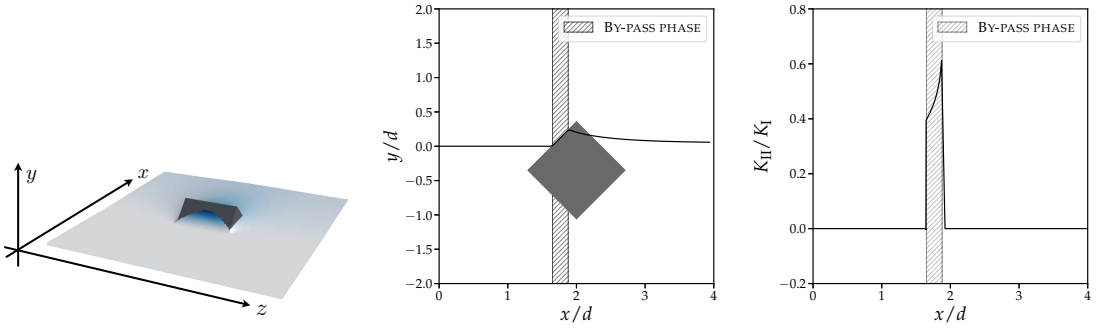

(a) 3D view (b) (x0y) plane (c) K_{II}/K_I

Figure 3.35: (a) Propagation in mixed Mode I+II during the by-pass of a tough cubical inclusion inclined at $\beta_{inc} = 45°$ with $G_c^{inc} = 1.6G_c^{mat}$: (b) Trajectory of the point of the crack front located in $z = L_z/2$. The inclusion is sufficiently tough to allow inclusion by-pass, which triggers a propagation in mixed mode until the crack repenetrates the inclusion (c)

We notice in Fig. 3.35.a-b that, after an initial phase where the crack by-passes the inclusion and propagates along the interface, it kinks and goes inside the inclusion. When the crack is propagating upwards along the interface, the points in contact are loaded in mixed mode with $K_{II} > 0$ (see Fig. 3.35.c), meaning that the kink angle prescribed by the MERR $\alpha_{max} \simeq -2K_{II}/K_I < 0$. G is thus maximal in a direction pointing inside the inclusion. It is then possible that the crack, whose path is dictated by the GMERR, chooses to repenetrate the inclusion during the by-pass.

Inclusion repenetration : a two-dimensional theoretical analysis

The occurrence of such a phenomenon can be analyzed within the LEFM framework thanks

to Amestoy-Leblond's formulæ. Let us consider once again the two-dimensional situation of a crack interacting with an inclusion invariant in the z-direction. During the propagation, the crack follows the interface so that $\theta_{\text{ini}} = \theta_{\text{tan}}$, leading to a zero kink angle in the by-pass direction $\alpha_{\text{tan}} = 0$. The ERR in this direction reads :

$$G_{\text{tan}} = \frac{1-\nu^2}{E} K_{\text{I}}^2 \left(1 + \rho_{\text{II}}^2\right) \tag{3.32}$$

G_{cross} is keeping the same expression as in Eq. (3.23). It gives the following repenetration condition :

$$\frac{G_{\text{c}}^{\text{inc}}}{G_{\text{c}}^{\text{int}}} = \frac{\left(F_{\text{I,I}}\left(\alpha_{\max}\right) + F_{\text{I,II}}\left(\alpha_{\max}\right)\rho_{\text{II}}\right)^2 + \left(F_{\text{II,I}}\left(\alpha_{\max}\right) + F_{\text{II,II}}\left(\alpha_{\max}\right)\rho_{\text{II}}\right)^2}{1 + \rho_{\text{II}}^2} \tag{3.33}$$

We plot such a condition in Fig. 3.36. We notice that LEFM dictates that repenetration does not occur for $G_{\text{c}}^{\text{inc}} > 1.812\, G_{\text{c}}^{\text{int}}$, even in the limit of very large K_{II}. It appears that repenetration happens for large SIF ratio $K_{\text{II}}/K_{\text{I}}$ or small toughness contrast. In the spherical case, large SIF ratio are caused by large out-of plane deviations, which are generated by very tough inclusions. It is then not surprising that such repenetration does not happen for the spherical geometry. In the case of cubical inclusions, large SIF ratio can be triggered at smaller inclusion toughness levels since the maximal height of the out-of-plane deviation depends on the landing height whereas the interaction choice (crossing/by-pass) depends on the inclusion inclination β_{inc}.

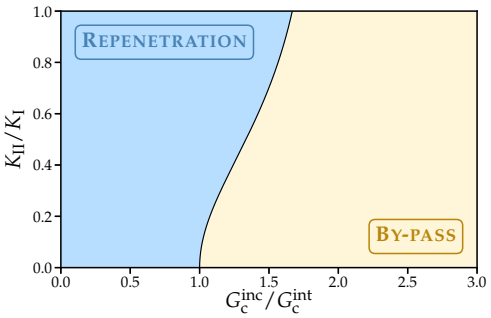

Figure 3.36: Repenetration diagram as a function of the SIF ratio $K_{\text{II}}/K_{\text{I}}$ and inclusion properties

Comparison of the two-dimensional theoretical model with three-dimensional numerical simulations on cubical inclusions

To study the actual occurrence of the repenetration mechanism, we consider periodic arrangements of cubical inclusions of edge length d inclined at varying inclination angles $\beta_{\text{inc}} \in \left[0, \frac{\pi}{2}\right]$ and inclusion toughness levels $G_{\text{c}}^{\text{inc}} \in \left[G_{\text{c}}^{\text{mat}}, 4\, G_{\text{c}}^{\text{mat}}\right]$. It interacts with a crack landing at varying landing heights $y_{\text{landing}} \in [0, h_{\text{up}}]$. 22,200 simulations, whose properties are summarized in Table 8.5, have been run to create a numerical transition diagram, taking this time into account the potential inclusion repenetration. This diagram is plotted in Fig. 3.37. Repenetration probability is defined from the behavior (crossing/by-pass with repenetration/pure by-pass) of the whole region $|z| \leq \frac{d}{2}$ of the crack front interacting with the inclusion. Note that in case of repenetration, some points may still pursue propagation

along the interface, leading to intermediary shades between blue and beige on the transition diagram.

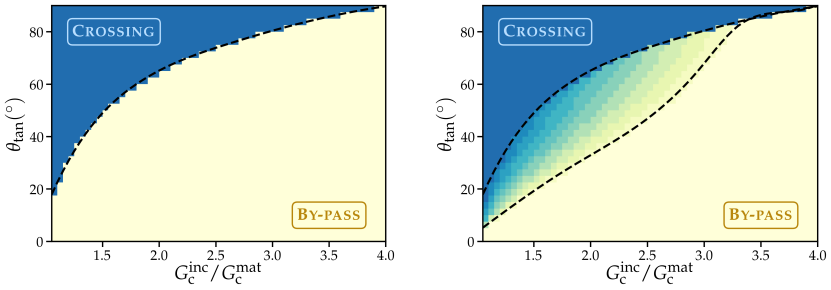

(a) (b)

Figure 3.37: Comparison of the prediction of the two-dimensional theoretical model of Eq. (3.27) (a) with the results of the three-dimensional numerical simulations in case of cubical inclusions: (b) Phase diagram obtained from 22'000 simulations with various toughness ratios $G_c^{\text{inc}}/G_c^{\text{mat}}$ and inclusion inclinations β_{inc} and landing heights y_{landing}/d. Pure crossing is plotted in blue, pure bypass in beige and intermediate cases with crack repenetration in shade from blue to beige

We see that inclusion repenetration occurs at toughness levels higher than the upper bound $G_c^{\text{inc}} \simeq 1.812\, G_c^{\text{mat}}$. These errors emerge from the fact that analytical predictions of Eq. (3.33) are computed at all orders while our numerical method is only accurate at first-order. In the case of cubical shape, the local curvature $\frac{\partial^2 f_y}{\partial z^2}$ is very high at the inclusion edges so that δK_{II} is non-negligeable. The out-of-plane perturbations and associated Mode II contributions are plotted in Fig. 3.38 for a cubical inclusion inclined at $\beta_{\text{inc}} = 45°$ and $G_c^{\text{inc}} = 1.8\, G_c^{\text{mat}}$ with a crack landing at $y_{\text{landing}} = 0.2\, h_{\text{up}}$. Large values of Mode II contributions are incompatible with the regularized G in Eq. (8.6) used in our simulations. If qualitative results can be derived for crack propagation on cubical inclusions, those results are probably no more quantitative above $G_c^{\text{inc}} = 1.8\, G_c^{\text{mat}}$.

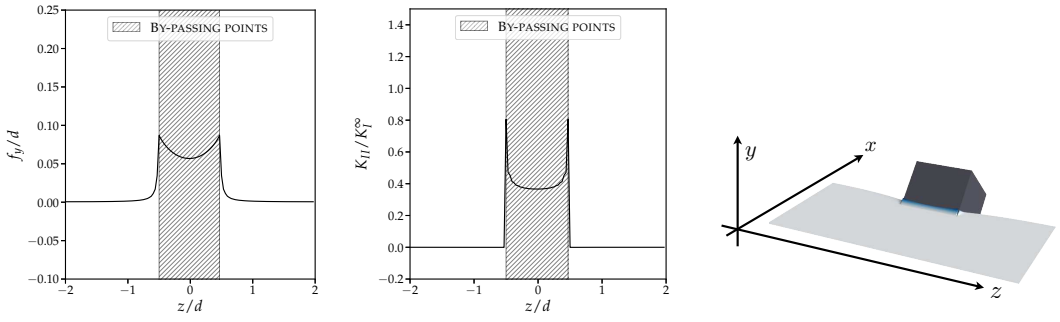

(a) Out-of-plane perturbations (b) Mode II contributions (c) 3D view

Figure 3.38: Crack front out-of-plane configuration (a) and associated SIF ratio $K_{\text{II}}/K_{\text{I}}$ (b) during the by-pass of a cubical inclusion inclined at $\beta_{\text{inc}} = 45°$ and $G_c^{\text{inc}} = 1.8\, G_c^{\text{mat}}$ with a crack landing at $y_{\text{landing}} = 0.2\, h$

When the inclusion toughness is increased, the transition between the crossing mechanism and the by-pass one is no more as sharp as in the spherical case. It is marked by a soft transition where inclusion repenetration may occur. The crossing and by-pass mechanisms then may both happen at the same time. Such a mechanism is likely to impact the effective fracture properties of composite materials with cubical tougher inclusions.

3.5.2 An improved toughening marked by repenetration processes

3.5.2.a Effective toughness of periodic arrays of tougher cubical inclusions

In the case of coplanar propagation (Section 3.2.2.c), circular and square inclusions had the same impact on the effective fracture properties. Such observation is unlikely to persist in the three-dimensional case since spherical and cubical inclusions do not interact in the same way with an incoming crack. To address this question, we consider a cubical inclusion of edge length d inclined at various inclination angles $\beta_{\text{inc}} \in \left[0, \frac{\pi}{2}\right]$. This inclusion interacts with a crack landing at different landing heights $y_{\text{landing}} =\in [0, h_{\text{up}}]$. Its toughness varies in $G_{\text{c}}^{\text{inc}} \in \left[G_{\text{c}}^{\text{mat}}, 4\,G_{\text{c}}^{\text{mat}}\right]$. Simulation properties are summarized in Table 8.5.

We first plot the results for an inclusion inclined at $\beta_{\text{inc}} = 45°$ interacting with a crack landing at $y_{\text{landing}} = 0.2\,h_{\text{up}}$ (Fig. 3.39.b). The effective toughness of the periodic heterogeneous medium is plotted in Fig. 3.39.a. We notice four main regimes :

1. at low inclusion toughness, up to $G_{\text{c}}^{\text{inc}} = 1.37\,G_{\text{c}}^{\text{mat}}$, the effective toughness follows a mixture rule characteristic of regular coplanar propagation ;
2. from $G_{\text{c}}^{\text{inc}} = 1.37\,G_{\text{c}}^{\text{mat}}$ to $G_{\text{c}}^{\text{inc}} = 2.1\,G_{\text{c}}^{\text{mat}}$, the effective toughness exceeds by a small amount the coplanar predictions but the toughening rate is smaller than for the coplanar case ;
3. from $G_{\text{c}}^{\text{inc}} = 2.1\,G_{\text{c}}^{\text{mat}}$ to $G_{\text{c}}^{\text{inc}} = 3.4\,G_{\text{c}}^{\text{mat}}$, the effective toughness decreases progressively and the toughening loss in comparison to the coplanar case is increasing accordingly ;
4. above $G_{\text{c}}^{\text{inc}} = 3.4\,G_{\text{c}}^{\text{mat}}$, the effective toughness reaches a plateau above which the inclusion toughness has no impact on the overall properties of our composite as in the spherical case.

Let us now discuss those four regimes. At low inclusion contrast, the inclusion is crossed (Fig. 3.39.b). The cut of the cube by the (zOx) plane is a rectangle. For the inclination β_{inc} and the landing height y_{landing} considered here, the penetration process happens to be regular and the effective toughness follows a mixture rule.

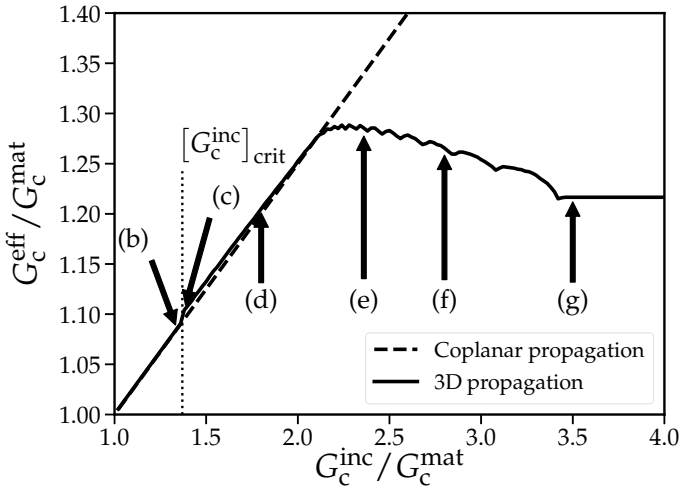

(a)

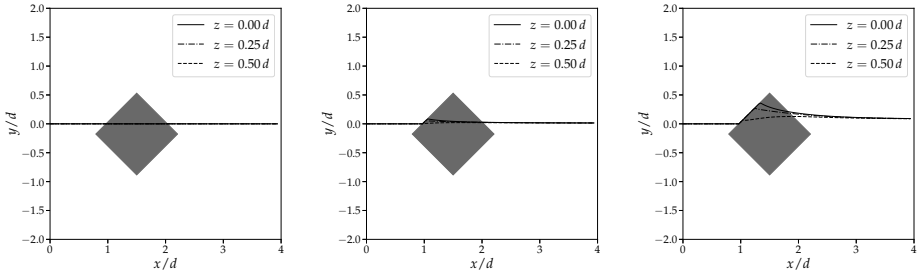

(b) $G_c^{inc} = 1.36\,G_c^{mat}$ (c) $G_c^{inc} = 1.38\,G_c^{mat}$ (d) $G_c^{inc} = 1.8\,G_c^{mat}$

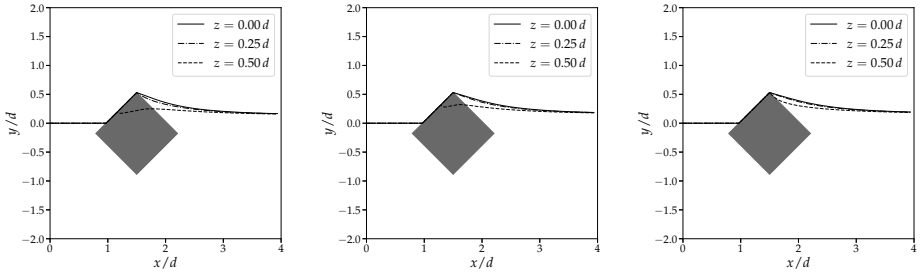

(e) $G_c^{inc} = 2.35\,G_c^{mat}$ (f) $G_c^{inc} = 2.8\,G_c^{mat}$ (g) $G_c^{inc} = 3.5\,G_c^{mat}$

Figure 3.39: Effective toughness G_c^{eff} for various inner toughness for a cubical inclusion inclined at $\beta_{inc} = 45°$ with a crack landing at $y_{landing} = 0.2\,h_{up}$ with $\left[G_c^{inc}\right]_{crit} \sim 1.37\,G_c^{mat}$ (a) and crack trajectory for three points of the crack front interacting with the inclusion at various propagation states (b)-(g)

At $G_c^{inc} = \left[G_c^{inc}\right]_{crit} \sim 1.37\, G_c^{mat}$, the inclusion begins to be by-passed as predicted by the two-dimensional predictions (Eq. (3.27)). Above this toughness level, points of the crack front interacting with the defect begin to by-pass it. As the points keep on climbing on the inclusion, the Mode II contribution δK_{II} increases (Fig. 3.35) and tries to drag the front back in the inclusion. Consequently, it is more and more difficult for the by-passing points to progress on the tangent direction θ_{tan} and the macroscopic loading has to be increased to make the crack advance.

At some point during the propagation, the local Mode II is so intense that the crack goes back in the inclusion and crosses it. Crack trapping is thus retrieved and the effective toughness of the composite is close to the one found for coplanar propagation. We notice that the points of the crack front near the edges of the inclusion go back in the inclusion earlier than the points located in the center of the inclusion due to a larger mode mixity (see Fig. 3.38). As the inclusion toughness increases, less and less points along the crack front repenetrate the inclusion (Fig. 3.39.d-f). The by-pass mechanism prevails here over inclusion repenetration, which induces a subsequent decrease in material toughening. The effective toughness thus reaches a peak and then decreases as repenetration processes are less and less frequent. The bumps displayed in Fig. 3.39.a are associated with the front discretization.

Above $G_c^{inc} = 3.4\, G_c^{mat}$, all points of the crack front interacting with an inclusion by-pass it (Fig. 3.39.g). No part of the inclusion is crossed anymore and the overall toughness of the material reaches a plateau. The effective toughness is no more related to the inclusion toughness properties but only to the one of the interface. The plateau value is nonetheless far larger in the case of a cubical inclusion than for a spherical inclusion. It is explained by the fact that during inclusion by-pass the tangent angle made by the interface is constant for the cubical shape whereas it vanishes in the spherical case. The crack cannot realign with its natural propagation direction (Ox), imposed by the loading, and additional loading is thus required to make it by-pass the inclusion.

3.5.2.b Impact of the landing height and inclusion inclination on the effective fracture properties

We now plot the effective toughness for the same inclusion properties for a crack landing at various heights in Fig. 3.40. As the crack lands closer to the center of the inclusion, the maximal out-of-plane deviations attained during inclusion by-pass are larger. It thus extends the range of inclusion toughness where the inclusion can be repenetrated during a by-pass and subsequently increase the effective toughness. We also notice that when the inclusion lands near the top of the inclusion, the effective toughness is close to the one obtained for by-passing a spherical inclusion. In that case, there is almost no out-of-plane propagation and crack depinning and by-passing take place almost simultaneously.

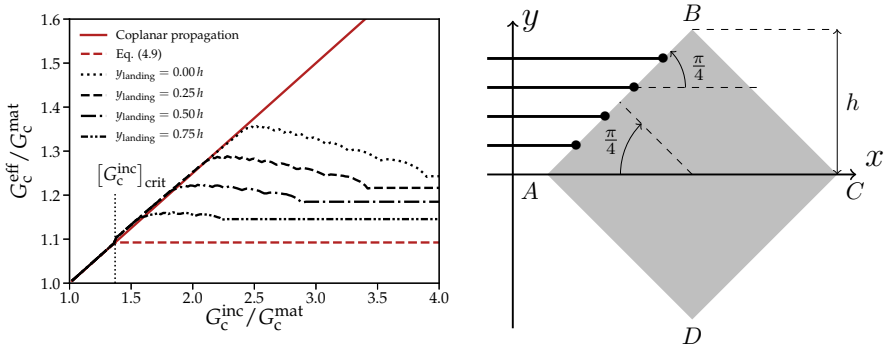

(a) G_c^{eff} (b) Plane (xOy)

Figure 3.40: Impact of the landing height y_{landing} on the effective toughness G_c^{eff} (a) for the interaction of a crack with periodic arrangements of cubical inclusions inclined at $\beta_{\text{inc}} = 45°$ (b)

We finally consider a crack landing at $y_{\text{landing}} = 0.5\,h_{\text{up}}$ on periodic arrangements of cubical inclusions with varying inclination angle $\beta_{\text{inc}} \in \left[0, \frac{\pi}{2}\right]$. Results are plotted in Fig. 3.41. Naturally, a bigger tangent angle θ_{tan}, i.e. a smaller inclination angle β_{inc}, delays the toughness ratio $\left[G_c^{\text{inc}}/G_c^{\text{mat}}\right]_{\text{crit}}$ at which the crossing to by-pass occurs. Moreover, the smaller the inclination angle, the larger the out-of-plane slope deviation during by-pass. The path the crack follows during by-pass is strongly diverted from its natural propagation direction (Ox) and the plateau value is thus increased. We notice that for $\beta_{\text{inc}} = 67.5°$, the combination of inclusion by-pass and crossing by repenetration can require a larger loading than the coplanar propagation. It underlines the fact, already highlighted in Section 3.5.1, that crack propagation results from a local maximization of the dissipated energy and not from a global one. The crack can be prompted by inclusion geometry to follow a path that requires in the end a larger loading to make the crack propagate.

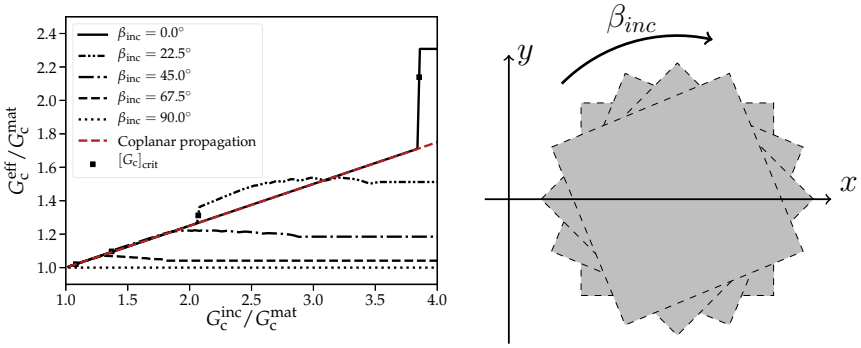

(a) G_c^{eff} (b) Plane (xOy)

Figure 3.41: Impact of the inclusion inclination β_{inc} on the effective toughness G_c^{eff} (a) for the interaction of a crack with periodic arrangements of cubical inclusions hit at a landing height $y_{\text{landing}} = 0.5\,h$ (b)

As opposed to the coplanar case, spherical and cubical inclusions do not have the same impact on inclusion toughness. Far from it, the cubical inclusions lead to effective toughness levels far superior to the one induced by spherical inclusion due to geometrical effects. The cubical geometry does not allow the crack to realign with the propagation direction imposed

by the loading (Ox), which increases the toughening potential of crack deflection. It can also trigger inclusion repenetration, where the crack goes back in the inclusion and crosses it, which delays the toughness levels at which inclusion by-pass occurs. Tailoring the inclusion shape can thus seriously limit the toughening loss by inclusion by-pass.

As underlined in Section 3.5.1.b, crack repenetration might not be modeled accurately by our first-order perturbative approach. The conclusion drawn in this section might be only qualitative and would need to be investigated further through more accurate numerical approaches such as phase-field simulations, the periodic cases considered in this study being still within reach of such approaches [Clayton and Knap, 2014; Nguyen et al., 2017a].

3.6 The by-pass mechanism, a limiting factor for both crack trapping and crack bridging ?

The last three sections were dedicated to highlighting how the by-pass mechanism may induce substantial toughening loss by limiting material toughening by crack trapping. But crack trapping can only increase the effective toughness by a factor two or three. Crack bridging is mentioned in the literature as a much more severe toughening mechanism, since it may increase the material toughness by a factor ten, as experimentally observed by Krstic et al. [1981] and Malik and Barthelat [2016] and confirmed by numerical simulations in Bower and Ortiz [1991]. When particles, such as fibers, remain unbroken in the wake of the crack, they pin the crack lips/surfaces together and a greater load is required to make the crack propagates. Moreover, crack bridging triggers a so-called R-curve effect, where the effective toughness of the material increases as the crack propagates. Such features have been observed in nature on biological materials displaying remarkable toughness properties such as bone and nacre [Barthelat et al., 2007; Wegst et al., 2015]. It has driven the development of bio-inspired materials where toughness properties were tuned to make crack bridging happen [Mirkhalaf et al., 2014; Wegst et al., 2015; Malik and Barthelat, 2016]. Yet if crack deflection allows crack bridging to happen in the case of fibers [Evans et al., 1991; Naslain, 1998], this section underlines that it may not be the case for any inclusion shape and that inclusion by-pass might also limit material toughening by preventing crack bridging to occur.

3.6.1 Crack bridging, a particularly efficient toughening mechanism threatened by inclusion by-pass ?

As explained above, crack bridging induces a major increase in effective fracture properties and is logically the primary mechanism to aim at if one wants to make brittle materials tougher. Crack bridging can occur for various reasons. For example, Mirkhalaf et al. [2014] designed weak interfaces in glass using a laser engraving technique. The crack followed those weak interfaces resulting in a geometrical interlocking situation leading to crack bridging.

Another possibility has been highlighted by Bower and Ortiz [1991] in numerical simulations of coplanar propagation of a crack interacting with tougher circular inclusions, which might depict the case of infinitely elongated fibers aligned in the direction perpendicular to

the crack front. If the inclusions are tough enough, the crack does not break the inclusion as illustrated in Fig. 3.42. The crack front bows around the inclusion and finally merges ahead as represented in Fig. 3.43. The bowing and merging mechanism could induce a loss of toughening since it prevails over inclusion crossing and thus limits crack trapping. But it leaves unbroken particles in the wake of the crack front, which pin the crack surfaces and toughen drastically the material.

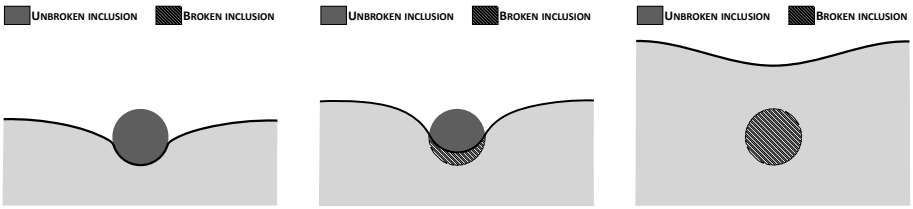

(a) (b) (c)

Figure 3.42: Crossing mechanism at three different propagation steps : pinning on the inclusion (a), inclusion crossing (b), matrix (c) leaving the inclusion broken in the wake of the crack

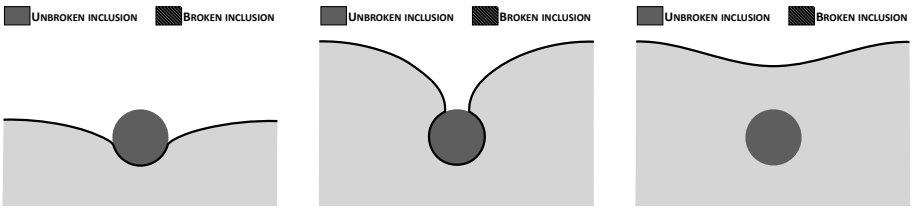

(a) (b) (c)

Figure 3.43: Bridging mechanism at three different propagation steps : pinning on the inclusion (a), coalescence around the inclusion (b), matrix relaxation (c) leaving the inclusion unbroken thus pinning the crack surfaces in the wake of the crack

When crack bridging occurs, Bower and Ortiz [1991] showed that the effective toughness reads :

$$\frac{G_{\mathrm{c}}^{\mathrm{eff}}}{G_{\mathrm{c}}^{\mathrm{mat}}} = 2.39\frac{d^2}{L_z^2}\frac{G_{\mathrm{c}}^{\mathrm{inc}}}{G_{\mathrm{c}}^{\mathrm{mat}}} \tag{3.34}$$

3.6.2 Influence of inclusion elongation on the trapping to bridging transition

Bower and Ortiz [1991] emphasized that crack bridging already occurs for inclusions 4.4 times tougher than the matrix, i.e. for $G_{\mathrm{c}}^{\mathrm{inc}}/G_{\mathrm{c}}^{\mathrm{mat}} \geq 4.4$ (see Fig. 3.44). However, we showed in Section 3.3.1 that by-pass systematically happens for spherical inclusions with toughness ratios $G_{\mathrm{c}}^{\mathrm{inc}}/G_{\mathrm{c}}^{\mathrm{mat}} \geq 3.82$, implying that bridging *cannot* occur for spherical inclusions since by-pass prevails over crack front trapping. Thus, as crack bridging *does* happen for infinitely elongated fibers along the y-direction, one may wonder how elongated should an inclusion be for crack bridging to prevail over inclusion by-pass.

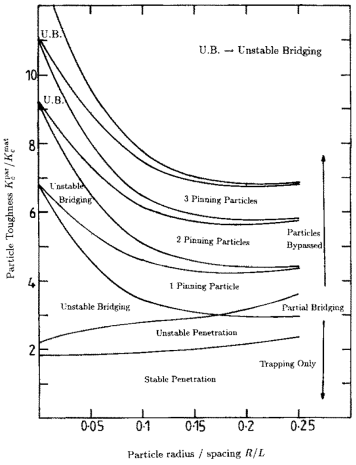

(a)

Figure 3.44: Regimes of behaviour for a semi-infinite crack propagating through a regular array of circular tough particles (after [Bower and Ortiz, 1991])

To address this issue, we consider the interaction of a semi-infinite crack with periodic arrangements of prolate spheroidal inclusions elongated in the y-direction, having $d_z = d_x = d$ and $0.1 \leq d_y/d \leq 4$ (see Fig. 3.45). We consider a toughness ratio $G_c^{inc} = 4\,G_c^{mat}$, that corresponds to the upper limit of the validity range of our model. We do not model crack bridging, but rather focus on the estimation of the conditions under which this mechanism may occur or not. We compare our results, based on the modeling of the coupling of crack trapping and inclusion by-pass, to those obtained for the coupling of crack trapping and bridging by Bower and Ortiz [1991].

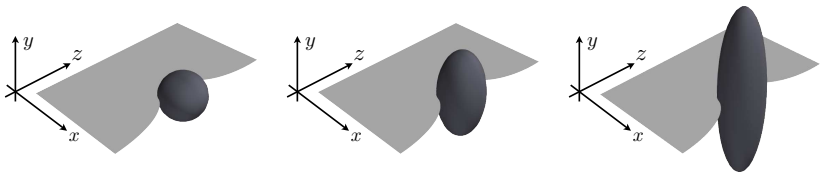

(a) $d_y = d_z = d_x$ (b) $d_y = 2\,d_z = 2\,d_x$ (c) $d_y = 4\,d_z = 4\,d_x$

Figure 3.45: Examples inclusion geometry considered in the following study : spherical (a), ellipsoidal prolate with $d_y = 2\,d_z = 2\,d_x$ (b) and $d_y = 4\,d_z = 4\,d_x$ (c)

For the toughness contrast and aspect ratios of inclusion considered here, the by-pass mechanism prevails over inclusion crossing. We then compute the loading required to by-pass the inclusion - that is the effective toughness of the composite - and compare it to that for which crack bridging is expected to occur. The latter, determined by Bower and Ortiz [1991], corresponds to the loading required to ensure crack coalescence around a cylindrical inclusion of axis perpendicular to the crack plane. It depends only on the ratio of the inclusion effective radius (that varies with the landing height) over the particle inter-distance L_z. The procedure, repeated for various landing height y_{landing}/d_y, leads to the results of Fig. 3.46.

For a given landing height y_{landing}, the effective toughness increases with the aspect ratio d_y/d_z. This is due to the fact that the crack front is dragged downwards because of the growing Mode II contribution δK_{II} while it is by-passing the inclusion upwards. The more elongated the inclusion, the harder the by-passing - and therefore the larger the load required to induce crack propagation - because of the larger difference between the propagation direction θ_{tan} and that, θ_{max}, corresponding to the maximum of G. We see that even for highly elongated inclusions, typically $d_y/d = 4$, crack bridging is not activated before by-pass can be fully completed.

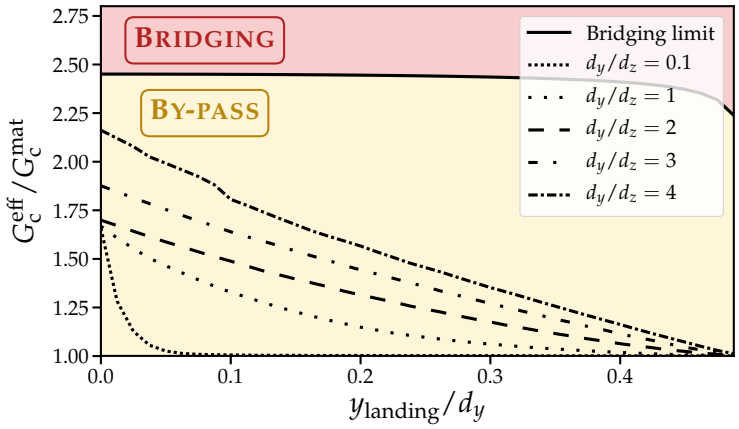

Figure 3.46: By-pass to bridging transition as a function of the normalized landing height y_{landing}/d_y for different inclusion elongation ratio d_y/d_z : the effective toughness of the by-pass mechanism (in dashed/dotted line) is compared to the prediction of the effective toughness at the crack trapping to bridging transition (in solid line).

We conclude that in the limit of very long fibers ($d_y/d_z \to +\infty$), Bower and Ortiz [1991]'s numerical predictions of toughening through crack bridging apply. Yet, as soon as inclusions of finite elongation are considered, inclusion by-pass prevents crack bridging, thus considerably reducing the material toughening due to inclusions. However, these conclusions remain qualitative insofar as, strictly speaking, our first-order model remains rigorously valid for small out-of-plane deviations, a condition which is violated as soon as the inclusion gets too much elongated. Moreover, Xu et al. [1998] showed that crack branching may occur at the matrix/inclusion interface. This type of branching is not included in our model which considers only a single macroscopic crack. It may induce an increase of the energy dissipated by crack propagation and thus delay inclusion by-pass, allowing the trapping/bridging transition to occur.

3.7 Presence of weak interface : the decisive role of the inclusion shape

Playing on the interface properties is often presented as a way to achieve greater toughness properties. Li and Zhou [2013b] showed that weakening interfaces toughens brittle materials, basing their conclusions on two-dimensional cohesive zone model simulations and analytical methods. From the results of their experimental campaign on fiber-reinforced

ceramics, both Evans et al. [1991] and Naslain [1998] recommend weak interfaces to favor crack deflection at the interface. As stressed out by Xu et al. [1998] and Ma et al. [2004], a weak interface can favor material toughening in the case of cylindrical fibers since it allows crack bridging to occur. But they also underline how a weak interface may reduce toughening by crack trapping, which is often a far less efficient toughening mechanism than crack bridging. We explore here the question of weak interfaces and their ultimate impact on crack-inclusion interactions and the effective toughness.

3.7.1 A weak interface limiting further crack trapping and bridging

To investigate the impact of weak interface on the effective toughness, we consider periodical arrangements of spherical inclusions with a system $L_z = 4d$ interacting with a crack landing at $y_{\text{landing}} = 0.1\,d$. The inclusion toughness varies from inclusion toughness $G_c^{\text{inc}} = G_c^{\text{mat}}$ to $G_c^{\text{inc}} = 4\,G_c^{\text{mat}}$. The interface toughness is no more equal to the matrix toughness and goes from $G_c^{\text{int}} = 0.6\,G_c^{\text{mat}}$ to $G_c^{\text{int}} = G_c^{\text{mat}}$. Simulation parameters correspond to the ones reported in Table 8.6. Results are plotted in Fig. 3.47.

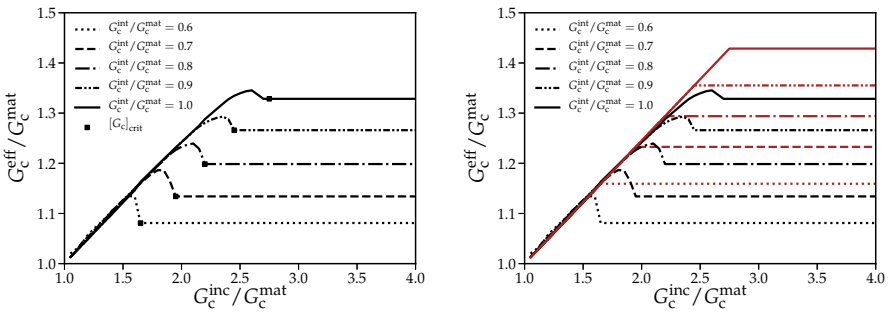

(a) (b)

Figure 3.47: Effective toughness G_c^{eff} for various inclusion toughness and interface toughness for a spherical inclusion hit at $y_{\text{landing}}/d = 0.1$ and comparison with upper bounds predictions from Eq. (3.29)

As may have been expected, the weaker the interface, the bigger the toughening loss in comparison to the coplanar case where only crack trapping occurs. Indeed, Eq. (3.26) tells us that reducing the interface toughness makes the by-pass easier, which is then triggered at smaller inclusion toughness levels. As explained in Section 3.3.2, the macroscopic loading reaches its maximum value when the crack kinks to by-pass the inclusion in the case of spherical inclusions. Since the kink is made easier by the weak interface, the effective toughness logically drops and its plateau value decreases as the interface gets weaker.

Deriving analytical predictions for the effective toughness is a complicated matter. We see in Fig. 3.47.a that the crossing to by-pass transition is well predicted by Eq. (3.26) for a spherical inclusion as it was in the case for $G_c^{\text{int}} = G_c^{\text{mat}}$. But the determination of the plateau value is complicated, as explained in Section 3.3.2 since the interaction process is irregular. Eq. (3.29), which predicted an upper bound for the case $G_c^{\text{int}} = G_c^{\text{mat}}$, remains nonetheless valid for weak interface as depicted in Fig. 3.47.b.

A weak interface can induce a substantial loss of toughening since it favors inclusion

by-pass. We illustrated this fact on spherical inclusions. The same conclusions could have been drawn for the composite with ellipsoidal prolate inclusions presented in Section 3.4. Its effective toughness, already reduced by collective behavior in the by-pass of tougher inclusions, is even lesser in the case of weak interface. In the same way, a weak interface may facilitate the by-pass of moderately elongated inclusions and thus prevent crack bridging to occur.

3.7.2 Weak interface : a potential toughening relying on material design

In all the cases discussed above, inclusion by-pass was always detrimental with respect to inclusion crossing as far as the effective fracture properties are concerned since crack deflection has a smaller toughening potential than crack trapping. Yet, the example of the cubical inclusion showed that one can work on the inclusion shape to increase the reinforcement induced by crack deflection. If this mechanism happens to be more efficient than crack trapping, one could achieve higher reinforcement levels by favoring inclusion by-pass through the introduction of a weak interface.

We thus consider periodical arrangements of cubical inclusions of edge width d and inclination $\beta_{inc} \in \left\{\frac{\pi}{8}, \frac{\pi}{4}\right\}$ separated by $L_z = 4d$. They interact with a crack landing at $y_{\text{landing}} = 0.2\, h_{\text{up}}$. The inclusion toughness varies from inclusion toughness $G_{\text{c}}^{\text{inc}} = G_{\text{c}}^{\text{mat}}$ to $G_{\text{c}}^{\text{inc}} = 4\, G_{\text{c}}^{\text{mat}}$. The interface toughness goes from $G_{\text{c}}^{\text{int}} = 0.6\, G_{\text{c}}^{\text{mat}}$ to $G_{\text{c}}^{\text{int}} = G_{\text{c}}^{\text{mat}}$. Simulation parameters are summarized in Table 8.6 and results are plotted in Fig. 3.48.

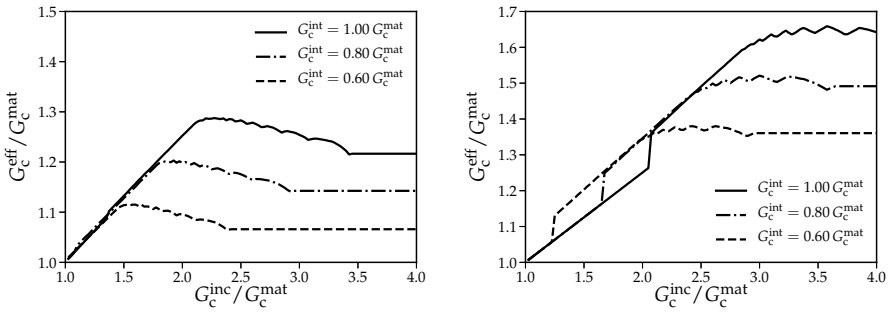

(a) $\beta_{inc} = \frac{\pi}{4}$ (b) $\beta_{inc} = \frac{\pi}{8}$

Figure 3.48: Effective toughness $G_{\text{c}}^{\text{eff}}$ for various inclusion toughness and interface toughness for a cubical inclusion of inclination $\beta_{inc} = \frac{\pi}{4}$ (a) and $\beta_{inc} = \frac{\pi}{8}$ (b) hit at $y_{\text{landing}} = 0.2\, h_{\text{up}}$.

We see in Fig. 3.48.a that for small tangent angle $\beta_{inc} = \frac{\pi}{4}$ (i.e. $\theta_{\text{tan}} = \frac{\pi}{4}$), the presence of a weak interface weakens the material. Yet in the case of large tangent angle $\beta_{inc} = \frac{\pi}{8}$ (i.e.$\theta_{\text{tan}} = \frac{3\pi}{8}$), there exists a regime where the effective toughness can be increased for smaller interface toughness levels (Fig. 3.48.b). From $G_{\text{c}}^{\text{inc}} = 1.2\, G_{\text{c}}^{\text{mat}}$ to $G_{\text{c}}^{\text{inc}} = 2\, G_{\text{c}}^{\text{mat}}$, the inclusion with $G_{\text{c}}^{\text{int}} = 0.6\, G_{\text{c}}^{\text{mat}}$ is initially by-passed then crossed after a repenetration, while the inclusion $G_{\text{c}}^{\text{int}} = G_{\text{c}}^{\text{mat}}$ is crossed. Around those inclusion toughness levels, the weaker configuration is tougher than the other by an amount $\Delta G \simeq 0.1 G_{\text{c}}^{\text{mat}}$, so 10% of toughness increase. As soon as inclusion by-pass remains the only mechanism involved, the weaker configuration displays a smaller effective toughness than the case where $G_{\text{c}}^{\text{int}} = G_{\text{c}}^{\text{mat}}$.

To conclude, a weak interface might be a parameter to consider if the mechanism it triggers is more energetically costly than crack trapping. In our study, such cases remains scarce and a weak interface generally leads to a decrease in the effective fracture properties.

3.8 Concluding remarks

This chapter was dedicated to the study of the mechanisms which take place during the interaction between a crack and tough inclusions and their ultimate impact on the effective toughness, estimated from the maximum loading attained during crack propagation.

In Section 3.2, we revisited the works of Gao and Rice [1989], Chopin et al. [2011] and Chopin et al. [2018] derived for coplanar crack propagation. The crack was bound to propagate within a plane by crossing the tougher defects. We showed that, when the crack interacts with periodic arrangements of tougher inclusions, its front distorts proportionally to the toughness of the inclusions. The non-local elastic interactions along the crack front triggered by the distortion of the crack front allow for the crossing of the inclusion together with an increase in the macroscopic loading due to *crack trapping*. The effective toughness has been proved to increase proportionally to the toughness contrast $G_{\mathrm{c}}^{\mathrm{inc}} - G_{\mathrm{c}}^{\mathrm{mat}}$. *Inclusion crossing* allows for an efficient toughening of composite materials by *crack trapping*.

The coplanar hypothesis is relieved in Section 3.3. The crack can interact with a tough inclusion either by *crossing* it or *by-passing* it. The conditions under which one mechanism prevails over the other have been derived analytically in a two-dimensional case where the inclusion is invariant in the front direction in Eq. (3.26). It has been shown to describe accurately the mechanisms observed numerically for spherical inclusions. At low inclusion toughness, the inclusion is crossed while it is by-passed at higher toughness levels. If the effective toughness increases linearly with the inclusion toughness in the case of inclusion crossing, it reaches a plateau when the inclusion is by-passed. *Crack deflection* is activated and proves to be less efficient than *crack trapping* to reinforce composite materials. The by-pass mechanism is then detrimental to the effective toughness since it limits material toughening by *crack trapping*.

One can play on the inclusion geometry to influence both the conditions under which one interaction mechanism is selected by the crack and the toughening it induces. First, considering in Section 3.4 ellipsoidal inclusions elongated along the front direction (Oz), we proved that the crossing to by-pass transition could occur at smaller inclusion toughness levels because of three-dimensional collective effects. This early by-pass consecutively limits further material reinforcement by crack trapping and reduces the effective toughness of the heterogeneous material. Second, cubical inclusions can on the contrary delay the toughness levels at which the by-pass mechanism prevails over inclusion crossing by triggering a new mechanism : *inclusion repenetration*. The latter mechanism toughens the composite efficiently by *crack trapping* for a larger range of inclusion toughness than in the spherical case. Moreover, the cubical geometry prevent the crack to realign with the propagation direction (Ox) imposed by the macroscopic tensile loading and consequently increases the potential of reinforcement of *crack deflection*. It paves the way for the design of more com-

plex geometries that prevent inclusion by-pass and allow for the activation of more efficient toughening mechanisms.

In Section 3.6, we show that the by-pass mechanism can not only limit material toughening by *crack trapping* but can also prevent *crack bridging* mechanisms to occur. Crack bridging has been proved to reinforce substantially the effective toughness up to a factor $10 - 50$ [Krstic et al., 1981; Bower and Ortiz, 1991]. Yet, inclusion by-pass might prevent crack bridging to occur. Considering ellipsoidal inclusions elongated along the direction perpendicular to the crack surface (Oy), we show that the by-pass mechanism prevents crack bridging to occur for elongation ratios up to $d_y/d_z = 4$.

Finally, we showed in Section 3.7 that weak interfaces are in general detrimental to the material reinforcement since it favors by-pass mechanisms to occur. Nonetheless, if one design inclusions where the toughening by crack deflection triggered by by-pass events exceeds the one induced by crack trapping and inclusion crossing, weak interfaces could produce tougher materials.

This chapter underlines the close relationship which links the interaction mechanisms that occur at the crack-tip and the effective fracture properties. The conditions under which one mechanism prevails over one another as well as the reinforcement potential of the activated toughening mechanism have been thoroughly investigated and have been shown to be dictated by both material properties and inclusion geometry. The next chapter aims at describing how such interaction mechanisms can be taken into account in a homogenization framework which allows for the prediction of the effective toughness of large-scale heterogeneous materials.

4

Homogenization of brittle fracture properties for large-scale composites : an insight from statistical physics

Contents

4.1 Introduction

Be they natural or artificial, heterogeneous materials are commonly found in everyday life. The recent boom of additive manufacturing techniques [Dimas et al., 2013; Wang and Xia, 2017] and the emergence of bio-source and recycled composite materials driven by pressing environmental concerns [Reis, 2006; Jo et al., 2008] have increased further the need to rationalize the failure behavior of microstructured solids. A comprehensive theoretical framework that allows for the prediction of the effective fracture properties of composite materials from their microstructural features has been a query for decades in solids mechanics and is still lacking today.

Nevertheless, homogenizing brittle fracture properties proves nevertheless especially challenging since brittle fracture is both an evolutive and a dissipative process, which additionally localizes at the crack tip or on the crack surfaces. It consequently does not allow for the use of well-established averaging methods dedicated to the homogenization of linear [Hashin and Shtrikman, 1963; Hill, 1965; Herve and Zaoui, 1993; Ponte-Castañeda and Willis, 1995] and non-linear [Ponte-Castañeda, 1991; Ponte-Castañeda and Suquet, 1997; Lahellec and Suquet, 2007; Agoras et al., 2016; Lucchetta et al., 2019] behaviors, that assume that the dissipation can be estimated from its volume average on all *representative volume elements* (RVE). For the homogenization of brittle fracture properties, Roux et al. [2003], Roux and Hild [2008] and Patinet et al. [2013b] proposed a numerical self-consistent approach which allows for the prediction of the homogenized fracture properties when a coplanar crack interacts with tougher defects. Démery et al. [2014b] and Démery et al. [2014a] addressed the same problem with tools borrowed from statistical physics [Larkin and Ovchinnikov, 1979] to develop a theoretical framework, which allows for analytical predictions of the effective fracture properties. If these works constitute major advances in the field of homogenization of brittle fracture properties, they are nonetheless restricted to coplanar crack propagation and thus can only account for the crossing mechanism of interaction between a crack and tough inclusions. Yet, as we saw in Chapter 3, effective fracture properties appear to strongly depend on the processes which take place at the crack tip (e.g. crack trapping [Gao and Rice, 1989; Bower and Ortiz, 1990; Vasoya et al., 2016a], crack deflection [Faber and Evans, 1983a; Suresh, 1985; Brach et al., 2019a; Lebihain et al., 2020a], crack de-nucleation/re-nucleation [Hossain et al., 2014; Brach et al., 2019a]) or in the wake of the crack (e.g. crack bridging [Evans et al., 1991; Bower and Ortiz, 1991; Naslain, 1998; Mirkhalaf et al., 2014] or surface wedging [Ritchie, 1988]).

After investigating thoroughly the mechanisms of interaction between a crack and a single inclusion in Chapter 3, we consider, in this chapter, crack propagation in composite materials containing millions of inclusions. We propose a theoretical framework extending the work of Démery et al. [2014b] to non-coplanar three-dimensional fracture and that includes all crack tip processes. We illustrate it on the various mechanisms (crossing, bypass, repenetration) considered in the manuscript. But at first, we revisit in Section 4.2 the results obtained by Démery et al. [2014b] within the theoretical formalism developed by Favier et al. [2006b]. Theoretical predictions of the effective fracture properties are then

compared to the results of our numerical model in the case of coplanar propagation, to investigate the predictive capabilities as well as the weaknesses of the theory. The coplanar hypothesis is relaxed in Section 4.3 where we consider non-coplanar propagation of a crack interacting with large-scale distributions of tougher spherical inclusions. We first question the definition of the effective fracture properties and then describe the conditions under which all possible definitions yield a unified value, which can be considered as intrinsic and called the *effective toughness* of the material. This is applied to the analysis of the influence of the inclusion toughness on the effective toughness, which appears to be highly non-trivial. It calls for the definition in Section 4.4 of a broader homogenization framework, which takes into account the different impacts of inclusion crossing and inclusion by-pass on the effective toughness. Finally, the theoretical predictions of this model are compared to some numerical results, for various microstructural properties (e.g. inclusion toughness, toughness disorder, interface toughness) in Section 4.5, and geometrical properties (e.g. inclusion shape, material texture) in Section 4.6.

4.2 Effective toughness for coplanar propagation in heterogeneous brittle materials

The question of the effective toughness of heterogeneous brittle materials has been previously studied in the coplanar case [Roux et al., 2003; Roux and Hild, 2008; Patinet et al., 2013b; Démery et al., 2014b,a]. Démery et al. [2014b] developed in particular a theoretical homogenization framework for the crossing mechanism inspired by theoretical concepts borrowed from statistical physics [Larkin and Ovchinnikov, 1979]. In Section 4.2.1, we revisit those results, derived in a discrete case by Démery et al. [2014b], within the continuous framework developed by Favier et al. [2006b]. It is then used in Section 4.2.2 to predict the impact of microstructural parameters (e.g. inclusion toughness, density or shape) on the effective toughness of disordered systems, with a comparison to some numerical results of large-scale coplanar simulations.

4.2.1 The decisive link between crack front deformation and the effective toughness

As we have seen in Section 3.2, information on the local toughness field is embedded in both the instantaneous crack front in-plane deformation and its evolution in time. We see in this section that the statistics of the in-plane distortions of the crack front also contain information on the macroscopic Mode I loading inducing fracture, and thus on the effective toughness of disordered heterogeneous materials.

4.2.1.a Coplanar propagation in disordered materials

We revisit here the problem of coplanar crack propagation in heterogeneous materials displaying toughness discontinuities. Let us consider a heterogeneous material described by a toughness field G_c of the type :

$$G_c(z,x) = \langle G_c \rangle + \sigma g_c(z,x) \tag{4.1}$$

where $\langle G_c \rangle$ is the spatial average of the toughness field, σ its standard deviation and $g_c(z,x)$, the disorder function, a dimensionless spatial field of unit variance and zero mean value [Démery et al., 2014b].

When the crack interacts with the toughness field, the front is deformed within its plane. At first-order the equation of motion reads (see Section 3.2.1.a) :

$$\begin{aligned}\frac{1}{v_0}\frac{\partial f_x}{\partial t}(z,t) =& \frac{v_m}{v_0} + \frac{G^\infty}{G_c^0}\left(1 - \frac{1}{\mathcal{L}} f_x(z,t) - \frac{1}{\pi}\,\mathrm{PV}\int_{-\infty}^{+\infty} \frac{f_x(z,t) - f_x(z',t)}{(z-z')^2}\,dz'\right) \\ &- \frac{\langle G_c \rangle}{G_c^0} + \frac{\sigma}{G_c^0} g_c(z, x = f_x(z,t))\end{aligned} \tag{4.2}$$

In the quasi-static limit where $v_m/v_0 \to 0$ and $\mathcal{L} \to +\infty$, we have :

$$\begin{aligned}\frac{1}{v_0}\frac{\partial f_x}{\partial t}(z,t) =& \frac{G_c^{\mathrm{eff}}}{G_c^0} - \frac{G_c^{\mathrm{eff}}}{\pi G_c^0}\,\mathrm{PV}\int_{-\infty}^{+\infty} \frac{f_x(z,t) - f_x(z',t)}{(z-z')^2}\,dz' \\ &- \frac{\langle G_c \rangle}{G_c^0} + \frac{\sigma}{G_c^0} g_c(z, x = f_x(z,t))\end{aligned} \tag{4.3}$$

where $G^\infty(t)$ is replaced by G_c^{eff}. Indeed, when $\mathcal{L} \to +\infty \Leftrightarrow \dfrac{\partial G^\infty}{\partial x} = 0$, the macroscopic loading does not decrease once reaching its maximum value G_c^{eff} (see Eq. (2.6)).

This equation slightly differs from the one given by Démery et al. [2014b] since the constant in front of the integral is $\frac{G_c^{\mathrm{eff}}}{\pi G_c^0}$ and not $\frac{1}{\pi}$, but agrees with Gao and Rice [1989]. Additional hypotheses are required to assume this factor to be $\frac{1}{\pi}$, as explained in the next part.

4.2.1.b Crack front statistics in the weak-pinning regime : the first Larkin hypothesis

Propagation equation in the weak-pinning regime

The main difficulty in dealing with Eq. (4.3) comes from the non-linearity induced by the disorder term $g_c(z, x = f_x(z,t))$. This difficulty can be circumvented if we consider that the crack front perturbations f_x are much smaller than the disorder correlation length ξ_x along the propagation direction x. Larkin and Ovchinnikov [1979] distinguished two cases :

1. If $f_x \gg \xi_x$, the crack is in a so-called *strong-pinning* regime. The crack displays an intermittent dynamics characterized by the fact that parts of the crack front are pinned by tougher inclusions ($G < G_c$) while other parts are propagating ($G = G_c$). This propagation generates, in the crack front, geometric structures called *clusters* whose spatial expansion verifies specific scaling laws [Bonamy, 2009];

2. If $f_x \ll \xi_x$, the crack is in the *weak-pinning* regime. During some period of time, the crack can propagate in a stationary manner so that $\frac{\partial f_x}{\partial t}(z,t) = 0$. Moreover, the x-dependence in the disorder term can be removed $G_c(z, x = f_x(z,t)) = G_c(z)$. This constitutes the *first Larkin hypothesis*.

In the weak-pinning regime Eq. (4.3) reduces to :

$$\frac{G_{\mathrm{c}}^{\mathrm{eff}}}{G_{\mathrm{c}}^{0}} - \frac{G_{\mathrm{c}}^{\mathrm{eff}}}{\pi G_{\mathrm{c}}^{0}} \mathrm{PV} \int_{-\infty}^{+\infty} \frac{f_x(z) - f_x(z')}{(z-z')^2} dz' - \frac{\langle G_{\mathrm{c}} \rangle}{G_{\mathrm{c}}^{0}} + \frac{\sigma}{G_{\mathrm{c}}^{0}} g_{\mathrm{c}}(z) = 0 \tag{4.4}$$

By identifying zero-order terms in the perturbation f_x, we get :

$$G_{\mathrm{c}}^{\mathrm{eff}} = \langle G_{\mathrm{c}} \rangle \tag{4.5}$$

The effective toughness verifies a simple mixture rule in the Larkin regime.

At first-order, it gives :

$$\frac{1}{\pi} \mathrm{PV} \int_{-\infty}^{+\infty} \frac{f_x(z) - f_x(z')}{(z-z')^2} dz' + \frac{\sigma}{\langle G_{\mathrm{c}} \rangle} g_{\mathrm{c}}(z) = 0 \tag{4.6}$$

We want now to extract information from the front roughness under the first Larkin hypothesis. We define the roughness in the z-direction as :

$$\Delta f_x^2(\Delta z) = \left\langle \left(f_x(z+\Delta z) - f_x(z) \right)^2 \right\rangle_z = 2 \left\langle f_x^2(z) \right\rangle_z - 2 \left\langle f_x(z+\Delta z) f_x(z) \right\rangle_z \tag{4.7}$$

Mathematical framework for crack front statistics calculation

As seen in Eq. (4.7), we aim at estimating averages over the crack front. These averages are difficult to handle theoretically. Following Favier et al. [2006b], we consider ensemble averages, where one looks at one point z at multiple front configurations resulting from the interaction of a coplanar crack with multiple heterogeneous materials. We then adopt the *ergodic hypothesis* which consists in assuming that ensemble averages are equivalent to averages over the crack front.

In the following, we consider a statistical ensemble Ω of possible realizations of a heterogeneous medium, associated to a specific real number ω. We note $p : \omega \mapsto p(\omega)$ its probability density function. Thus, the probability that the variable ω' lies in some neighborhood of ω of measure $d\omega$ is $p(\omega)\, d\omega$. The mathematical expectation $E[u(z)]$ of any spatial observable $u : z \mapsto u(z)$ is defined as :

$$E[u(z)] = \int_{\Omega} u(z;\omega)\, p(\omega)\, d\omega \tag{4.8}$$

The 2-point correlation function $E[u(z_2)\, u(z_1)]$ is defined as :

$$E[u(z_2)\, u(z_1)] = \int_{\Omega} u(z_2;\omega)\, u(z_1;\omega)\, p(\omega)\, d\omega \tag{4.9}$$

The calculation of the 2-point correlation function $E[f_x(z_2)\, f_x(z_1)]$ of f_x constitutes a decisive step to estimate the crack front roughness $\Delta f_x^2(\Delta z)$, since the two are related via the ergodic hypothesis. We know that Eq. (4.6) has a much more simple expression in the Fourier space. Thus we will work in both the real space and the Fourier space. Let

$\widetilde{E\left[u_1 u_2\right]}\left(k_1, k_2\right)$ denote the double (z_1, z_2)-Fourier transform of the function $E\left[u\left(z_2\right) u\left(z_1\right)\right]$. A simple calculation shows that [Favier et al., 2006b] :

$$\widetilde{E\left[u_1 u_2\right]}\left(k_1, k_2\right) = E\left[\hat{u}\left(k_1\right) \hat{u}\left(k_2\right)\right] \tag{4.10}$$

Moreover, in the case of statistical invariance of the observable u in the crack front direction, the two-point autocorrelation function takes the form :

$$E\left[u\left(z_2\right) u\left(z_1\right)\right] = \mathcal{U}\left(z_2 - z_1\right) \tag{4.11}$$

One gets from there in the Fourier space [Favier et al., 2006b] :

$$\widetilde{E\left[u_1 u_2\right]}\left(k_1, k_2\right) = 2\pi\delta\left(k_2 + k_1\right)\hat{\mathcal{U}}\left(k_2\right) \tag{4.12}$$

In-plane roughness in the Larkin regime

We can apply this formalism to the calculation of $E\left[f_x\left(z_1\right) f_x\left(z_2\right)\right]$ through that of $E\left[\hat{f}_x\left(k_1\right) \hat{f}_x\left(k_2\right)\right]$. First, we assume that the spatial disorder g_c is uniformly distributed so that :

$$E\left[g_c\left(z_1\right) g_c\left(z_2\right)\right] = \mathcal{G}\left(z_2 - z_1\right) \tag{4.13}$$

The Fourier transform of Eq. (4.6) yields :

$$\hat{f}_x\left(k\right) = -\frac{\sigma}{\langle G_c \rangle}\frac{\hat{g}_c\left(k\right)}{|k|} \tag{4.14}$$

Following Eq. (4.10), the double Fourier transform $\widetilde{E\left[f_x^1 f_x^2\right]}$ reads :

$$\widetilde{E\left[f_x^1 f_x^2\right]}\left(k_1, k_2\right) = E\left[\hat{f}_x\left(k_1\right) \hat{f}_x\left(k_2\right)\right] = \left(\frac{\sigma}{\langle G_c \rangle}\right)^2 \frac{E\left[\hat{g}_c\left(k_1\right) \hat{g}_c\left(k_2\right)\right]}{|k_1|\,|k_2|} \tag{4.15}$$

Now Eq. (4.10) and Eq. (4.12) yield, for the observable g_c :

$$E\left[\hat{g}_c\left(k_1\right) \hat{g}_c\left(k_2\right)\right] = \widetilde{E\left[g_{c,1} g_{c,2}\right]}\left(k_1, k_2\right) = 2\pi\delta\left(k_2 + k_1\right)\hat{\mathcal{G}}\left(k_2\right) \tag{4.16}$$

Therefore :

$$\widetilde{E\left[f_x^1 f_x^2\right]}\left(k_1, k_2\right) = \left(\frac{\sigma}{\langle G_c \rangle}\right)^2 \frac{\hat{\mathcal{G}}\left(k_2\right)}{k_2^2} \cdot 2\pi\delta\left(k_2 + k_1\right) \tag{4.17}$$

The statistical invariance of G_c implies that of f_x. One gets therefore :

$$E\left[f_x\left(z_2\right) f_x\left(z_1\right)\right] = \mathcal{F}\left(z_2 - z_1\right) \tag{4.18}$$

Using Eq. (4.12) for f_x, we identify the auto-correlation function $\mathcal{F}$ in the Fourier space in Eq. (4.17) :

$$\hat{\mathcal{F}}\left(k\right) = \left(\frac{\sigma}{\langle G_c \rangle}\right)^2 \frac{\hat{\mathcal{G}}\left(k\right)}{k^2} \tag{4.19}$$

If we go back in the real space and use the ergodic hypothesis combined with Eq. (4.19), we get :

$$\Delta f_x^2(\Delta z) = \mathcal{F}(0) - \mathcal{F}(k) = \frac{1}{\pi}\left(\frac{\sigma}{\langle G_c \rangle}\right)^2 \int_0^{+\infty} \hat{\mathcal{G}}(k) \frac{1-\cos(k\Delta z)}{k^2} dk \tag{4.20}$$

This integral can be calculated for specific expressions of $\hat{\mathcal{G}}$. For example, if we assume that the toughness disorder correlations decay exponentially :

$$\mathcal{G}(z_2 - z_1) = e^{-\frac{|z_2 - z_1|}{\xi_z}} \Leftrightarrow \hat{\mathcal{G}}(k) = \frac{\frac{2}{\xi_z}}{k^2 + \left(\frac{1}{\xi_z}\right)^2} \tag{4.21}$$

From Eq. (4.20) and Gradshteyn and Ryzhik [2014] formula (3.725.1), one can deduce that the in-plane roughness Δf_x reads :

$$\Delta f_x^2(\Delta z) = \left(\frac{\sigma}{\langle G_c \rangle}\right)^2 \xi_z \left[\Delta z + \xi_z \left(-e^{-\Delta z/\xi_z} - 1\right)\right] \tag{4.22}$$

For $\Delta z \gg \xi_z$, Eq. (4.22) reduces to :

$$\Delta f_x^2(\Delta z) = \left(\frac{\sigma}{\langle G_c \rangle}\right)^2 \xi_z \Delta z \tag{4.23}$$

In the same way, if the toughness spatial correlations follow a Lorentz decay, which happens to be much slower than the exponential one :

$$\mathcal{G}(z_2 - z_1) = \frac{1}{1 + \left(\frac{\Delta z}{\xi_z}\right)^2} \Leftrightarrow \hat{\mathcal{G}}(k) = \pi \xi_z e^{-\xi_z |k|} \tag{4.24}$$

Using Eq. (4.20) and Gradshteyn and Ryzhik [2014] formula (3.948.1), the expression of the in-plane roughness Δf_x reads :

$$\Delta f_x^2(\Delta z) = \left(\frac{\sigma}{\langle G_c \rangle}\right)^2 \xi_z \left[\arctan\left(\frac{\Delta z}{\xi_z}\right)\Delta z - \frac{\xi_z}{2}\ln\left(1 + \left(\frac{\Delta z}{\xi_z}\right)^2\right)\right] \tag{4.25}$$

For $\Delta z \gg \xi_z$, Eq. (4.25) reduces to :

$$\Delta f_x^2(\Delta z) = \frac{\pi}{2}\left(\frac{\sigma}{\langle G_c \rangle}\right)^2 \xi_z \Delta z \tag{4.26}$$

The disorder geometry changes the pre-factor of the crack front in-plane roughness Δf_x. We have just calculated those pre-factors for an exponential and a Lorentz disorder correlation function. Moreover, we confirm the property that the weak-pinning regime is characterized by a Hurst exponent $\zeta = 0.5$, given that the crack front roughness evolves as $\Delta f_x \propto \Delta z^{\zeta}$.

It ultimately allows us to define the Larkin length L_c, which separates the weak-pinning regime from the strong-pinning one. The weak-pinning regime is based on the assumption that the crack does not see that the disorder varies in the x-direction. This assumption breaks down when :

$$\Delta f_x^2 (L_c) = \xi_x^2 \tag{4.27}$$

This equation allows us to estimate the Larkin length :

$$L_c = \gamma \left(\frac{\langle G_c \rangle}{\sigma} \right)^2 \frac{\xi_x^2}{\xi_z} \tag{4.28}$$

where γ is a pre-factor determined by the disorder geometry.

4.2.1.c From crack front roughness to effective toughness : the second Larkin hypothesis

The crack front in-plane perturbations f_x and their statistics, characterized by the roughness Δf_x, are consequences of the toughness field, characterized by its mean value $\langle G_c \rangle$ and its standard deviation σ. Notably, they define a characteristic length L_c, which separates the weak-pinning regime from the strong one. This lengthscale plays a decisive role in the determination of the effective toughness of the heterogeneous material.

Indeed the *second Larkin hypothesis* consists in assuming that the loading required to break the material is given by the toughness visited by a Larkin domain of length L_c [Larkin and Ovchinnikov, 1979]. Démery et al. [2014b] distinguished two regimes :

1. $L_c \geq \xi_z$: the Larkin length L_c is greater than the inclusion size in the z-direction, characterized by the correlation length ξ_z. This regime is called *collective-pinning* ;
2. $L_c \leq \xi_z$: the Larkin length L_c is smaller than the inclusion size. A Larkin domain sees only one defect. This regime is called *individual-pinning*.

In the collective-pinning regime, a Larkin domain contains $N = L_c/\xi_z$ uncorrelated inclusions (see Fig. 4.1). The toughness experienced by this domain can be estimated from the Central Limit Theorem, which states that :

- the toughness distribution inside the Larkin domain is Gaussian;
- its average toughness is $\langle G_c \rangle$;
- its toughness standard deviation is equal to $\sigma_{\text{Larkin}} = \frac{\sigma}{\sqrt{N}} = \sigma \sqrt{\xi_z / L_c}$.

Its maximum can then be approximated roughly by :

$$\max G_c \sim \langle G_c \rangle + \beta \sigma \sqrt{\frac{\xi_z}{L_c}} \tag{4.29}$$

where β is a constant. $\beta = 4$ is usually found as a good approximation for a Gaussian distribution.

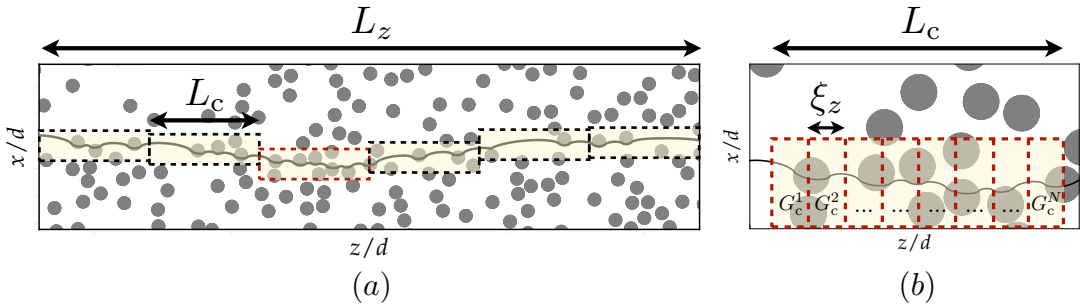

Figure 4.1: Schematic of the second Larkin hypothesis : (a) the effective toughness is inferred from the material toughness visited by a Larkin domain of length L_c (in beige) ; this domain, which contains $N = L_c/\xi_z$ inclusions, is characterized by an average toughness $\langle G_c \rangle$ and a toughness disorder $\sigma\sqrt{\xi_z/L_c}$.

In the end, the effective toughness reads :

$$G_c^{\text{eff}} = \langle G_c \rangle + \alpha \frac{\sigma^2}{\langle G_c \rangle} \frac{\xi_z}{\xi_x} \tag{4.30}$$

where α is a constant depending on the toughness distribution. It is set to $\alpha = 1$ in Démery et al. [2014b]. We notice that we find back the weak-pinning predictions $G_c^{\text{eff}} = \langle G_c \rangle$ when $\xi_x/\xi_z \to +\infty$.

Démery et al. [2014b] considered a large system size L_z so that the Larkin length is always smaller than the system size $L_z \geq L_c$. Yet it might not be the case in our numerical study as well as in the experiments. Similar reasoning, that takes into account the finite size of the system, leads to :

$$G_c^{\text{eff}} = \langle G_c \rangle + \max\left(\sigma\sqrt{\frac{\xi_z}{L_z}}, \frac{\sigma^2}{\langle G_c \rangle}\frac{\xi_z}{\xi_x}\right) \tag{4.31}$$

In the individual-pinning regime, the effective toughness is given by the maximal toughness of a defect so that Démery et al. [2014b] could only derive a lower bound for the effective toughness :

$$G_c^{\text{eff}} \geq \langle G_c \rangle + \sigma \tag{4.32}$$

Démery et al. [2014b] finally compared those theoretical formulæ to numerical results using different disorder distributions $p(G_c)$. The comparison is shown in Fig. 4.2, where K_{Ic} is considered instead of G_c. They distinguish the collective regime from the individual one via the introduction of a disorder parameter :

$$\Sigma = \frac{\sigma}{\langle G_c \rangle}\frac{\xi_z}{\xi_x} \tag{4.33}$$

If $\Sigma < 1$ the interaction between the crack and the inclusion distribution is collective. Otherwise, it is described by the individual-pinning regime.

To conclude, the theoretical reasoning of Démery et al. [2014b], inspired by the seminal work of Larkin and Ovchinnikov [1979], has been revisited within the formalism developed

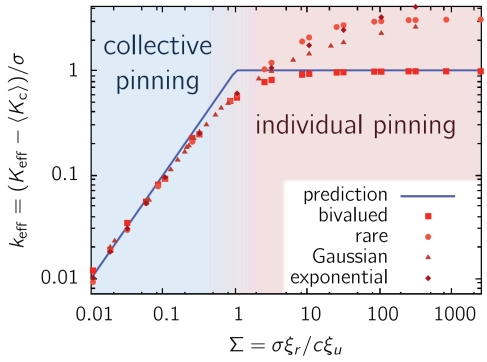

Figure 4.2: Dimensionless disorder-induced toughening $\tilde{k}_{\text{eff}}$ for different disorder distributions as a function of the disorder parameter Σ (after Démery et al. [2014b])

by Favier et al. [2006b]. It relates the effective toughness G_c^{eff} to the estimation of the Larkin length L_c, which describes the roughness of the crack front perturbations. This reasoning highlights in the disordered case the subtle relation between the macroscopic fracture properties and the crack front in-plane perturbations, a link which has been already exposed for periodical arrangements in Chapter 3. In a coplanar setting, the effective toughness G_c^{eff} can be inferred from only 4 statistical features of the local toughness distribution : its spatial average $\langle G_c \rangle$, its standard deviation σ, and its correlation lengths ξ_z and ξ_x. This approach is now used to predict the effective fracture properties of disordered systems in the coplanar case.

4.2.2 Impact of microstructural features on the coplanar effective toughness

Previous studies predicting the effective properties of disordered systems for coplanar propagation [Roux et al., 2003; Roux and Hild, 2008; Patinet et al., 2013b; Démery et al., 2014b,a] introduced microstructural disorder as a spatial toughness field G_c drawn from a statistical distribution characterized by its average $\langle G_c \rangle$, its standard deviation σ and its correlation lengths ξ_z and ξ_x respectively in the z- and x-direction. We present here a study on the effective toughness for a coplanar crack interacting with disordered arrangements of realistic inclusions. It allows to study the impact of microstructural parameters (inclusion toughness, inclusion density, inclusion shape, etc.) on the effective toughness of disordered systems. Moreover, we conduct a systematic comparison between the numerical results and the analytical predictions from Eq. (4.31) to investigate the strengths and limitations of the coplanar homogenization framework.

4.2.2.a Inclusion toughness

Problem statement

Let us first consider a composite constituted of a homogeneous matrix and tougher circular fibers of diameter d infinitely elongated and perfectly aligned in the y-direction. An half-plane crack is propagating in the (zOx) plane perpendicular to the y-direction. The inclusions have a circular shape in this plane. They are characterized by their diameter d, their density ρ_{inc} and their toughness G_c^{inc}. During the interaction with the tougher

inclusions, the crack is trapped and the macroscopic loading G^∞ has to increase to make the crack advance. The maximum loading attained during propagation defines the effective toughness of the material G_c^{eff} (see Section 3.2.2.a).

We consider large-scale systems of size $L_z \times L_x = 256d \times 256d$, containing hundreds of thousands inclusions. The inclusion density is fixed at $\rho_{\text{inc}} = 25\%$. All inclusion share the same toughness G_c^{inc}, which varies from $G_c^{\text{inc}} = G_c^{\text{mat}}$ to $G_c^{\text{inc}} = 4.5\, G_c^{\text{mat}}$ between simulations (see Section 2.2.4). We average the results on five different realizations of inclusion distribution, as it will be the case in the remainder of the manuscript. An example of inclusion distribution at varying inclusion toughness levels is plotted in Fig. 4.3. Simulations parameters are summarized in Table 8.7.

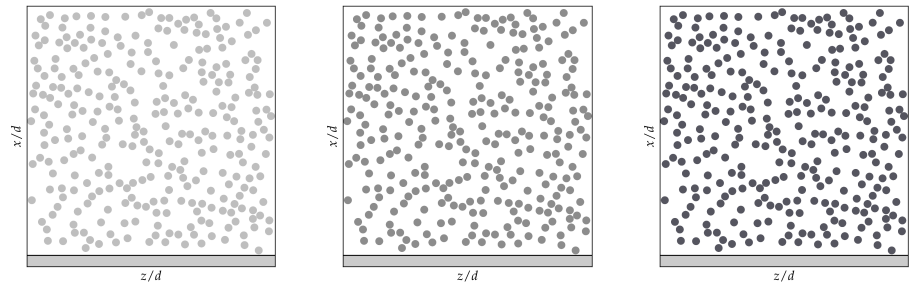

(a) $G_c^{\text{inc}} = 1.25\, G_c^{\text{mat}}$ (b) $G_c^{\text{inc}} = 2\, G_c^{\text{mat}}$ (c) $G_c^{\text{inc}} = 4\, G_c^{\text{mat}}$

Figure 4.3: Coplanar half-plane crack propagating in a disordered material constituted of spherical inclusions of varying toughness G_c^{inc} ($L_z \times L_x = 32d \times 32d$ for visualization purpose)

Numerical results and comparison to model predictions

130 simulations have been run to investigate the impact of inclusion toughness on the effective toughness. Numerical results are plotted in Fig. 4.4, where individual simulation points are displayed as cross markers.

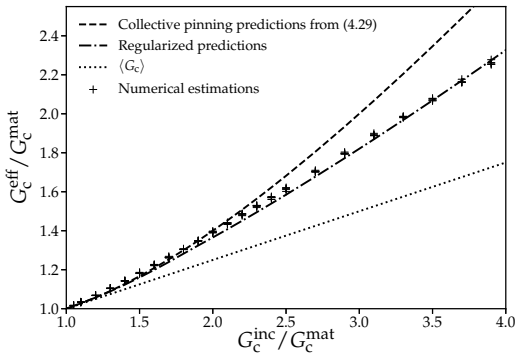

Figure 4.4: Impact of the inclusion toughness G_c^{inc} on the effective toughness G_c^{eff} : the effective toughness is predicted from Eq. (3.19) as the maximal macroscopic loading required to make propagate a coplanar crack interacting with a distribution of circular inclusions of varying toughness. Numerical results in cross markers are compared to mixture rule predictions from Eq. (3.20) in dotted line, collective pinning predictions from Eq. (4.31) in dashed line and regularized predictions from Fig. 4.2 in dash-dotted line.

First, we notice that the disorder induces an additional toughening in comparison to the periodic case so that $G_c^{\text{eff}} \geq \langle G_c \rangle$. In contrast with elastic properties, the results on the

effective fracture properties derived from the homogenization of periodic media do not allow for a quantitative prediction of the effective toughness. Second, the effective toughness does not increase linearly with the inclusion toughness. Indeed in the case of circular inclusions of diameter d and toughness G_c^{inc} leading to a toughness contrast $c_{inc} = \frac{G_c^{inc} - G_c^{mat}}{G_c^{mat}}$, and density ρ_{inc}, one gets :

$$\begin{cases} \langle G_c \rangle = G_c^{mat} \left(1 + \rho_{inc} c_{inc}\right) \\ \sigma = G_c^{mat} \sqrt{\rho_{inc} \left(1 - \rho_{inc}\right)}\, c_{inc} \\ \xi_z = \xi_x = d \end{cases} \tag{4.34}$$

In the case of isotropic distribution of circular inclusions, one obtains $\xi_z/\xi_x = 1$[1]. It finally gives :

$$\begin{cases} G_c^{eff} = G_c^{mat} \left(1 + \left[\rho_{inc} + \sqrt{\rho_{inc}\left(1-\rho_{inc}\right)}\sqrt{\dfrac{\xi_z}{L_z}}\right] c_{inc}\right), \text{ if } L_c > L_z \\ G_c^{eff} = G_c^{mat} \left(1 + \rho_{inc} c_{inc} + \dfrac{\rho_{inc}\left(1-\rho_{inc}\right) c_{inc}^2}{1 + \rho_{inc} c_{inc}}\right), \text{ if } \xi_z \leq L_c \leq L_z \\ G_c^{eff} \geq G_c^{mat} \left(1 + \left[\rho_{inc} + \sqrt{\rho_{inc}\left(1-\rho_{inc}\right)}\right] c_{inc}\right), \text{ if } L_c < \xi_z \end{cases} \tag{4.35}$$

Fig. 4.5.a shows the evolution of the Larkin length L_c measured in our simulations from Eq. (4.27) and compared to theoretical predictions of Eq. (4.28) for $\gamma = 1$. We see that up to a pre-factor γ the evolution of the Larkin length follows the theoretical predictions of Eq. (4.28).

If we come back to the effective toughness variations, at a very low inclusion toughness $G_c^{inc}/G_c^{mat} \leq 1.2$ the system size is smaller than the Larkin length, $L_z < L_c$, and the effective toughness increases linearly with the inclusion toughness contrast. The linearity loss is typical of the collective regime, which characterizes most of our simulations. Yet as shown in Fig. 4.4, Eq. (4.31) does not fully capture the effective toughness resulting from our coplanar simulations. This is explained by the fact that the material disorder parameter Σ introduced by Démery et al. [2014b] is in the range between $0.1 - 1$ in our simulations as shown in Fig. 4.5.b. In this range, the effective toughness is not accurately predicted by Eq. (4.31). As a result, the effect of the soft cross-over between the collective and the individual regime displayed in Fig. 4.2 has to be taken into account.

If we model this cross-over by interpolating the data of Démery et al. [2014b], the comparison between numerical results and theoretical predictions becomes much more satisfactory (dash-dotted lines in Fig. 4.4). It constitutes a numerical validation of the theoretical model presented in Section 4.2.1. Improvements would consist in modeling in detail the cross-over between the collective-pinning regime and the individual-pinning one since propagation often happens in this cross-over regime. But for the remaining part of the manuscript, the

[1] ξ_z and ξ_x are not *per se* the correlation lengths of our microstructure. In the case of non-overlapping disks, Torquato [2002] notes that exclusion (hard-core) effects induce oscillations on the correlation function, which make the precise definition of the correlation length difficult.

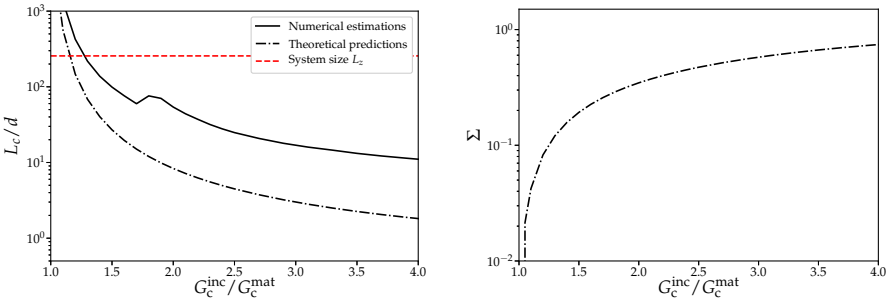

(a) (b)

Figure 4.5: Impact of the inclusion toughness G_c^{inc} on the Larkin length L_c (a) and disorder parameter Σ (b) for the crack trapping mechanism : the Larkin length is estimated from the in-plane roughness with Eq. (4.27) and compared to theoretical predictions from Eq. (4.28) in dash-dotted lines. The disorder parameter Σ is computed analytically from Eq. (4.33).

cross-over is modeled by a numerical interpolation of the results presented in Démery et al. [2014b].

Convergence study

We now investigate how sensitive are our results on the effective toughness with the mesh size Δz of the crack front. We saw in Section 8.C that Δz had a large impact on the numerical performances of our model. It is thus mandatory to explore the impact of Δz on the effective toughness to reach a reasonable compromise between numerical accuracy and computational performances. We consider various mesh sizes ranging from $\Delta z/d = 4$ (four points by inclusions in average) to $\Delta z/d = 32$ (thirty-two points by inclusions in average). Simulation parameters are summarized in Table 8.7. Results of the 200 simulations are plotted in Fig. 4.6.

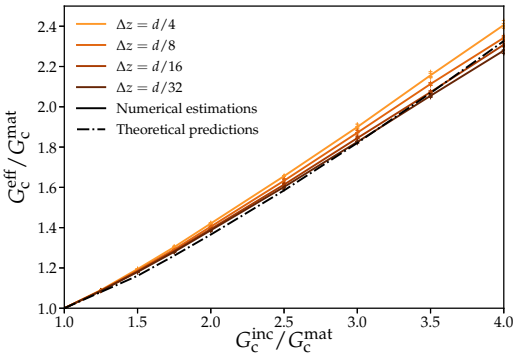

Figure 4.6: Impact of the front discretization step Δz on the effective toughness G_c^{eff} : the effective toughness is predicted from Eq. (3.19) s the maximal macroscopic loading required to make propagate a coplanar crack interacting with a distribution of circular inclusions of varying toughness. Numerical results in solid line are compared to regularized predictions from Fig. 4.2 in black dashed line.

We see that the effective toughness is overestimated for large mesh size. As illustrated in Fig. 4.7, a coarse mesh leads to an overestimation of both the inclusion size and its area, subsequently leading to an overestimation on $\langle G_c \rangle$ and an error on the effective toughness as

predicted by Eq. (4.30). In the following, we take a mesh size $\Delta z = d/16$ which constitutes a satisfying compromise between a fine modeling of the microstructure and reasonable numerical performances.

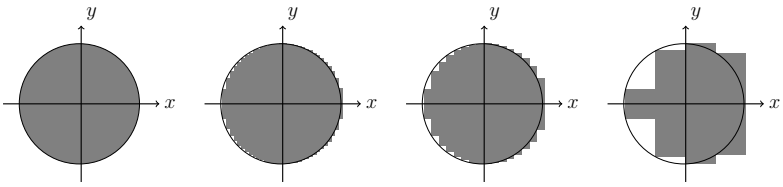

(a) Real geometry (b) $\Delta z = d/32$ (c) $\Delta z = d/16$ (d) $\Delta z = d/4$

Figure 4.7: Impact of the discretization step on the geometrical modeling of a circular inclusion : real geometry (a), fine mesh (b-c), coarse mesh (d)

4.2.2.b System size

Problem statement

The inclusion toughness plays a decisive role on the determination of the effective toughness since it dictates the propagation regime (collective or individual). Yet, if the crack is propagating in the collective regime, the system size may play a role on the estimation of the effective toughness as predicted by Eq. (4.31). We consider an inclusion distribution with $G_c^{\text{inc}} = 1.5\, G_c^{\text{mat}}$ and a density $\rho_{\text{inc}} = 25\%$ to set the Larkin length to $L_c \simeq 74\, d$ (see Fig. 4.5). It allows us to explore the impact of the system size L_z several order of magnitude below and above the Larkin length L_c. We thus consider systems whose size is ranging from $L_z = 8\, d$ up to $L_z = 4096\, d$. The size in the x-direction is fixed at $L_x = 384\, d$ to allow small-scale systems to visit enough blocking configurations and have a better estimate of the effective toughness [Kolton et al., 2013]. An example of inclusion distribution for various system sizes is showed in Fig. 4.8. Simulations parameters are summarized in Table 8.8.

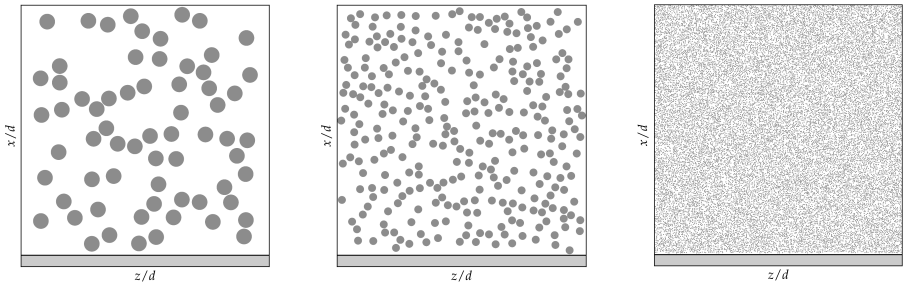

(a) $L_z = 16\, d$ (b) $L_z = 64\, d$ (c) $L_z = 256\, d$

Figure 4.8: Coplanar half-plane crack propagating in a disordered material with varying size L_z, period of our system

Numerical results and comparison to model predictions

Results of the 100 simulations run for the study are plotted in Fig. 4.9. The Larkin length $L_c \simeq 74\, d$ is calculated from the in-plane roughness of large-scale systems $L_z = 4096\, d$ with Eq. (4.27) As predicted from Eq. (4.31), the effective toughness G_c^{eff} does not depend on the system size when the system size is far larger than the Larkin length $L_z \gg L_c$. Yet as

soon as the system size is of the order of the Larkin length, the effective fracture properties increase when the system size decreases.

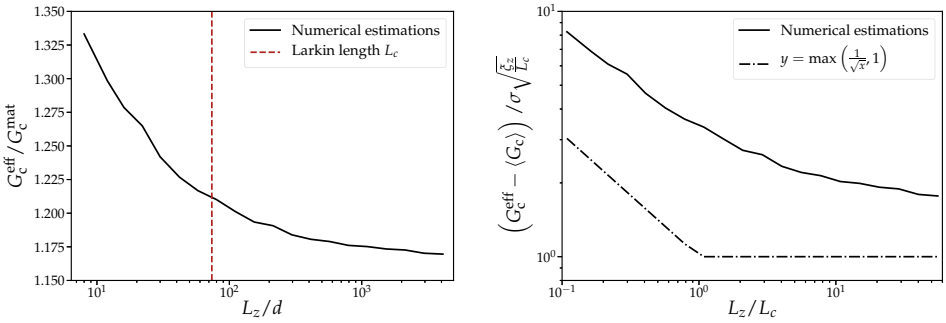

(a) (b)

Figure 4.9: (a) Impact of the system size L_z on the effective toughness G_c^{eff} for the crack trapping mechanism : the effective toughness is predicted from Eq. (3.19) as the maximal macroscopic loading required to make propagate a coplanar crack interacting by a crossing mechanism with a distribution of circular inclusions of toughness. (b) The effective toughness is normalized following Eq. (4.36) to highlight the influence of the system size.

Quantitative comparison can be inferred from Eq. (4.31). Indeed, the effective toughness can be renormalized in such way :

$$\frac{G_c^{\text{eff}} - \langle G_c \rangle}{\sigma\sqrt{\frac{\xi_z}{L_c}}} = \max\left(\sqrt{\frac{L_c}{L_z}}, 1\right) \tag{4.36}$$

We see in Fig. 4.36.b that Eq. (4.36) is verified up to a pre-factor 2, which presence has been explained by the disorder geometry in Section 4.2.1.c. In particular, the normalized effective toughness actually displays a dependence in $\sqrt{\frac{L_c}{L_z}}$ when $L_z \leq L_c$. The presence of both a pre-factor and a soft transition between the two regimes $L_z \ll L_c$ and $L_z \gg L_c$ is nonetheless likely to induce errors in theoretical predictions of the effective toughness for $L_z \sim L_c$, i.e. when the inclusion toughness or the inclusion density is low. Overall, we note that Larkin's approximations, on which the effective toughness predictions are based, do not take into account the size of the system, and the statistical size effects associated with it.

4.2.2.c Inclusion density

Problem statement

The system size is now set at $L_z \times L_x = 256d \times 256d$ for the remaining coplanar studies. We now explore the impact of the inclusion density on the effective toughness. We consider circular inclusion distributions whose densities are ranging from $\rho_{\text{inc}} = 0.1$ to $\rho_{\text{inc}} = 0.4$ for various inclusion toughnesses. An example of inclusion distribution at varying density levels are shown in Fig. 4.10. Simulations parameters are summarized in Table 8.9.

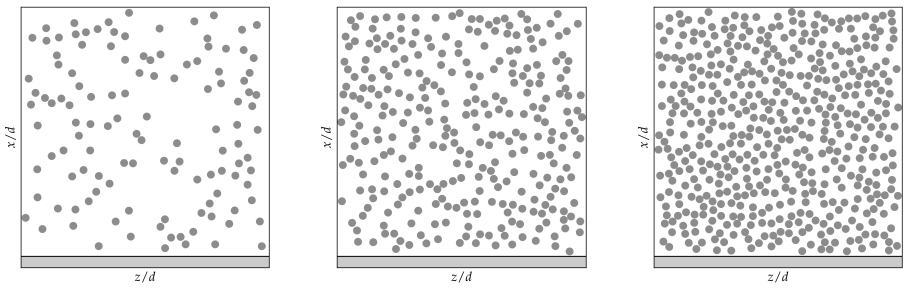

(a) $\rho_{\text{inc}} = 0.1$ (b) $\rho_{\text{inc}} = 0.25$ (c) $\rho_{\text{inc}} = 0.4$

Figure 4.10: Coplanar half-plane crack propagating in a disordered material with varying inclusion density ρ_{inc} ($L_z \times L_x = 32d \times 32d$ for visualization purpose)

Numerical results and comparison to model predictions

Results of the 260 simulations run for the study are plotted in Fig. 4.11. Averaged numerical results are plotted in solid line and individual simulation points are represented as cross markers. Theoretical results are plotted in dash-dotted line. Finally, the inclusion density level is pictured in orange to dark red levels.

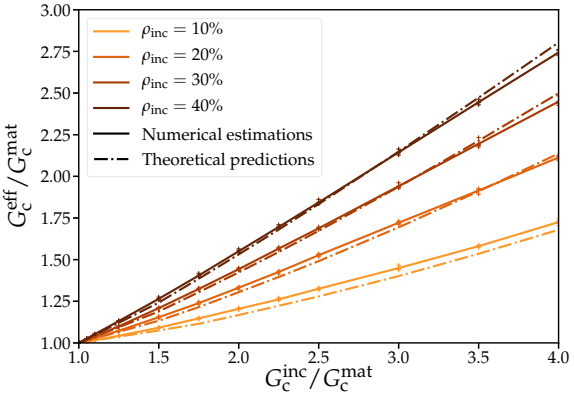

Figure 4.11: Impact of the inclusion density ρ_{inc} on the effective toughness G_c^{eff} : the effective toughness is predicted from Eq. (3.19) as the maximal macroscopic loading required to make propagate a coplanar crack interacting with a distribution of circular inclusions of varying toughness at various density levels. Numerical results (in solid lines) are compared to regularized predictions from Fig. 4.2 (in dashed lines).

We see that the denser the distribution, the higher the effective toughness. Moreover, the theoretical predictions match fairly well the numerical results both qualitatively and quantitatively. Discrepancies are found at small inclusion density $\rho_{\text{inc}} = 0.1$, since the

Larkin length L_c is bigger than the system size L_z (see Section 4.2.2.b). The comparison remains otherwise satisfactory.

4.2.2.d Toughness disorder

Problem statement

Up to now, all the inclusions within the composite shared the same inclusion toughness. We now consider cases where the inclusion toughness varies from an inclusion to the other. Inclusions are characterized by their toughness G_c^{inc} or alternatively their toughness contrast with respect to the matrix $c_{\text{inc}} = \frac{G_c^{\text{inc}} - G_c^{\text{mat}}}{G_c^{\text{mat}}}$. We take here a polydisperse contrast distribution c_{inc} characterized by its mean value $\langle c \rangle$ and its standard deviation $\sigma\left(c_{\text{inc}}\right)$. We define $\tilde{\sigma}$, our contrast disorder parameter, as :

$$\tilde{\sigma} = \frac{\sigma\left(c_{\text{inc}}\right)}{\langle c_{\text{inc}} \rangle} \tag{4.37}$$

We assume that the toughness contrast of the inclusion follows a log-normal distribution characterized by the parameters (μ_c, σ_c). Its probability density function can be expressed as :

$$f\left(c_{\text{inc}}\right) = \frac{1}{c_{\text{inc}} \sigma_c \sqrt{2}} \exp\left[-\frac{\left(\ln(c_{\text{inc}}) - \mu_c\right)^2}{2\sigma_c^2} \right] \tag{4.38}$$

(μ_c, σ_c) are linked to $\langle c \rangle$ and $\tilde{\sigma}$ through the following relationships :

$$\begin{cases} \langle c \rangle = e^{\mu_c + \frac{\sigma_c^2}{2}} \\ \tilde{\sigma} = e^{\sigma_c^2} - 1 \end{cases} \Leftrightarrow \begin{cases} \mu_c = \ln\langle c \rangle - \dfrac{1}{2}\ln\left(1 + \tilde{\sigma}^2\right) \\ \sigma_c^2 = \ln\left(1 + \tilde{\sigma}^2\right) \end{cases} \tag{4.39}$$

Examples of c_{inc} distribution for various $\tilde{\sigma}$ are given in Fig. 4.12.

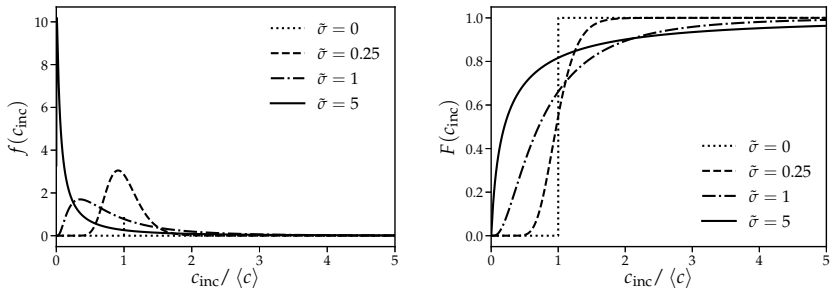

(a) Probability density (b) Cumulative distribution

Figure 4.12: Probability density function f (a) and cumulative distribution F (b) of the inclusion toughness for various contrast disorder $\tilde{\sigma}$

In order to study the impact of the contrast disorder parameter $\tilde{\sigma}$ in our simulations, we consider circular inclusion distributions with $\tilde{\sigma}$ ranging from $\tilde{\sigma} = 0$ (monodisperse) to $\tilde{\sigma} = 5$ (highly polydisperse) for various inclusion toughnesses. The inclusion density is fixed at $\rho_{\text{inc}} = 25\%$. Examples of inclusion distribution at varying toughness disorder levels are shown in Fig. 4.13. Simulations parameters are summarized in Table 8.10.

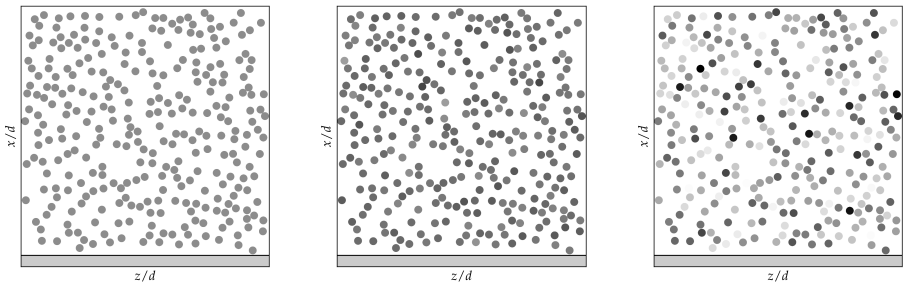

(a) $\tilde{\sigma} = 0$ (b) $\tilde{\sigma} = 1$ (c) $\tilde{\sigma} = 5$

Figure 4.13: Coplanar half-plane crack propagating in a disordered material with the same average toughness contrast $\langle c_{\text{inc}} \rangle$ but varying inclusion from inclusion leading with a disorder parameter $\tilde{\sigma}$ ($L_z \times L_x = 32d \times 32d$ for visualization purpose)

Numerical results and comparison to model predictions

Results of the 540 simulations run for the study are summarized in Fig. 4.11 where the evolution of the effective toughness is shown as a function of the mean inclusion toughness. The disorder level is pictured in orange to dark red levels.

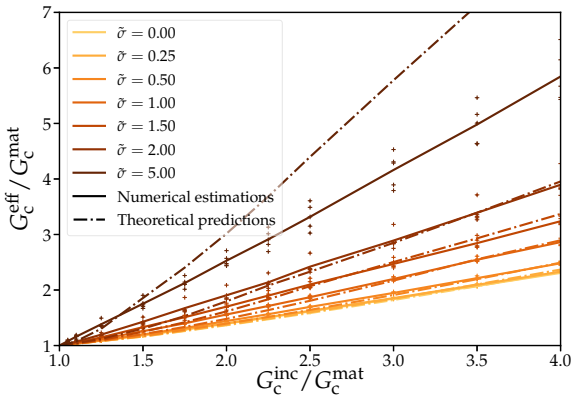

Figure 4.14: Impact of the toughness disorder $\tilde{\sigma}$ on the effective toughness G_c^{eff} : the effective toughness is predicted from Eq. (3.19) as the maximal macroscopic loading required to make propagate a coplanar crack interacting with a distribution of circular inclusions with a varying average toughness at various toughness disorder levels. Numerical results (in solid lines) are compared to regularized predictions from Fig. 4.2 (in dashed lines).

We see that the toughness disorder has an important effect on the effective toughness of heterogeneous materials. Even if the inclusion distribution has the same average toughness $\left\langle G_c^{\text{inc}} \right\rangle$, an increase in the toughness disorder $\tilde{\sigma}$ leads to an increase of toughening by a factor 3-4. In the presence of toughness disorder, Eq. (4.35) becomes :

$$\begin{cases} G_c^{\text{eff}} = G_c^{\text{mat}} \left(1 + \left[\rho_{\text{inc}} + \sqrt{\rho_{\text{inc}} \left(1 + \tilde{\sigma}^2 - \rho_{\text{inc}} \right)} \sqrt{\dfrac{\xi_z}{L_z}} \right] c_{\text{inc}} \right), \text{ if } L_c > L_z \\ G_c^{\text{eff}} = G_c^{\text{mat}} \left(1 + \rho_{\text{inc}} c_{\text{inc}} + \dfrac{\rho_{\text{inc}} \left(1 + \tilde{\sigma}^2 - \rho_{\text{inc}} \right) c_{\text{inc}}^2}{1 + \rho_{\text{inc}} c_{\text{inc}}} \right), \text{ if } \xi_z \leq L_c \leq L_z \\ G_c^{\text{eff}} \geq G_c^{\text{mat}} \left(1 + \left[\rho_{\text{inc}} + \sqrt{\rho_{\text{inc}} \left(1 - + \tilde{\sigma}^2 \rho_{\text{inc}} \right)} \right] c_{\text{inc}} \right), \text{ if } L_c < \xi_z \end{cases} \tag{4.40}$$

We notice that the theoretical predictions match quantitatively the numerical results at a low disorder level. Yet for $\tilde{\sigma} = 5$, the results are only qualitative and no more quantitative. It is explained by the fact that such a large level of disorder $\sigma = \sqrt{\rho_{\text{inc}}\,(1 + \tilde{\sigma}^2 - \rho_{\text{inc}})}$ makes the Larkin length L_c decrease below the inclusion size d in Eq. (4.28). The propagation shifts in the *individual-pinning* regime, where the effective toughness can no more be quantitatively predicted by our collective pinning based approach.

4.2.2.e Inclusion shape

Problem statement

In the case of the interaction between a coplanar crack and periodic arrangements of tougher inclusions, the inclusion shape has been shown to strongly influence the effective toughness. Yet, circular and square inclusions have been shown to induce the same toughening. We here investigate if those observations survive in presence of disorder.

We then consider square inclusions whose densities are ranging from $\rho_{\text{inc}} = 0.1$ to $\rho_{\text{inc}} = 0.3$ for a varying inclusion toughness $G_{\text{c}}^{\text{inc}}/G_{\text{c}}^{\text{mat}} \in [1, 4]$. An example of square inclusion distribution is given in Fig. 4.15. Simulations parameters are summarized in Table 8.9.

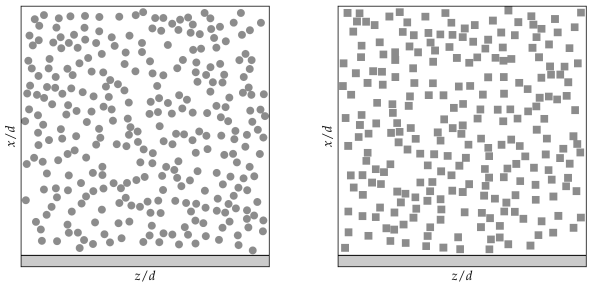

(a) Circular inclusion (b) Square inclusion

Figure 4.15: Coplanar half-plane crack propagating in a disordered material with various inclusion shape ($L_z \times L_x = 32d \times 32d$ for visualization purpose)

Numerical results and comparison to model predictions

Results of the 180 simulations are plotted in Fig. 4.16. In Fig. 4.16.a, we compare the numerical results for square inclusions to the one found for circular inclusions. We see that, as in the periodic case, the square and circular inclusions toughen the material identically. It is explained by the fact that the effective toughness is only influenced by the inclusion shape through the correlation length ratio ξ_z/ξ_x, which is identical for square and circular inclusions. It is thus no wonder that theoretical predictions, which were quantitatively correct for circular inclusions, describe well the case of square inclusions as it is shown in Fig. 4.16.b.

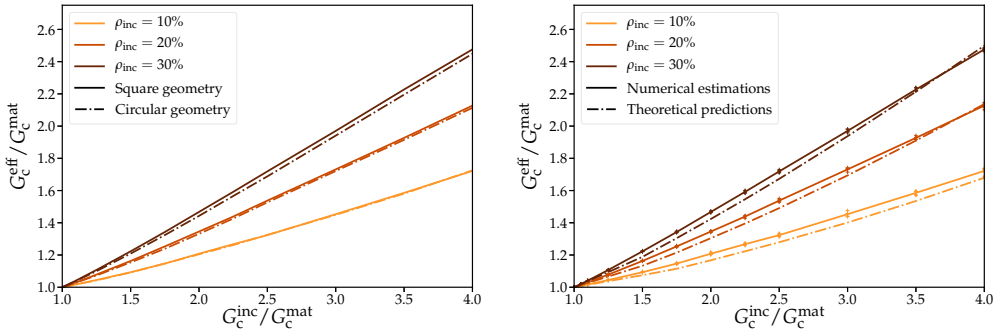

(a) (b)

Figure 4.16: Impact of the inclusion shape on the effective toughness G_c^{eff} : the effective toughness is predicted from Eq. (3.19) as the maximal macroscopic loading required to make propagate a coplanar crack interacting with a distribution of square inclusions. Numerical results are compared to the ones of circular inclusions (a) and to regularized predictions for square inclusions from Fig. 4.2 (b).

4.2.2.f Inclusion elongation

Problem statement

In the periodic case, irregular processes in inclusion crossing lowered the effective toughness of periodical arrangements of tougher elliptic inclusions (Fig. 3.12). To close this study on the effective toughness for coplanar crack propagation, we propose to revisit the case of the elliptic inclusions elongated in the z-direction, in a disordered setting.

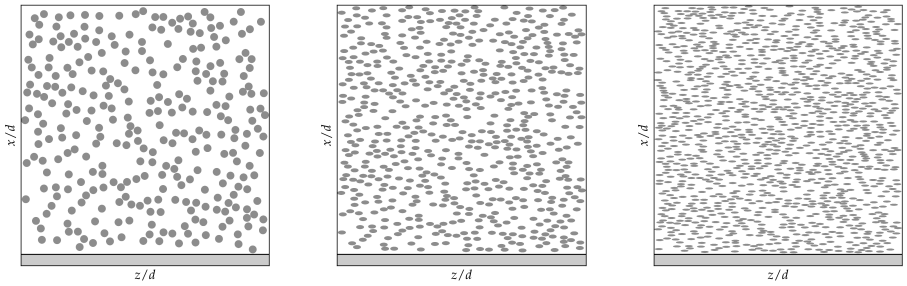

(a) $d_z = d_x$ (b) $d_z = 2d_x$ (c) $d_z = 4\,d_x$

Figure 4.17: Coplanar half-plane crack propagating in a disordered material with various inclusion elongation in the z-direction ($L_z \times L_x = 32d \times 32d$ for visualization purpose)

We thus consider distributions of elliptic inclusions elongated in the z-direction, with an elongation ranging from $d_z = d_x$ to $d_z = 4\,d_x$ at varying inclusion toughness levels $G_c^{\text{inc}}/G_c^{\text{mat}} \in [1, 4]$. The inclusion density is fixed at $\rho_{\text{inc}} = 25\%$. Examples of inclusion distribution for various elongation ratios are plotted in Fig. 4.17. Simulations parameters are summarized in Table 8.11.

Numerical results and comparison to model predictions

The results on the effective toughness of the 240 simulations required for the study are plotted in Fig. 4.18 along with the associated disorder parameter Σ. Theoretical predictions on the effective toughness are superposed in dash-dotted line.

If no discrepancy was observed in the case of square inclusions, the results are here striking. The introduction of elongated inclusions does not decrease the effective toughness but rather increases it. What was a weakness in the periodic case constitutes a strength as soon as disorder is introduced. The more elongated the inclusion in the z-direction, the greater the effective toughness. This trend is predicted by the theoretical model since the effective toughness increase linearly with the correlation length ratio ξ_z/ξ_x in the collective regime (see Eq. (4.30)). Theoretical predictions are in accordance with the numerical results for $d_z = d_x$ and $d_z = 2\,d_x$ but not for $d_z = 4\,d_x$. It is explained in Fig. 4.18.b by the fact that the crack is propagating in the individual-pinning regime ($L_c < d$), where theoretical predictions are no more quantitative.

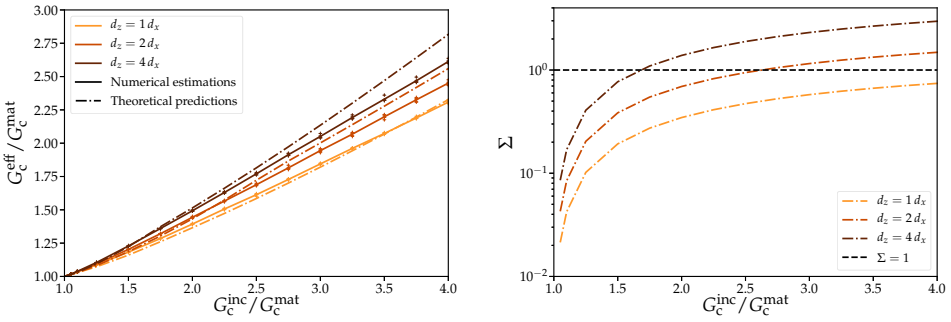

(a) (b)

Figure 4.18: Impact of the inclusion elongation d_z/d_x on the effective toughness G_c^{eff} (a) and and disorder parameter Σ (b) : the effective toughness is predicted from Eq. (3.19) as the maximal macroscopic loading required to make propagate a coplanar crack interacting with a distribution of elliptical inclusions. Numerical results are compared to regularized predictions from Fig. 4.2 in dashed lines.

To conclude, the theoretical model of Démery et al. [2014b] revisited in Section 4.2.1 has been successfully confronted to the results of numerical simulations of coplanar crack propagation in disordered systems displaying toughness discontinuities of varying properties and shapes. It stresses out that, in brittle fracture, the periodic case is not representative at all of the disordered one when it comes to homogenizing fracture properties. Moreover, theoretical approaches adapted from statistical physics allows to tackle the difficult question of the homogenization of brittle fracture properties. A correct description of the cross-over between the collective ($\xi_z < L_c < L_z$) and the individual-pinning regime ($L_c < \xi_z$) is nonetheless required to produce quantitative predictions on the effective toughness within the range of parameters considered in our studies. In the same manner, an accurate description of the cross-over between the collective and the finite system size regime ($L_c > L_z$) would produce better predictions at a low toughness contrast between the matrix and the inclusion or a low inclusion density. Moreover, when the crack enters the individual-pinning regime, the predictions are no more quantitative as it can be the case for large toughness disorder $\tilde{\sigma}$ or large elongation ratio ξ_z/ξ_x. These current limitations constitute future challenges in statistical physics of fracture.

The coplanar situation being explored, it is now time to investigate the impact of out-of-plane excursions of the crack front on the effective toughness of disordered materials.

4.3 Effective toughness for three-dimensional propagation in heterogeneous brittle materials

4.3.1 Questioning the definition of effective toughness

Up to now, the effective toughness has been defined in Chapter 3 as the maximal ERR imposed by the macroscopic loading. This definition takes advantage of the fact that a homogenized material property, the effective toughness, can be estimated from the evolution of a structural problem, as it is stated by Griffith's criterion. If such an approach provides a unique perspective to tackle the difficult problem of homogenizing brittle fracture properties, one can wonder if the resulting effective fracture properties can be decoupled from the structural problem and *in fine* can be intrinsic to the considered composite. In this section, we question the possible definitions of the effective fracture properties and stress out the conditions under which an *intrinsic* effective toughness can be defined.

4.3.1.a The effective toughness : three possible definitions for a single material property

Hossain et al. [2014] considered three possible definitions for the *effective toughness* G_c^{eff}:

1. the *maximum energy release rate* imposed by the loading during crack propagation G^{∞}_{max}, selected by Hossain et al. [2014] and Brach et al. [2019a] in two-dimensional phase-field simulations of the interaction of a crack with elastic and toughness heterogeneities. The loading has to be increased up to G^{∞}_{max} to break the whole specimen;

2. the *average energy release rate* imposed by the loading during crack propagation G^{∞}_{mean}, adopted by Patinet et al. [2013b] in numerical simulations of three-dimensional coplanar crack propagation of disordered systems and Li and Zhou [2013a] in cohesive zone model simulations of two-dimensional crack propagation in composite ceramics. It quantifies loading levels G^{∞}_{mean} at which crack propagation occurs, without necessarily leading to total failure of the structure;

3. the *effective fracture energy* $\left\langle G_c^{\text{frac}} \right\rangle$ defined as the average energy dissipated on a unitary surface during crack propagation.

Crack propagation in disordered materials has been proved to be highly intermittent [Bonamy et al., 2008; Bonamy, 2009; Barès et al., 2014]. This intermittency can be noticed in Fig. 4.19.a that provides the evolution of the macroscopic ERR G^{∞} imposed by the loading during crack propagation. This evolution is characterized by two phases : pinning ones, where the crack does not progress and the macroscopic loading increases, separated by phases of sudden propagation where the loading decreases at a rate $\frac{\partial G^{\infty}}{\partial x} = -\frac{G_0}{\mathcal{L}}$ (see Eq. (2.6)). During the phases of sudden propagation, the crack visits multiple pinning configurations, which might not be strong enough to pin the crack front for a given macroscopic loading $G^{\infty}(x)$. As shown by Roux and Hild [2008], these peculiar dynamics lead to a Gaussian probability density function for $G^{\infty}(x)$ centered in G^{∞}_{mean}, as we also observe in our numerical simulations (see Fig. 4.21.a). Note that this Gaussian behavior allows for a proper definition of the *maximum energy release rate* G^{∞}_{max}.

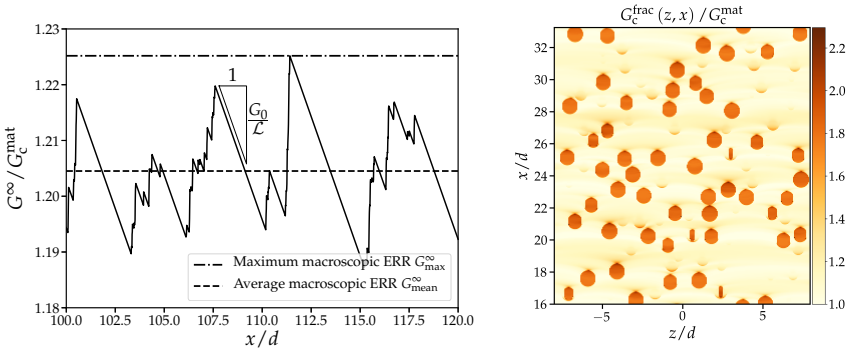

(a) (b)

Figure 4.19: Definitions of the effective toughness : G^∞_{mean} (in dashed line) and G^∞_{max} (in dash-dotted line) defined respectively as the average and the maximum of the macroscopic ERR G^∞ imposed by the tensile loading during crack propagation (a). $\langle G_c^{\text{frac}} \rangle$ defined as the spatial average of the fracture energy $G_c^{\text{frac}}(z,x)$ dissipated during crack propagation (b)

Our numerical method allows us to track the energy dissipated locally by the fracture process. Local maps of dissipated fracture energy $G_c^{\text{frac}}(z,x)$ can be computed from the following procedure. As pictured in Fig. 4.20, we can discretize the heterogeneous medium on a grid in the (zOx) plane of cell size $\Delta\ell$. For a grid cell located in (x_i, z_j), we denote t_{in} and t_{out} the time at which the crack front enters and exits the cell (Fig. 4.20.a). The energy dissipated by fracture during propagation reads :

$$E^{\text{frac}}_{i,j} = \int_{t_{\text{in}}}^{t_{\text{out}}} \int_{z_j-\Delta\ell/2}^{z_j+\Delta\ell/2} G(z,t)\, v(z,t)\, dz\, dt \tag{4.41}$$

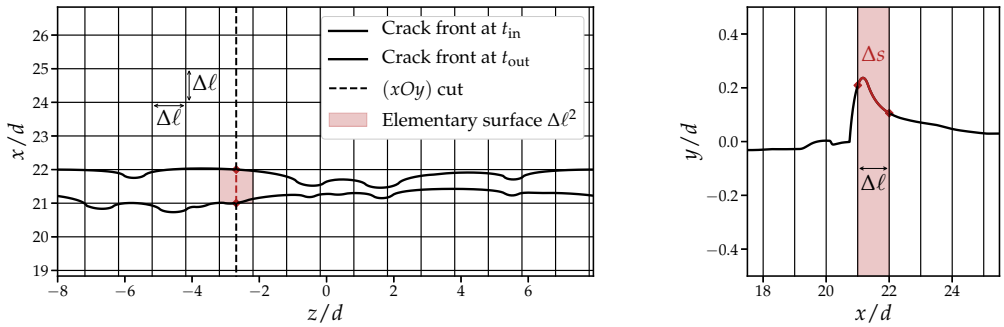

(a) (zOx) plane (b) (xOy) plane

Figure 4.20: Effective fracture energy, defined as the dissipated energy per unit surface required to crack an elementary surface in the (zOx) plane (a) taking into account the out-of-plane excursions (b)

We have to normalize this dissipated energy by the cracked surface area. Due to out-of-plane excursions of the crack front, a crack does not propagate along a distance $\Delta\ell$ but along a distance Δs in the propagation direction (see Fig. 4.43.b), which reads :

$$\Delta s(z) = \int_{t_{\text{in}}}^{t_{\text{out}}} v(z,t)\, dt \tag{4.42}$$

We normalize the local dissipated energy $E^{\text{frac}}_{i,j}$ by $\Delta\ell^2$ rather than $\Delta\ell \cdot \Delta s$ to take into account the crack tortuosity. The local fracture energy finally reads :

$$\left[G_{\text{c}}^{\text{frac}}\right]_{i,j} = \frac{E^{\text{frac}}_{i,j}}{\Delta\ell^2} = \frac{1}{\Delta\ell^2}\int_{t_{\text{in}}}^{t_{\text{out}}}\int_{z_j-\Delta\ell/2}^{z_j+\Delta\ell/2} G\left(z,t\right) v\left(z,t\right) dz\, dt \tag{4.43}$$

It allows us to construct local maps of dissipated fracture energy $G_{\text{c}}^{\text{frac}}\left(z,x\right)$ as pictured in Fig. 4.19.b. Circular domains are characteristic of inclusion crossing, while moon shaped patterns can be attributed to by-pass events. Larger fracture energy patterns are associated with kinetic effects evidenced during the relaxation of the crack front perturbation out of a defect by [Chopin et al., 2018] (see Section 3.2.1.b). The probability density function of $G_{\text{c}}^{\text{frac}}$, which is plotted in Fig. 4.21.b, shows a behavior markedly different from the one of the macroscopic loading G^{∞} plotted in Fig. 4.21.a. We can notice two peaks, one located around the matrix toughness $G_{\text{c}}^{\text{mat}}$ and another one around the inclusion toughness $G_{\text{c}}^{\text{inc}}$. Those two peaks are surrounded by two regimes corresponding to the relaxation of the crack front perturbation out-of the defects. Yet, we observe that the *effective fracture energy* $\left\langle G_{\text{c}}^{\text{frac}}\right\rangle$, defined as the spatial average of $G_{\text{c}}^{\text{frac}}\left(z,x\right)$, is nonetheless equal to the *average energy release rate* G^{∞}_{mean}. It comes from the fact that a composite made of multiple Griffith's materials is a Griffith's material [Dal Maso and Toader, 2002; Giacomini and Ponsiglione, 2006; Cagnetti et al., 2019], a property that ultimately enforces the equality $\left\langle G_{\text{c}}^{\text{frac}}\right\rangle = G^{\infty}_{\text{mean}}$.

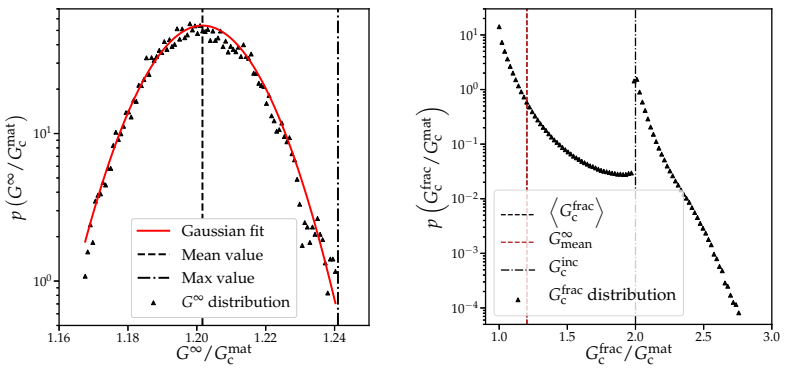

(a) (b)

Figure 4.21: Probability density function of the macroscopic loading (a) and of the effective fracture energy (b) for a crack interacting with a large-scale disordered distribution of tougher inclusions of density $\rho_{\text{inc}} = 25\%$ and toughness $G_{\text{c}}^{\text{inc}} = 2\,G_{\text{c}}^{\text{mat}}$.

If $\left\langle G_{\text{c}}^{\text{frac}}\right\rangle$ and G^{∞}_{mean} are equal, they do not always coincide with the *maximum energy release rate* G^{∞}_{max}. In particular, the discrepancy between the *average energy release rate* G^{∞}_{mean} and the *maximum energy release rate* G^{∞}_{max} seems to strongly depend on the structural length $\mathcal{L}$ that controls the evolution of G^{∞} (see Fig. 4.19) and consequently the respective values of G^{∞}_{mean} and G^{∞}_{max}.

4.3.1.b Towards a unified value of the effective toughness : the decisive impact of the loading conditions

Problem statement

In this section, we investigate the impact of the structural length $\mathcal{L}$ on the *maximum energy release rate* $G^{\infty}_{\max}$, the *average energy release rate* G^{∞}_{mean} and the *effective fracture energy* $\langle G_c^{\text{frac}} \rangle$ to determine the conditions under which a single *intrinsic* value for the effective toughness G_c^{eff} can be measured by decoupling the material problem related to G_c^{eff} from the structural one related to G^{∞}.

We run numerical simulations on large-scale disordered systems of size $L_z \times L_x \times L_y = 256d \times 288d \times 16d$ containing hundreds of thousands inclusions. We consider a distribution of monodisperse spherical inclusions of diameter d at an inclusion density $\rho_{\text{inc}} = 25\%$ for three different inclusion toughness levels : $G_c^{\text{inc}} = 1.5\, G_c^{\text{mat}}$, $G_c^{\text{inc}} = 2\, G_c^{\text{mat}}$ to $G_c^{\text{inc}} = 3\, G_c^{\text{mat}}$. The interface toughness is taken equal to the one of the matrix $G_c^{\text{int}} = G_c^{\text{mat}}$. Finally, the structural length $\mathcal{L}$, characteristic of the loading variations, is varying from $10^{-1}\, d$ to $10^{6}\, d$. Simulation parameters are summarized in Table 8.12.

Impact of the structural length $\mathcal{L}$ on $G^{\infty}_{\max}$, G^{∞}_{mean} and $\langle G_c^{\text{frac}} \rangle$

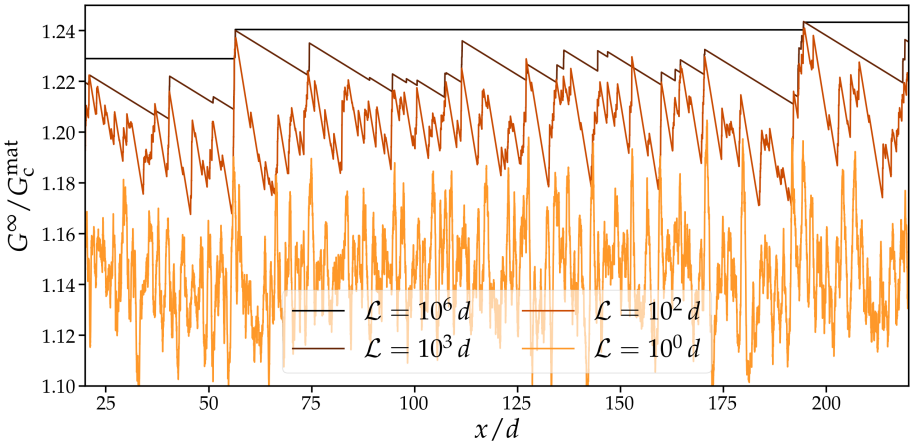

Figure 4.22: Impact of the structural length $\mathcal{L}$ on the evolution of the macroscopic ERR G^{∞} during crack propagation : the crack is interacting through crossing and by-pass mechanisms with a distribution of tougher inclusions of density $\rho_{\text{inc}} = 25\%$ and toughness $G_c^{\text{inc}} = 2\, G_c^{\text{mat}}$.

We plot the evolution of the macroscopic ERR G^{∞} imposed by the loading for various structural length values $\mathcal{L}$ in Fig. 4.22. The larger the structural length $\mathcal{L}$, the lower the G^{∞} decrease when the crack is propagating (see Fig. 4.19.a). Thus, a large structural length $\mathcal{L} \simeq 10^6\, d$ induces a screening of almost all the subsequent stable pinning configurations. The macroscopic ERR probability density function is almost reduced to a Dirac function (Fig. 4.23.a) and G^{∞}_{mean} coincides with $G^{\infty}_{\max}$. For an intermediate structural length $\mathcal{L} \simeq 10^2\, d$, the crack visits more numerous pinning configurations due to the rapid decrease of G^{∞} during crack propagation. Consequently the probability density function of G^{∞} is wider (Fig. 4.23.a). The average value of the macroscopic loading G^{∞}_{mean} is lowered while its

maximum value $G^{\infty}_{\max}$ does not change since it is determined from the toughest configuration which is visited by the crack in both cases $\mathcal{L} \simeq 10^2\, d$ and $\mathcal{L} \simeq 10^6\, d$. When $\mathcal{L}$ approaches the size of the inclusion d, we observe a shift of behavior and both the average value G^{∞}_{mean} and the maximum $G^{\infty}_{\max}$ of the macroscopic ERR are reduced. It is explained by the fact that the interaction between a crack and the inclusions is no more governed by long-range elastic interactions but rather by the local term $\frac{f_x}{\mathcal{L}}$ in Eq. (2.14), which corresponds to spring forces. The macroscopic loading required to make the crack propagates is lowered due to the dominant contributions of the spring forces. The author wants to stress out that this effect is purely three-dimensional since it relies on in-plane perturbations along the crack front. Thus $G^{\infty}_{\max}$ is not expected to decay as $\mathcal{L}$ decreases in a two-dimensional setting.

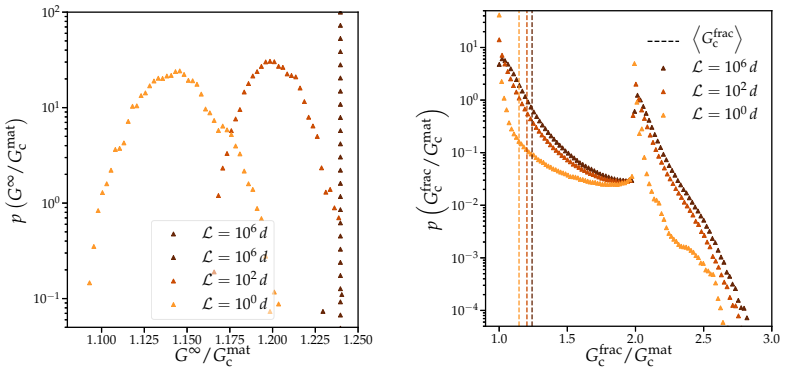

(a) (b)

Figure 4.23: Impact of the structural length $\mathcal{L}$ on the macroscopic ERR imposed by the loading G^{∞} and dissipated fracture energy G_c^{frac} distributions : probability density function of G^{∞} (a) and G_c^{frac} (b) for a crack interacting with a distribution of tougher spherical inclusions of density $\rho_{\text{inc}} = 25\%$ and inclusion toughness $G_c^{\text{inc}} = 2\, G_c^{\text{mat}}$ for various structural length $\mathcal{L}$.

The impact of the structural length $\mathcal{L}$, characteristic of loading variations, on G_c^{eff} is finally plotted in Fig. 4.24. We see that for $\mathcal{L} = 10^6 d$ the three possible definitions for the effective toughness converge towards a unique value, which can then be unambiguously refered to as the *effective toughness* G_c^{eff} of the composite. Moreover, as it was intuited by Hossain et al. [2014], the *maximum energy release rate* $G^{\infty}_{\max}$ appears to be the most suited choice if one wants to measure the intrinsic effective fracture properties of heterogeneous materials, as it appears to be less sensitive to the specimen geometry. Indeed variations on $G^{\infty}_{\max}$ start to appear only below $\mathcal{L} \simeq 10^2 - 10^3\, d$ while they appear at $\mathcal{L} \simeq 10^4 - 10^5\, d$ on G^{∞}_{mean} and $\left\langle G_c^{\text{frac}}\right\rangle$. Measuring the effective toughness G_c^{eff} with G^{∞}_{mean} at $\mathcal{L} \simeq 10^3\, d$ induces an error around 20% on the reinforcement. At $\mathcal{L} \simeq 10^2\, d$, the error ranges between 30% and 40%.

Given that the *effective toughness*, defined as the *maximum energy release rate*, is attained when the crack meets the strongest pinning configuration, one can wonder if such configuration is necessarily visited by the crack front during crack propagation. Kolton

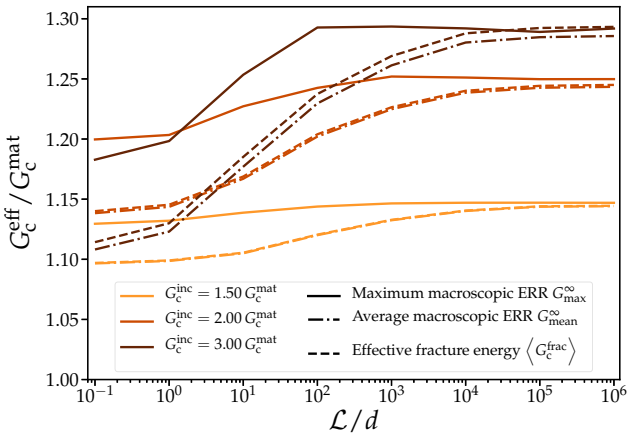

Figure 4.24: Impact of the structural length $\mathcal{L}$ on the various variables $G^{\infty}_{\mathrm{max}}$, $G^{\infty}_{\mathrm{mean}}$, $\langle G_c^{\mathrm{frac}} \rangle$ describing the effective fracture properties for various inclusion toughness G_c^{inc}

et al. [2013] proved that the maximum value is attained for a propagation length :

$$\frac{L_x^{min}}{d} = \left(\frac{L_z}{d}\right)^{\zeta} \tag{4.44}$$

where ζ is the roughness exponent of the crack front, which ranges from $\zeta = 0.388$ [Rosso and Krauth, 2002] to $\zeta = 0.5$ (see Démery et al. [2014b] or Section 4.2.1) depending on the regime (weak or strong) in which the crack is propagating.

Kolton et al. [2013] report that if $L_x > L_x^{min}$, the effective toughness could be overestimated due to extreme statistics. If it might be theoretically the case when the sole crossing mechanism is modeled, such extreme events, where the crack front is pinned by an inclusion presenting a considerably high toughness, cannot actually happen since crack deflection (see Section 3.3) or crack bridging [Bower and Ortiz, 1991] mechanisms would prevail over crack trapping at such toughness levels. Thus one has to ensure that the crack propagates at least on a distance $L_x \propto \sqrt{L_z}$.

Under the following *scale separation* conditions relating the inclusion size d to the structural lengthscale $\mathcal{L}$:

$$\begin{cases} \mathcal{L} \geq 10^3\, d \\ L_x \geq \sqrt{L_z d} \end{cases} \tag{4.45}$$

the *maximum energy release rate* $G^{\infty}_{\mathrm{max}}$, measured from the evolution of the macroscopic loading G^{∞}, can be considered as the intrinsic *effective toughness* of the heterogeneous brittle material.

4.3.1.c Implications on experimental set-ups and computational modeling

Implications on experimental set-ups

From an experimental point of view, the *average energy release rate* $G^{\infty}_{\mathrm{mean}}$ is the easiest variable to measure since it can be estimated from the total energy released during crack propagation and thus extracted from the force-displacement curve. Estimating the *maxi-*

mum energy release rate $G^{\infty}_{\max}$ assumes to be able to track the evolution of the macroscopic elastic release rate during crack propagation. The procedure is naturally more complex but can be achieved through the compliance method [Wang and Xia, 2017; Vasudevan et al., 2019] or integrated DIC computations [Roux and Hild, 2006; Grabois et al., 2018]. The estimation of the local map of dissipated fracture energy G_c^{frac} happens to constitute a particular conundrum since it requires to be able to track in real time the local ERR along the crack front $G(z,t)$ as well as the crack trajectory and dynamics, which allows for the estimation of the local velocity $v(z,t)$. In the case of three-dimensional crack propagation, this proves possible but nonetheless costly since observing three-dimensional crack front configurations requires powerful imaging techniques such as in-situ micro-tomography [Nguyen et al., 2016]. Moreover, complex digital volume correlation (DVC) procedures have to be developed in order to estimate the local ERR distribution from the data brought by the imaging techniques [Lachambre et al., 2015]. Finally, Eq. (4.41) supposes to be able to get all this information at very fine temporal and spatial scales. If the recent progress in imaging techniques allows to get such "4D" data sets, it is highly unlikely that such methods become systematic.

It ultimately enforces conditions on the specimen geometry since it sets the structural length $\mathcal{L}$. We here give examples of such conditions for the Tampered Double Cantilever Beam (TDCB) (Fig. 4.25) and Double Cleavage Drilled Compression (DCDC) (Fig. 4.26).

First let us consider a TDCB specimen, whose geometry is represented in Fig. 4.25.a. We note L the specimen length, ℓ the crack length, h and H the minor and major height of the specimen. The sample is loaded with prescribed displacement δ and deforms under plane stress conditions. Vasudevan et al. [2019] showed through numerical FEM simulations confirmed by experiments on PMMA that for a crack length $\ell \in [L/3, 2L/3]$:

$$G(\ell,\delta) \simeq E\frac{\delta^2}{2\lambda_0\ell_0}e^{-\ell/\ell_0} \tag{4.46}$$

where $\ell_0 = 0.39, L - 22.9$ for L expressed in millimeters and $\lambda_0 = \frac{\ell_0^2}{hL}$.

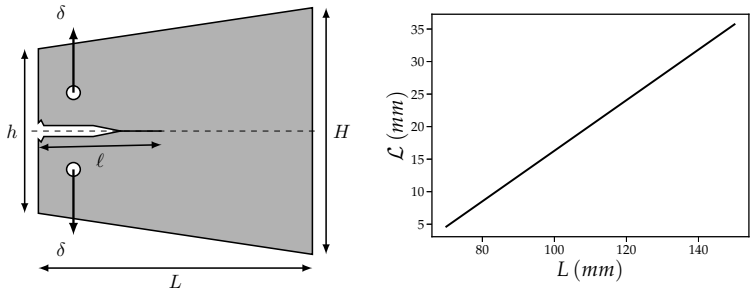

(a) TDCB geometry (b) $\mathcal{L}$ variations

Figure 4.25: TDCB geometry (a) and variations of the structural length $\mathcal{L}$ with respect to the sample length L

In that case, the structural length $\mathcal{L}$ determined from Eq. (2.7) reads :

$$\mathcal{L} = \ell_0 \tag{4.47}$$

The numerical estimate of $\mathcal{L}$ is provided as a function of the specimen length L in Fig. 4.25.b. We see that for a sample length $L = 10\text{cm}$, $\mathcal{L} = 16.3\,\text{mm}$. The inclusion size has then to be at most $160\mu\text{m}$ if one wants to measure accurately the effective toughness G_c^{eff} using the *maximum energy release rate* $G_{\max}^{\infty}$ obtained e.g. from compliance or DIC methods and $1.6\mu\text{m}$ using the *average energy release rate* G_{mean}^{∞} obtained e.g. from the force-displacement curve. Finally, if the sample is 2cm thick, the crack has to propagate over $\simeq 1\text{cm}$ so that the crack front may visit a configuration corresponding to the maximal value of the ERR.

We now consider a DCDC specimen of width $w = 1\text{cm}$ with prescribed forces σ at both ends as pictured in Fig. 4.26.a. We note ℓ the crack length and R the radius of the central hole. Following Pallares et al. [2009], the expression of G for $\ell \in [5R, 20R]$ reads :

$$G(\ell, \sigma) = \frac{1-\nu^2}{E} \pi R \sigma^2 \frac{1}{\left(a_1 + a_2 \frac{\ell}{R}\right)^2} \tag{4.48}$$

where $a_1 = 0.316 + 0.735\left(\frac{w}{R}\right) + 0.0346\left(\frac{w}{R}\right)^2$ and $a_2 = -0.409 + 0379\left(\frac{w}{R}\right) - 0.0257\left(\frac{w}{R}\right)^2$.

The structural length $\mathcal{L}$ variations with the crack length are given by :

$$\mathcal{L} = \frac{a_1 + a_2 \frac{\ell}{R}}{2a_2} R \tag{4.49}$$

Examples of $\mathcal{L}$ values are given in Fig. 4.26.b for $w = 10\,\text{mm}$ and various hole radius R. We see that $\mathcal{L}$ is of the same order of magnitude than for the TDCB specimen. It consequently imposes the same constraints on the inclusion size d. In contrast with the TDCB geometry, the relevant parameter to play on $\mathcal{L}$ is no more the specimen length L but the ratio $\frac{w}{R}$.

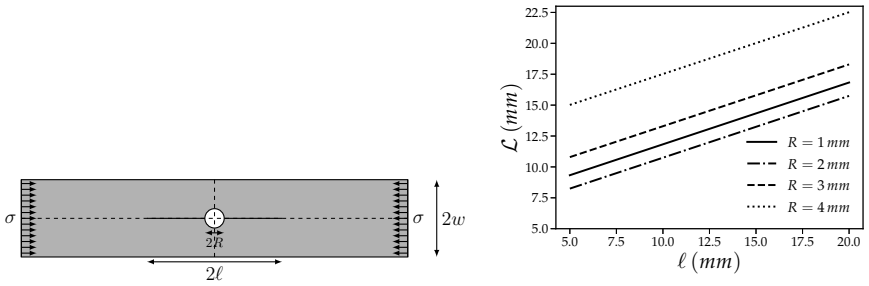

(a) DCDC geometry (b) $\mathcal{L}$ variations

Figure 4.26: DCDC geometry (a) and variations of the structural length $\mathcal{L}$ with respect to crack length ℓ for $w = 10\,mm$ and various hole radius R (b).

In conclusion, the choice of the specimen geometry sets the structural length $\mathcal{L}$, which subsequently constrains the choice of the experimental technique to measure G_c^{eff}. One can either ensure that the structural length is large enough on front of the heterogeneity size, $\mathcal{L} \simeq 10^4\, d$, and measure G_{mean}^{∞} from the force-displacement curve or deploy more advanced experimental techniques and extract the effective toughness from G_{max}^{∞} for $\mathcal{L} \simeq 10^2\, d$. In fracture experiments on brittle rocks, the latter condition is easily satisfied while the former is often violated given the size of the heterogeneities [Nasseri and Mohanty, 2008; Chandler et al., 2016]. This remark drives the need for the democratization of advanced experimental methods for fracture properties measurements. Otherwise, experimental measures might lead to an underestimation of the effective fracture properties.

Implications on numerical simulations

Our findings also raise the question of the choice of the boundary conditions and specimen size in numerical simulations. In our numerical method, the structural length $\mathcal{L}$ is a parameter of the model and can be set manually. In FEM-based computational methods, $\mathcal{L}$ is often set by loading conditions. Recent forefront numerical studies measured the effective toughness of two-dimensional heterogeneous materials from phase-field simulations using a surfing boundary condition [Hossain et al., 2014; Brach et al., 2019a]. This condition appears to set $\mathcal{L} \sim L_y$, where L_y is the height of the simulation domain in the direction perpendicular to crack propagation. L_y is typically one order of magnitude larger than the defect size, due to computational costs. It enforces to measure the effective toughness from the maximum energy release rate G_{max}^{∞}, an option that was indeed selected by Hossain et al. [2014]. It allows actually to predict accurately the effective toughness in the two-dimensional case since the decrease of G_{max}^{∞} for $\mathcal{L} < 10^3\, d$ is due to three-dimensional effects. However, it is worth noticing that such boundary conditions might lead to an underestimation of the effective toughness of disordered materials when transposed into a three-dimensional setting.

4.3.2 Effective toughness of heterogeneous materials : the impact of inclusion contrast

In the remainder of this manuscript, we set the structural length $\mathcal{L} = 10^6\, d$ to fully decouple the effective toughness measurements from the structural problem. Crack propagation is made along a distance $L_x = L_z$ to ensure that the toughest pinning configuration is visited. Variables of interest (front position, local maps of effective fracture energy, etc.) are recorded after a propagation length $L_{save} = \sqrt{L_z d}$ to attain a stationary regime independent of the initial condition [Patinet et al., 2013b]. Under those assumptions, the effective toughness G_c^{eff} can be measured through the evaluation maximum value of the macroscopic ERR imposed by the loading G_{max}^{∞} :

$$G_c^{\text{eff}} = \max_{x \in [0, L_x]} G^{\infty}(x) \tag{4.50}$$

4.3.2.a Problem statement

We now investigate the impact of microstructural features on effective fracture properties and start by studying the influence of the inclusion toughness on the effective toughness. We consider the case of a single crack propagating in large-scale disordered systems of size $L_z \times L_x \times L_y = 256d \times 288d \times 16d$. L_y can be taken smaller than L_z and L_x because the crack does not explore regions far away from the mean fracture plane (see for example Fig. 2.23).

We consider monodisperse distributions of spherical inclusions of diameter d for an inclusion density $\rho_{\text{inc}} = 25\%$. The inclusion toughness varies from $G_{\text{c}}^{\text{inc}} = G_{\text{c}}^{\text{mat}}$ to $G_{\text{c}}^{\text{inc}} = 4.5\, G_{\text{c}}^{\text{mat}}$, which remains within the range of validity of the perturbative approach (Section 2.2.4). The interface shares the mechanical properties of the matrix $G_{\text{c}}^{\text{int}} = G_{\text{c}}^{\text{mat}}$. The results are averaged on five inclusion distribution realizations. Simulation parameters are summarized in Table 8.13. Examples of considered distributions are given in Fig. 4.27.

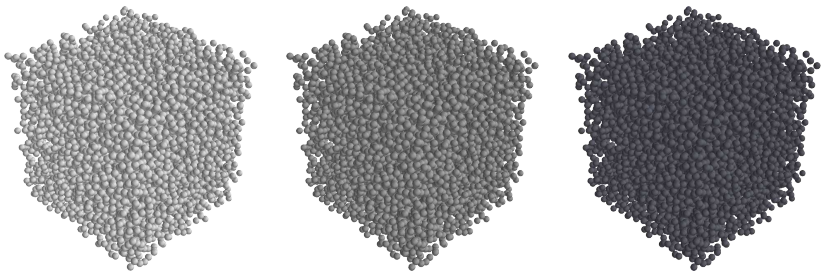

(a) $G_{\text{c}}^{\text{inc}} = 1.5\, G_{\text{c}}^{\text{mat}}$ (b) $G_{\text{c}}^{\text{inc}} = 2\, G_{\text{c}}^{\text{mat}}$ (c) $G_{\text{c}}^{\text{inc}} = 4\, G_{\text{c}}^{\text{mat}}$

Figure 4.27: Monodisperse spherical inclusion distribution with varying inclusion toughness $G_{\text{c}}^{\text{inc}}$ ($L_z \times L_x \times L_x = 25d \times 25d \times 25d$ for visualization purpose)

4.3.2.b Numerical results

The evolution of the effective toughness with the inclusion toughness is predicted from 135 simulations in which the crack front propagates in a medium containing hundreds of thousand inclusions. Each computation lasts 1 to 2 hours while the front mesh size is relatively fine since there are 16 points per inclusion diameter ($\Delta z = d/16$). It is important to stress out that such numerical performance is achieved thanks to the perturbative framework adopted in our approach.

The evolution of the effective toughness with the inclusion toughness is plotted in Fig. 4.28. Averaged results are plotted in solid lines while individual simulation points are plotted with cross markers. We can distinguish three main regimes :

1. at low inclusion toughness levels $G_{\text{c}}^{\text{inc}} \leq 1.5\, G_{\text{c}}^{\text{mat}}$, the effective toughness increases almost linearly with the inclusion toughness. The toughening clearly impacts the overall toughness of the composite ;

2. at intermediate toughness levels ranging from $G_{\text{c}}^{\text{inc}} = 1.5\, G_{\text{c}}^{\text{mat}}$ to $G_{\text{c}}^{\text{inc}} = 3.2\, G_{\text{c}}^{\text{mat}}$, the toughening rate $\frac{\partial G_{\text{c}}^{\text{eff}}}{\partial G_{\text{c}}^{\text{inc}}}$ progressively decreases; additional inclusion toughening contributes less and less to the increase of the material toughness. The effective

toughness reaches a maximum at $G_c^{inc} = 2.7\, G_c^{mat}$. The toughening rate becomes negative after the peak and the effective toughness decreases ;

3. at high inclusion toughness levels $G_c^{inc} \geq 3.2\, G_c^{mat}$, the effective toughness reaches a plateau. Increasing the inclusion toughness does not contribute any more to an overall reinforcement of the composite.

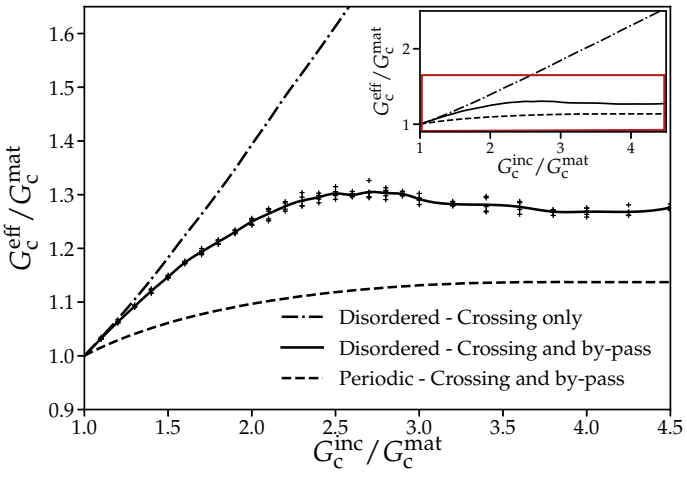

Figure 4.28: Impact of the inclusion toughness G_c^{inc} on the effective toughness G_c^{eff} for the coupling of crack trapping and crack deflection : the effective toughness is predicted from Eq. (4.50) as the maximal macroscopic loading obtained during the crack evolution. Numerical estimates (in solid line) are compared to numerical results of coplanar simulations where the crack can interact through the sole crossing mechanism (in dash-dotted line) and periodic simulations from Chapter 3 taking into account both inclusion crossing and by-pass (in dashed line).

We observe that this behavior cannot be grasped both qualitatively and quantitatively by the periodic case [2], stressing out the decisive influence of the material disorder. Moreover, Fig. 4.28 also shows that the mechanisms of interaction plays a decisive role in material reinforcement. The question then is : is it possible to predict quantitatively the effective toughness of composite materials in a disordered setting for the competing crossing and by-pass mechanisms ? It drives the need for the development of an analytical homogenization framework for non-coplanar crack propagation in three-dimensional brittle composites. The next section is dedicated to the construction of such a homogenization procedure.

4.3.2.c Convergence study

Before tackling the crucial question of toughness homogenization, we investigate the impact of the front mesh size Δz. We reproduce the study described above for various mesh size ranging from $\Delta z = d/4$ to $\Delta z = d/32$. Simulations parameters are summarized in Table 8.13. Numerical results are plotted in Fig. 4.29.

[2]The periodic results are estimated from effective fracture properties measured in Section 3.3, averaged with respect to the landing height of the crack on the inclusion.

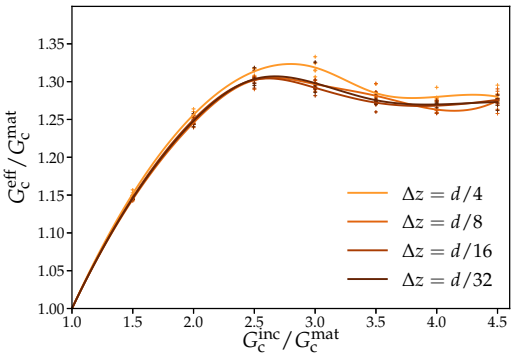

Figure 4.29: Impact of the front mesh size Δz on the effective toughness G_c^{eff} : the effective toughness is predicted from Eq. (4.3.2) as the maximal macroscopic loading required to make propagate a coplanar crack interacting with a monodisperse distribution of spherical inclusions with varying toughness.

A coarser discretization induces an overestimation of the effective toughness, especially at high inclusion toughness levels where by-pass events are predominant. It is due to the fact that a coarser mesh may lead to overestimate the angle at which out-of-plane deviations occurs (see Fig. 4.30). This deflection angle has been proven to control the effective toughness of heterogeneous materials (see Section 3.3). As soon as $\Delta z \leq d/8$ the effective toughness values converge towards the same value. We thus adopt a fine mesh $\Delta z \leq d/16$, which constitutes a reasonable compromise between computational cost and numerical accuracy.

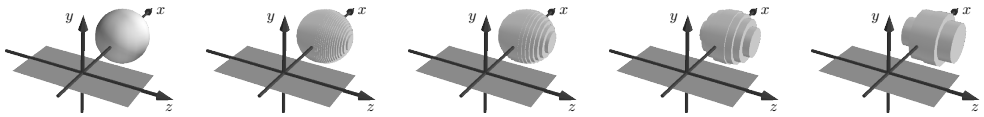

(a) (b) (c) (d) (e)

Figure 4.30: Impact of the discretization step on the geometrical modeling of a spherical inclusion : real geometry (a), fine mesh for $\Delta z = d/32$ (b) and $\Delta z = d/16$ (c), coarse mesh for $\Delta z = d/8$ (d) and $\Delta z = d/4$ (e)

4.4 Semi-analytical homogenization technique for effective toughness predictions of three-dimensional composites

This section is dedicated to the construction of a semi-analytical technique for the homogenization of the effective fracture properties, accounting for both crossing and by-pass mechanisms of interaction between a crack and tough inclusions. It relies on the results of Démery et al. [2014b], which developed a theoretical framework for the homogenization of fracture properties in the case of coplanar propagation, where the toughness field the crack effectively experiences corresponds to the local material toughness properties. The method developed here proposes a new framework, which takes into account the differential impact of the interaction mechanisms occurring at the crack tip on the effective fracture properties for three-dimensional crack loaded in tensile Mode I. It is applied to the competing crossing, by-pass and repenetration mechanisms to rationalize the impact of the inclusion toughness on the effective toughness plotted in Fig. 4.28.

4.4.1 Summary of a three-step homogenization technique

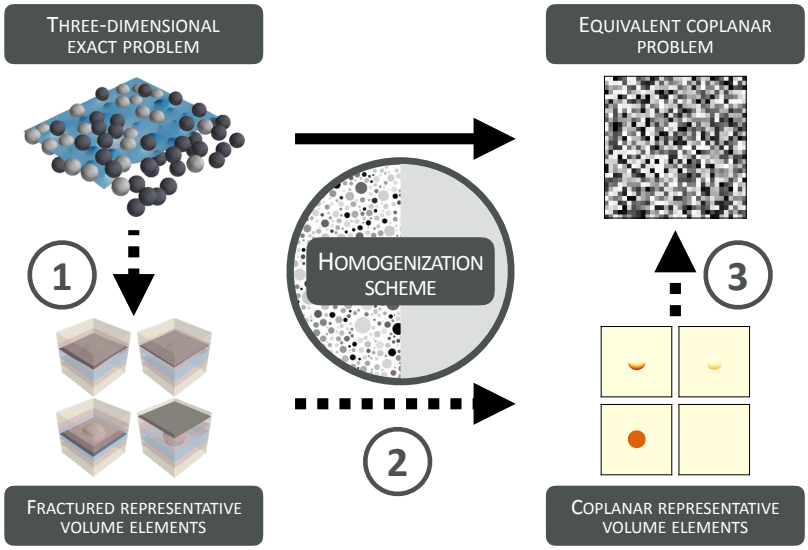

Figure 4.31: Three-step homogenization technique developed to predict effective toughness properties in a three-dimensional non-coplanar setting.

Démery et al. [2014b] developed a theoretical framework to predict the effective toughness from the statistical features of the toughness distribution, namely its average toughness $\langle G_c \rangle$, its standard deviation σ and its correlation length ξ_z, ξ_x. This framework has been developed in the case of coplanar crack propagation where the crack can only interact with the material disorder through the crossing mechanism. We notice in Fig. 2.23 that the out-of-plane deviation of the crack happens to be relatively small in our simulations so that crack propagation remains approximately planar. A homogenization scheme may thus be adapted from Démery et al. [2014b] to tackle the case of non-coplanar propagation through the means of an equivalent coplanar problem.

Yet, the statistical features of the equivalent coplanar distribution of toughness cannot be directly inferred from the three-dimensional distribution of the toughness $G_c(z, x, y)$. Indeed, we saw in Chapter 3 that the mechanism of interaction selected by the crack governs the local toughness the crack effectively experiences during the propagation : if the inclusion is crossed, the crack visits the inclusion toughness whereas if the inclusion is by-passed it sees the one of the interface. The determination of the equivalent coplanar problem should then take into account the differential impact of the crack-tip interaction mechanisms on the ultimate toughness distribution.

Inspired by micromechanical models, we propose a three-step homogenization scheme :

1. first, we break down the full problem of the propagation of a crack in a disordered distribution of inclusions into multiple simpler problems, referred to as *fractured representative volume elements* (FRVEs), considering all the possible ways a crack interact with a single inclusion and its respective probability. This decomposition relies on the absence of interaction during the out-of-plane by-pass of neighboring inclusions. As a result, we refer to this as the *dilute* hypothesis ;

2. second, the three-dimensional cell problems provide equivalent coplanar ones, called *coplanar representative volume elements* (CRVEs), which derive from the way the crack interacts with the inclusion (crossing or by-pass).

3. third, the superposition of all the coplanar cell problems allows to get back to an equivalent coplanar toughness distribution, from which the statistical features ($\langle G_c \rangle$, σ, ξ_z, ξ_x) can be inferred under the *ergodic assumption*. It ultimately allows to estimate the effective toughness of three-dimensional heterogeneous brittle materials from the coplanar theory of Démery et al. [2014b] using Eq. (4.31).

The procedure is summarized in Fig. 4.31.

4.4.2 From an original three-dimensional problem to a cell three-dimensional problem : the fractured representative volume element

In the following, we consider the sole case of spherical inclusions. It is nonetheless possible to generalize this homogenization method to any inclusion shape as it will be illustrated in Section 4.6.

4.4.2.a Definition of a microstructural representative volume element

The first step of our method consists in breaking down the original non-coplanar problem into a superposition of cell problems called *fractured representative volume elements* (FRVEs), where a crack interacts with a single inclusion only.

In the most general case, the composite material is constituted of a homogeneous matrix and an isotropic distribution of spherical inclusions $\mathcal{S} = (\mathcal{S}_i)$. The diameter $(d_{\mathrm{inc},i})$ of the inclusions $(\mathcal{S}_i)$, follows a distribution characterized by its probability density function p_d. In the same manner, the toughness $\left(G_{c,i}^{\mathrm{inc}}\right)$ of the inclusions and the toughness $\left(G_{c,i}^{\mathrm{int}}\right)$ of their interface follow distributions described by the respective probability density functions

p_{inc} and p_{int}. The density of inclusions is denoted ρ_{inc}.

We call *representative volume element* (RVE) the cell medium ω constituted of a single inclusion of diameter d_{inc}, inclusion toughness $G_{\text{c}}^{\text{inc}}$ and interface toughness $G_{\text{c}}^{\text{int}}$ embedded at the center of a cube constituted of the matrix material, whose edge length L_ρ is given by :

$$L_\rho = \left(\frac{\pi}{6\rho_{\text{inc}}}\right)^{\frac{1}{3}} d_{\text{inc}} \tag{4.51}$$

so that the inclusion density inside the spherical RVE equals to ρ_{inc}. An example of such a cell medium is pictured in Fig. 4.32.

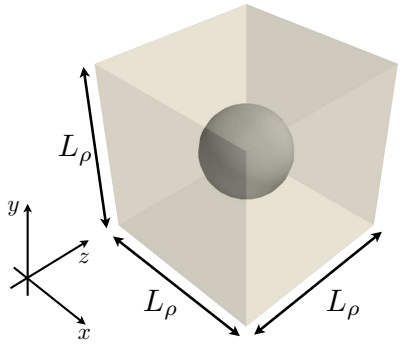

Figure 4.32: RVE of size L_ρ containing an inclusion of size d of inclusion toughness $G_{\text{c}}^{\text{inc}}$ and interface toughness $G_{\text{c}}^{\text{int}}$ for $\rho_{\text{inc}} = 25\%$

Ω is the statistical ensemble of possible realizations of such a RVE. With the ensemble Ω is associated a probability density function p_{RVE}. Given that the inclusion diameter and fracture properties are assumed to be independent variables, it reads :

$$p_{\text{RVE}}\left(d_{\text{inc}}, G_{\text{c}}^{\text{inc}}, G_{\text{c}}^{\text{int}}\right) = p_d\left(d_{\text{inc}}\right) \cdot p_{\text{inc}}\left(G_{\text{c}}^{\text{inc}}\right) \cdot p_{\text{int}}\left(G_{\text{c}}^{\text{int}}\right) \tag{4.52}$$

4.4.2.b Interaction of a crack with a representative volume element : the fractured representative volume element

The interaction of the microstructural RVE with an incoming half-plane crack constitutes a realization of a *fractured representative volume element* (FRVE) ω_{F}. This interaction is described by the height y, at which the crack penetrates the RVE. Given that the inclusions are isotropically distributed, the distribution of y is uniform in $\left[-\frac{L_\rho}{2}, \frac{L_\rho}{2}\right]$. Its probability density function p_y reads :

$$p_y\left(y\right) = \frac{1}{L_\rho} \tag{4.53}$$

As stated in Chapter 3, there are three possibilities for the interaction between the crack and the FRVE :

1. the crack does not encounter the inclusion and propagates in the matrix (Fig. 4.33.b);
2. the crack encounters the inclusion and by-passes it (Fig. 4.33.c);
3. the crack encounters the inclusion and crosses it (Fig. 4.33.d).

As exposed in Section 3.3.1, this interaction can be summarized in an interaction diagram, which is either constructed numerically or inferred analytically from Eq. (3.27) as possible for spherical inclusions. Such a diagram is shown in Fig. 4.33 along with the three interaction mechanisms for a given FRVE.

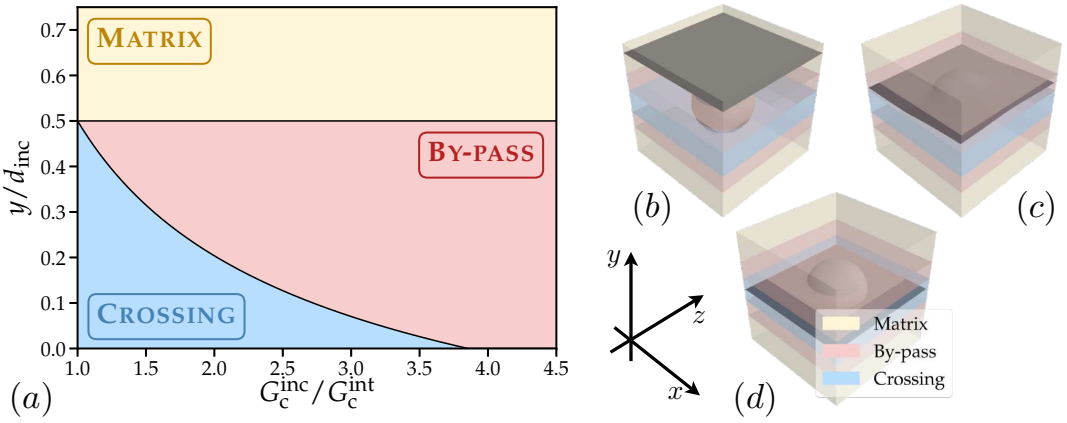

Figure 4.33: (a) Interaction diagram providing the interaction mechanism as a crack meets a tough inclusion. The landing height y and the inclusion toughness ratio $G_{\text{c}}^{\text{inc}}/G_{\text{c}}^{\text{int}}$ are the two parameters that governs the mechanism selection. This interaction mechanism is either matrix cracking (b), inclusion by-pass (c) or inclusion crossing (d)

The microstructural properties of the inclusion and the landing height being independent variables, its probability density function reads :

$$p_{\text{FRVE}}\left(\omega_{\text{F}}\right) = p_y\left(y\right) \cdot p_d\left(d_{\text{inc}}\right) \cdot p_{\text{inc}}\left(G_{\text{c}}^{\text{inc}}\right) \cdot p_{\text{int}}\left(G_{\text{c}}^{\text{int}}\right) \tag{4.54}$$

We note Ω_{F} the statistical ensemble of possible realizations of FRVE. The superposition of all the FRVE in Ω_{F} is representative of the interaction between a crack and a disordered distribution of tough inclusions in the *dilute* limit, when the mechanism selection in one RVE is independent of the one in a neighboring RVE. One thus expects that our homogenization model works well at small inclusion toughness and density where the out-of-plane deviations are small.

4.4.3 From a cell three-dimensional problem to an equivalent coplanar problem : the interaction mechanisms

4.4.3.a Construction of an equivalent coplanar toughness field

We now have to translate the three-dimensional FRVE problem into a coplanar one. $G_{\text{c}}^{\text{cop}}\left(z,x\right)$ denotes the toughness field that the crack front actually visits during crack propagation in a given $\omega_{\text{F}} = \left(y, d_{\text{inc}}, G_{\text{c}}^{\text{inc}}, G_{\text{c}}^{\text{int}}\right) \in \Omega_{\text{F}}$. Matrix cracking and inclusion crossing corresponding to coplanar propagation, computing $G_{\text{c}}^{\text{cop}}$ is rather straight forward in that case.

For matrix cracking, it is given by :

$$G_{\text{c}}^{\text{cop}}\left(z,x;\omega\right) = G_{\text{c}}^{\text{mat}} \tag{4.55}$$

For inclusion crossing, $G_{\mathrm{c}}^{\mathrm{cop}}$ reads :

$$\begin{cases} G_{\mathrm{c}}^{\mathrm{cop}}(z,x;\omega) = G_{\mathrm{c}}^{\mathrm{mat}}, \text{ if } z^2 + x^2 > \left(\frac{d_{\mathrm{inc}}}{2}\right)^2 - y^2 \\ G_{\mathrm{c}}^{\mathrm{cop}}(z,x;\omega) = G_{\mathrm{c}}^{\mathrm{inc}} \text{ otherwise} \end{cases} \tag{4.56}$$

We now have to translate the impact of inclusion by-pass into an equivalent coplanar defect. Analytical results cannot be derived given the complexity of the non-linear equation of motion. Yet it is possible to compute it numerically from simulations of periodic arrangements of spherical inclusions.

In-plane distortions of the crack front and their dynamics have been explored in Section 3.2.1. They have been shown to be the local mirror images of the toughness field visited by the crack during propagation. The equivalent coplanar toughness field $G_{\mathrm{c}}^{\mathrm{cop}}(z,x)$ can thus be inferred from the in-plane perturbation observed in periodic simulations of inclusion by-pass. We define G^{cop} as the ERR the crack would develop if the propagation was coplanar. G^{cop} reads at first-order in the perturbation :

$$G^{\mathrm{cop}}(z,t) = G^{\infty}(t)\left(1 - \frac{1}{\mathcal{L}} f_x(z,t) - \frac{1}{\pi}\,\mathrm{PV}\int_{-\infty}^{+\infty} \frac{f_x(z,t) - f_x(z',t)}{(z-z')^2}\,dz'\right) \tag{4.57}$$

As $G_{\mathrm{c}}^{\mathrm{frac}}$, G^{cop} can be tracked during crack propagation (see Fig. 4.34) and stored in a grid, each value $G^{\mathrm{cop}}(z,x)$ corresponding to the average coplanar ERR G^{cop} in this cell.

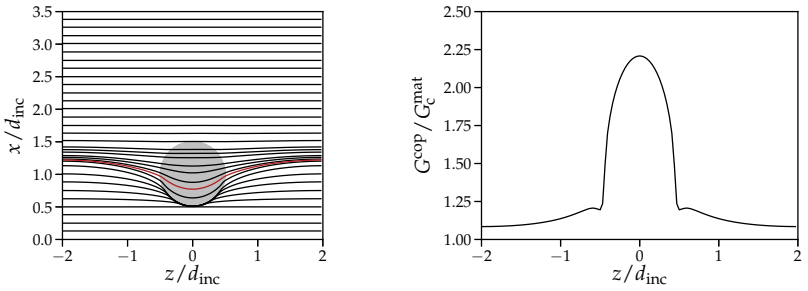

(a) (b)

Figure 4.34: In-plane distortions of the crack front during inclusion by-pass : (a) profiles of the crack front in-plane perturbation at various instant of propagation and (b) associated equivalent coplanar ERR G^{cop} for the profile marked in red.

We first test this method on the in-plane crossing of an inclusion twice tougher than the matrix $G_{\mathrm{c}}^{\mathrm{inc}} = 2\,G_{\mathrm{c}}^{\mathrm{mat}}$ interacting with a crack landing at $y_{\mathrm{landing}} = 0$. The results are plotted in Fig. 4.35.a. It appears that such a definition of the equivalent coplanar toughness does not provide the expected toughness field of Eq. (4.56). Indeed, as $G^{\mathrm{cop}}(z,t) = G_{\mathrm{c}}[v(z,t)]$, our method is not able to distinguish the dissipation resulting from the raw toughness $G_{\mathrm{c}}(z,x)$ of the material from the one resulting from the kinetic effects which take place during the depinning phase out of the defect (see Section 3.2.1). Thus G^{cop} corresponds to the *kinetic equivalent coplanar toughness field*.

In order to remove the impact of kinetic effects, we estimate the average crack velocity on the grid following :

$$v\left(z_j, x_i\right) = \frac{\Delta\ell}{t_{\text{out}} - t_{\text{in}}} \tag{4.58}$$

where $\Delta\ell$ t_{out}, t_{in} are defined in Fig. 4.20.

Inverting the kinetic law of Eq. (2.23), we have access to the *static equivalent coplanar toughness field* $G_{\text{c}}^{\text{cop}}$:

$$G_{\text{c}}^{\text{cop}}\left(z_j, x_i\right) = G^{\text{cop}}\left(z_j, x_i\right) - G_{\text{c}}^{\text{mat}}\left(\frac{v\left(z_j, x_i\right) - v_m}{v_0}\right) \tag{4.59}$$

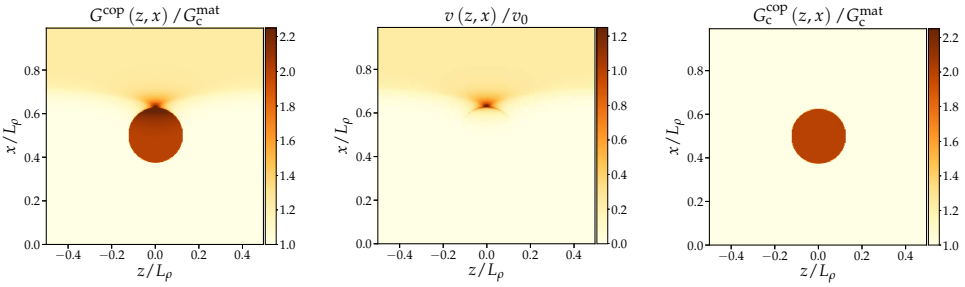

(a) (b) (c)

Figure 4.35: Kinetic equivalent coplanar toughness field for the inclusion crossing (a) taking into account kinetic effects (b) and its static value (c)

As pictured in Fig. 4.35.c, $G_{\text{c}}^{\text{cop}}$ corresponds now to the expected equivalent coplanar toughness field for inclusion crossing. Besides, such a static field $G_{\text{c}}^{\text{cop}}\left(z, x\right)$ happens to be independent on the inclusion spacing L_ρ, as we could verify it from simulations on periodical arrangements of tough inclusions.

4.4.3.b Equivalent coplanar defect for the by-pass mechanism

Validated on inclusion crossing, this method can be now applied to predict the equivalent in-plane defect emerging from the by-pass mechanism. The results are plotted in Fig. 4.36. As it was intuited in Fig. 3.3.2.a from the observation of the in-plane perturbations evolution for inclusion by-pass, the by-pass mechanism is equivalent to a coplanar defect vanishing quickly in the x-direction, due to the re-alignment of the front with the (Ox)-direction imposed by the loading. When the crack propagation direction realigns with the loading direction, its velocity increases until the front fully relaxes. For the spherical inclusion, the crack is thus pinned by the inclusion only at the begin of the by-pass as observed in Section 3.3.2.

We finally plot the static equivalent coplanar toughness field for an inclusion toughness at the crossing to by-pass transition for $y_{\text{landing}} = 0$, $G_{\text{c}}^{\text{inc}} \simeq \left[G_{\text{c}}^{\text{inc}}\right]_{\text{crit}} = 3.852\, G_{\text{c}}^{\text{mat}}$, in Fig. 4.36. We see that a slight change in the inclusion toughness modifies drastically the equivalent coplanar defect shape and its intensity, as the propagation mechanism shifts from in-plane to out-of-plane. In turn, it will also affect the effective toughness, as we describe in the next part.

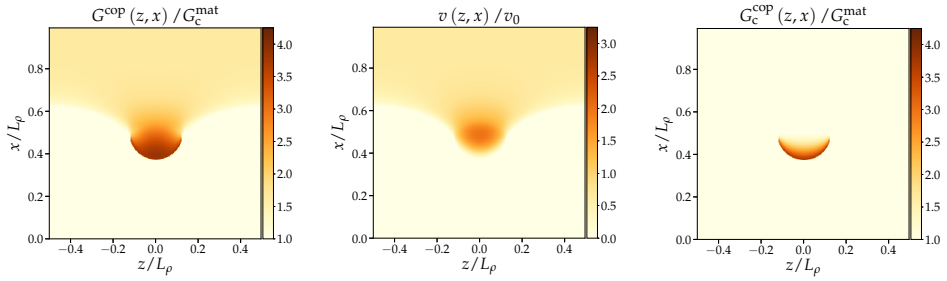

(a) (b) (c)

Figure 4.36: Equivalent coplanar toughness field for the inclusion by-pass : kinetic equivalent coplanar toughness field (a) taking into account kinetic effects (b) and its static value (c)

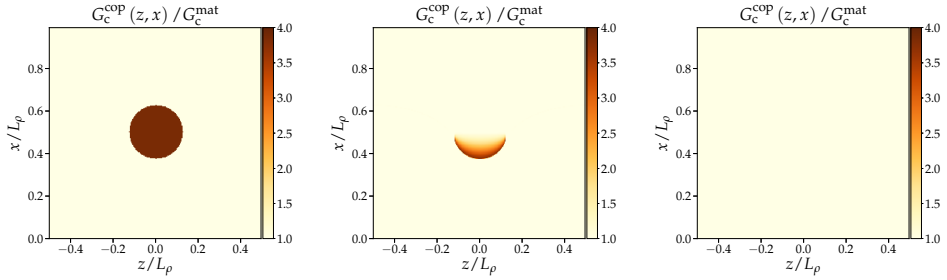

(a) Inclusion crossing $G_{\mathrm{c}}^{\mathrm{inc}} = \left[G_{\mathrm{c}}^{\mathrm{inc}}\right]_{\mathrm{crit}} - \varepsilon$

(b) Inclusion by-pass $G_{\mathrm{c}}^{\mathrm{inc}} = \left[G_{\mathrm{c}}^{\mathrm{inc}}\right]_{\mathrm{crit}} + \varepsilon$

(c) Matrix cracking

Figure 4.37: Equivalent coplanar representative volume element (CRVE) associated to the three mechanisms considered in the study : (a) inclusion crossing, (b) inclusion by-pass at the transition $G_{\mathrm{c}}^{\mathrm{inc}} = 3.854\, G_{\mathrm{c}}^{\mathrm{mat}}$ from crossing to by-pass for a crack landing on the equatorial plane $y = 0$ and (c) matrix cracking.

4.4.4 From a coplanar cell problem to a full coplanar problem : the reconstructed toughness distribution

Thanks to the procedure described before combined with the interaction diagram of Fig. 4.33.a, we can determine an equivalent *coplanar representative volume element* (CRVE) for each FRVE realization $\omega_{\mathrm{F}} \in \Omega_{\mathrm{F}}$. Under the *ergodic assumption*, the spatial average of an observable f on $L_z \times L_x$, is equal to the ensemble average on both the surface of the CRVEs $L_\rho \times L_\rho$ and the realizations Ω_{F}. This assumption writes as :

$$\left\langle f(z,x)\right\rangle_{z\in[0,L_z],x\in[0,L_x]} = \left\langle f(z,x;\omega_{\mathrm{F}})\right\rangle_{z\in[0,L_\rho],x\in[0,L_\rho],\omega_{\mathrm{F}}\in\Omega_{\mathrm{F}}} \tag{4.60}$$

Thus $\langle G_{\mathrm{c}}\rangle$, σ, ξ_z, ξ_x, the four parameters required to predict $G_{\mathrm{c}}^{\mathrm{eff}}$, can be inferred from the superposition of all the CRVE associated to a FRVE realization $\omega_{\mathrm{F}} \in \Omega_{\mathrm{F}}$ from the

following expressions :

$$\begin{cases} \langle G_{\mathrm{c}} \rangle = \dfrac{1}{L_\rho^2} \displaystyle\int_{\omega_{\mathrm{F}}} \int_x \int_z G_{\mathrm{c}}^{\mathrm{cop}}\left(z, x; \omega_{\mathrm{F}}\right) p_{\mathrm{FRVE}}\left(\omega_{\mathrm{F}}\right) dz\, dx\, d\omega_{\mathrm{F}} \\ \left\langle G_{\mathrm{c}}^2 \right\rangle = \dfrac{1}{L_\rho^2} \displaystyle\int_{\omega_{\mathrm{F}}} \int_x \int_z G_{\mathrm{c}}^{\mathrm{cop}}\left(z, x; \omega_{\mathrm{F}}\right)^2 p_{\mathrm{FRVE}}\left(\omega_{\mathrm{F}}\right) dz\, dx\, d\omega_{\mathrm{F}} \\ \xi_{z/x} = \dfrac{1}{L_\rho^2} \displaystyle\int_{\omega_{\mathrm{F}}} \int_x \int_z \xi_{z/x}\left(\omega_{\mathrm{F}}\right) p_{\mathrm{FRVE}}\left(\omega_{\mathrm{F}}\right) dz\, dx\, d\omega_{\mathrm{F}} \\ \sigma\left(G_{\mathrm{c}}\right)^2 = \left\langle G_{\mathrm{c}}^2 \right\rangle - \langle G_{\mathrm{c}} \rangle^2 \end{cases} \tag{4.61}$$

where $\int_\omega \int_x \int_z$ denotes the integrals over $\omega_{\mathrm{F}} \in \Omega_{\mathrm{F}}$, $z \in [0, L_\rho]$ and $x \in [0, L_\rho]$.

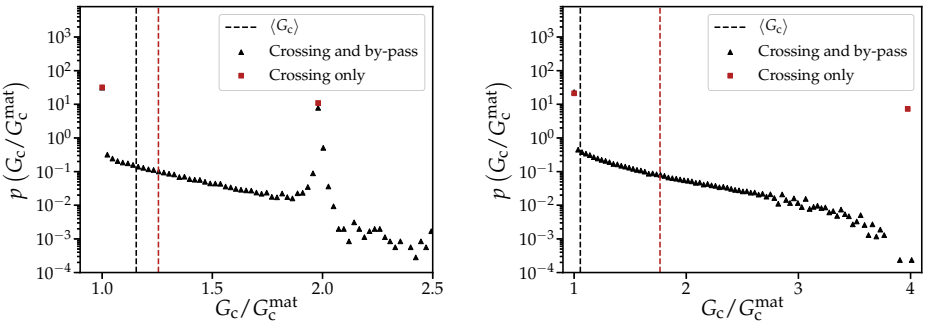

(a) $G_{\mathrm{c}}^{\mathrm{inc}} = 2\, G_{\mathrm{c}}^{\mathrm{mat}}$ (b) $G_{\mathrm{c}}^{\mathrm{inc}} = 3\, G_{\mathrm{c}}^{\mathrm{mat}}$

Figure 4.38: Equivalent coplanar toughness distribution accounting for the competing crossing and by-pass mechanisms : the toughness distribution is extracted from the homogenization procedure for an inclusion density $\rho_{\mathrm{inc}} = 25\%$ and inclusion toughness $G_{\mathrm{c}}^{\mathrm{inc}} = 2\, G_{\mathrm{c}}^{\mathrm{mat}}$ (a) and $G_{\mathrm{c}}^{\mathrm{inc}} = 4\, G_{\mathrm{c}}^{\mathrm{mat}}$ (b). Red square markers corresponds to bi-valued coplanar distribution where the sole crossing mechanism is accounted for, while black triangle markers combined the competing effect of both crossing and by-pass mechanisms.

Examples of the distribution of toughness $G_c^{\mathrm{coplanar}}\left(z, x\right)$ effectively visited during crack propagation and computed from the superposition of all CRVE realizations are plotted in Fig. 4.38 for an inclusion toughness $G_{\mathrm{c}}^{\mathrm{inc}} = 2\, G_{\mathrm{c}}^{\mathrm{mat}}$ and $G_{\mathrm{c}}^{\mathrm{inc}} = 4\, G_{\mathrm{c}}^{\mathrm{mat}}$. The toughness distribution obtained from the superposition of the CRVEs is plotted in black triangle markers, while the bi-valued distribution for the sole inclusion crossing mechanism is plotted in red square markers. We notice that the by-pass mechanism drastically changes the equivalent coplanar toughness distribution. In particular, the average value of the distribution is decreased by the out-of-plane excursions. Moreover, as pictured in Fig. 4.38.b, after a given contrast level $G_{\mathrm{c}}^{\mathrm{inc}} \geq \left[G_{\mathrm{c}}^{\mathrm{inc}}\right]_{\mathrm{crit}}$, all inclusions are by-passed and the equivalent coplanar toughness distribution does not depend on the inclusion toughness anymore. In this case, the average toughness $\langle G_{\mathrm{c}} \rangle$ is significantly smaller, close to $G_{\mathrm{c}}^{\mathrm{mat}}$.

Now that the parameters $\langle G_{\mathrm{c}} \rangle$, σ, ξ_z, ξ_x governing $G_{\mathrm{c}}^{\mathrm{eff}}$ are known, one can finally inject them in Eq. (4.31) to predict the effective toughness.

4.4.5 Model predictions for increasing inclusion toughness

We apply now the newly developed homogenization scheme to study the influence of the inclusion toughness on the effective toughness and rationalize the simulation results of Fig. 4.28.

In that case, the probability density function p_{FRVE} of a FRVE realization $\omega_{\mathrm{F}} \in \Omega_{\mathrm{F}}$ reads :

$$p_{\mathrm{FRVE}}\left(\omega_{\mathrm{F}}\right) = \frac{1}{L_\rho} \cdot \delta\left(d_{\mathrm{inc}} - d\right) \cdot \delta\left(G_{\mathrm{c}}^{\mathrm{inclusion}} - G_{\mathrm{c}}^{\mathrm{inc}}\right) \cdot \delta\left(G_{\mathrm{c}}^{\mathrm{interface}} - G_{\mathrm{c}}^{\mathrm{int}}\right) \tag{4.62}$$

where δ is the Dirac function, since we consider a composite with one type of inclusions with size d and toughnesses $G_{\mathrm{c}}^{\mathrm{inc}}$ and $G_{\mathrm{c}}^{\mathrm{int}}$.

The homogenization scheme allows for the prediction of the effective fracture properties but also for a better understanding of its relationship with the microstructural parameters. Model predictions are compared with numerical simulations in Fig. 4.39.

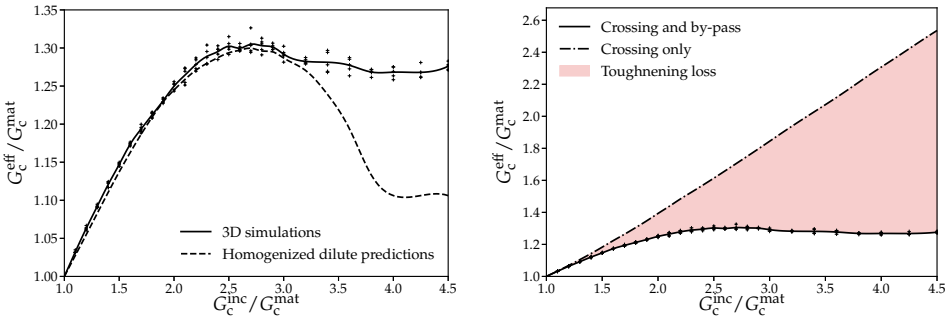

(a) (b)

Figure 4.39: Impact of the inclusion toughness $G_{\mathrm{c}}^{\mathrm{inc}}$ on the effective toughness $G_{\mathrm{c}}^{\mathrm{eff}}$ for the coupling of crack trapping and crack deflection : the effective toughness predicted numerical simulations following Eq. (4.50) (in solid black line) is compared semi-analytical predictions of homogenized dilute model (in dashed black line) (a). The non-coplanar results (in solid black line) are also compared to coplanar simulations (in dashed black line) where the sole crack trapping mechanism is taken into account, highlighting the large toughening loss (in light red) induced by inclusion by-pass (b).

As the inclusion toughness increases, by-pass interactions progressively prevail over inclusion crossing. The contribution of the by-passed inclusions to material toughening is frozen and does not increase with the inclusion toughness, while the one of the crossed inclusion keeps increasing. It accounts for the progressive loss of toughening rate. Moreover, the by-passed inclusions have a smaller contribution to material toughening than the crossed one, decreasing both the average value $\langle G_{\mathrm{c}} \rangle$ and the standard deviation σ of the equivalent coplanar distribution. The effective toughness then goes by a maximum at $G_{\mathrm{c}}^{\mathrm{inc}} \simeq 2.7\, G_{\mathrm{c}}^{\mathrm{mat}}$ and decreases for larger inclusion toughness levels.

We see that the homogenized dilute model is in excellent agreement with numerical results up to $G_{\mathrm{c}}^{\mathrm{inc}} \simeq 3.4\, G_{\mathrm{c}}^{\mathrm{mat}}$, which shows that the semi-analytical method developed here contains the fundamental ingredients for the homogenization of fracture properties under tensile loading. The homogenized dilute model reproduces with great accuracy the loss of

toughening rate as well as the position and the value of the maximum effective toughness. Above this inclusion toughness level, the homogenized model predicts a subsequent decrease of the effective toughness but over-estimates it substantially.

Such a discrepancy can have multiple origins, which can be related to each step of the homogenization procedure : the dilute approximation for the FRVE definition, the determination of the equivalent coplanar defect or the homogenization framework for coplanar propagation. In particular, the dilute hypothesis might be put at stake by large inclusion toughness ratio G_c^{inc}/G_c^{mat} since more intense by-pass events occur. It may challenge the assumption that the crack is perfectly plane when it lands on an inclusion and thus modify the way crack and inclusions interact with each other. In Fig. 4.40, we plot the respective probability of occurrence of the crossing and by-pass mechanisms during the computed interaction of a crack with a large-scale distribution of inclusions. We see that theoretical predictions from Eq. (3.27) are only valid at a low toughness ratio $G_c^{inc}/G_c^{mat} = 2$ (Fig. 4.40.a) while they differ from numerically observed interactions at high toughness ratio $G_c^{inc}/G_c^{mat} = 4$ (Fig. 4.40.b). In particular, a larger portion of inclusion is crossed, which accounts for the mismatch in the plateau value of the effective toughness curve in Fig. 4.39.

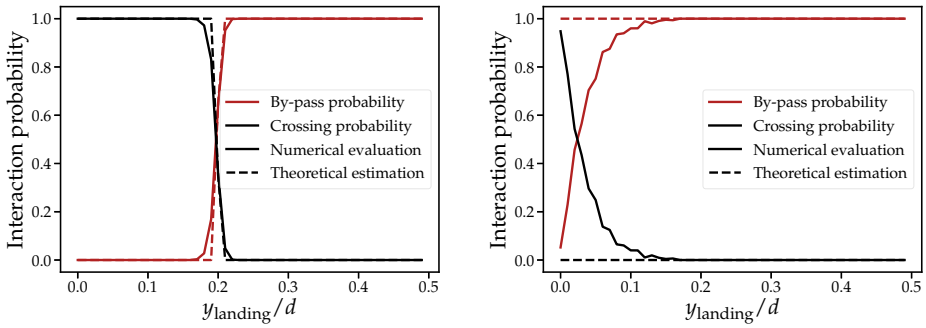

(a) $G_c^{inc} = 2\,G_c^{mat}$ (b) $G_c^{inc} = 3\,G_c^{mat}$

Figure 4.40: Probability of the crossing and by-pass mechanisms as a function of the crack landing position $y_{landing}$: the probability is calculated via numerical simulation of a crack interacting with an inclusion distribution of density $\rho_{inc} = 25\%$ and toughness $G_c^{inc} = 2\,G_c^{mat}$ (a) and $G_c^{inc} = 4\,G_c^{mat}$ (b). Numerical results in solid line are compared with theoretical predictions from Eq. (3.27) in dashed lines.

This discrepancy comes from the fact that the crack may land on an inclusion with a non-zero angle, resulting from its interaction with another inclusion met previously by the crack front, and is loaded in local mixed Mode I+II due to long-range elastic interactions along the crack front. This effect motivates the extension of the previous homogenized model to a non-dilute situation, which is described in Section 8.D.

Results of the non-dilute scheme are plotted in Fig. 4.41. We notice that the introduction of the landing angle improves the estimation of the effective toughness for large toughness ratios G_c^{inc}/G_c^{mat} without any fitting parameters. Nonetheless, the discrepancy remains substantial, suggesting that the non-dilute model should probably take into consideration the impact of the long-range elastic interactions. It constitutes a future challenge for homogenizing effective fracture properties whose basis has been established here.

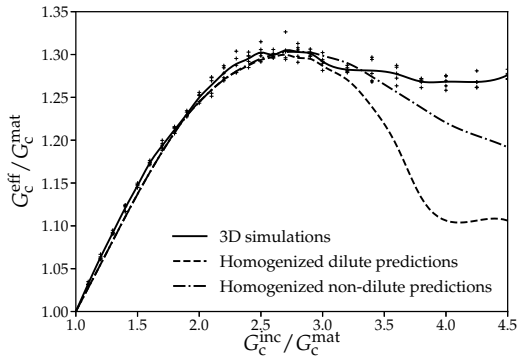

Figure 4.41: Effective toughness for a non-coplanar crack interacting with a three-dimensional monodisperse distribution of spherical inclusions of density $\rho_{\text{inc}} = 25\%$ with varying inclusion toughness G_c^{inc} (solid line) and comparison with homogenized predictions for dilute model (dashed line) and non-dilute one (dash-dotted line)

4.5 Microstructural effects on the effective toughness of heterogeneous materials

The objective of this section is twofold : (i) to investigate the impact of microstructural properties on the effective toughness of large-scale disordered systems through numerical simulations based on our perturbative approach; (ii) to validate our homogenization model by comparing numerical results to analytical homogenized predictions. On top of it, we will see that the homogenization results provide some physical insights on the effect of structural parameters on G_c^{eff}.

In the following, we study consecutively the impact on the effective fracture properties of : the system size (Section 4.5.1), the inclusion density (Section 4.5.2), the toughness disorder (Section 4.5.3) and the interface toughness (Section 4.5.4).

4.5.1 Impact of the system size

4.5.1.a Problem statement

We start by investing the impact of the system size L_z on the effective toughness. We consider a semi-infinite crack propagating in a heterogeneous medium consisting in a homogeneous matrix and a monodisperse distribution of spherical inclusions of diameter d and density $\rho_{\text{inc}} = 25\%$. The width of the system in the (Oz) direction varies from $L_z = 16\,d$ to $L_z = 512\,d$. The crack propagates along a distance $L_x = 588\,d$ to allow small-scale systems to visit enough pinning configurations. Moreover, we consider three inclusion toughness levels $G_c^{\text{inc}}/G_c^{\text{mat}} \in \{1.5, 2, 3\}$ while the interface toughness remains equal to the one of the matrix $G_c^{\text{int}} = G_c^{\text{mat}}$[3]. Simulation parameters are summarized in Table 8.15. Examples of considered distributions are given in Fig. 4.42.

[3]This hypothesis is only relaxed in Section 4.5.4.

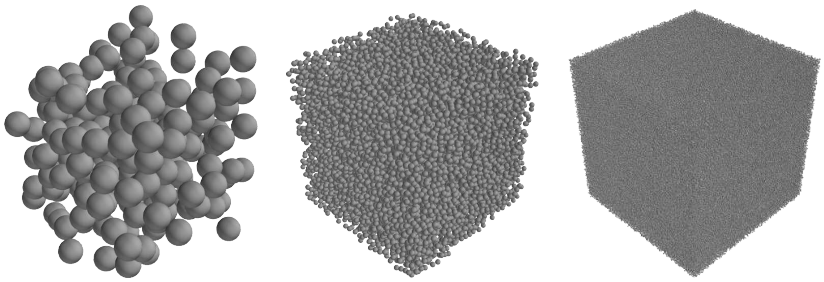

(a) $L_z = 8\,d$ (b) $L_z = 32\,d$ (c) $L_z = 128\,d$

Figure 4.42: Monodisperse spherical inclusion distribution for varying system size L_z

4.5.1.b Numerical results and comparison to model predictions

The results of the 360 simulations are plotted in Fig. 4.43. The effective toughness G_c^{eff} is plotted as a function of the system size L_z at various inclusion toughness levels (in yellow to dark red). Averaged results are plotted in solid lines while individual simulation points are depicted in cross markers. The Larkin length, extracted from the roughness of the in-plane perturbations (Eq. (4.27)) is plotted in vertical dashed lines.

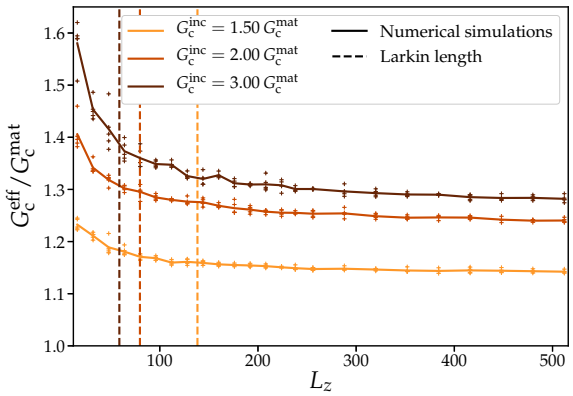

Figure 4.43: Impact of the system size L_z on the effective toughness G_c^{eff} : the effective toughness is predicted from Eq. (4.50) as the maximal macroscopic loading required to make propagate a crack interacting with a monodisperse distribution of spherical inclusions with varying size in the crack front direction ($0z$) at various inclusion toughness levels (in yellow to dark red). The Larkin length L_c where the shift of behavior occurs is plotted in dashed line.

We notice that the effective toughness is constant for large system size but increases for small L_z. This behavior is reminiscent of the in-plane problem studied in Section 4.2.2.b and the Larkin length L_c sets the position of the crossover between both regimes. As in the coplanar case, such a behavior ultimately leads to an overestimation of the effective toughness compared to the infinitely large system limit $L_z \to +\infty$. In order to define an effective toughness independent of the system size, we choose $L_z = 256\,d$ for all the following simulations.

4.5.2 Impact of the inclusion density

4.5.2.a Problem statement

We now explore the impact of the inclusion density on the effective toughness of heterogeneous materials. In the coplanar case (see Section 4.2.2.c), it has been proven to toughen efficiently the material. We consider crack propagation in large-scale monodisperse distributions of spherical inclusions of diameter d at varying density levels $\rho_{\text{inc}} \in [10\%, 50\%]$. The inclusion toughness varies from $G_{\text{c}}^{\text{inc}} = G_{\text{c}}^{\text{mat}}$ to $G_{\text{c}}^{\text{inc}} = 4.5\, G_{\text{c}}^{\text{mat}}$. Simulation parameters are summarized in Table 8.16. Examples of considered distributions are given in Fig. 4.44.

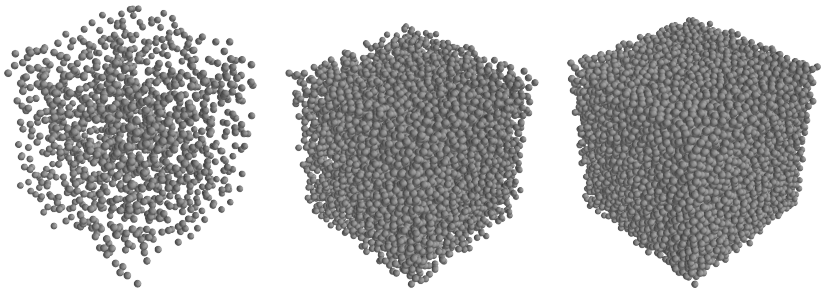

(a) $\rho_{\text{inc}} = 10\%$ (b) $\rho_{\text{inc}} = 30\%$ (c) $\rho_{\text{inc}} = 50\%$

Figure 4.44: Monodisperse spherical inclusion distribution for varying inclusion density ρ_{inc} ($L_z \times L_x \times L_x = 25d \times 25d \times 25d$ for visualization purpose)

4.5.2.b Numerical results and comparison to model predictions

The results of 480 simulations are plotted in Fig. 4.45. The effective toughness $G_{\text{c}}^{\text{eff}}$ is plotted as a function of the inclusion toughness $G_{\text{c}}^{\text{inc}}$ at various density levels ρ_{inc} (in yellow to dark red). Averaged results are plotted in solid lines while individual simulation points are depicted in cross markers. The numerical results are compared to dilute (Fig. 4.45.a) and non-dilute (Fig. 4.45.b) predictions of the homogenized model exposed in Section 4.4.

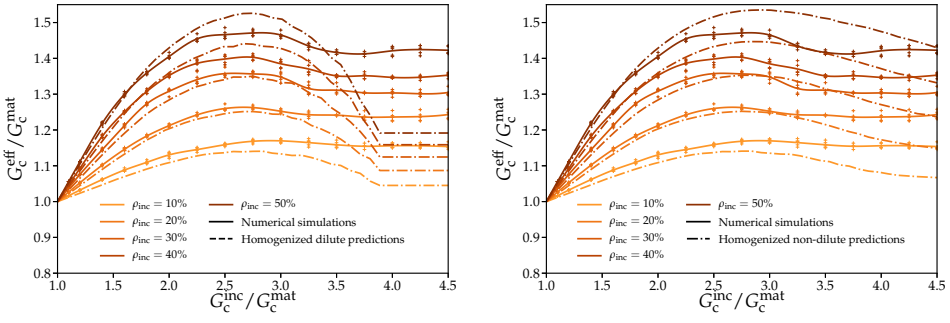

(a) (b)

Figure 4.45: Impact of the inclusion density ρ_{inc} on the effective toughness $G_{\text{c}}^{\text{eff}}$: numerical results of Eq. (4.50) in solid lines are compared to theoretical predictions of the dilute homogenized model (in dashed lines) (a) and the non-dilute one (in dash-dotted lines) (b)

Similarly to coplanar fracture, the effective toughness increases with inclusion density. From our homogenization method perspective, toughness results from the increase of the

local toughness values. Interestingly, the position of the maximum of G_c^{eff} at $G_c^{\text{inc}} \simeq 2.7\, G_c^{\text{mat}}$ does not vary with the inclusion density. It relies on the fact that it is determined by the relative contributions of the mechanisms selected by the crack (crossing or by-pass), which are independent of the inclusion density (see Section 3.3.2.b). We see that both dilute and non-dilute homogenized models give quantitative predictions up to $G_c^{\text{inc}} \simeq 3\, G_c^{\text{mat}}$, which account for a precise determination of the maximum position. We can nonetheless notice some significant differences for both high inclusion densities, where collective out-of-plane events occur, and for low inclusion densities due to finite-size effects[4]. Above $2.7\, G_c^{\text{mat}}$, the dilute model is no more quantitative at it was noticed in Section 4.4.5. Non-dilute model allows to reduce the discrepancy but the comparison remains only qualitative.

We now seek to determine an analytical expression between the inclusion density on the effective toughness. For each FRVE $\omega_F \in \Omega_F$, we first define an equivalent coplanar defect of area S_{defect} and toughness contrast c_{defect} so that the toughness field of the CRVE G_c^{cop} reads :

$$\begin{cases} G_c^{\text{cop}}(z,x) = G_c^{\text{mat}}\left[1 + c_{\text{defect}}(z,x)\right] & \text{inside the defect} \\ G_c^{\text{cop}}(z,x) = G_c^{\text{mat}} & \text{outside of it} \end{cases} \tag{4.63}$$

The reader can refer to Fig. 4.37 for examples of such a coplanar toughness field.

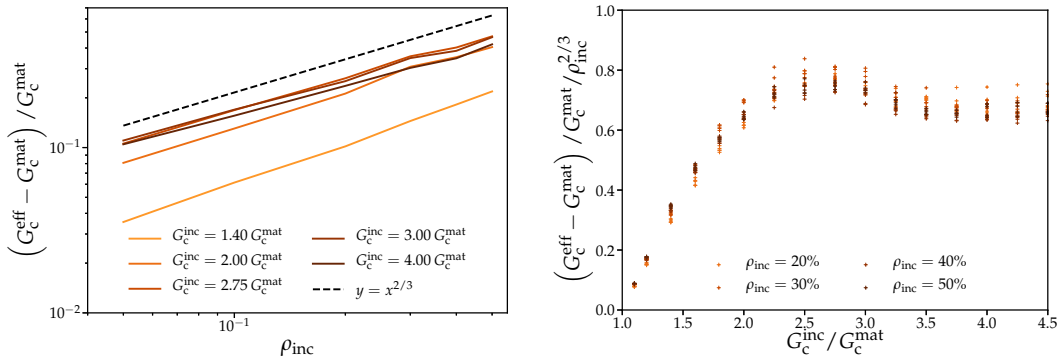

(a) (b)

Figure 4.46: Impact of the inclusion density on the effective toughness : (a) scaling between $\left(G_c^{\text{eff}} - G_c^{\text{mat}}\right)/G_c^{\text{mat}}$ and the inclusion density ρ_{inc} and comparison with the theoretical prediction of Eq. (4.65); (b) rescaling of the curves of Fig. 4.46.a using the relation (4.65)

We then use the homogenization procedure of Eq. (4.61) that provides :

$$\begin{cases} \langle G_c \rangle / G_c^{\text{mat}} = 1 + \dfrac{1}{L_\rho^2} \langle c_{\text{defect}} S_{\text{defect}} \rangle \\ \sigma^2 = \dfrac{1}{L_\rho^2} \left(\langle c_{\text{defect}}^2 S_{\text{defect}} \rangle - 2 \langle c_{\text{defect}} S_{\text{defect}} \rangle \right) + \dfrac{1}{L_\rho^4} \langle c_{\text{defect}} S_{\text{defect}} \rangle^2 \end{cases} \tag{4.64}$$

Here $\langle \cdot \rangle$ denotes the average on both the surface $L_\rho \times L_\rho$ of the CRVEs and realizations Ω_F.

[4]The crack is only pinned by rare defects and propagates in the weak pinning regime. The associated Larkin length is then larger than the system size, $L_c \leq L_z$

Using these expressions, Eq. (4.31) provides at the lowest order in ρ_{inc} :

$$\frac{G_{\text{c}}^{\text{eff}} - G_{\text{c}}^{\text{mat}}}{G_{\text{c}}^{\text{mat}}} \propto \rho_{\text{inc}}^{2/3} \tag{4.65}$$

This scaling is confronted to numerical simulations in Fig. 4.46.a. The rescaling of the effective toughness using the relation (4.65) is shown in Fig. 4.46.b.

4.5.3 Impact of the inclusion toughness disorder

4.5.3.a Problem statement

In the coplanar situation, the effective toughness has been showed to increase when the inclusions did not share the same toughness $G_{\text{c}}^{\text{inc}}$. Yet, only inclusion crossing is involved during planar crack propagation. Here, the crack can also by-pass inclusions. In particular, the toughest inclusions are likely to be by-passed, hindering the material reinforcement.

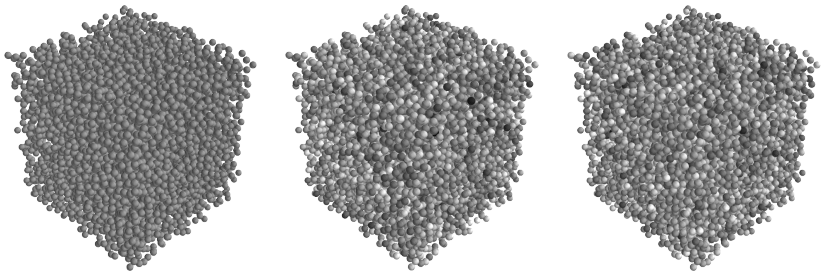

(a) $\tilde{\sigma} = 0$ (b) $\tilde{\sigma} = 1$ (c) $\tilde{\sigma} = 5$

Figure 4.47: Monodisperse spherical inclusion distribution for varying contrast disorder $\tilde{\sigma}$, with inclusion toughness represented in shade from white to black ($L_z \times L_x \times L_x = 25d \times 25d \times 25d$ for visualization purpose).

We consider here monodisperse distributions of spherical inclusions of density $\rho_{\text{inc}} = 25\%$. Contrary to the previous situations, the inclusion toughness contrast distribution c_{inc} is not constant, but follows a log-normal distribution characterized by its average $\langle c_{\text{inc}} \rangle$ and its normalized standard deviation $\tilde{\sigma} = \sigma\left(c_{\text{inc}}\right) / \langle c_{\text{inc}} \rangle$. The average toughness $\left\langle G_{\text{c}}^{\text{inc}} \right\rangle = G_{\text{c}}^{\text{mat}}\left(1 + \langle c_{\text{inc}} \rangle\right)$ varies from $G_{\text{c}}^{\text{mat}}$ to $4.5\, G_{\text{c}}^{\text{mat}}$, while the toughness disorder varies from $\tilde{\sigma} = 0$ (homogeneous inclusion toughness) to $\tilde{\sigma} = 5$ (highly dispersed inclusion toughness). Those distribution are shown in Fig. 4.12. As usual, the interface toughness is constant among the inclusions and is taken equal to the one of the matrix $G_{\text{c}}^{\text{int}} = G_{\text{c}}^{\text{mat}}$. Simulation parameters are summarized in Table 8.17. Examples of considered distributions are given in Fig. 4.47.

4.5.3.b Numerical results and comparison to model predictions

The results of 350 simulations are shown in Fig. 4.48 with the same plotting conventions as before.

We first notice that the inclusion disorder is detrimental to the effective toughness in the case of non-coplanar propagation while it was beneficial to it in the coplanar case. The

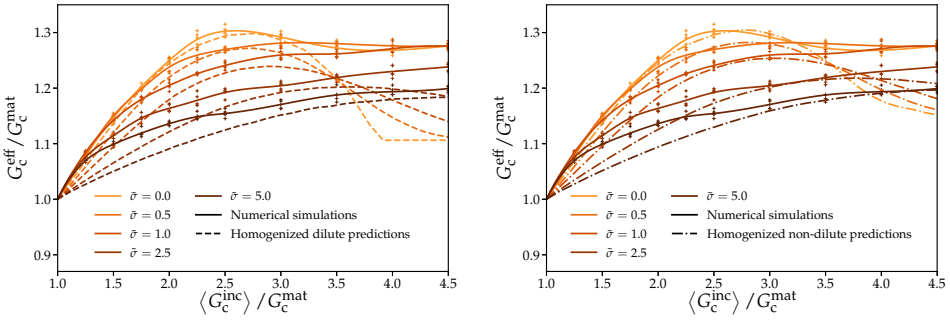

(a) (b)

Figure 4.48: Impact of the inclusion toughness disorder $\tilde{\sigma}$ on the effective toughness G_c^{eff} : numerical results of Eq. (4.50) (in solid lines) are compared to theoretical predictions of the dilute homogenized model (in dashed lines) (a) and the non-dilute one (in dash-dotted lines) (b)

larger the toughness disorder, the smaller the inclusion toughness. This can be explained by two effects, related to the spreading of the toughness inclusions its average value : (i) low toughness inclusion are now more likely to be crossed. However, their contribution to the effective toughness is lowered due to their low toughness. (ii) High toughness inclusions are more likely to be by-passed. As a result, their contribution to material toughening is reduced by the activation of a less efficient toughening mechanism.

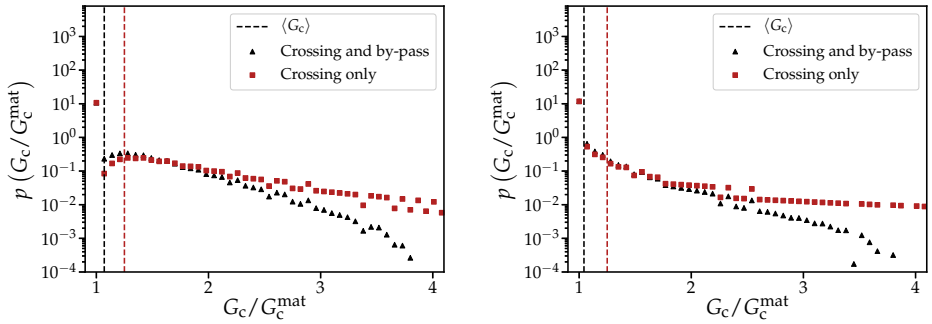

(a) $\tilde{\sigma}=1$ (b) $\tilde{\sigma}=5$

Figure 4.49: Impact of inclusion by-pass on the equivalent coplanar toughness distribution : the toughness distribution is extracted from the homogenization procedure for an inclusion toughness disorder $\tilde{\sigma}=1$ (a) and $\tilde{\sigma}=5$ (b). Red square markers corresponds to the distribution emerging from the crossing mechanism only while black triangle markers provides the actual toughness distribution taking into account both crossing and by-pass mechanisms.

To illustrate the second effect, we plot the equivalent coplanar toughness distribution computed from the dilute homogenization model for two toughness disorders (Fig. 4.49). We observe that the by-pass mechanism cuts the tail of the distribution towards lower toughness levels, thus leading to smaller values of $\langle G_c\rangle$ and in turn G_c^{eff}. Interestingly, the local maximum of the effective toughness disappears when the toughness disorder increases. Such a feature is captured qualitatively by the homogenized model.

4.5.4 Impact of the interface toughness

4.5.4.a Problem statement

We finally investigate the impact of weak interfaces on the effective toughness of disordered brittle materials. As a reminder, weak interfaces were shown to be detrimental to material toughening in the periodic case (see Section 3.7).

We consider here monodisperse distributions of spherical inclusions of density $\rho_{\text{inc}} = 25\%$. The inclusion toughness is constant and is varied from $G_{\text{c}}^{\text{inc}} = G_{\text{c}}^{\text{mat}}$ to $G_{\text{c}}^{\text{inc}} = 4.5\, G_{\text{c}}^{\text{mat}}$.The interface toughness ranges from $G_{\text{c}}^{\text{int}} = G_{\text{c}}^{\text{mat}}$ to $G_{\text{c}}^{\text{int}} = 0.6\, G_{\text{c}}^{\text{mat}}$. Simulation parameters are summarized in Table 8.18. Examples of considered distributions are given in Fig. 4.50.

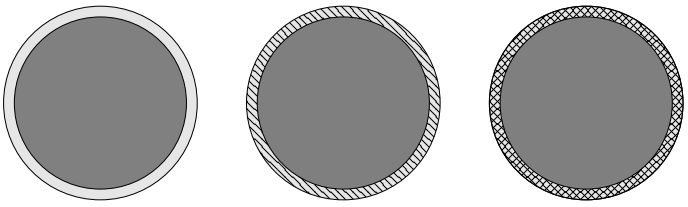

(a) $G_{\text{c}}^{\text{int}}/G_{\text{c}}^{\text{mat}} = 1$ (b) $G_{\text{c}}^{\text{int}}/G_{\text{c}}^{\text{mat}} = 0.8$ (c) $G_{\text{c}}^{\text{int}}/G_{\text{c}}^{\text{mat}} = 0.6$

Figure 4.50: Spherical inclusions with varying interface toughness $G_{\text{c}}^{\text{int}}/G_{\text{c}}^{\text{mat}}$ represented by the density of dashed lines.

4.5.4.b Numerical results and comparison to model predictions

The results of 350 simulations are shown in Fig. 4.51 with the same plotting conventions as before.

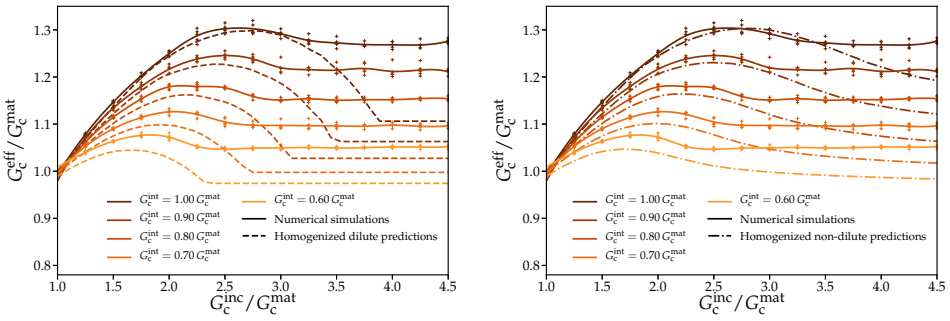

(a) (b)

Figure 4.51: Impact of a weak interface $G_{\text{c}}^{\text{int}}$ on the effective toughness $G_{\text{c}}^{\text{eff}}$ for the coupling of crack trapping and crack deflection. Numerical results of Eq. (4.50) in solid lines are compared to theoretical predictions of the dilute homogenized model in dashed lines (a) and the non-dilute one in dash-dotted lines (b)

The effective toughness decreases with the interface toughness. The regime at low inclusion toughness displays a smaller toughening rate. In addition, the position of the maximum is shifted to smaller inclusion toughness levels while the plateau value at large inclusion toughness, characteristic of the crack deflection mechanism is also reduced. All

those features are rather well captured by the homogenization framework. To understand these observations, let us remind that the competition between crossing and by-pass is controlled by the toughness ratio G_c^{inc}/G_c^{int} (Eq. (3.26)). As a result, the transition happens at a smaller inclusion toughness G_c^{inc} if the interface is weak. This explains why the maximum position is shifted towards smaller inclusion toughness levels. Moreover, for a given inclusion toughness, more inclusions are by-passed, so they do not contribute any more to the overall toughening when the inclusion toughness is increased further. This accounts for the diminution of the toughening rate during the initial linear phase. Finally, the toughening induced by crack deflection depends on the toughness of the interface, since the crack propagation along the interface during the by-pass events. In Fig. 4.52 we plot the equivalent coplanar defect for the by-pass mechanism for varying interface toughness levels. We see that the equivalent coplanar defect is less tough as the interface gets weaker. This effect accounts for the lower value of the plateau value for smaller interface toughness values.

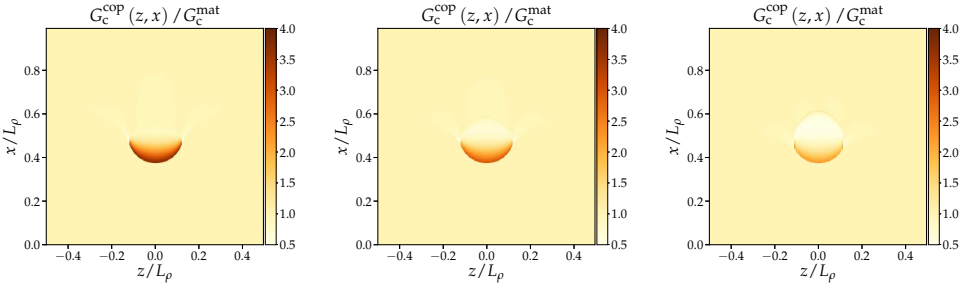

(a) (b) (c)

Figure 4.52: Equivalent coplanar toughness field for the by-pass mechanism of inclusion with weak interfaces : reference case where $G_c^{int} = G_c^{mat}$ (a) and weak interfaces with $G_c^{int} = 0.8\,G_c^{mat}$ (b) and $G_c^{int} = 0.6\,G_c^{mat}$ (c) for a crack landing on the equatorial plane of the inclusion ($y_{\text{landing}} = 0$).

4.6 Effects of the inclusion geometry on the effective toughness of disordered materials

The last part of this chapter focuses on the impact of geometrical parameters on G_c^{eff}. The inclusion shape is expected to strongly influence the effective fracture properties since : (i) it controls the interaction mechanism selection as well as its toughening contribution (see Chapter 3); (ii) the effective toughness is partly governed by the ratio ξ_z/ξ_x of the correlation lengths of the local toughness distribution. After investigating the impact of the inclusion size disorder (Section 4.6.1), we explore the influence of the first effect on disordered distributions of square inclusions (Section 4.6.2) . The second effect is put into light through textured disordered materials constituted by elongated oriented spheroidal inclusions (Section 4.6.3).

4.6.1 Impact of the inclusion size disorder

4.6.1.a Problem statement

Up to now, the inclusions all shared the same diameter d. Yet, in natural materials, the size of the heterogeneities is usually widely spread. We thus consider polydisperse distributions of spherical inclusion where the inclusion diameter d_{inc} varies from an inclusion to the other. The diameter distribution is characterized by its average value d and its standard deviation σ_d. It follows a log-normal distribution characterized by the parameters (μ_d, ς_d). Its probability density function can be expressed as :

$$f\left(d_{\text{inc}}\right) = \frac{1}{d_{\text{inc}}\varsigma_d\sqrt{2}}\exp\left[-\frac{\left(\ln(d_{\text{inc}}) - \mu_d\right)^2}{\varsigma_d^2}\right] \tag{4.66}$$

(μ_c, σ_c) are linked to d and σ_d through the following relationships :

$$\begin{cases} d = e^{\mu_d + \frac{\varsigma_d^2}{2}} \\ \sigma_d/d = e^{\varsigma_d^2} - 1 \end{cases} \Leftrightarrow \begin{cases} \mu_d = \ln\left(d\right) - \dfrac{1}{2}\ln\left[1 + \left(\dfrac{\sigma_d}{d}\right)^2\right] \\ \varsigma_d^2 = \ln\left[1 + \left(\dfrac{\sigma_d}{d}\right)^2\right] \end{cases} \tag{4.67}$$

Examples of diameter distributions are shown in Fig. 4.53.

We consider polydisperse distributions of spherical inclusions of average diameter d, size disorder σ_d and density $\rho_{\text{inc}} = 25\%$. The inclusion toughness G_c^{inc} is varied G_c^{mat} to $4.5\,G_c^{\text{mat}}$ while the interface toughness is constant and equal to the one of the matrix $G_c^{\text{int}} = G_c^{\text{mat}}$. Simulation parameters are summarized in Table 8.19. Examples of inclusion distributions are shown in Fig. 4.54.(a-c).

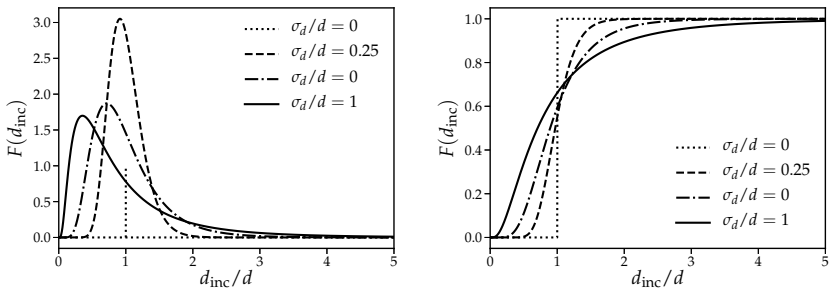

Figure 4.53: Probability density function f (a) and cumulative distribution F (b) of the inclusion diameter for various size disorder σ_d/d

4.6.1.b Numerical results and comparison to model predictions

The results of 220 simulations are plotted in Fig. 4.54 with the same plotting conventions as before. We observe that the inclusion size disorder has only a minor impact on the effective toughness of the composite material. No matter the size of the inclusion, its interaction with a crack only depends on its fracture properties G_c^{inc} and G_c^{int} and the height y_{landing} at which the crack lands on its. Thus the equivalent coplanar distribution of toughness does not depend on the inclusion size. Moreover, the effective toughness is only dictated by the ratio ξ_z/ξ_x between the average correlation lengths of the toughness distribution in the z- and x-directions, which prevent any effect of the inclusion size. This observation is nonetheless restricted to the case of inclusion sharing the same elastic properties as the matrix. Elastic heterogeneities have a non-local impact on crack propagation [Gao, 1991] and may trigger re-nucleation/de-nucleation processes [He and Hutchinson, 1989], which induce a size-dependent toughening [Leguillon et al., 2007]. The inclusion size distribution might impact the effective fracture properties in this case.

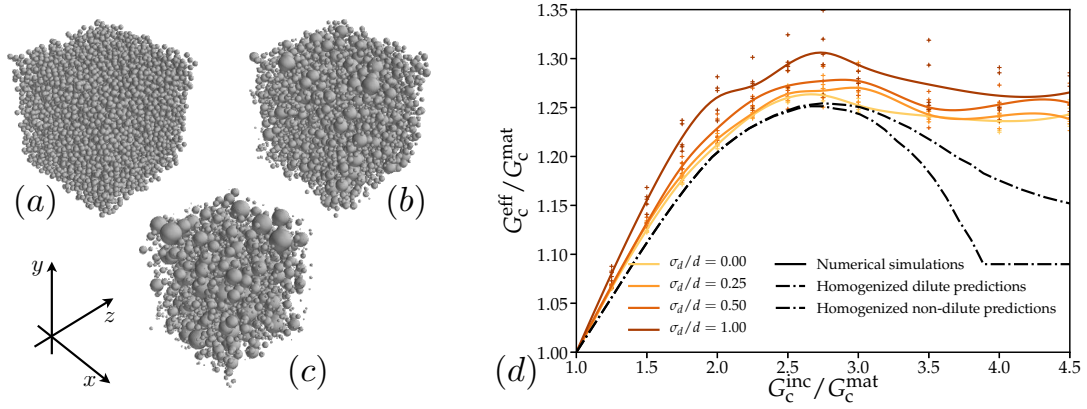

Figure 4.54: Impact of the inclusion size disorder $\sigma_d$on the effective toughness G_c^{eff} : the crack interacts with a polydisperse distribution of sphericall inclusions with various disorder parameter $\sigma_d = 0$ (a), $\sigma_d = 0.5$ (b) and $\sigma_d = 1$ (c) ; numerical results (in solid lines) are compared to dilute (in dashed lines) and non-dilute (in dash-dotted lines) homogenized predictions (d).

4.6.2 Impact of the inclusion shape

4.6.2.a Problem statement

The example of the cubical geometry has been of particular interest when investigating periodic arrays of tougher inclusions. It has been shown to reinforce composite materials in a very efficient way by triggering inclusion repenetration and improving toughening by crack deflection. One can wonder how such a behavior fares in the disordered case.

We investigate the case where the crack with large-scale monodisperse distributions of cubical inclusions of edge width d and density $\rho_{\text{inc}} = 20\%$. We make the inclusion toughness $G_{\text{c}}^{\text{inc}}$ vary $G_{\text{c}}^{\text{mat}}$ to $4.5\,G_{\text{c}}^{\text{mat}}$. Simulation parameters are summarized in Table 8.20. Examples of considered distributions are given in Fig. 4.55.a.

4.6.2.b Numerical results and comparison to model predictions

The results of 90 simulations are plotted in Fig. 4.55 in solid black line. They are compared to numerical results of the interaction of a crack with large-scale distributions of spherical inclusions in dash-dotted line and coplanar simulations in dashed lines. All simulations are performed for the same inclusion density $\rho_{\text{inc}} = 20\%$ to allow for quantitative comparison.

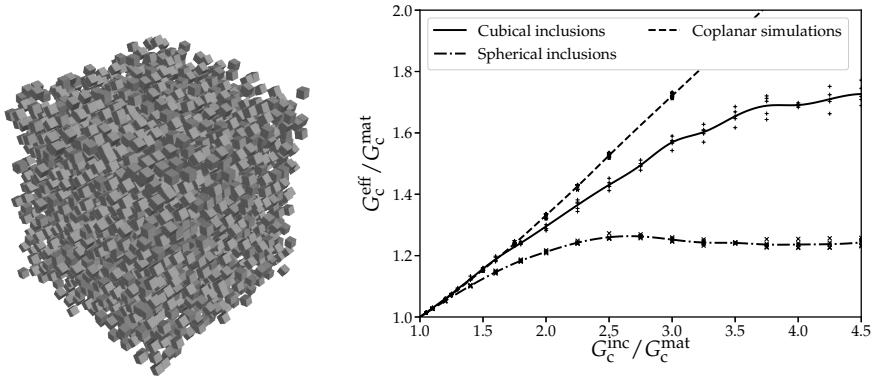

(a) (b)

Figure 4.55: Impact of the inclusion shape on the effective toughness $G_{\text{c}}^{\text{eff}}$: the effective toughness is measured from the evolution of the macroscopic loading during the interaction of a crack with a monodisperse distribution cubical (a); numerical results (in solid line) are compared to the one obtained for spherical inclusions (in dash-dotted lines) and coplanar simulations (in dashed line) (b).

We notice that cubical inclusions allow for a much more efficient reinforcement, whose origins lay in the enriched interaction mechanisms triggered by the inclusion shape. First, the cubical geometry allows for inclusion repenetration to occur, where the crack propagates inside the tough inclusion after an initial by-passing phase. Its toughening potential being thus similar to inclusion crossing (see Fig. 4.56.b), it extends the range of inclusion toughness, where the inclusion is efficiently reinforced by crack trapping, up to $G_{\text{c}}^{\text{inc}} \sim 3\,G_{\text{c}}^{\text{mat}}$. Second, the cubical geometry has been shown to improve the toughening potential of crack deflection by preventing the crack to realign with the direction of propagation (Ox) imposed

by the macroscopic loading (see Fig. 4.56.c). It accounts for the higher effective toughness plateau which appears from $G_c^{\text{inc}} \sim 3.7\, G_c^{\text{mat}}$. It also explains why we do not observe a local maximum of G_c^{eff}.

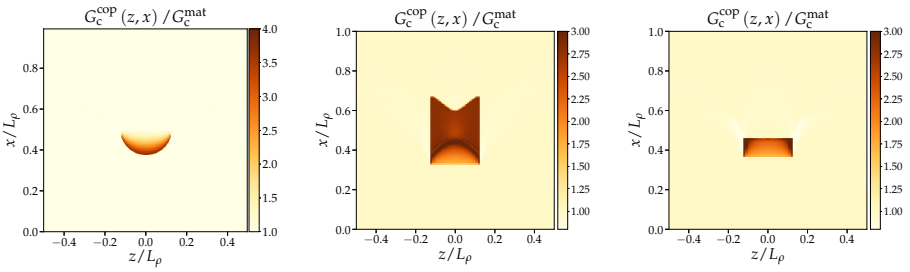

(a) (b) (c)

Figure 4.56: Equivalent coplanar toughness field for the by-pass of a tough inclusion with $G_c^{\text{inc}} = 2.8\, G_c^{\text{mat}}$: by-pass of a spherical inclusion for a crack landing at a height $y_{\text{landing}}/d = 0$ making an angle $\theta_{\text{tan}} = 60°$ with the interface (a), by-pass with crack repenetration (b) and pure-bypass (c) for a cubical inclusion inclined from an angle $\theta_{\text{tan}} = 60°$ for a crack landing respectively at a height $y_{\text{landing}}/h = 0$ and $y_{\text{landing}}/h = 0.3$

We performed simulations of crack-inclusion interaction for monodisperse distribution of cubical inclusions at varying density levels $\rho_{\text{inc}} \in \{10\%, 30\%\}$. The results are plotted Fig. 4.57 with the usual plotting conventions. The numerical results are compared with theoretical predictions of a dilute homogenized model in dashed lines.

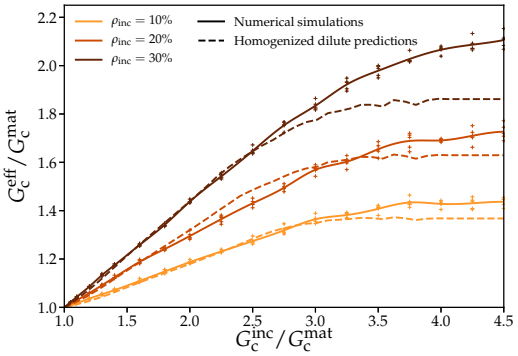

Figure 4.57: Impact of the inclusion density ρ_{inc} on the effective toughness G_c^{eff} for the coupling of crack trapping and crack deflection; numerical results of Eq. (4.50) in solid lines are compared to theoretical predictions of the dilute homogenized model in dashed lines.

The dilute homogenization framework for the interaction between a crack and cubical inclusions has been derived following the same strategy as in Section 4.4 except that (i) the FRVEs now take into account the inclination angle β_{inc} of the inclusion and (ii) the transition diagram (see Fig. 3.37) and the CRVEs (see Fig. 4.58) have been constructed numerically from tens of thousands efficient simulations on periodic arrangements of tough cubical inclusions. It ultimately allows to predict the impact of the inclusion geometry on the effective toughness under the hypothesis of dilute out-of-plane interactions.

We notice that the dilute model reproduces fairly well the impact of inclusion toughness

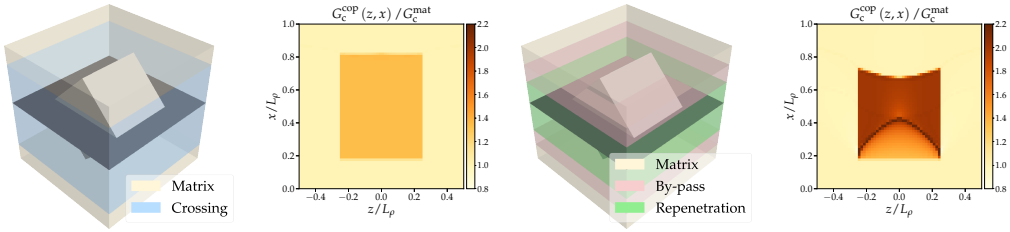

(a) (b) (c) (d)

Figure 4.58: Dilute scheme for the prediction of homogenized fracture properties of a composite material with cubical inclusions : fracture representative volume element (FRVE) for a plane crack interacting with a cubical inclusion with $G_c^{inc} = 1.35\, G_c^{mat}$ inclined at $\beta_{inc} = 45°$ through the crossing mechanism (a) and associated CRVE (b). FRVE for the interaction through repenetration and by-pass mechanisms for a with a cubical inclusion with $G_c^{inc} = 2\, G_c^{mat}$ inclined at $\beta_{inc} = 45°$ (c) and associated CRVE (d)

G_c^{inc} and inclusion density ρ_{inc} on the effective properties, especially up to $G_c^{inc} = 3G_c^{mat}$. It confirms that the proper ingredients were introduced in the homogenization framework. For large inclusion toughness, out-of-plane deviations of the crack front might impact the interaction mechanisms between neighboring inclusions, increasing the discrepancy between numerical simulations and theoretical homogenized predictions.

4.6.3 Impact of the microstructural texture

In this last part, we explore the impact of a texture in the composite micro-structure. We consider three different cases, where the principal axis of spheroidal prolate inclusions is oriented along : (i) the direction perpendicular to the crack surface (Oy), (ii) the propagation direction (Ox) and (iii) the front direction (Oz). It gives rise to strongly anisotropic effective fracture properties that are well captured by our homogenization scheme.

4.6.3.a Anisotropy in the perpendicular direction (Oy)

Problem statement

We first investigate the case where the inclusions are oriented in the (Oy) direction, perpendicular to the crack surface. Investigated in the case of periodic arrangements in Section 3.6, such an inclusion geometry has been shown to increase the reinforcement induced by the crack deflection mechanism, even above crack trapping for elongated enough inclusions.

We consider monodisperse distributions $L_z \times L_x \times L_y = 256 d_z \times 288 d_z \times 16 d_z$ of elongated prolate spheroidal inclusions oriented in the y-direction and of density $\rho_{inc} = 20\%$. Three inclusion elongations are considered : a spherical inclusion $d_y = d_z = d_x$, a moderately elongated spheroidal inclusion $d_y = 2\, d_z = 2\, d_x$ and a largely elongated one $d_y = 4\, d_z = 4\, d_x$. Simulation parameters are summarized in Table 8.21. Examples of considered distributions are given in Fig. 4.59.(a-c).

Numerical results and comparison to model predictions

The results of 80 simulations are shown in Fig. 4.63.d. The effective toughness G_c^{eff} is plotted as a function of the inclusion toughness G_c^{inc} for various elongation ratio d_x/d_z (in yellow to dark red) and then compared to theoretical predictions of a dilute scheme developed

for ellipsoidal inclusions (in dashed lines) and coplanar simulations (in dashed-dotted black line).

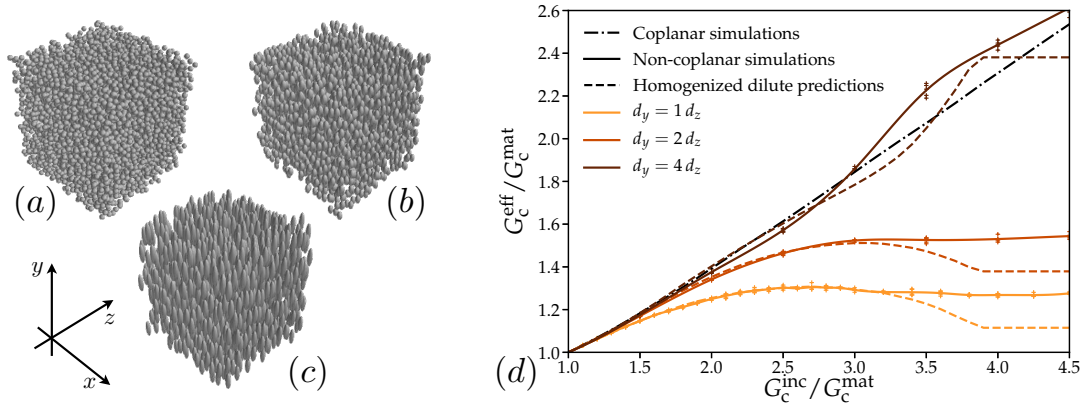

Figure 4.59: Impact of the elongation ratio d_y/d_z on the effective toughness G_c^{eff} : the crack interacts with a monodisperse distribution of prolate spheroidal inclusions oriented in the y-direction with various elongation ratio $d_y = d_z$ (a), $d_y = 2\,d_z$ (b) and $d_y = 4\,d_z$ (c) ; numerical results (in solid lines) are compared to homogenized predictions (in dashed lines) and coplanar simulations (in dash-dotted black line)(d).

We notice that an increase in the elongation ratio of the inclusion can induce a substantial reinforcement of the composite material. In Fig. 4.59.a, we observe that in some cases, the effective toughness can even overtake the value corresponding to coplanar propagation. When the crack by-passes such an inclusion, it propagates in the tangent direction θ_{tan}, which is different from its natural propagation direction $\theta = 0°$ imposed by the macroscopic tensile loading. This appears to be very detrimental to the driving G and the by-pass thus requires a substantial load increase. Moreover, as it deviates out-of-plane, it is dragged inwards in the inclusion due to Mode II contributions induced by long-range elastic interactions, which increase even further the angle mismatch between the maximal ERR direction θ_{max} and its actual propagation direction θ_{tan} along the interface. The more elongated the inclusion in the y-direction, the harder the by-pass. Thus inclusion geometry increases the reinforcement induced by crack deflection, itself activated by the by-pass mechanism. Such a behavior can be noticed from the toughness spatial distribution of the equivalent coplanar defect for inclusion by-pass in Fig. 4.60. A more efficient deflection mechanism increases the toughness of the effective coplanar defects related to inclusion by-pass.

As before, the dilute homogenization framework for the interaction between a crack and ellipsoidal inclusions is derived following the same strategy as in Section 4.4, with the difference that the FRVE is here anisotropic. Its dimensions $L_\rho^z, L_\rho^x, L_\rho^y$ respectively in the z-, x- and y-directions read :

$$L_\rho^i = \left(\frac{\pi}{6\rho_{\text{inc}}}\right)^{\frac{1}{3}} d_i, \text{ for } i \in \{z, x, y\} \tag{4.68}$$

An example of such a FRVE is shown in Fig. 4.60.a.

The interaction mechanism can be inferred from Eq. (3.27), which happens to depict

accurately the crossing to by-pass transition in the case of elongated inclusions in the y-direction. CRVEs are constructed from hundreds of periodic simulations. Their superposition for all possible realizations finally allows for the determination of the average $\langle G_c \rangle$, standard deviation $\sigma(G_c)$, and correlation lengths ξ_z, ξ_x of the equivalent coplanar distribution under the ergodic assumption. Eq. (4.31) finally allows for the predictions of the effective toughness.

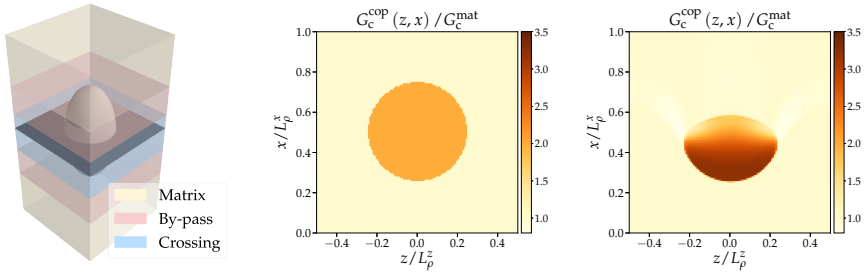

(a) (b) (c)

Figure 4.60: Dilute scheme for the prediction of homogenized fracture properties of a composite material with ellipsoidal inclusions elongated along the direction (Oy) : fracture representative volume element (FRVE) for a plane crack interacting with a ellipsoidal inclusion of elongation ratio $d_y/d_z = 2$ at a height $y_{\text{landing}} = 0.1\, d_y$ (a). Associated CRVE for the crossing interaction at $G_c^{\text{inc}} = 2\, G_c^{\text{mat}}$ (b) and the by-pass interaction $G_c^{\text{inc}} = 3\, G_c^{\text{mat}}$ (c)

We see in Fig. 4.59.d that the dilute model captures quantitatively the impact of the elongation ratio for inclusions up to $G_c^{\text{inc}} = 3\, G_c^{\text{mat}}$ and that it remains qualitatively correct above those levels.

4.6.3.b Anisotropy in the propagation direction (Ox)

Problem statement

We investigate now the case where the inclusions are oriented in the (Ox) direction, parallel to the propagation direction. The results in the periodic case have not been discussed in Chapter 3 since they gave the same results as the spherical inclusions. It is thus of particular interest to explore how those observations fare in the disordered case.

We first consider monodisperse distributions $L_z \times L_x \times L_y = 256 d_z \times 288 d_z \times 16 d_z$ of ellipsoidal inclusions elongated in the x-direction for a density $\rho_{\text{inc}} = 20\%$. We consider the same elongation ratio d_x/d_z as before. Simulation parameters are summarized in Table 8.21. Examples of considered distributions are given in Fig. 4.61.(a-c).

Numerical results and comparison to model predictions

The results of 80 simulations are shown in Fig. 4.61.d. The effective toughness G_c^{eff} is plotted as a function of the inclusion toughness G_c^{inc} for various elongation ratio d_x/d_z (in yellow to dark red) and then compared to theoretical predictions of the dilute scheme developed for ellipsoidal inclusions.

Whereas the effective toughness is increased when the inclusions are elongated along the y-direction, those oriented along the x-direction render the material weaker. This reduction in the material toughening comes from two mechanisms :

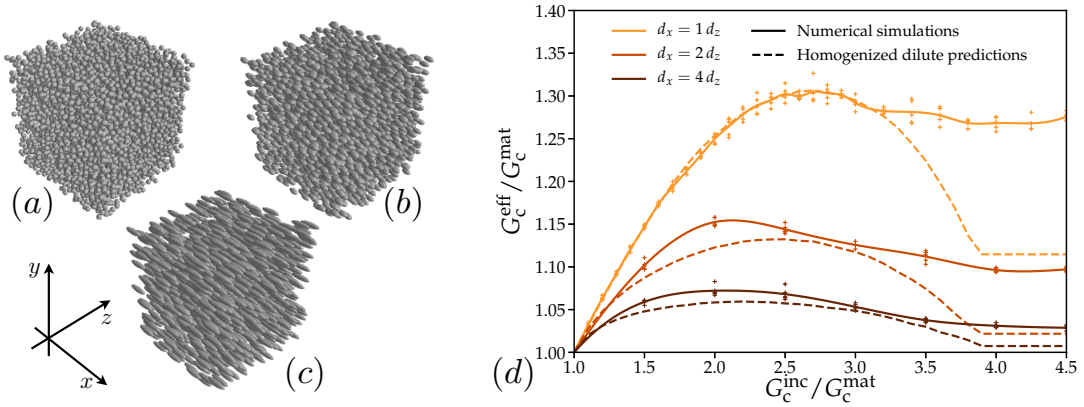

Figure 4.61: Impact of the elongation ratio d_x/d_z on the effective toughness G_c^{eff} : the crack interacts with a monodisperse distribution of prolate spheroidal inclusions oriented in the x-direction with various elongation ratio $d_x = d_z$ (a), $d_x = 2\,d_z$ (b) and $d_x = 4\,d_z$ (c) ; numerical results (in solid lines) are compared to homogenized predictions (in dashed lines).

1. first, the theoretically predicted effective toughness increases with the ratio ξ_z/ξ_x (see Eq. (4.31)), which is proportional to d_z/d_x, at least for crossed inclusions. Thus, the disorder-induced toughening is expected to decrease for inclusions elongated along the x-direction. It accounts for the lesser initial toughening rate at low inclusion toughness levels, where the inclusions are mainly crossed ;

2. second, the effective coplanar defect for inclusion by-pass (see Fig. 4.62c) vanishes very quickly in the x-direction. Above the by-pass transition threshold, the average $\langle G_c \rangle$ and the standard deviation $\sigma\,(G_c)$ of the equivalent coplanar distribution of toughness decrease, leading to a lesser toughening by crack deflection. It explains both the shift of the maximum position and the lowered plateau value.

The dilute homogenization framework for the interaction between a crack and ellipsoidal inclusions can be derived following the same strategy as for the y-direction. To each FRVE is associated with a CRVE (Fig. 4.62.) resulting from the interaction mechanism inferred from Eq. (3.27), which depicts accurately the crossing to by-pass transition in this case. The effective toughness is estimated analytically from the superposition of all CRVEs, which are computed numerically from efficient periodic simulations.

We see that the homogenized dilute predictions capture well the simulations. Yet some discrepancy is noticeable such as the position of the maximum for moderately elongated inclusions. The results are nonetheless satisfying and reproduce fairly well the impact of the fiber elongation along the propagation direction.

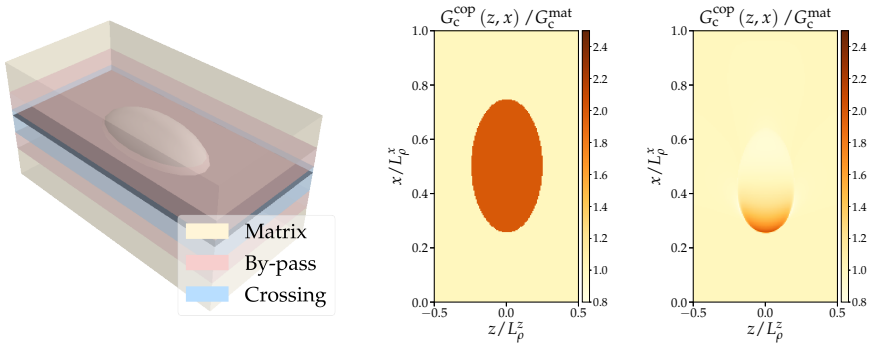

(a) (b) (c)

Figure 4.62: Dilute scheme for the prediction of homogenized fracture properties of a composite material with ellipsoidal inclusions elongated along the direction (Ox) : fracture representative volume element (FRVE) for a plane crack interacting with a ellipsoidal inclusion of elongation ratio $d_x/d_z = 2$ at a height $y_{\text{landing}} = 0.1\, d_y$ (a). Associated CRVE for the crossing interaction at $G_c^{\text{inc}} = 2\, G_c^{\text{mat}}$ (b) and the by-pass interaction $G_c^{\text{inc}} = 3\, G_c^{\text{mat}}$ (c)

4.6.3.c Anisotropy in the front direction (Oz)

Problem statement

To close the loop, we finally investigate the case where the inclusions are oriented in the direction (Oz), parallel to the crack front direction. In the periodic case, such an inclusion shape has been proved to facilitate inclusion by-pass through three-dimensional collective effects along the crack front. This early by-pass is expected to lower the effective toughness in a disordered setting too.

We thus consider monodisperse distributions $L_z \times L_x \times L_y = 256 d_z \times 288 d_z \times 16 d_z$ of spheroidal prolate inclusions elongated along the z-direction for a density $\rho_{\text{inc}} = 20\%$. Three inclusion elongations are considered : the spherical case $d_x = d_z = d_y$, a moderately elongated inclusion $d_z = 0.5\, d_x = 0.5\, d_y$ and a largely elongated one $d_z = 0.25\, d_x = 0.25\, d_y$. We chose here to reduce the elongation in the x- and y-direction to keep the ratio L_z/d_z constant and thus remove the impact of the system size. Simulation parameters are summarized in Table 8.21. Examples of considered distributions are given in Fig. 4.63.(a-c).

Numerical results and comparison to model predictions

The results of 80 simulations are shown in Fig. 4.63.d. The effective toughness G_c^{eff} is plotted as a function of the inclusion toughness G_c^{inc} for various elongation ratio d_z/d_x (in yellow to dark red) and then compared to theoretical predictions of a dilute scheme developed for ellipsoidal inclusions.

We saw in Section 3.4, that by-pass mechanisms are facilitated in the case of elongated inclusions oriented along the z-direction of the crack front, which leads to a decrease of the effective toughness in a periodic setting. Given that crack deflection is a less efficient mechanism, we expect the effective toughness to decrease with the fiber elongation. Yet, it is noticeable in Fig. 4.63, the effective toughness remains almost the constant for the three elongation ratios. If the deflection mechanisms indeed appear to be less efficient (see

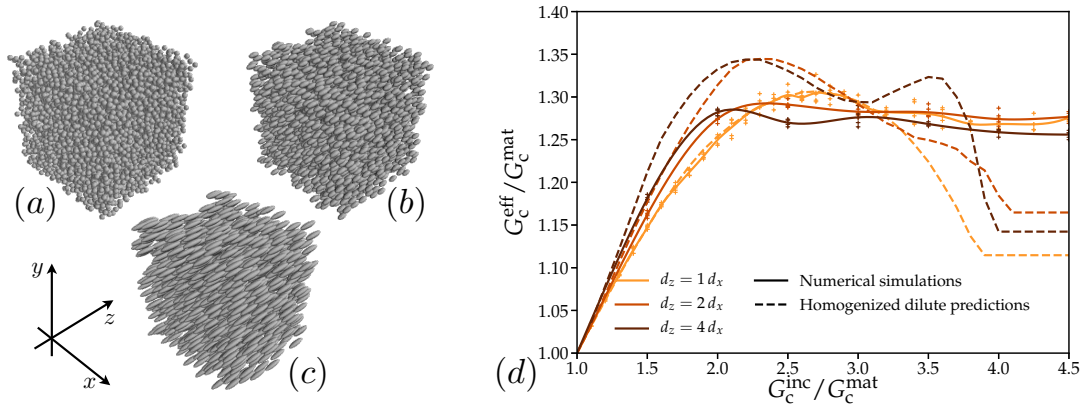

Figure 4.63: Impact of the elongation ratio d_z/d_x on the effective toughness G_c^{eff} : the crack interacts with a monodisperse distribution of prolate spheroidal inclusions oriented in the z-direction with various elongation ratio $d_z = d_x$ (a), $d_z = 2\,d_x$ (b) and $d_z = 4\,d_x$ (c) ; numerical results (in solid lines) are compared to homogenized predictions (in dashed lines).

Fig. 4.64c), the effective toughness depends on the ratio $\xi_z/\xi_x \sim d_z/d_x$, which increases here with the elongation and compensates the toughness decrease due to the early by-pass of the inclusions. It also accounts for the slightly improved toughening rate at low inclusion toughness where the inclusions are mainly crossed.

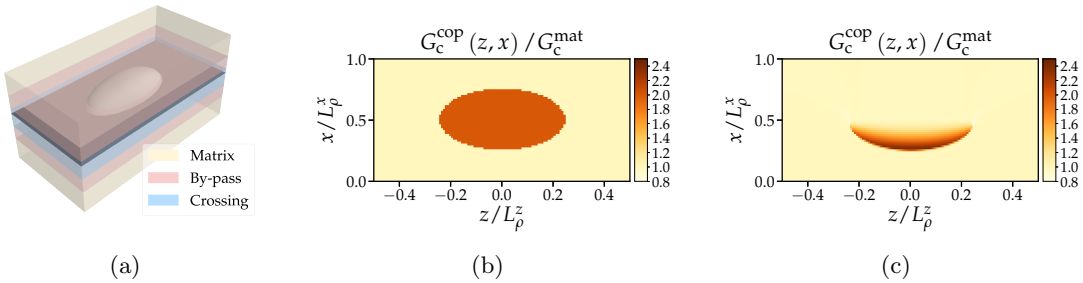

Figure 4.64: Dilute scheme for the prediction of homogenized fracture properties of a composite material with ellipsoidal inclusions elongated along the direction (Oz) : fracture representative volume element (FRVE) for a plane crack interacting with a ellipsoidal inclusion of elongation ratio $d_z/d_x = 2$ at a height $y_{\text{landing}} = 0.1\,d_y$ (a). Associated CRVE for the crossing interaction at $G_c^{\text{inc}} = 2\,G_c^{\text{mat}}$ (b) and the by-pass interaction $G_c^{\text{inc}} = 3\,G_c^{\text{mat}}$ (c)

The dilute homogenization framework is derived following the same strategy, with the sole difference that the crossing to by-pass transition is inferred from numerical simulations (see Fig. 3.26 and Fig. 3.27). The predictions of the homogenized model are in qualitative accordance with the numerical results. The initial increase in the toughening rate is captured as well as the shift in the position of the maximum towards smaller inclusion toughness values. The value of the maximum is nonetheless a bit overestimated. Such an effect might be due to the overestimation of the effective toughness for large elongation ratio in the direction of the crack front as it was observed in the coplanar case (see Section 4.2.2.f). Finally, we notice that for a large elongation ratio $d_z/d_x = 4$, the homogenized dilute model presents a second local maximum. Such a feature can be observed

around the same inclusion toughness levels in our numerical simulations.

To conclude, we notice that introducing texture in the microstructure at a small scale results in toughness anisotropy at a large scale. The toughening induced by the microstructure strongly depends on the direction of propagation of the crack. It may pave the way for functionalizing materials displaying unique toughness properties as it has been proposed by Xia et al. [2013] for the coplanar adhesive problem.

4.7 Concluding remarks

This chapter was dedicated to the homogenization of fracture properties both from a numerical and theoretical point of view. We first revisited the concept of effective toughness G_c^{eff}, and unified the three definitions proposed so far, namely :

1. the effective toughness as the averaged fracture energy dissipated by the fracture process $\left\langle G_c^{\text{frac}} \right\rangle$;
2. the average value G^{∞}_{mean} of the ERR during crack evolution, taking advantage of the coupling between the material problem and the structural one;
3. the maximum value G^{∞}_{max} of the ERR during crack evolution.

In particular, we showed that these three definitions converge to a single value under the condition that the structural length $\mathcal{L}$, characteristic of the loading variations, is large enough with respect to the characteristic microstructural size, the inclusion size d. Such a condition is standard in the homogenization theory but the fact that it involves $\mathcal{L}$, which is related to the structural problem and the boundary conditions, highlights the specificities of brittle fracture.

Numerical simulations on large-scale disordered systems, computed from the model described in Chapter 2, have been conducted to investigate the impact of microstructural disorder on the effective toughness. Our results illustrate that material disorder plays a decisive role in the determination of the effective fracture properties so that estimating the effective toughness from periodic situations can produce results which are both quantitatively and qualitatively wrong. These numerical results have then been compared to theoretical predictions derived from the homogenization scheme developed in Section 4.4. Inspired by micromechanics and statistical physics, it extends the approach of Démery et al. [2014a], limited to planar crack propagation to fully 3D fracture, to incorporate the crucial effect of inclusion by-pass on the resulting effective fracture properties.

It relies on an accurate description of both the conditions under which each mechanism is taking place and its subsequent toughening contribution, which have been thoroughly investigated in Chapter 3. As seen in Section 4.5 and Section 4.6, this homogenization method has been shown to successfully capture the impact of by-pass mechanism on the effective toughness of heterogeneous brittle materials, as well as the one of various microstructural (inclusion density, toughness disorder, weak interfaces) and geometrical (size disorder, inclusion shape, inclusion orientation) parameters. It has been shown to produce

quantitative predictions for inclusion up to 3.4 tougher than the matrix $G_c^{inc} \simeq 3.4\, G_c^{mat}$, for densities as large as $\rho_{inc} = 50\%$. Above this toughness level, collective effects emerging from the out-of-plane deviations of the crack front cannot be neglected anymore. To take into account the interactions between neighboring inclusions during their interaction with the crack front, a non-dilute scheme has been proposed. It significantly improves our predictions, even though it does not allow a perfect match between numerical results and theoretical predictions.

Both numerical and theoretical results highlight the substantial impact on material reinforcement of a wide range of microstructural parameters, from which one can infer guidelines for microstructural design :

- no matter the toughening mechanism involved, the toughness increase has been shown to scale with the inclusion density as $\rho_{inc}^{2/3}$;
- the by-pass mechanism is detrimental to material reinforcement since it activates crack deflection whose contribution to material toughening is often lesser than crack trapping ;
- the interface between the inclusion and the matrix should have a toughness as close as possible to the one of the matrix to delay inclusion by-pass ;
- one can play on the inclusion geometry to defer inclusion by-pass by promoting inclusion repenetration. One can use cubical inclusions or alternatively pellets to promote such a mechanism ;
- one can tune the material texture to control the toughness anisotropy of the material. It has been shown that the toughness varies substantially depending on the direction of the incoming crack in the case of spheroidal prolate inclusions.

Even though this method has been here applied to the crossing, by-pass and repenetration mechanisms, it has been designed to allow for the homogenization of brittle fracture properties in a much wider scope. In a first step, elementary toughening mechanisms, such as inclusion debonding or crack de-nucleation/re-nucleation at an elastic interface, could be modeled accurately through powerful computational methods such as phase-field simulations, which allow nowadays to tackle the single inclusion problem in all its complexity. And then, their effect on the toughness of disordered solids could be deduced from the homogenization scheme by looking at the way the crack front deforms in-plane during its interaction with an inclusion, just as it has been performed here for both the crossing and the by-pass mechanisms. This study then sets up the foundations for homogenizing brittle fracture properties of three-dimensional composite materials in all their complexity, thus paving the way to integrate a wide variety of microscopic fracture mechanisms into a unified theoretical homogenization framework relying on statistical physics.

5

Deciphering fracture surfaces of brittle materials

Contents

5.1 Introduction

Fracture surfaces, as persistent traces of crack propagation, contain unexpected information on the broken material and its mechanical properties, the applied loading conditions during failure as well as the microscopic fracture processes which took place at the crack tip during crack propagation. Fractography, the study of fracture surfaces, tackles this challenge and aims at understanding what caused structural failure and identifying the underlying fracture processes from their examination. It relies on the observation of the fracture surfaces from the microscopic scale (through scanning or transmission electron microscopy) to the macroscopic scale (through optical microscopy) and the subsequent identification of fracture patterns (e.g. chevrons, beach or ratchet marks, ridges, shear lips). Fractography allows for a qualitative understanding of the material failure behavior. Yet, recent developments in the mechanics and physics of fracture have led to a new approach referred to as *statistical fractography* that relies on the statistical analysis of the fracture surface topography.

The statistical properties of fracture surfaces were first studied in the pioneer work of Mandelbrot et al. [1984]. Fracture surfaces have been shown to display a peculiar scaling behavior referred to as *self-affinity*. It means that they are statistically invariant under the transformation $\underline{r} \to \lambda \underline{r}$ and $h \to \lambda^{\zeta} h$, where $\underline{r}$ characterizes a location in the mean fracture plane, h is the surface elevation, and ζ is the so-called self-affine or Hurst exponent. Early experimental studies performed on a wide range of materials (metallic alloys [Mandelbrot et al., 1984; Bouchaud et al., 1990; Dauskardt et al., 1990; Morel et al., 2004]), ceramics [Mecholsky et al., 1989], silica glass [Ponson et al., 2006b; Ponson, 2007], rocks [Schmittbuhl et al., 1995; Lôpez and Schmittbuhl, 1998], mortar [Mourot et al., 2005] or wood [Engøy et al., 1994; Morel et al., 1998]) suggested that the roughness exponent might have an universal value $\zeta \simeq 0.8$. Fracture surfaces have latter been shown to exhibit anisotropic scaling [Ponson et al., 2006b; Bonamy et al., 2006; Ponson, 2007], with a larger roughness exponent $\zeta \simeq 0.8$ in the direction of the crack front than in the propagation direction $\beta \simeq 0.6$. Additionally, fracture experiments on sandstone [Boffa and Allain, 1998; Ponson et al., 2007] or artificial materials composed of sintered glass/polystyrene beads [Ponson et al., 2006a; Cambonie et al., 2015] evidenced a new class of fracture roughness characterized by a lower exponent $\zeta \simeq 0.4 - 0.5$. The first type of roughness, characterized by a high roughness exponent $\zeta \simeq 0.8$, has been shown to emerge from damage percolation processes happening below the process zone size ℓ_{FPZ} in ductile or quasi-brittle materials [Hansen and Schmittbuhl, 2003] while the second class $\zeta \simeq 0.4$ is attributed to brittle processes [Bonamy et al., 2006]. Morel et al. [2008] studied the surface roughness of mortar and confirmed experimentally that a high exponent regime $\zeta \simeq 0.8$ is indeed found at length scales below the process zone size while a second regime with $\zeta \sim 0.4$ is observed at large length scales, above ℓ_{FPZ}. Those experimental observations were latter supported by Vernède et al. [2015] on various materials (aluminum alloy, mortar, ceramics).

The quantitative study of fracture surfaces presents two main challenges today : first, from a more academic perspective, the mechanisms leading to the brittle regime of roughness remains poorly understood since experiments on brittle porous rocks produce self-affine surfaces with $\zeta \simeq 0.4$ [Boffa and Allain, 1998; Ponson et al., 2006a; Cambonie et al., 2015] while fracture tests of phase-separated [Dalmas et al., 2008] or oxide brittle glass [Pallares et al., 2018] generate logarithmically rough surfaces, as predicted theoretically [Ramanathan et al., 1997] and observed numerically [Barès et al., 2014] for crack propagation in disordered brittle materials. Today, there is no clear understanding of the mechanisms that control the transition from the logarithmic to the self-affine ($\zeta \simeq 0.4$) roughness. Secondly, from a more engineering perspective, fractographic methods based on the scaling properties of fracture surfaces have been developed recently to extract quantitative information from the surface roughness. Ponson [2007] used the scaling anisotropy to find back the propagation direction of the crack from the fracture surfaces. More recently, Vernède et al. [2016] took advantage of the existence of two self-affine regimes to extract quantitative information on the process zone size ℓ_{FPZ} and ultimately on the toughness G_{c}. Such experimental methods have been further validated with numerical simulations of heterogeneous ductile fracture [Osovski et al., 2015; Barak et al., 2019]. Yet one can wonder how such methods can be

adapted to purely brittle failure where only one roughness regime, a self-affine one with $\zeta \sim 0.4$ or a logarithmic one, can be observed on the fracture surface.

This chapter addresses both these challenges by investigating the surface roughness of brittle composites constituted by toughness heterogeneities. Section 5.2 is devoted to the theoretical analysis of fracture surface statistics. The full 2D statistical structure of the surface roughness is predicted for the first time. It is shown to be logarithmic with an anisotropic scaling. In Section 5.3, these theoretical predictions are compared to numerical simulations of crack propagation in large-scale disordered materials. We study the impact of microstructural parameters on the surface roughness and finally quantify which information can be extracted from logarithmically rough fracture surfaces.

5.2 Theoretical predictions for the roughness of brittle materials

Since the work of Ramanathan et al. [1997], non-coplanar crack propagation in disordered brittle materials under tensile loading (Mode I) has been considered to result in logarithmically rough surfaces. This fact has been supported by both numerical simulations [Barès et al., 2014] and experimental observations [Dalmas et al., 2008]. Yet, to the author's best knowledge, the full two-dimensional structure of the height-height correlations of the fracture surface has not been established yet. This section aims at filling this gap by revisiting the problem of crack trajectory in brittle materials within the rigorous theoretical framework developed in Favier et al. [2006b].

5.2.1 Trajectory equation

5.2.1.a Crack propagation in heterogeneous materials

First, we establish the equation of motion of a semi-infinite crack propagating in a heterogeneous brittle material. As before, f_x denotes the in-plane perturbation of the crack front $\mathcal{F}$, while f_y represents its out-of-plane component. A point M of the crack front has the coordinates $(z, f_x(z,t), f_y(z,t))$. If we note h, the height profile of the fracture surface resulting from the interaction of the crack with the material disorder, it reads :

$$h\left(z, x = f_x\left(z,t\right)\right) = f_y\left(z,t\right) \tag{5.1}$$

Given that the crack angle $\theta = \arctan\left(\frac{\partial f_y}{\partial x}\right)$ remains small during crack propagation, the expression of the Mode II perturbed SIF is given by Eq. (2.14). If the crack propagated in a homogeneous phase, the (G)MERR criterion would give at first-order in the perturbation (see Section 8.D.2) :

$$\frac{\partial h}{\partial x}\left(z, x = f_x\left(z,t^+\right)\right) - \frac{\partial h}{\partial x}\left(z, x = f_x\left(z,t^-\right)\right) \sim -2\frac{\delta K_{\mathrm{II}}}{K_{\mathrm{I}}^{\infty}}\left(z,t^-\right) \tag{5.2}$$

where t^+ and t^- denote respectively the time before and after the kink event which occurs at time t.

Yet, in presence of material heterogeneities (e.g. toughness discontinuities), we saw in Chapter 3 that the crack does not follow necessarily the direction prescribed by the MERR criterion. Eq. (5.2) becomes then :

$$\frac{\partial h}{\partial x}\left(z, x=f_x\left(z,t^+\right)\right)-\frac{\partial h}{\partial x}\left(z, x=f_x\left(z,t^-\right)\right) \sim -2\frac{\delta K_{\mathrm{II}}}{K_{\mathrm{I}}^{\infty}}\left(z,t^-\right)+\eta\left(z, x=f_x\left(z,t^-\right), y=h\left(z,x\right)\right) \tag{5.3}$$

where η is a stochastic noise, which represents the discrepancy between the direction the crack would take in the homogeneous case and the one it actually takes during propagation.

Combining Eq. (2.14) with Eq. (2.14), one gets :

$$\begin{aligned}\frac{\partial h}{\partial x}\left(z, x=f_x\left(z,t\right)\right) = &-\frac{A\left(\nu\right)}{\pi}\mathrm{PV}\int_{-\infty}^{+\infty}\frac{h\left(z, x=f_x\left(z,t\right)\right)-h\left(z', x=f_x\left(z',t\right)\right)}{\left(z-z'\right)^2}dz' \\ &+\eta\left(z, x=f_x\left(z,t\right), y=h\left(z,x\right)\right)\end{aligned} \tag{5.4}$$

where $A\left(\nu\right)=\frac{2-3\nu}{2-\nu}$ is a coefficient depending on the Poisson ratio ν.

This equation is highly non-linear and resembles the coplanar equation of motion derived in Eq. (4.3). Like in the in-plane problem, the difficulties arising from the non-linearity of Eq. (5.4) can be circumvented under given hypotheses.

5.2.1.b Equation of motion in the Larkin regime

In this part, we make three main assumptions :

1. first, we follow Bonamy et al. [2006] and Barès et al. [2014] and suppose that the disorder η is quenched so that it only depends on the position of the crack front (z, x, y) and not on the time t ;
2. second, we assume that the in-plane perturbation of the crack front f_x are far smaller than the correlation length ξ_x of the disorder η in the propagation direction (Ox) so that the crack propagates in the Larkin regime. The height profile of the fracture surface $h\left(z, x=f_x\left(z,t\right)\right)$ can be defined at the mean position $x\left(t\right)=\left\langle f_x\left(z,t\right)\right\rangle_z$ of the crack front.
3. third, we neglect the dependence of η on h, assuming that the height variations are much smaller that the correlation length ξ_y if the disorder along the (Oy) direction.

Under those assumptions, the stochastic term $\eta\left(z, x, y=h\left(z,x\right)\right)$ acts effectively as "thermal" noise $\eta\left(z,x\right)$, since x varies with time.

With these hypotheses, Eq. (5.4) becomes :

$$\frac{\partial h}{\partial x}\left(z,x\right) = -\frac{A\left(\nu\right)}{\pi}\mathrm{PV}\int_{-\infty}^{+\infty}\frac{h\left(z,x\right)-h\left(z',x\right)}{\left(z-z'\right)^2}dz'+\eta\left(z,x\right) \tag{5.5}$$

We notice that the trajectory equation of the crack front in the Larkin regime is linear in h. It calls for a theoretical analysis of the surface roughness within the framework developed by Favier et al. [2006b] and already used in Section 4.2 for the in-plane situation.

5.2.2 Statistics of the fracture surface

In this section, we aim at characterizing the statistical properties of the fracture surface of brittle heterogeneous materials. As a result, we look at : the two-points height-height correlation function Δh and the power spectrum density PSD, defined as :

$$\begin{cases} \Delta h^2(\Delta z, \Delta x) = < (h(z+\Delta z, x+\Delta x) - h(z,x))^2 >_{z,x} \\ \qquad\qquad = 2 < h(z,x) >_{z,x} - 2 < h(z+\Delta z, x+\Delta x)\, h(z,x) >_{z,x} \\ \mathrm{PSD}(k) = < \hat{h}\hat{h}^*(k,x) >_x \end{cases} \tag{5.6}$$

where a^* denotes the conjugate of the complex variable a and $\hat{h}$ the Fourier transform with respect to the z variable of the function h.

5.2.2.a Mathematical framework for statistics calculation

We see in Eq. (5.6) that we have to estimate averages over the crack front. Following Favier et al. [2006b], we consider ensemble averages, where one looks, at one point of coordinates (z,x), for multiple front configurations resulting from the interaction of a three-dimensional crack with multiple disordered systems. The *ergodic assumption* consists in assuming that ensemble averages are equivalent to averages over the crack surface.

In the following, we consider a statistical ensemble Ω of possible realizations of a heterogeneous material associated to a specific real number ω. We note $p : \omega \mapsto p(\omega)$ its probability density function. Thus, the probability that the variable ω' lies in some neighborhood of ω of measure $d\omega$ is $p(\omega)\, d\omega$. The mathematical expectation $E[u(x,z)]$ of any spatial observable $u : (x,z) \mapsto u(x,z)$ is defined as :

$$E[u(x,z)] = \int_\Omega u(x,z;\omega)\, p(\omega)\, d\omega \tag{5.7}$$

The 2-point auto-correlation function $E[u(z_2,x_2)\, u(z_1,x_1)]$ thus reads :

$$E[u(z_2,x_2)\, u(z_1,x_1)] = \int_\Omega u(z_2,x_2;\omega)\, u(z_1,x_1;\omega)\, p(\omega)\, d\omega \tag{5.8}$$

Following the method developed by Favier et al. [2006b], we note $\widetilde{E[u_1 u_2]}(k_1,x_1,k_2,x_2)$ the double (z_1,z_2)-Fourier transform of the function $E[u(z_2,x_2)\, u(z_1,x_1)]$. One can easily prove that :

$$\widetilde{E[u_1 u_2]}(k_1,x_1,k_2,x_2) = E[\hat{u}(k_1,x_1)\, \hat{u}(k_2,x_2)] \tag{5.9}$$

Moreover, if the spatial observable u is statistically invariant in both the (Oz) and (Ox) directions, one gets :

$$\begin{aligned} & E[u(z_2,x_2)\, u(z_1,x_1)] = \mathcal{U}(z_2-z_1, x_2-x_1) \\ \Rightarrow \quad & \widetilde{E[u_1 u_2]}(k_1,x_1,k_2,x_2) = 2\pi\delta(k_2+k_1)\, \hat{\mathcal{U}}(k_2, x_2-x_1) \end{aligned} \tag{5.10}$$

5.2.2.b Two-dimensional surface roughness in the Larkin regime

Thanks to the mathematical framework developed above, we can study the roughness of brittle fracture surfaces. Assuming that the crack front is initially flat, i.e. $h(z,0)=0$, Eq. (5.5) gives :

$$\hat{h}(k,x) = e^{-A(\nu)|k|x}\int_0^x \tilde{\eta}(k,u)\, e^{A(\nu)|k|u} du \tag{5.11}$$

Combining Eq. (5.11) with Eq. (5.9), one gets :

$$\begin{aligned}\widetilde{E[h_1 h_2]}(k_1,x_1,k_2,x_2) =& e^{-A(\nu)(|k_1|x_1+|k_2|x_2)} \\ &\cdot \int_0^{x_1}\int_0^{x_2} \widetilde{E[\eta_1\eta_2]}(k_1,u_1,k_2,u_2)\, e^{A(\nu)(|k_1|u_1+|k_2|u_2)} du_1 du_2\end{aligned} \tag{5.12}$$

We assume here that the material disorder η is statistically invariant in both the crack front direction (Oz) and the propagation direction (Ox) so that one can write :

$$E[\eta(z_1,x_1)\,\eta(z_2,x_2)] = \mathcal{N}(z_2-z_1, x_2-x_1) \tag{5.13}$$

The disorder correlations are assumed to be characterized by the correlation lengths ξ_z and ξ_x respectively in the crack front direction and the propagation direction. By exploiting the statistical invariance of η in Eq. (5.13) with Eq. (5.11), Eq. (5.12) finally gives :

$$\begin{aligned}\widetilde{E[h_1 h_2]}(k_1,x_1,k_2,x_2) =& 2\pi\delta(k_2+k_1)\, e^{-A(\nu)(|k_1|x_1+|k_2|x_2)} \\ &\cdot \int_0^{x_1}\int_0^{x_2} \hat{\mathcal{N}}(k_2,u_2-u_1)\, e^{A(\nu)(|k_1|u_1+|k_2|u_2)} du_1 du_2\end{aligned} \tag{5.14}$$

The statistical invariance of η is preserved in h (see Eq. (5.5)), thus :

$$E[h(z_1,x_1)\,h(z_2,x_2)] = \mathcal{H}(z_2-z_1, x_2-x_1) \tag{5.15}$$

Identifying terms in Eq. (5.14), one gets :

$$\hat{\mathcal{H}}(k,x_2-x_1) = e^{-A(\nu)|k|(x_1+x_2)}\cdot\int_0^{x_1}\int_0^{x_2}\hat{\mathcal{N}}(k,u_2-u_1)\, e^{A(\nu)|k|(u_1+u_2)} du_1 du_2 \tag{5.16}$$

Using Eq. (5.16), we shall now derive the asymptotic expression of the power spectrum density of h. Our reasoning is based on the argument of domination of the diagonal in integration over the square $[0,x_1]\times[0,x_2]$ [Perrin and Rice, 1994]. Use of the change of variables defined by :

$$r = \frac{1}{2}(u_1,u_2),\ s = u_2-u_1 \tag{5.17}$$

in Eq. (5.16) yields :

$$\hat{\mathcal{H}}(k,x_2-x_1) = \int_0^{\frac{x_1+x_2}{2}} \left\{ \int_{s_r^{\min}}^{s_r^{\max}} \hat{\mathcal{N}}(k,s)\, e^{-A(\nu)|k|(x_1+x_2-2r)} ds \right\} dr \tag{5.18}$$

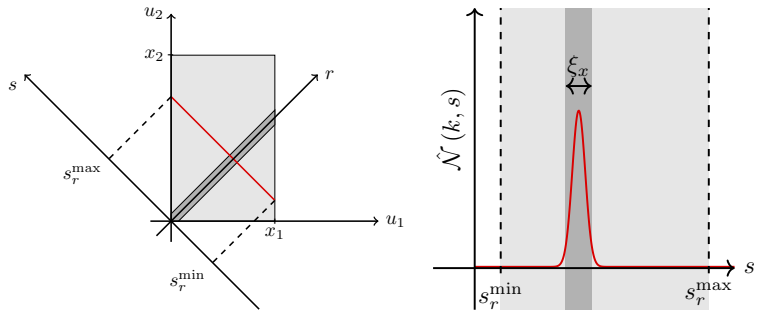

(a) (b)

Figure 5.1: Illustration of the argument of the diagonal domination : when integrating over the square $[0, x_1] \times [0, x_2]$ (a), $\hat{\mathcal{N}}(k, s)$ takes non-negligible values only when $s \ll \xi_x$ (b).

where $s_r^{\min}$ and $s_r^{\max}$ are the minimum and maximum values of s allowed by the inequalities $0 \leq r - s/2 \leq x_1$ and $0 \leq r + s/2 \leq x_2$. An example of such integration bounds is plotted in Fig. 5.1.

Following Perrin and Rice [1994], $\hat{\mathcal{N}}(k, s)$ takes non-negligible values only when $s \ll \xi_x$. Thus non-negligible values of the integrand in Eq. (5.18) only occur when $r < \min(x_1, x_2)$. When this is done, one may safely extend the integral over the interval $\left[s_r^{\min}, s_r^{\max}\right]$ to the entire real line; indeed, $s_r^{\min}$ and $s_r^{\max}$ are large for almost every r in the interval $[0, \min(x_1, x_2)]$ when $x_1, x_2 \to +\infty$. The interval over which $\hat{\mathcal{N}}(k, s)$ takes non-negligible values is "concentrated" near the centre of the interval of integration $\left[s_r^{\min}, s_r^{\max}\right]$. The integral of $\hat{\mathcal{N}}(k, s)$ then becomes identical to $\tilde{\mathcal{N}}(k, 0)$, where $\tilde{\mathcal{N}}$ is the double (z, x)-Fourier transform of the function $\mathcal{N}$. Eq. (5.18) finally boils down to :

$$\hat{\mathcal{H}}(k, x_2 - x_1) = \tilde{\mathcal{N}}(k, 0) \frac{e^{-A(\nu)|k||x_2 - x_1|}}{2A(\nu)|k|} \tag{5.19}$$

which gives the expression of the power spectrum density of h :

$$\mathrm{PSD}(k) = \hat{\mathcal{H}}(k, 0) = \frac{\tilde{\mathcal{N}}(k, 0)}{2A(\nu)|k|} \tag{5.20}$$

It also allows for the calculation of the surface roughness Δh in two steps, assuming that $k \to \tilde{\mathcal{N}}(k, 0)$ is an odd function. First :

$$\begin{aligned} \Delta h^2(\Delta z, 0) &= 2\left(\mathcal{H}(\Delta z, 0) - \mathcal{H}(0, 0)\right) \\ &= \frac{1}{\pi A(\nu)} \int_0^\infty \tilde{\mathcal{N}}(k, 0) \frac{1 - \cos(k\Delta z)}{k} dk \end{aligned} \tag{5.21}$$

Second :

$$\begin{aligned} \Delta h^2(\Delta z, \Delta x) - \Delta h^2(\Delta z, 0) &= 2\left(\mathcal{H}(\Delta z, \Delta x) - \mathcal{H}(\Delta z, 0)\right) \\ &= \frac{1}{\pi A(\nu)} \int_0^\infty \tilde{\mathcal{N}}(k, 0) \frac{1 - e^{-A(\nu)|k|\Delta x}}{k} \cos(k\Delta z)\, dk \end{aligned} \tag{5.22}$$

Eq. (5.21) and Eq. (5.22) cannot be further simplified without any further information on $\tilde{\mathcal{N}}(k,0)$. In the following, we assume that the auto-correlation function $\mathcal{N}$ of the material disorder η follows a Lorentz-distribution :

$$\mathcal{N}(\Delta z,\Delta x)=D_\eta\frac{1}{1+\left(\frac{\Delta z}{\xi_z}\right)^2}\frac{1}{1+\left(\frac{\Delta x}{\xi_x}\right)^2}\Longleftrightarrow\tilde{\mathcal{N}}(k,p)=D_\eta\pi^2\xi_z\xi_x e^{-|k|\xi_z}e^{-|p|\xi_x} \tag{5.23}$$

where D_η denotes the variance of the disorder η and ξ_z and ξ_x its correlation lengths in the crack front direction and the propagation direction, respectively.

Using Gradshteyn and Ryzhik [2014] (3.943), Eq. (5.21) gives :

$$\Delta h^2(\Delta z,0)=\frac{\pi D_\eta\xi_z\xi_x}{2A(\nu)}\ln\left[1+\left(\frac{\Delta z}{\xi_z}\right)^2\right] \tag{5.24}$$

while, using Gradshteyn and Ryzhik [2014] (3.951.3), Eq. (5.22) yields :

$$\Delta h^2(\Delta z,\Delta x)-\Delta h^2(\Delta z,0)=\frac{\pi D_\eta\xi_z\xi_x}{2A(\nu)}\ln\left[\frac{\Delta z^2+(\xi_z+A(\nu)\Delta x)^2}{\Delta z^2+\xi_z^2}\right] \tag{5.25}$$

One finally gets for the height-height correlations :

$$\Delta h^2(\Delta z,\Delta x)=\frac{\pi D_\eta\xi_z\xi_x}{2A(\nu)}\ln\left[\left(\frac{\Delta z}{\xi_z}\right)^2+\left(1+\frac{A(\nu)\Delta x}{\xi_x}\right)^2\right] \tag{5.26}$$

If one looks at the surface roughness at large-scales $\Delta z\gg\xi_z$ and $\Delta x\gg\xi_x$, one gets :

$$\Delta h^2(\Delta z,\Delta x)\propto\frac{D_\eta\xi_z\xi_x}{A(\nu)}\ln\left[\left(\frac{\Delta z}{\xi_z}\right)^2+A(\nu)^2\left(\frac{\Delta x}{\xi_x}\right)^2\right] \tag{5.27}$$

where the pre-factor depends on the geometry of the material disorder η. This expression for the two-point correlation function of the out-of-plane perturbation of the fracture surface is apparently derived here for the first time.

Following Eq. (5.19) and Eq. (5.27), we can make several remarks :

- the surface roughness of brittle heterogeneous materials is indeed logarithmic. The relaxations of the various modes in the direction (Ox) of propagation appear to be independent of each other, and small-wavelength perturbations decay at a much faster rate than large-wavelength ones both in the z- and the x-direction (see Eq. (5.19)). In particular, the decay length along the propagation direction is proportional to the perturbation size $\lambda\sim\frac{1}{k}$ along the crack front direction. Such behavior is expected to produce logarithmic correlations of the fracture surface ;
- contrary to the assumption made in Dalmas et al. [2008], Δh^2 and not Δh scales as a logarithm function ;

- the surface roughness appears to be anisotropic due to the influence of the Poisson ratio ν through the term $A(\nu)$ which varies from $\frac{1}{3}$ ($\nu = 0.5$) to 1 ($\nu = 0$). The fracture surface is isotropic in the sole case where the Poisson ratio equals to zero. Thus one should be able to extract information on both the Poisson ratio and the propagation direction from the statistics of brittle fracture surfaces.
- the fracture surface roughness contains information on the variance D_η of the material disorder as well as on the surface area $\xi_z \xi_x$ of typical heterogeneities.

Finally, the theoretical predictions of Eq. (5.27) are in perfect agreement with the numerical results of Barès et al. [2014], which simulated crack trajectory in disordered brittle materials.

Theoretical predictions of the roughness structure function Δh can now be compared with numerical observations resulting from large-scale simulations of crack propagation in brittle materials displaying toughness heterogeneities.

5.3 Numerical roughness of large-scale heterogeneous materials

This section is devoted to a numerical study of the surface roughness measured on fracture surfaces generated with the computational method developed in Chapter 2. In Section 5.3.1, we compare the numerical observations to theoretical predictions from Section 5.2. The impact of microstructural features on the surface roughness is studied in Section 5.3.2. Section 5.3.3 finally summarizes the information one can extract from those surfaces.

5.3.1 Comparison between numerical simulations and theoretical predictions

5.3.1.a Fracture surfaces of brittle heterogeneous material : a logarithmic roughness

In our numerical simulations, no assumption is made on the material disorder η, which arises from the actual interaction between the crack and the physically realistic microstructure. However as η represents the discrepancy between the direction the crack follows during the by-pass events $\theta_{\tan}$ and the direction $\theta_{\max}$ it would have followed in a homogeneous material, one can use our numerical simulations to compute :

$$\eta(z, x) \sim \theta_{\tan} - \theta_{\max} \tag{5.28}$$

at each position along the fracture plane.

But we first investigate how the theoretical predictions of Eq. (5.27) compare to numerical simulations. As a result, we compute crack propagation in composite materials composed of a large-scale distribution $L_z \times L_x \times L_y = 1024\,d \times 1224\,d \times 20\,d$ of cubical inclusions of edge width d at a density $\rho_{\text{inc}} = 15\%$. The cubical inclusions all share the same inclusion toughness $G_{\text{c}}^{\text{inc}} = 1.75\,G_{\text{c}}^{\text{mat}}$ while the interface toughness is equal to the one of the matrix $G_{\text{c}}^{\text{int}} = G_{\text{c}}^{\text{mat}}$. This set of microstructural parameters ensures that the Larkin length L_c is superior to the system size $L_z = 1024\,d$ as it is assumed in Section 5.2. An example of a

generated fracture surface is plotted in Fig. 5.2.a.

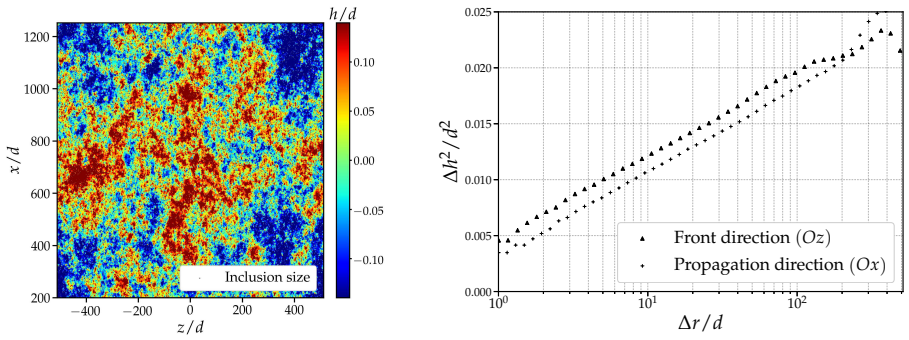

(a) (b)

Figure 5.2: Surface roughness resulting from crack propagation in a composite material containing approximately one million cubical inclusion (a) and associated roughness function in the both front direction (Oz) and propagation direction (Ox) (b).

We first characterize the roughness of those fracture surfaces through their height-height correlations in both the front direction (Oz) and the propagation direction (Ox) :

$$\begin{cases} \Delta h_z^2(\Delta z) =< (h(z+\Delta z, x) - h(z,x))^2 >_{z,x} \\ \Delta h_x^2(\Delta x) =< (h(z, x+\Delta x) - h(z,x))^2 >_{z,x} \end{cases} \tag{5.29}$$

that are plotted in Fig. 5.2.b.

We notice that the surface roughness is logarithmic as it has been predicted in Section 5.2. It reads:

$$\begin{cases} \Delta h_z^2(\Delta z) = \Delta h_d^{z\,2} + 2\Delta h_0^{z\,2} \ln(\Delta z/d) \\ \Delta h_x^2(\Delta x) = \Delta h_d^{x\,2} + 2\Delta h_0^{x\,2} \ln(\Delta x/d) \end{cases} \tag{5.30}$$

where Δh_d denotes the amplitude of the surface roughness at the inclusion scale d (a) and Δh_0 the slope of the logarithmic roughness.

We notice that the two correlation functions share the same slope $\Delta h_0^z = \Delta h_0^x$ and only differs from an offset $\Delta h_d^z \leq \Delta h_d^x$. Such features where predicted in Eq. (5.27), which yields:

$$\begin{cases} \Delta h_0^x = \Delta h_0^z \\ \Delta h_d^{x\,2} = \Delta h_d^{z\,2} + 2\Delta h_0^{z\,2} \ln(A(\nu)) \end{cases} \tag{5.31}$$

Given that for all $\nu \in [0, 0.5]$, $A(\nu) \leq 1$, the roughness in the propagation direction (Ox) is expected to be lower than the one in the front direction (Oz) as it is observed in Fig. 5.2.b. Such numerical observations have already been made in Barès et al. [2014].

Similar anisotropy in the height-height correlations has already been observed for self-affine roughness with low exponent in homogeneous glass and glassy ceramics [Bonamy et al., 2006] and with high exponent in silica glass and aluminium alloys [Ponson et al.,

2006b]. Their two-dimensional height-height correlations have been shown to collapse into a single curve following a so-called Family–Vicsek scaling. In our case, Eq. (5.27) yields :

$$\Delta h^2(\Delta z, \Delta x) - \Delta h^2(\Delta z, 0) \propto \ln\left[1 + \left(\frac{A(\nu)\,\Delta x}{\Delta z}\right)^2\right] \tag{5.32}$$

We plot in Fig. 5.3.a the two-points height-height correlations along Δz for multiple Δx values. After renormalization following Eq. (5.32), such curves finally collapse into a single one in Fig. 5.3.b.

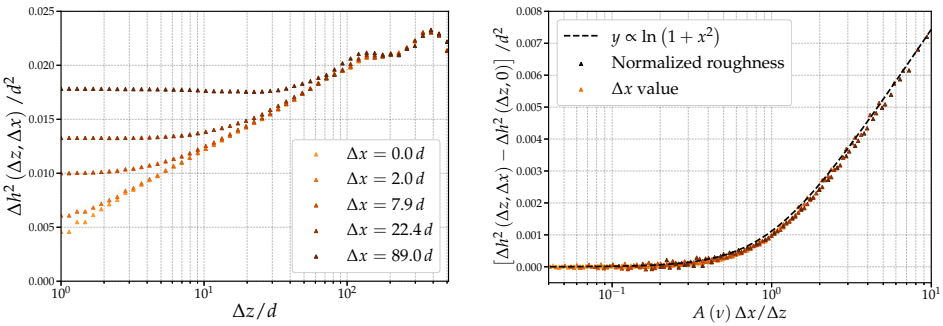

(a) (b)

Figure 5.3: Two-points height-height correlations $\Delta h^2(\Delta z, \Delta x)$ for various Δx (a) and renormalization from the structure function predicted in Eq. (5.32) (b).

This data collapse validates further the theoretical predictions derived in the previous Section 5.2.

5.3.1.b Impact of the Poisson ratio on the surface roughness

The Poisson ratio appears to play a significant role in the surface roughness of heterogeneous brittle materials. We thus consider crack propagation in a brittle composite with varying Poisson's ratio $\nu \in [0, 0.5]$. As before, the crack is interacting with a large-scale distribution $L_z \times L_x \times L_y = 1024\,d \times 1224\,d \times 20\,d$ of cubical inclusions of edge width d at a density $\rho_{\text{inc}} = 15\%$. The inclusion toughness varies from $G_c^{\text{inc}} = G_c^{\text{mat}}$ to $G_c^{\text{inc}} = 2\,G_c^{\text{mat}}$ while the interface toughness is equal to the one of the matrix $G_c^{\text{int}} = G_c^{\text{mat}}$. Five distribution realizations are considered for each set of parameters.

We plot an example of fracture surface and the associated one-dimensional height-height correlations for a small Poisson ratio $\nu = 0$ in Fig. 5.4 and a larger one $\nu = 0.5$ in Fig. 5.5. Those examples show that the Poisson ratio actually controls the anisotropy of the fracture surface through the coefficient $A(\nu)$. At a low Poisson's ratio value $\nu = 0$, $A(\nu) = 1$ so that the surface roughness is expected to be isotropic (see Eq. (5.27)), which is confirmed in Fig. 5.4.b. The fracture surface does not display any preferential direction and the patches of out-of-plane excursions of the crack front appear to be isotropic (see Fig. 5.4.a). One the contrary, at a large Poisson's ratio value $\nu = 0.5$, $A(\nu) = \frac{1}{3}$, those same patches appear to be elongated in the propagation direction (Ox) (Fig. 5.5.a) and the surface roughness displays a strong level of anisotropy (Fig. 5.5.b).

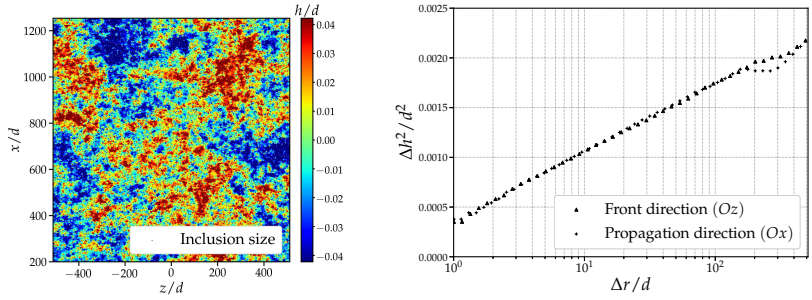

(a) (b)

Figure 5.4: Surface roughness resulting from crack propagation in a composite material with a low Poisson ratio $\nu = 0$ (a) and associated isotropic one-dimensional correlation functions in both the front direction (Oz) and the propagation direction (Ox) (b).

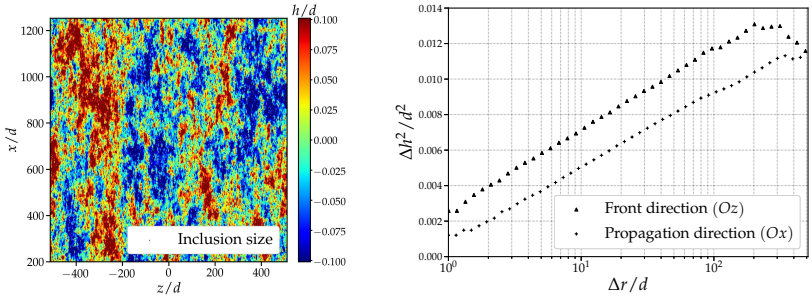

(a) (b)

Figure 5.5: Surface roughness resulting from crack propagation in a composite material with a large Poisson ratio $\nu = 0.5$ (a) and associated anisotropic one-dimensional correlation functions in both the front direction (Oz) and the propagation direction (Ox) (b).

Such behavior can be explained through the dependency of the long-range elastic interactions with respect to the Poisson ratio ν. As it has been exposed in Section 8.D.2, the relaxation of an out-of-plane boxcar function perturbation $\mathcal{H}(z)$ of amplitude Δh reads :

$$h(z,x) = \Delta h \mathcal{H}(z) - \frac{\Delta h}{\pi}\left[\arctan\left(\frac{A(\nu)\,x}{D/2+z}\right) - \arctan\left(\frac{A(\nu)\,x}{-D/2+z}\right)\right] \tag{5.33}$$

so that one can renormalize the distance in the x-direction by $A(\nu)$. The patches of out-of-plane excursions, which come from by-pass events and the subsequent relaxation of the crack front, are thus expected to be elongated in the propagation direction when $A(\nu) \neq 1$ i.e. $\nu > 0$.

One can take advantage of this surface anisotropy to measure the Poisson ratio ν from the surface roughness, either from the off-set in the one-dimensional height-height correlation functions in both directions (Oz) and (Ox) with Eq. (5.31), or from the renormalization of the two-dimensional height-height correlation function. Indeed, assuming that the Poisson

ratio is not known, one can find the optimized parameters $(a_{\text{fit}}, b_{\text{fit}})$ (see Fig. 5.6.b) so that :

$$\Delta h^2(\Delta z, \Delta x) - \Delta h^2(\Delta z, 0) = a_{\text{fit}} \ln\left[1 + b_{\text{fit}}\left(\frac{\Delta x}{\Delta z}\right)^2\right] \tag{5.34}$$

and measure ν knowing that $b_{\text{fit}} = A(\nu)^2$.

Predictions of the Poisson ratio ν from the surface roughness are plotted in Fig. 5.6.a. One can notice that the method lying on the 1D correlation functions appears to produce more consistent results since it allows for the measurement of the Poisson ratio directly from the off-set of the surface correlations rather than from an optimization procedure.

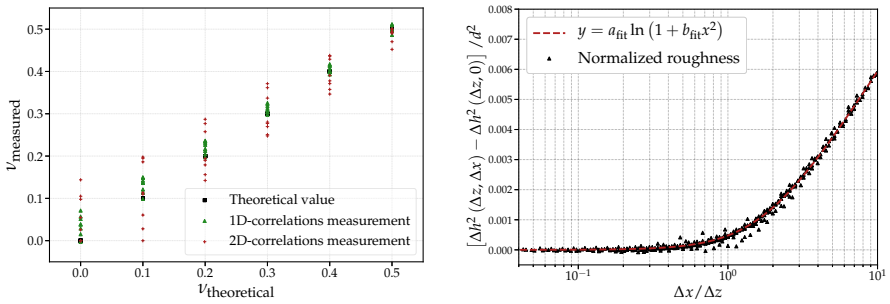

(a) (b)

Figure 5.6: Poisson ratio ν measured from the surface roughness (a) either from the roughness anisotropy in Fig. 5.5 (in green triangle marker) or from the renormalization of the two-point roughness function (in red cross marker) (b).

Finally, Eq. (5.27) predicts that the slope of the logarithmic roughness Δh_0^2 is inversely proportional to $A(\nu)$, as it has been observed in Barès et al. [2014]. In Fig. 5.7, we plot Δh_0^2 as a function of the coefficient $A(\nu)$ for two values of inclusion toughness $G_{\text{c}}^{\text{inc}} = 1.25\, G_{\text{c}}^{\text{mat}}$ and $G_{\text{c}}^{\text{inc}} = 1.75\, G_{\text{c}}^{\text{mat}}$.

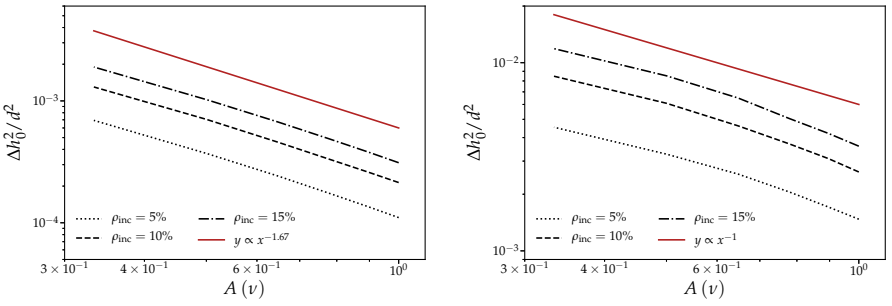

(a) (b)

Figure 5.7: Impact of the Poisson ratio ν the slope of the logarithmic roughness Δh_0 : at low inclusion toughness level $G_{\text{c}}^{\text{inc}} = 1.25\, G_{\text{c}}^{\text{mat}}$ (a) and a larger one $G_{\text{c}}^{\text{inc}} = 1.75\, G_{\text{c}}^{\text{mat}}$ (b).

We see that such property is not reproduced in our numerical simulations. It is explained by the fact that the material disorder η depends on the Poisson ratio ν. Indeed η corresponds to the angular mismatch between the direction θ_{tan} the crack follows during the by-pass

events and the direction $\theta_{\max}$ that would have been selected in a homogeneous material (see Eq. (5.28)). While $\theta_{\tan}$ depends only on the geometry, $\theta_{\max}$ is related to δK_{II} and thus on $A(\nu)$ (see Eq. (2.14)). Thus, when the angle $\theta_{\tan}$ is dominant in Eq. (5.28) i.e. for large inclusion toughness and low $A(\nu)$, η does not depend on ν and $\Delta h_0^2 \propto A(\nu)^{-1}$ (Fig. 5.7.b). Otherwise, η and thus D_η, ξ_z and ξ_x depend on ν and numerical simulations give $\Delta h_0^2 \propto A(\nu)^{-1.67}$ (Fig. 5.7.a).

5.3.1.c From logarithmic to self-affine behavior ?

Even though theoretical predictions from Section 5.2 and numerical simulations are in perfect agreement, they still do not allow to explain the self-affine behavior with a low Hurst exponent $\zeta \simeq 0.4$ observed on experimental brittle fracture surfaces. Self-affine roughness has been experimentally observed for glassy ceramics [Bonamy et al., 2006] or sintered polystyrene beads [Cambonie et al., 2015]. Yet our computational model only produces logarithmically rough surfaces.

A logarithmic behavior is typical of the propagation of an elastic line (the crack front) in a thermal disorder. It is characterized by an excess of small wavelengths, created by by-pass events, with respect to larger ones. This might be due, in our model, to the low collectivity observed in the by-pass of tough inclusions. Indeed, we saw in Section 8.D.1 with the bi-inclusion problem that collective behavior, where the by-pass of the first inclusion triggers a by-pass of the second one, are essentially local and very scarce with the sole by-pass mechanism. Thus one can expect that the effective disorder η involved in the path equation does not show long-range correlations and can thus be reduced to a thermal contribution $\eta(z,x)$, compatible with a logarithmic roughness.

Increasing the Hurst exponent ζ from $\zeta \simeq 0$ (logarithmic behavior) to $\zeta \simeq 0.35$ would require a greater collectivity in the interaction mechanisms between the crack and tough inclusions. We saw in Section 8.D.1 that a local mode mixity can change the way a crack interacts with an inclusion : when the crack is loaded with a positive mixed mode ratio $\rho_{\text{II}} = K_{\text{II}}^\infty / K_{\text{I}}^\infty$, the inclusions are more likely to be by-passed downward or to cross the inclusions. Thus, in presence of Mode II loading imperfections $\rho_{\text{II}} \neq 0$, situations where two inclusions located nearby are by-passed upwards for the first one and downwards for the second one becomes rarer. Consequently, fewer small-wavelength components are developed in the system and ζ might increase. Ponson [2007] pointed out that the presence of Mode II imperfections in the Mode I macroscopic loading ρ_{II} may prove to be decisive in the development of self-affine correlations.

We thus investigate the influence of loading imperfections by introducing an additional constant contribution ρ_{II} in the expression of the Mode II perturbations :

$$\frac{\delta K_{\text{II}}(z,t)}{K_{\text{I}}^\infty(t)} = \rho_{\text{II}} + \frac{1}{2}\frac{\partial f_y}{\partial x}(z,t) + \frac{2-3\nu}{2-\nu}\frac{1}{2\pi}\,\text{PV}\int_{-\infty}^{+\infty}\frac{f_y(z,t)-f_y(z',t)}{(z-z')^2}\,dz' \tag{5.35}$$

Other contributions from Gao and Rice [1986] and Movchan et al. [1998] are of second-order in the perturbation and can be neglected in our first-order approach, see Leblond and Ponson [2016].

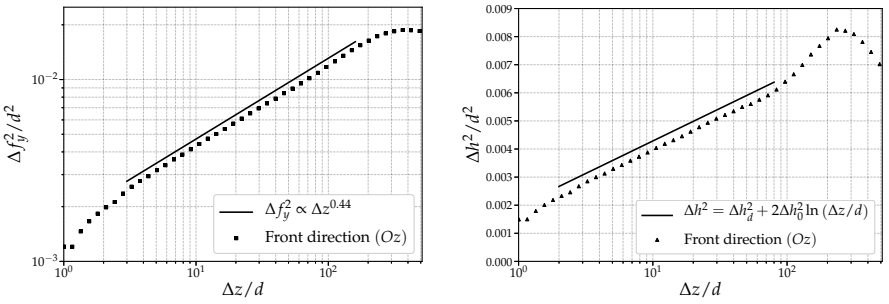

(a) (b)

Figure 5.8: Roughness in the direction of the crack front for a mixed Mode I+II propagation : the roughness of the out-of-plane perturbation f_y are self-affine with an exponent $\zeta = 0.22$ (a) while the roughness of the fracture surface remains logarithmic (b) for a mode mixity $\rho_{\text{II}} = 5\%$.

In Fig. 5.8, we see that such loading imperfections render the surface correlations self-affine with $\zeta = 0.22$ when we focus on the correlations of f_y i.e. along a line $(z, x(t))$. The loading imperfections prevent situations, where one inclusion is by-passed upwards while its neighbor is by-passed downwards and consequently decreases the ratio of small-wavelengths. Yet, as soon as the out-of-plane perturbation f_y are mixed with the in-plane perturbation f_x to create the fracture surface $h(z, x(t) + f_x(z, t))$, correlations are logarithmic again (see Fig. 5.8.b).

If the considerations proposed in Ponson [2007] are qualitatively correct, they cannot explain the shift from a logarithmic to a self-affine behavior. Yet it stresses out that greater collectivity levels in the interaction mechanisms occurring at the crack tip are required to go beyond the logarithmic behavior. Such collectivity could be induced in porous sandstone or sintered glass beads materials by debonding mechanisms at the grain scale which would attract the crack tip and favor collective propagation through a more complex correlated disorder η. Those processes may not happen in the case of phase-separated glasses where the process zone size ℓ_{FPZ} is far smaller than the grain size d, leading to logarithmically rough surfaces as produced by our model. Another possibility, which constitutes an interesting extension to this work, is to investigate the impact of elastic heterogeneities on the surface roughness within the perturbative approach developed by Gao [1991] and extended by Muju [2000]. The impact of elastic heterogeneities on crack trajectory being non-local, η could take the form of a quenched noise $\eta(z, x, h)$ rather than a thermal one $\eta(z, x)$ as in the case of toughness heterogeneities.

5.3.2 Impact of microstructural features on the logarithmic roughness

The fracture surfaces of the simulated materials display logarithmic correlations, characterized by the amplitude of the surface roughness at the inclusion scale Δh_d and the slope Δh_0 of the one-dimensional height-height correlations. One can wonder, as it was performed for the effective fracture properties, how microstructural features impact the surface roughness and in particular Δh_d and Δh_0.

5.3.2.a Amplitude Δh_d and slope Δh_0 of the roughness correlations

For all sets of microstructural parameters considered in this study, the fracture surface correlations remain logarithmic. The roughness is then characterized by the amplitude of the surface roughness at the inclusion scale Δh_d and the slope of the logarithmic roughness Δh_0, which are measured from the one-dimensional correlation function (see for example Fig. 5.8.b).

We first investigate the impact of the inclusion toughness G_c^{inc} and the inclusion density ρ_{inc} on the surface roughness. The fracture surfaces are extracted from the simulations performed in Chapter 4. The results are plotted in Fig. 5.9.

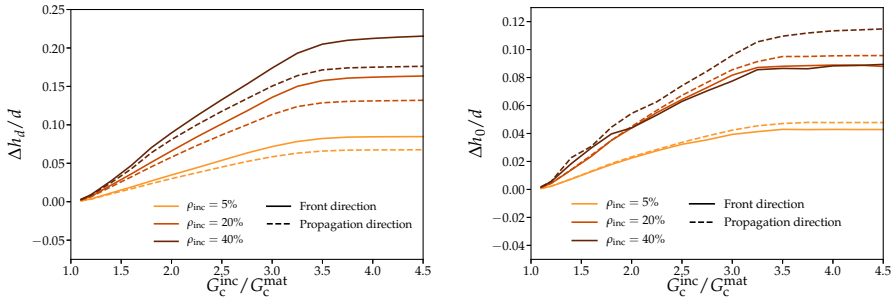

(a) (b)

Figure 5.9: Impact of the inclusion toughness G_c^{inc} and the inclusion density ρ_{inc} on the parameters characterizing the surface roughness : the amplitude of the surface roughness at the inclusion scale Δh_d (a) and the slope of the logarithmic roughness Δh_0 (b).

We first observe that both Δh_d and Δh_0 increase with the inclusion toughness. It is explained by the fact that, during inclusion by-pass, the crack has to follow the direction imposed by the inclusion geometry, which induces a noise η of larger amplitude (see Eq. (5.28)). As the inclusion gets tougher, the by-pass events are both more frequent (more by-passed inclusions) and more intense (increase of the out-of-plane deviations induced by a single by-pass). Thus, the variance D_η of the effective disorder η increases. At higher inclusion toughness levels, the proportion of by-passed inclusion does not increase anymore and both Δh_d and Δh_0 reach a plateau.

The effect of both inclusion toughness and inclusion density can be rationalized through the adaption of the homogenization procedure developed in Chapter 4. The material disorder $\eta(z, x)$ induced by each interaction mechanism is estimated numerically from the interaction of a crack with periodic arrangements of tough inclusions following Eq. (5.28). Examples of local maps of the effective disorder η for each interaction mechanism are plotted in Fig. 5.10. It allows for the estimation of D_η, ξ_z and ξ_x, which control the surface roughness. Thus, one shows that the $D_\eta \propto \rho_{\text{inc}}^{2/3}$ so that $\Delta h_0 \propto \rho_{\text{inc}}^{1/3}$ (see Section 4.5.2).

In Fig. 5.9.a, we observe that Δh_d^x is lower than Δh_d^z due to Poisson effects as predicted in Eq. (5.31). Yet Δh_0^x and Δh_0^z are no more equal when the inclusion toughness and density increase. This phenomenon can be attributed to the fact that the crack no more propagates

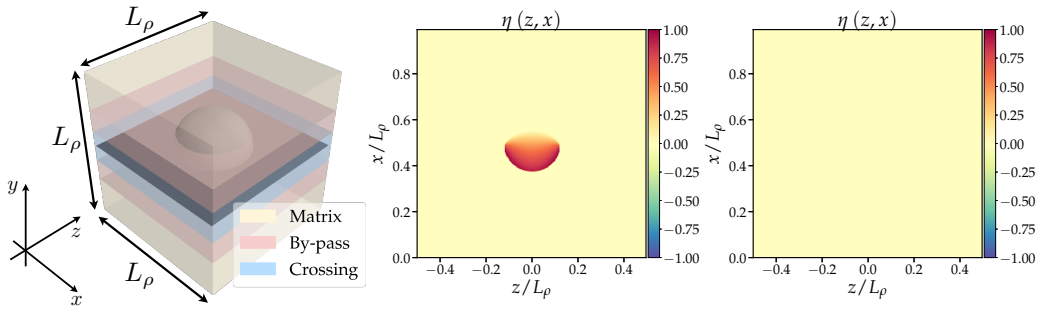

(a) (b) (c)

Figure 5.10: Fractured representative volume element (FRVE) of size L_ρ describing the interaction between a crack landing at a height y on a spherical inclusion of diameter d_{inc}, inclusion toughness $G_{\text{c}}^{\text{inc}}$ and interface toughness $G_{\text{c}}^{\text{int}}$ (a) : material disorder η induced by a by-pass event (b) and by the inclusion crossing/matrix cracking mechanisms (c)

in the Larkin regime at such toughness and density levels so that the Assumption 2 made in Section 5.2 may not be valid anymore.

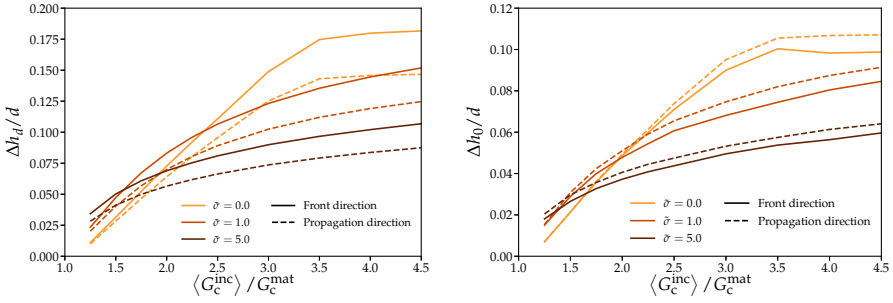

(a) (b)

Figure 5.11: Impact of the toughness disorder $\tilde{\sigma}$ on the parameters characterizing the surface roughness : the amplitude of the surface roughness at the inclusion scale Δh_d (a) and the slope of the logarithmic roughness Δh_0 (b).

The impact of the toughness disorder is plotted in Fig. 5.11. We notice that, for the same average inclusion toughness, the fracture surface appears to be less rough. The trends are similar to the ones displayed for the effective toughness in Section 4.5.3 and call for the same explanation. For a given average inclusion toughness level, when the toughness disorder $\tilde{\sigma}$ increases, there is a larger proportion of inclusions with low inclusion toughness, which are crossed and do not contribute to the surface roughness. The toughest inclusions are by-passed and roughen the fracture surface but by-pass events remain scarce due to the log-normal distribution of toughness contrast. If it allows for an increase of the surface roughness at low average toughness, it induces otherwise a decrease of the surface roughness.

Similar considerations allow for a qualitative description of the impact of the interface toughness on the surface roughness plotted in Fig. 5.12. As the interface gets weaker, more and more inclusions get by-passed and the surface roughness increases. Yet, one

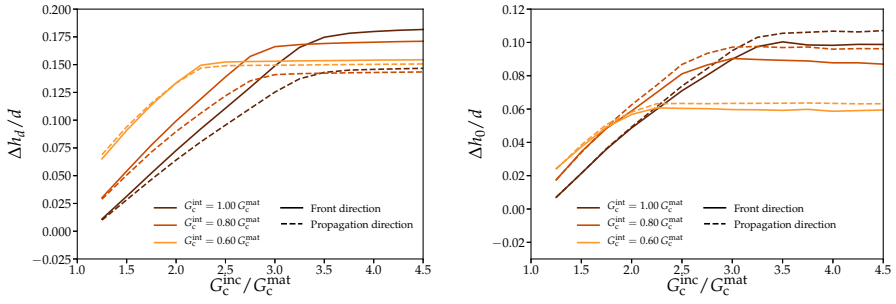

(a) (b)

Figure 5.12: Impact of the interface toughness G_c^{int} on the parameters characterizing the surface roughness : the amplitude of the surface roughness at the inclusion scale Δh_d (a) and the slope of the logarithmic roughness Δh_0 (b).

could expect that at high inclusion toughness levels, the roughness converges towards the same value since all inclusions are by-passed. The dynamics of the by-pass event appears to be quite different in presence of a weak interface G_c^{int} as depicted in Fig. 5.13. The weak interface makes the by-pass event so sudden that the crack front feels only partly the by-pass event (Fig. 5.13.a). Both the effective out-of-plane perturbation induced by the by-pass mechanism and the surface roughness are then decreased (Fig. 5.13.b). Yet the spatial distribution of the material disorder $\eta(z,x)$ for the by-pass event, plotted in Fig. 5.13.c, does not take this effect into account. The homogenization procedure is thus expected to overestimate D_η and ξ_x in the case of weak interface.

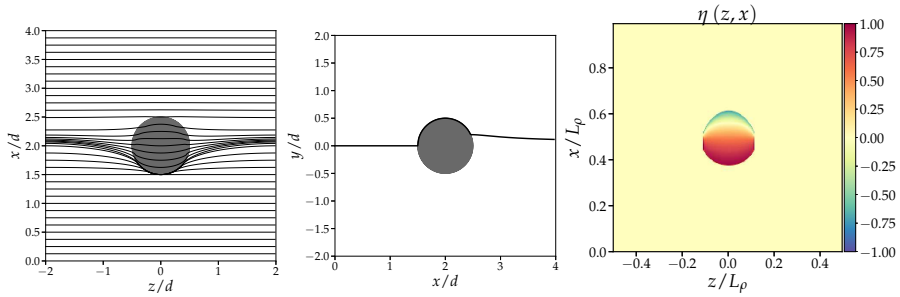

(a) (b) (c)

Figure 5.13: Inclusion by-pass for a weak interface $G_c^{int} = 0.4\,G_c^{mat}$: in-plane perturbation in the equatorial plane (zOx) (a), trajectory of the crack in the central plane (xOy) (b) and associated material disorder η (c).

Finally, we investigate the impact of size disorder on the surface roughness. The size disorder has been shown in Section 4.6.1 to have no substantial effect on the effective toughness. We see in Fig. 5.14 that it impacts substantially both the amplitude of the surface roughness Δh_d and its slope Δh_0. Regarding the effective toughness, the size disorder had no impact since ξ_z/ξ_x remained constant. Yet, what matters for the surface roughness is the product $\xi_z\xi_x$ of the material disorder η, which is directly linked to the inclusion size d_{inc}. The roughness is thus expected to increase with the size disorder.

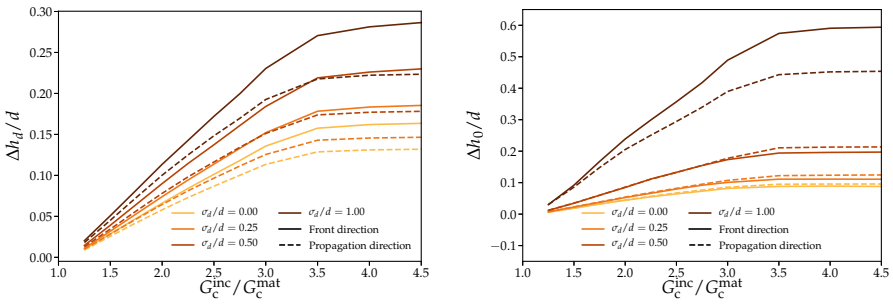

(a) (b)

Figure 5.14: Impact of the size disorder σ_d/d on the parameters characterizing the surface roughness : the amplitude of the surface roughness at the inclusion scale Δh_d (a) and the slope of the logarithmic roughness Δh_0 (b).

5.3.2.b Renormalization of Δh_0

The homogenization procedure developed in Section 4.4 can be tuned to predict D_η, ξ_z and ξ_x for the whole set of microstructural parameters. We see in Fig. 5.15 that all data collapse into a single curve. Only the simulations related to the influence of the interface toughness do not collapse due to the overestimation of D_η and ξ_z, as mentioned above. It validates the scaling $\Delta h_0^2 \propto D_\eta \xi_z \xi_x$ predicted in Eq. (5.27).

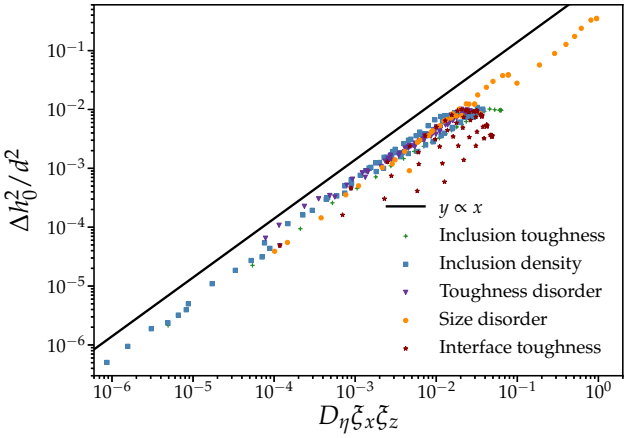

Figure 5.15: Renormalization of the slope of the logarithmic roughness Δh_0 with the material disorder parameters D_η, ξ_z and ξ_x estimated from the homogenization procedure.

Tackling the inverse problem and try to extract quantitative information on the material microstructure from the surface correlations appears to be especially challenging. Indeed we can see in Fig. 5.15 that a given value of Δh_0 corresponds to multiple sets of parameters. Nonetheless, if one knows that out-plane-deviations are caused by a particular mechanism, one could possibly extract the amplitude of such a mechanism from the fracture surface morphology. Collaborations with Tanguy Rouxel's team at Institut de Physique de Rennes are planned to apply such a method to estimate the level of residual stresses that form around inclusions in composite glass during the manufacturing processes.

5.3.3 Statistical fractography

5.3.3.a Find back information on the effective toughness from the surface roughness : a vain wish ?

We have shown earlier that one could take advantage of the anisotropy of the roughness to extract information on both the propagation direction and on the Poisson ratio. The Holy Grail pursued by material science however is to extract information on the effective fracture properties from the statistics of brittle fracture surfaces, as it is performed for ductile and quasi-brittle materials [Vernède et al., 2015; Barak et al., 2019].

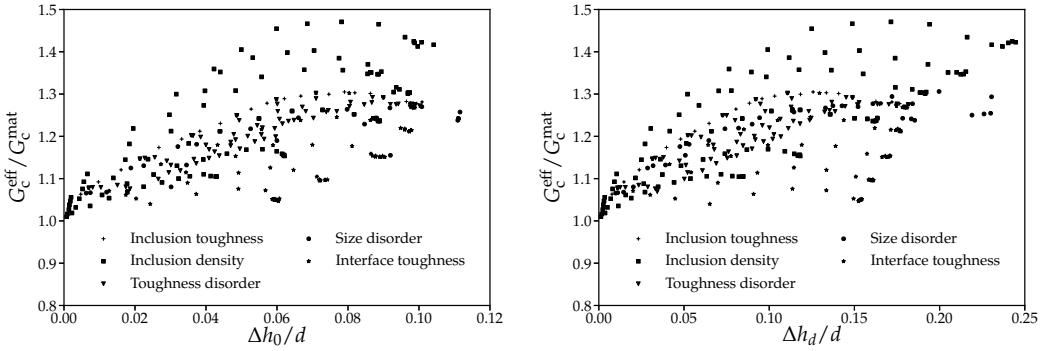

Figure 5.16: Relation between the effective toughness G_c^{eff} and the variables characteristic of the surface roughness Δh_0 and Δh_d for a wide range of microstructural parameters.

We plot in Fig. 5.16 the effective toughness G_c^{eff} as a function of the slope of the logarithmic roughness Δh_0 and the amplitude of the surface roughness at the inclusion scale Δh_d. We see that the effective fracture properties cannot be inferred from the surface roughness. This is no surprise for two main reasons :

- the crossing mechanism, which strongly impacts the effective toughness, has no impact on the surface roughness (see Fig. 5.10.c). The crack behaves identically when it propagates in the matrix or the inclusion has they are both homogeneous phase, which allows to follow the path selected by the MERR criterion ;

- there is no common trend between the impact of a given microstructural parameter on the effective toughness and the surface roughness. Some microstructural parameters increase the surface roughness while decreasing the effective toughness (e.g. the interface toughness G_c^{int}), whereas others have both a positive impact on the surface roughness and the effective toughness (e.g. the inclusion toughness G_c^{inc}). Some parameters have a positive impact on the surface roughness while having no impact on the effective fracture properties (e.g. the size disorder).

5.3.3.b Surface roughness : beyond the Larkin regime

If no information on toughness can be extracted from the amplitude of the surface roughness, salvation could come from the cut-off which separates various regimes of roughness. Vernède et al. [2015] used surface correlations to distinguish a multi-affine regime with $\zeta \simeq 0.8$ attributed to damage processes to a self-affine regime with $\zeta \simeq 0.4$ reminiscent of brittle fracture. The lengthscale characteristic of the transition between the two regimes is naturally linked to the process zone size ℓ_{FPZ}, in which are embedded precious information on the fracture properties [Barenblatt, 1962]. In our case, the logarithmic roughness has been shown to be characteristic of the Larkin regime (Section 5.2). One can wonder how the roughness correlations behave beyond this regime and explore whether or not one can measure from them the Larkin length L_c, which proves decisive in the determination of the effective fracture properties (see Chapter 4).

Examples of surface roughness for various Larkin lengths L_c are plotted in Fig. 5.17. The Larkin length L_c can be tuned by varying the inclusion toughness G_c^{inc}. It is then extracted from the roughness of the in-plane perturbations according to Eq. (4.27). We observe no clear shift of behavior below and above the Larkin length L_c. The logarithmic roughness extends above the Larkin length with no saturation or change of slope.

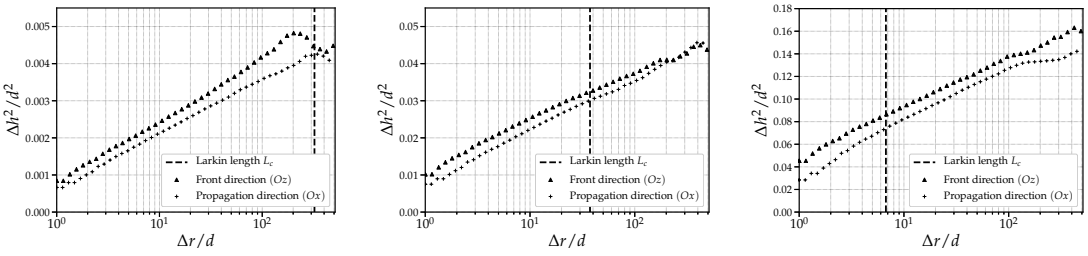

(a) (b) (c)

Figure 5.17: Roughness in the direction of the crack front below and above the Larkin length L_c (in dash-dotted line) : for monodisperse distribution of cubical inclusion for a density $\rho_{\text{inc}} = 15\%$ and inclusion toughnesses $G_c^{\text{inc}} = 1.25\, G_c^{\text{mat}}$ (a) $G_c^{\text{inc}} = 1.75\, G_c^{\text{mat}}$ (b) and $G_c^{\text{inc}} = 3\, G_c^{\text{mat}}$ (c).

In conclusion, brittle fracture surfaces do not appear to contain any significant information on the effective fracture properties. Only information on the propagation direction and the Poisson ratio ν can be extracted from those surfaces.

5.4 Concluding remarks

In this chapter, we conducted a theoretical and numerical analysis of the surface roughness of brittle heterogeneous materials by considering disordered distribution of tough inclusions.

First, the impact of toughness heterogeneities has been modeled in Section 5.2 by the introduction of a thermal disorder term $\eta(z,x)$ in the crack trajectory equation (5.5). Studied within the framework developed in Favier et al. [2006b], the crack surface statistics have been shown to display logarithmic correlations in both the crack front direction and the propagation direction. The analytical results are in perfect agreement with the numerical simulations of Barès et al. [2014] and the experiments on phase-separated glass conducted by Dalmas et al. [2008]. Moreover, a two-dimensional structure function for the surface correlations has been derived for the first time in Eq. (5.27). It predicts an anisotropy in the surface scaling, similarly to what has been observed for self-affine surfaces in Ponson et al. [2006b]. Second, these analytical predictions have been compared in Section 5.3 to numerically generated fracture surfaces resulting from the interaction between a crack and large-scale distribution of tough inclusions. The numerical results are in a perfect agreement with the fore-mentioned theoretical predictions : the generated surfaces appear to be logarithmically correlated and display an anisotropy related to Poisson's effects. Moreover, numerical data all collapse to a single curve predicted from the 2D structure function derived in Eq. (5.27). The impact of various microstructural parameters have been studied numerically and successfully compared to theoretical predictions resulting from the combination of Eq. (5.27) with the homogenization model developed in Chapter 4. Armed with a deep understanding of the origin of logarithmic surface roughness, we proved that information on the propagation direction, as well as the Poisson ratio ν, could be extracted from the surface statistics. Yet no information on the effective toughness G_c^{eff} or the Larkin length L_c seem to be contained in the surface roughness, which is only reminiscent of the by-pass events and thus contains only part of the required information to trace back the effective fracture properties.

Our study offers a detailed description of logarithmically rough fracture surface, from the underlying mechanisms at their origin to the information it contains. Yet, the sole crossing and by-pass mechanisms do not allow to explain the two regimes of logarithmic and self-regime roughness observed experimentally [Dalmas et al., 2008; Ponson et al., 2006a], even in presence of loading imperfections as it was suggested by Ponson [2007]. The by-pass mechanism has been shown in Chapter 4 to be scarcely collective, which accounts for the logarithmic behavior. A greater collectivity in the mechanisms of interaction is required to shift from the logarithmic behavior to a self-affine behavior. Increased collectivity levels could be explained in granular consolidated materials as sandstone by microscopic mechanisms taking place at the grain scale such as interface debonding and pore connection. The fracture surface roughness of brittle materials would be logarithmic when the typical size d of the heterogeneities is far greater than the process zone size ℓ_{FPZ}, whereas it would be self-affine ($\zeta \simeq 0.4$) when ℓ_{FPZ} is of the order of d. Such a scenario could be tested

through leading-edge experimental set-ups in fracture mechanics which allow for an in-situ observation of the fracture processes by X-ray microtomography [Lachambre et al., 2015; Chateau et al., 2018; Renard et al., 2019]. The impact of elastic heterogeneities on the surface roughness also need to be better apprehended. The extension of the perturbative approach developed in this manuscript to elastic inclusions via the works of Gao [1991] and Muju [2000] would constitute a relevant extension of this study.

6

Experimental study of crack propagation in 3D printed heterogeneous polymers

Contents

6.1 Introduction

Recent developments in additive manufacturing of polymers allow to design multi-material structures architectured at the micrometer scale [Wang et al., 2017b]. Such unprecedented features paved the way to the investigation fracture properties of bio-inspired [Dimas et al., 2013; Gu et al., 2016b,a, 2017a,b] or micro-architectured [Raney et al., 2018; Mueller et al., 2018] composites. They can also provide particularly valuable insights on the homogenization of fracture properties through model experiments, where both the shape, the disposition and the mechanical properties of the inclusions are entirely controlled [Wang and Xia, 2017; Avellar, 2018].

Investigating the fracture of brittle materials requires nonetheless to track crack propagation at fine spatial and temporal scales. One can rely on the fact that a crack is markedly characterized by a local displacement discontinuity to make use of one of the most widespread experimental method of displacement field measurement, the Digital Image Correlation (DIC). This procedure, based on the comparison of images acquired at different stages of a mechanical test, provides quantitative descriptions of the local displacement. Since the pioneer works of Peters and Ranson [1982], Sutton et al. [1983] and Chu et al. [1985], DIC techniques have been successfully applied in the research field of solid mechanics in general [Soppa et al., 2001; Besnard et al., 2006; Bornert et al., 2010; Dautriat et al., 2011] but also in fracture mechanics [McNeill et al., 1987; Sutton et al., 2000; Forquin et al., 2004] or damage [Nguyen, 2015; Renard et al., 2017, 2019]. It provides quantitative insights on the position of the crack tip [Abanto-Bueno and Lambros, 2002; Henninger et al., 2010; Chateau et al., 2018] as well as on the local stress intensity factors [Réthoré et al., 2005; Roux and Hild, 2006; Lachambre et al., 2015; Roux-Langlois et al., 2015], quantities that constitute a pre-requisite to address the difficult question of homogenizing fracture properties.

In this chapter, we investigate the fracture of heterogeneous 3D printed polymers and their homogenized fracture properties. Section 6.2 is devoted to the study of quasi-static crack propagation in homogeneous 3D printed specimens, which display a complex behavior marked by the influence of the viscosity of the material as well as a stick-slip behavior. To address those issues, the crack is driven at much higher driving rates, leading to the dynamic fracture of the sample. Standard experimental methods used in a quasi-static setting cannot be applied anymore. Thus, a DIC-based procedure is developed in Section 6.3 to track crack propagation at a fine scale, using the in-house correlation software CMV. It allows for the estimation of both crack tip position and stress intensity factors through the use of a local DIC approach. It is finally applied in Section 6.4 to the homogenization of fracture properties of striped composites with a rate-dependent fracture energy. This final section relies on a joint work performed during the doctoral exchange of Gabriele Albertini, PhD student at Cornell University under the supervision of David Kammer.

6.2 Fracture of 3D printed polymers

6.2.1 Fracture test

Accurately measuring the toughness of a material constitutes a particular challenge in fracture mechanics since it requires to quantify the critical elastic energy release rate at which a crack propagates. Additionally, the measured toughness may depend on the velocity of the propagating crack [Ponson and Bonamy, 2010]. Characterizing toughness properties thus requires to perform experiments where both the crack tip position and the total dissipated energy are tracked during crack advance, for a broad range of crack velocities. Conducting such advanced fracture tests might prove difficult for brittle materials, where crack propagation often proves sudden and brutal. Such difficulties have been circumvented by developing specimen geometries which allow for a stable crack propagation

at a prescribed velocity [Gallagher, 1971; ASTM, 2017; Pallares et al., 2009].

Notably the Tampered double Cantilever Beam (TDCB) geometry, proposed by Marcus and Sih [1971] and Gallagher [1971], enables for significant stability of the fracture process in tensile Mode I at a controlled speed [Davalos et al., 1998]. It has been used to measure the fracture properties of adhesively bonded joints [Blackman et al., 2003] and heterogeneous materials such as wood [Morel et al., 2003] or striped polymers [Wang and Xia, 2017]. In this study, we use a slightly different version of the TDCB geometry as shown in Fig. 6.1.a & b. Indeed, we removed the narrow arms before the taper part of the sample, resulting in a better control of the crack propagation thanks to the exponential decay of the ERR with the crack advance [Vasudevan et al., 2019].

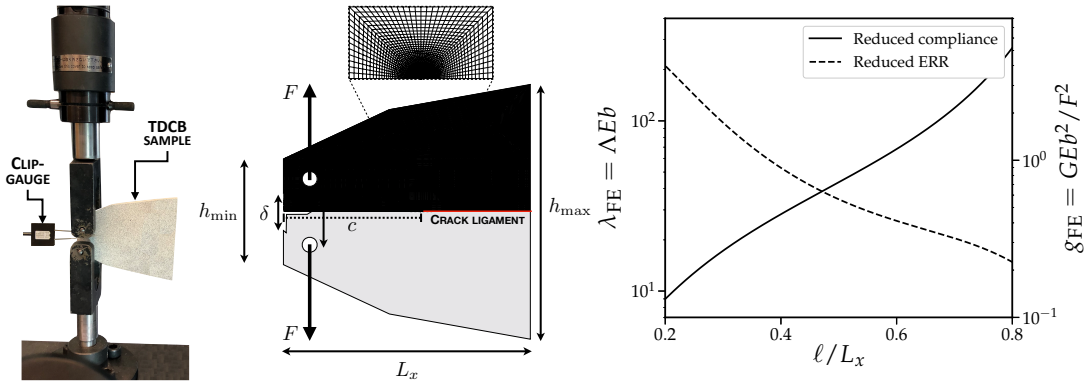

(a) (b) (c)

Figure 6.1: Fracture test of a TDCB specimen : (a) experimental set-up with a TDCB sample instrumented with a clip-gauge to measure the crack opening displacement δ. (b) Schematic of the sample geometry with the finite element mesh ($\sim 2.10^2$ nodes) superposed on the upper half. (c) Variations of the reduced compliance $\lambda = Eb\Lambda$ and the reduced ERR $g = \frac{G}{\delta^2 E}$ with the crack length ℓ (c).

Sample dimensions

A typical specimen has the dimensions $L_x = 70$mm in the propagation direction, $h_{\min} = 30$mm, $h_{\max} = 72$mm in the direction perpendicular to the propagation direction and a width $b = 8$mm.

Compliance method for material characterization

The TDCB specimen is loaded on a Schimadzu universal testing machine (Model AG-Xplus) of 10 kN maximum loading capacity. In this setup, we use a 1kN load cell to measure the force F_{exp} and a clip gauge to measure the displacement δ_{exp} between the lips of the crack (see Fig. 6.1.a & b). The tests are controlled by the clip gauge with a constant opening rate $\dot{\delta}$, which is tuned to make the crack propagate on a wide range of crack velocity [Vasudevan et al., 2019]. From the data of the force F and the displacement δ of the crack lips, one can deduce both the crack position ℓ and the ERR G from the compliance method and finite elements simulations [Morel et al., 2003; Grabois et al., 2018].

In this work we use CASTEM, an open-source finite element software developed by CEA (France), to model numerically the crack propagation in the TDCB sample under two-dimensional plane stress conditions. Exploiting the sample symmetry, we carry out

the simulations on the sole upper half of the sample. The behavior of the material is assumed to be linear elastic with a unitary Young modulus $E_{\text{FE}} = 1\,\text{Pa}$ and a Poisson ratio $\nu_{\text{FE}} = 0.35$ corresponding to the polymers used in the experiments (see the Section 6.2.2). Displacement are fixed to zero on the unbroken crack ligament (in red in Fig. 6.1.b) and a unit vertical force $F_{\text{FE}} = 1\,\text{N}$ is applied on the upper segment of the hole to describe the force imposed by the machine to the sample. Under these loading conditions, the crack propagates in pure Mode I and the crack length is increased incrementally during each step of the simulation. A typical mesh used in the analysis is shown in Fig. 6.1.b, with finer mesh of element size $10^{-9}L_x$ in the vicinity of the crack tip to grasp the stress singularities. We extract from the FEM analysis the displacement $\delta_{\text{FE}}(\ell)$ at the position of the clip-gauge, from which we deduce the compliance at this point $\lambda_{\text{FE}}(\ell) = \delta_{\text{FE}}(\ell)/F_{\text{FE}}$. Additionally, we measure the ERR $g_{\text{FE}}(\ell)$ from the G-theta method. The results of the FEM analysis are plotted in Fig. 6.1.c. We can notice than $g_{\text{FE}}(\ell)$ decreases indeed exponentially with the crack advance, which ensures stable crack propagation during the fracture test.

From the experimental data, one can estimate the compliance Λ_{exp} at the clip-gauge position from :

$$\Lambda_{\text{exp}} = \frac{\delta_{\text{exp}}}{F_{\text{exp}}} = \frac{\lambda_{\text{exp}}}{Eb} \tag{6.1}$$

The crack tip position ℓ_{exp} is inferred by comparing the experimental reduced compliance $\lambda_{\text{exp}} = \Lambda_{\text{exp}}/Eb$ to the results of the FEM simulations λ_{FE}. From the data of ℓ_{exp}, one can estimate the local crack velocity $v_{\text{exp}} = \dfrac{\partial \ell_{\text{exp}}}{\partial t}$. The experimental ERR is finally deduced from the equation :

$$G_{\text{exp}} = \frac{F_{\text{exp}}^2}{Eb^2} g_{\text{FE}}(\ell_{\text{exp}}) \tag{6.2}$$

The experimental procedure, which has been validated by Vasudevan et al. [2019], is summarized in Fig. 6.2. An example of the method is given in Section 6.2.3.

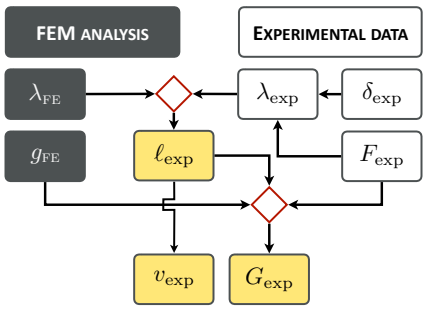

Figure 6.2: Overview of the proposed crack tracking and ERR measurement procedure based on the analysis of the macroscopic mechanical response of the specimen (adapted from [Grabois et al., 2018]).

6.2.2 Material description

Recent developments in additive manufacturing of polymers allow to design multi-material structures architectured at the micrometer scale [Wang et al., 2017b], so that one can take advantage of those unprecedented features to investigate the fracture of heterogeneous materials through model experiments. However manufactured specimen properties appear to

strongly depend on structural and process parameters rather than purely on material properties [Mueller et al., 2015; Wittbrodt and Pearce, 2015; Raney et al., 2018], so that the selected 3D printing technology proves decisive in the physical mechanisms activated during experiments.

We use here a Stratasys Objet260 Connex3 printer based a PolyJet technology, which is classified among the direct 3D printing processes (direct 3DP). Successive layers of fine droplets of photopolymer resin are jetted through 512 nozzles distributed on 8 inkjet print heads, which moves in the (xOy) plane (see Fig. 6.3). Each photopolymer droplet is cured by UV lamps positioned on either side of print heads and the newly deposited layer is flattened by a roller located behind the print heads. The process is reproduced by adding a new layer on the vertical z-axis until the printing is completed. It allows to print heterogeneous specimens at a fine resolution $\Delta x = \Delta y \simeq 42\,\mu$m in the (xOy) plane and $\Delta z \simeq 32\,\mu$m in the z-direction.

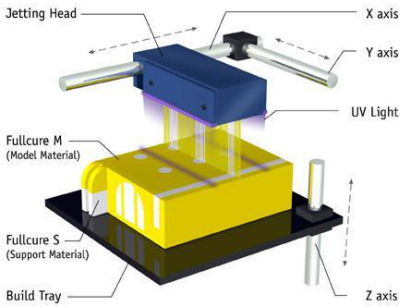

Figure 6.3: Additive manufacturing of heterogeneous polymer samples using poly-jet process (courtesy of Stratasys).

The base resins used in this work are Stratasys' VeroClear, VeroWhitePlus (Vero) and DurusWhite (Durus). Vero and Durus materials are made from proprietary acrylic-based photopolymer resins, which aim at simulating the flexibility, strength, and toughness of polymethyl methacrylate (PMMA) and polypropylene, respectively. In this study, we print heterogeneous specimens composed of a transparent matrix of Veroclear containing obstacles of DM4310, which is a rigid mix of VeroWhitePlus and DurusWhite. These materials have been selected to display significantly different toughness properties while keeping similar elastic properties to stick to the assumptions made in the theoretical and numerical study. Our characterization study yields a Young modulus $E_{\text{mat}} = 2.9 \pm 0.5$GPa and a fracture energy $G_{\text{c}}^{\text{mat}} = 80 \pm 15\text{J.m}^{-2}$ for the Veroclear and $E_{\text{obs}} = 1.9 \pm 0.3$GPa and $G_{\text{c}}^{\text{mat}} = 110 \pm 20\text{J.m}^{-2}$ for the DM4310. The high dispersion of the mechanical properties in between experiments can be explained by their strong dependence on both the temperature during the manufacturing process and the room temperature during the test [Mueller et al., 2015; Wang et al., 2017a], which is not a controlled parameter in our case. Finally, we assume, in concordance with other studies [Avellar, 2018], a Poisson ratio $\nu_{\text{mat}} = \nu_{\text{obs}} = 0.35$, which is standard for polymer materials.

Following the recommendations of Mueller et al. [2015], we always print the samples at the same position on the building tray and along the same direction to reduce the variability

of our results. Moreover, the crack propagation direction is aligned with the x-printing direction of the building tray (see Fig. 6.3) to prevent the presence of weak layers induced by the manufacturing process in the direction on propagation. The specimens are cleaned with water after printing to remove the support material. They are allowed to dry for two consecutive days to mitigate the effects of absorbed water on the mechanical properties of the material [Avellar, 2018]. The fracture test is thus performed at a constant time interval (approximately two days) from the production to prevent any influence of material ageing [Bass et al., 2016].

6.2.3 Preliminary experiments of quasi-static fracture of homogeneous 3D printed polymers

The experimental set-up presented in Section 6.2.1 is now applied to characterize separately the fracture properties of both Veroclear and DM4310 materials. In order to separate the problem of crack initiation, which involves both the material strength σ_c and its toughness G_c [Leguillon, 2002], from the one of crack propagation, where only G_c intervenes, a crack is initiated up to a length ℓ_{ini} under compressive loading by inserting a wedge (cutter blade) with a hammer inside the 3D printed pre-notched sample (see Fig. 6.4). The compressive zone confines the propagation up to $\ell_{ini} \simeq 35\,\text{mm}$.

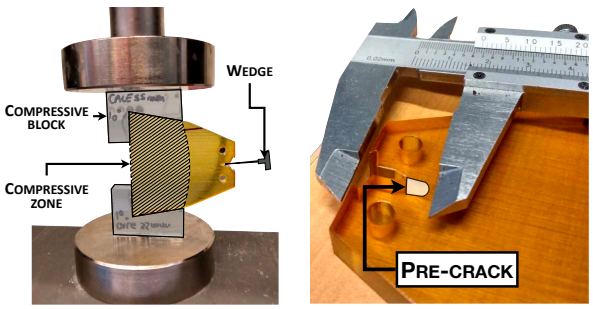

(a) (b)

Figure 6.4: Preparation of a VeroClear TDCB sample : the specimen is pre-cracked by inserting a wedge between the lips of TDCB partially compressed sample (a) and the initial crack length is measured before the fracture test (b).

The fracture test is then conducted under controlled displacement at a loading rate $\dot{\delta} = 0.9 \cdot 10^{-5}\text{m.s}^{-1}$. The force-displacement curve acquired during the test is plotted in Fig. 6.5.a and the toughness-velocity curve resulting from the compliance method is plotted in Fig. 6.5.b for a Veroclear sample.

If stable quasi-static crack propagation ($v \simeq 10^{-4}\,\text{m.s}^{-1}$) can be obtained on the Veroclear, the success rate of such experiments is nonetheless very low (6 successful experiments over $\simeq$ 50 samples) and almost null for more compliant materials such as DurusWhite and DM4310. The first difficulty lies in the fact that both Veroclear and DM4310 show stick-slip behavior under a constant loading rate : crack propagation oscillates between a stick regime, where the crack propagates quasi-statically, and a slip regime characteristic of phases of sudden propagation, in which inertial effects cannot be neglected. Stick-slip

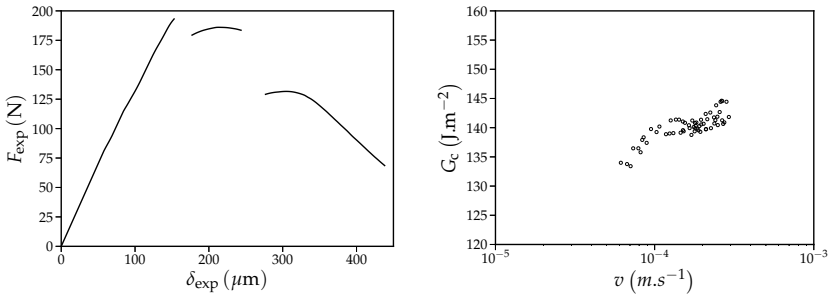

Figure 6.5: Quasi-static crack propagation in a VeroClear TDCB sample : the force F_{exp} and displacement of the crack lips δ_{exp} are recorded during the experiment (a) and the compliance method is used to measure the evolution of the material toughness G_{c} with the crack speed v (b).

events have been observed extensively in similar materials such as PMMA [Ravi-Chandar and Balzano, 1988], thermosetting polymers [Leevers, 1986] or epoxy resins [Yamini and Young, 1979]. Such a behavior is attributed to a non-monotonous variation of the fracture energy with velocity (see Fig. 6.6.a). The $G_{\text{c}} - v$ curve of the material consists in two stable branches, one at low velocity (Region I) and one at high velocity (Region III), supposedly separated by a branch where the toughness decreases with the velocity (Region II). If the crack is driven in Region II or if the crack accelerates as the crack propagates (A from B), it may leave the stable branch (B from C), decelerate as the crack comes closer to the sample end (C from D) and finally go back in the stable branch (D from E). If the initial crack is not sharp, the imposed ERR G at initiation is high so that the crack propagates in Region III at high velocities (see Fig. 6.6b & c), often up to the complete failure of the specimen. Stick-slip behavior thus imposes a ceiling value to the driving rate $\dot{\delta}$ one can use during experiments.

On the contrary, if one drives the crack at a very slow rate $\dot{\delta} \leq 0.6 \cdot 10^{-5}\,\text{m.s}^{-1}$, the viscosity of the material is activated and the fracture behavior is no more brittle. As shown in Fig. 6.6.d, intense crazes are developed on the crack surface and the fracture toughness increases dramatically ($G_{\text{c}} \simeq 800\,\text{J.m}^2$), suggesting a transition from a brittle to a ductile behavior. The viscosity of the material thus constitutes the second main difficulty raised by the polymers used in the study. It imposes a lower threshold on the driving rate one can use to test 3D printed polymers.

In conclusion, stable crack propagation in the stick regime can only be obtained on Veroclear from a perfectly clean pre-crack and for a very narrow range of driving speed ($\dot{\delta} \in \left[0.6 \cdot 10^{-5}, 10^{-5}\right]$). In the case of the more compliant DM4310, brittle fracture experiments of a crack propagating in the stable stick regime are almost impossible to perform in ambient conditions. One could overcome those difficulties by conducting experiments at very low temperatures to prevent viscous effects. Yet one should keep in mind that our goal is to conduct fracture tests on heterogeneous materials, in which a crack propagates with characteristic jerky dynamics [Bonamy, 2009]. It appears thus more convenient to work in the dynamic branch of the $G_{\text{c}} - v$ curve to overcome the issues raised by both the stick-slip behavior and the material viscosity. Investigating fracture processes at such temporal scales

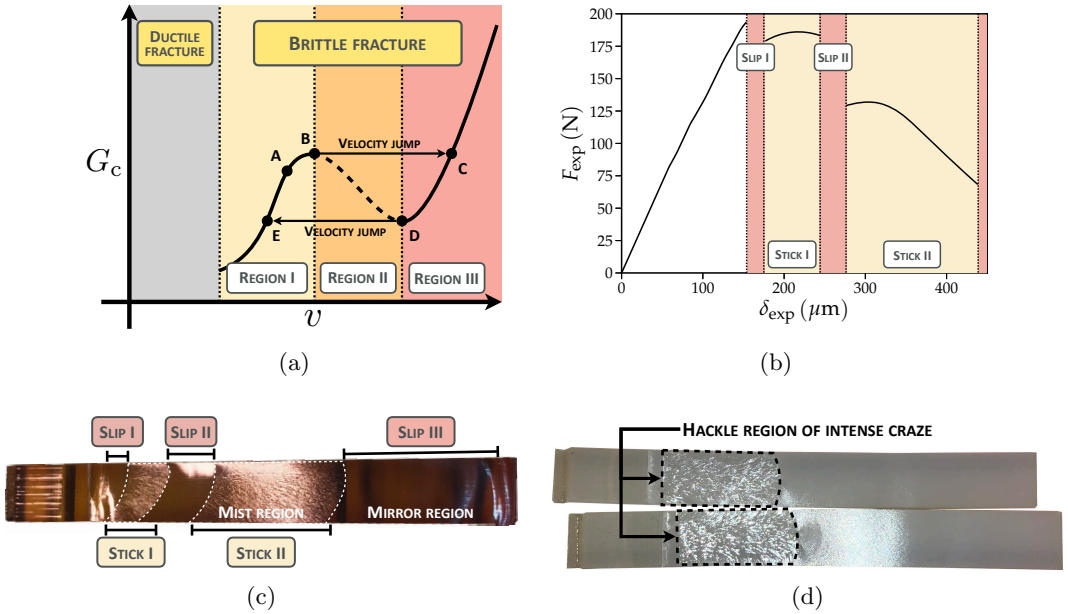

Figure 6.6: Stick-slip behavior in Vero and Durus materials : evolution of the fracture energy G_c with the crack velocity for Veroclear and DM4310, showing stick-slip behavior (a) ; if the crack is driven in Region II (initiation), it oscillates between phases of stable quasi-static crack propagation in Region I and dynamic phases at high velocity in Region III. This behavior can be noted on the force-displacement curve (b) as well as on the fracture surface displaying a mist profile characteristic of Region I and a mirror one typical from Region III (c). If the crack is driven at a very low rate, the fracture process becomes ductile and the fracture surface displays a hackle region (d).

requires nonetheless to implement new techniques based on Digital Image Correlation as detailed in the next section.

6.3 Digital Image Correlations methods for crack tracking and SIF estimation in dynamic fracture

In the following, experiments are performed at a driving rate $\dot{\delta} = 2.5 \cdot 10^{-2}\,\mathrm{m.s^{-1}}$. The TDCB is pre-notched in the manufacturing process but is not pre-cracked so that the ERR at initiation is large enough to prevent any slip-to-stick transition during the experiments (D to E in Fig. 6.6.a). Cracks propagate at speeds ranging from $20\mathrm{m.s^{-1}}$ to $300\mathrm{m.s^{-1}}$ so that the time scales involved in the fracture process are well below the time characteristic of the viscous relaxation of our 3D printed polymers, which are very similar to PMMA and polypropylene [Read and Duncan, 1981]. Moreover, post-mortem fracture surfaces are smooth and micro-crack branching from the main crack are absent. All experiments have crack velocities lower than the critical velocity for the micro-branching instability to occur Scheibert et al. [2010]. The fracture is thus perfectly brittle and can be analyzed within a LEFM framework.

If the load cell and the clip-gauge can track the elastic response of the specimen during the loading phase ($\simeq 10^{-1}$s), they cannot provide any quantitative information at the time scales of the fracture process ($\simeq 10^{-4}$s). Digital Image Correlation calculations, which rely on image acquisition performed at high rate $\simeq$ 100kHz by a high-speed camera, offer a convenient way to track crack propagation at a fine temporal scale. The crack, considered as a local jump in displacements, can be identified through DIC methods, which provide direct access to the local displacement field from the comparison of two images acquired at different loading instants [Sutton et al., 2000]. We propose a method to track with great accuracy the fracture process through a local DIC approach, exposed in Section 6.3.1. The crack tip position and the stress intensity factors are then measured in Section 6.3.2 from a continuous approximation of the transformation [Chateau et al., 2018] thanks to William's expansion of the displacement field at the crack tip [Henninger et al., 2010]. This approach is finally compared to the results obtained by image subtraction [Chateau et al., 2018] and by a DIC-based compliance method [Grabois et al., 2018] in Section 6.3.3.

6.3.1 Local DIC method for displacement measurement

6.3.1.a Principle of DIC

Let us consider a pair of two-dimensional digital images associated with the reference and deformed states of the loaded sample. They are described by their grey-scale fields, respectively noted f and g. A point at coordinates $\mathbf{X}$ in the reference image is related to its position $\mathbf{x}$ in the deformed image by the mechanical transformation :

$$\mathbf{x} = \mathbf{\Phi}(\mathbf{X}) = \mathbf{X} + \mathbf{u}(\mathbf{X}) \tag{6.3}$$

where $\mathbf{u}$, the displacement field, can be obtained as the optimal solution of a variational problem.

The relation between f and g is given by the formulation of a relaxed grey-level conservation principle :

$$g(\mathbf{\Phi}(\mathbf{X})) = a\, f(\mathbf{x}) + b + g'(\mathbf{x}) \tag{6.4}$$

where a and b are the coefficients of overall contrast and brightness evolution between images while g' is the noise present in both reference and deformed image.

The DIC method consists in finding the homologous position $\mathbf{x}$ of a material point $\mathbf{X}$ by optimizing a correlation coefficient C, that measures the similarity of the grey level distribution between the two images. The estimation of the transformation $\mathbf{\Phi}$ on the basis of the above image pair represents a severely ill-posed inverse problem. To address this issue, one may approximate the transformation $\mathbf{\Phi}$ at a material point $\mathbf{X_0}$, called *correlation point*, by a transformation $\mathbf{\Phi_0}$ by optimizing the correlation coefficient $C(\mathbf{\Phi_0})$ on a small domain D located around the correlation point, called the *correlation window*. The shape of the approximate transformation is prescribed and can consist for example in a simple translation (two components in 2D) or a combination of a translation and a linear transformation (six components in 2D). In the same manner, various choices are possible for the expression of the correlation coefficient $C(\mathbf{\Phi_0})$. In this study, we use the *zero-centred normalised cross-correlation coefficient* formulation (ZCNCC), which reads :

$$C(\mathbf{\Phi_0}) = 1 - \frac{\sum_{\mathbf{X}_i \in D} \left(f(\mathbf{X}_i) - \bar{f}_{\mathrm{D}}\right) \cdot \left(g(\Phi_0(\mathbf{X}_i)) - \bar{g}_{\mathrm{D}}\right)}{\sqrt{\sum_{\mathbf{X}_i \in D} \left(f(\mathbf{X}_i) - \bar{f}_{\mathrm{D}}\right)^2} \cdot \sqrt{\sum_{\mathbf{X}_i \in D} \left(g(\Phi_0(\mathbf{X}_i)) - \bar{g}_{\mathrm{D}}\right)^2}} \tag{6.5}$$

where $\mathbf{X}_i$ and $\mathbf{\Phi_0}(\mathbf{X}_i)$ are respectively the coordinates (in pixels) of homologous points in the sub-domain D in the reference image and in the deformed image. $\bar{f}_{\mathrm{D}}$ and $\bar{g}_{\mathrm{D}}$ are respectively the averages of the grey levels on the domain D and on the homologous domain transformed by $\mathbf{\Phi_0}$. While positions $(\mathbf{X}_i)$ in the reference image coincide with pixel centers, their coordinates $\Phi_0(\mathbf{X}_i)$ in the deformed image might not be integers, so that one can access them through a bilinear or bicubic interpolation of the deformed image. The correlation criterion C varies from 0 (perfect match) to a maximum of 2 (when fluctuations of f and g are opposite), the value 1 corresponding to no match at all. This measure of similarity is insensitive to a global contrast or brightness variation on the windows between both configurations [Dautriat et al., 2011]. This approach is called *local* DIC in contrast with the *global* approach where this problem is tackled on the whole image within a variational approach [Besnard et al., 2006].

6.3.1.b Experimental set-up for image acquisition

Because there is no natural contrast at the surface of our 3D printed sample, a speckle pattern is deposited into the surface of the specimen with black painting on a white coating (see Fig. 6.7.c & d). The typical dimensions of the resulting speckle, obtained through its auto-correlation function, is around $100 - 150\,\mathrm{mm}$ (2-3 pixels).

A high-speed camera (Phantom v2511) records the crack dynamics in the immediate vicinity of the crack path at an acquisition rate ranging from 100,000 to 232,000 frames per second (Fig. 6.7.a) with a resolution ranging from 896x96 to 1024x176 pixels (Fig. 6.7.d).

Particular attention is paid to position the camera on a perpendicular axis to the specimen plane. Additionally, the specimen is placed in a guide (Fig. 6.7.b) to prevent large out-of-plane motion of the sample due to its rotation around the loading axis during the fracture test. However, the sample is not squeezed by the guide not to influence the experiments. As a result, rotations are still possible but are restricted to small angles. It ultimately allows to reduce errors in the DIC analysis due to out-of-plane motion of the sample [Dautriat et al., 2011; Grabois et al., 2018].

Finally, the pixel size is measured from a reference image of the full specimen with a ruler fixed on the side of the guide (Fig. 6.7.c). The pixel size is inferred from the ruler by measuring the typical wave-length of the grey levels variations along a segment. In average, the pixel size amounts to $d_{\text{pix}} \simeq 50\,\mu\text{m}$.

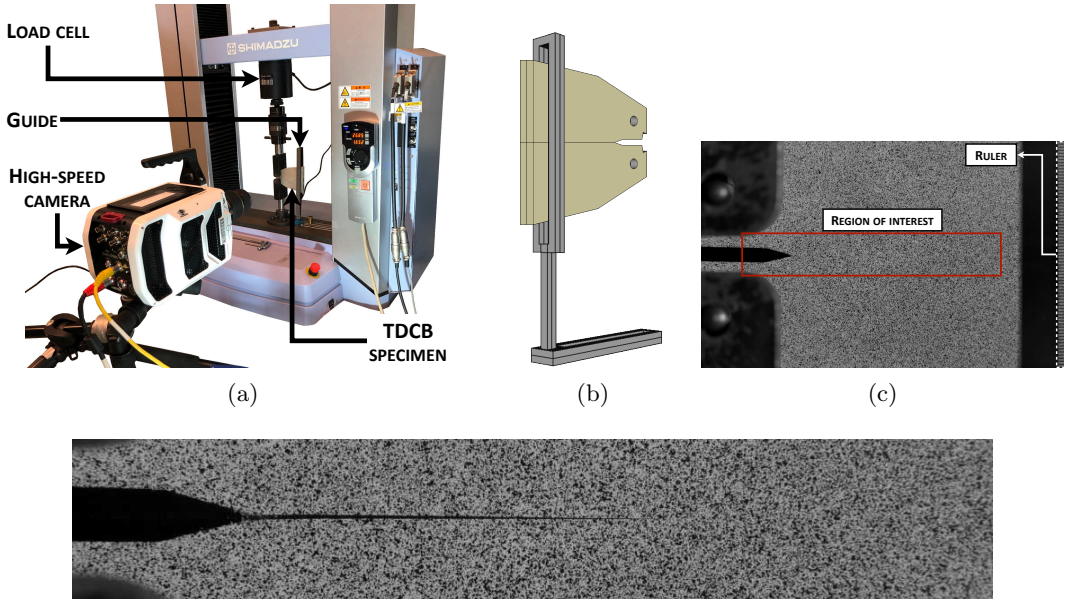

(a) (b) (c)

(d)

Figure 6.7: Experimental set-up for the fracture test analyzed by DIC : crack propagation under tensile loading is recorded on the speckled TDCB sample via a high-speed camera (a). The specimen is inserted in a guide to avoid DIC errors through out-of-plane motion of the sample (b). The pixel size is measured from a ruler attached to the guide (c) and crack propagation is recorded on a reduced region of interest (ROI) located in the vicinity of the predicted crack path to allow for higher acquisition rates (d).

6.3.1.c Correlation points selection and DIC procedure

Given the properties of the material used in the study, the deformation of the 3D printed polymers is fairly limited and does not exceed 0.2-0.3% except at the crack tip. Yet the left part of the region of interest (ROI) is subjected to large displacements due to the crack opening so that correlation errors can emerge if a correlation window goes out of the ROI. Other significant errors in the correlation procedure can arise from cases where a correlation window is crossed by the crack. In order to prevent such situations from arising, particular attention is paid in the generation of the grid of correlation points through the following procedure :

1. first, a grid of correlation points with a correlation domain of 12 pixels is generated on the final image acquired during the fracture test, when the crack has gone through the whole ROI. The correlation points are carefully placed on both sides of the crack lips up to the edge of the ROI (Fig. 6.8.a) ;

2. second, a preliminary DIC procedure is performed using the in-house software CMV between this final image and the first one acquired during the test. The procedure is run at a pixel precision with a correlation coefficient criterion set to 0.3 assuming that the approximate transformation $\mathbf{\Phi_0}$ consists in a pure translation ;

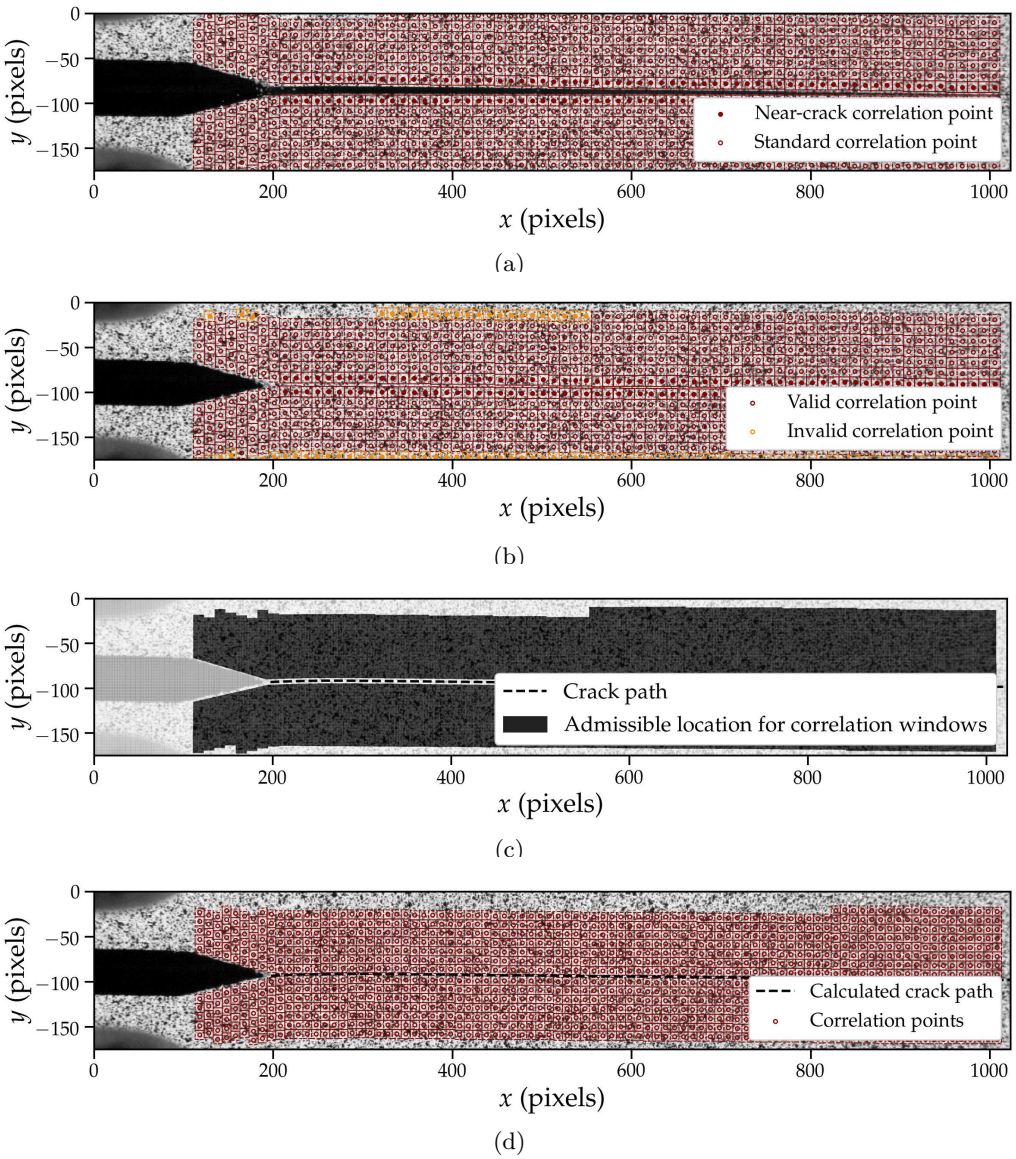

Figure 6.8: Generation of an optimized grid from the correlation procedure : a first set of correlation points is generated on the final image of the fractured specimen around the crack lips (a). From their position in the reference image (b), we infer both the crack path and the domain of admissible points (i.e. reliably correlated and remaining in the ROI during the experiments) (c). The final grid of correlation points used in the DIC procedure is generated inside this domain (d).

3. third, the crack path in the reference image (intact sample) is inferred from the position of the correlation points which were located on the lips of the crack in the final image (Fig. 6.8.a & b). A domain of admissible points is constructed from the correlation points which fully remain within the ROI during the fracture test. This domain is then eroded through morphological operations in the vicinity of the crack path and around the domains where the correlation criterion has not been validated (due to poor local image contrast or presence of painting fragments ejected during the fracture test) (Fig. 6.8.c). The final grid of correlation points is generated inside the resulting domain. They are placed with a constant spacing in the x-direction of crack propagation but not in the y-direction due to the presence of the crack. Such a grid is shown in Fig. 6.8.d.

The procedure allows to keep only the more reliable points for the subsequent DIC calculation. The DIC analysis is performed on the generated grid following a standard two-step procedure :

1. first, a correlation calculation is carried out assuming pure translation at a pixel precision. The correlation coefficient criterion is set to 0.3 ;

2. second, a correlation procedure is performed with a subvoxel optimization, using domains of the same edge-length but assuming a combination of a translation and a linear local transformation.

6.3.1.d DIC error assessment

If the procedure detailed above aims at improving as much as possible the precision of our analysis, DIC measurements always prone to errors, which can be classified in the following [Bornert et al., 2009; Dautriat et al., 2011; Nguyen, 2015] : image noise (SE1), geometric errors due to optical distortions (SE2), DIC algorithm with shape function mismatch errors (SE3a) and systematic error (SE3b), out of plane rigid body motion (SE4).

(SE1) is related to the characteristics of the sensor of the camera and the contrast within the correlation domains. If we cannot work on the former, the latter has been addressed by applying speckle painting. (SE2) might emerge from issues with instabilities or distortions the imaging system. Such errors might be significant in our case since we use a non-telecentric lens. Additionally, the fracture test is characterized by large displacements on both sides of the crack lips. We try to address this issue in the grid generation procedure by only selecting correlation domains which remain within the ROI during the whole experiment. (SE3a) depend on the intensity of the local strain field [Bornert et al., 2009] and are expected to be very low on the bulk material and potentially significant around the crack tip. (SE3b) are related to the available contrast, image quality, noise, chosen image correlation algorithm and interpolation of gray levels in the correlation domain, which is performed to get the displacement with sub-pixel accuracy [Nguyen, 2015]. Finally, (SE4) might be of major importance in our work but we tried to keep them as low as possible thanks to the positioning of the camera and the guide inserted around the sample.

We analyze errors coming from (SE1) and (SE3b) by measuring the displacement between

100 images acquired before the beginning of the test. Such errors amount to $\simeq 0.1$ pixels at most (see Fig. 6.9).

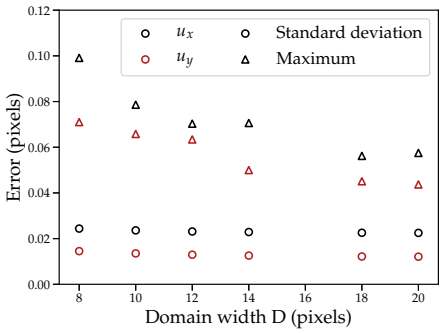

Figure 6.9: Influence of the size of the correlation window on the DIC results : the errors on the displacement field reach $\simeq 0.1$ pixels at most.

6.3.2 Tracking of the fracture problem from DIC measurements

6.3.2.a Local transformation approximation

DIC calculations, performed on the set of images acquired during the fracture test, give information on the displacement field on the sole correlation points. A correlation point is considered well-correlated if is correlation coefficient is lower than a value prescribed here to 0.1. The transformation $\mathbf{\Phi}$ can be approximated on each pixel following the work of Chateau et al. [2018].

We note $\mathbf{X}$ the position of a pixel center in the reference image and $\mathbf{X_0}$ the position of its nearest neighbor correlation point with measured displacement. At first order, the transformation $\mathbf{\Phi}$ at point $\mathbf{X}$ can be approximated by $\mathbf{\Phi_1}$, which reads :

$$\mathbf{\Phi_1}(\mathbf{X}) = \mathbf{X} + \mathbf{u}(\mathbf{X_0}) + \frac{\partial \mathbf{u}}{\partial \mathbf{X}}(\mathbf{X_0}) \cdot (\mathbf{X} - \mathbf{X_0}) \tag{6.6}$$

In two-dimensions $\mathbf{\Phi_1}$ is defined by 6 parameters (2 components for the displacement and 4 for the gradient of the displacement). By definition of the deformation gradient $\mathbf{F} = \frac{\partial \mathbf{\Phi}}{\partial \mathbf{X}}$:

$$\frac{\partial \mathbf{u}}{\partial \mathbf{X}}(\mathbf{X_0}) = \mathbf{F}(\mathbf{X_0}) - \mathbf{I} \tag{6.7}$$

where $\mathbf{I}$ is the identity tensor.

Since $\mathbf{u}(\mathbf{X_0})$ has already been provided by the DIC computation, one only needs to determine $\mathbf{F}(\mathbf{X_0})$ to approximate $\mathbf{\Phi}$. As proposed by Chateau et al. [2018], $\mathbf{F}(\mathbf{X_0})$ can be inferred from affine best-fit $\mathbf{\Phi_N}$ of the DIC measured displacements of N neighboring well-correlated correlation points $(\mathbf{X_i})_{i \in [\![1,N]\!]}$ of the considered pixel $\mathbf{X}$. It reads :

$$\mathbf{\Phi_N}(\mathbf{X}) = \mathbf{T_N}(\mathbf{X}) + \mathbf{F_N}(\mathbf{X}) \cdot \mathbf{X} \tag{6.8}$$

where $\mathbf{F_N}$ and $\mathbf{T_N}$ are defined as the solution of the following weighted least square problem :

$$\mathbf{T_N}, \mathbf{F_N} = \text{Argmin} \sum_{i=1}^{N} \omega_i \left\| \mathbf{x_i} - \mathbf{T_N} + \mathbf{F_N} \cdot \mathbf{X_i} \right\|^2 \tag{6.9}$$

The neighboring correlation points are selected according to a criterion of maximum distance d from the considered pixel $\mathbf{X}$:

$$\|\mathbf{X} - \mathbf{X_i}\| \leq d \tag{6.10}$$

where $\|\cdot\|$ is the Euclidian norm. As noted by Chateau et al. [2018], a small distance d reflects more accurately the local strain heterogeneities in the material while a large distance d allows the result to be less sensitive to the DIC errors. In the following, the distance d is set to 30 pixels, i.e. three times the size of the correlation window. Only correlations points located on the same side of the crack lips as the considered pixel are taken into account into the affine fit. It allows to model properly the displacement discontinuity at the crack lips. This last criterion is nonetheless relieved for pixels located on the immediate vicinity of the predicted crack path.

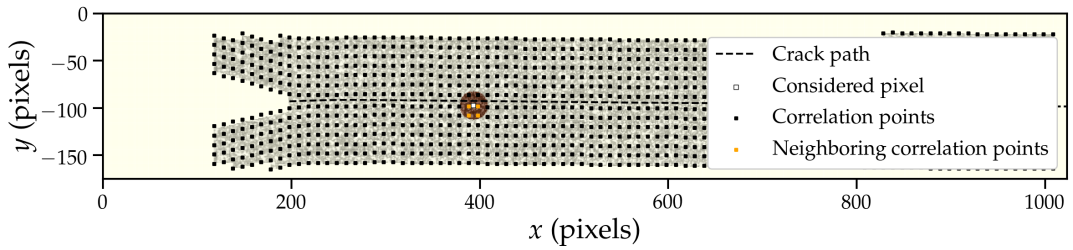

Figure 6.10: Approximation of the dense transformation $\mathbf{\Phi_N}$ at a pixel value (in orange) from the displacement of neighboring well-correlated points (in red).

Two-dimensional computations are performed at a low computational cost. Thus we follow the suggestions addressed by Chateau et al. [2018] and consider a weighted least square problem (see Eq. (6.9)) with weights ω_i continuously decreasing to zero when the distance $\|\mathbf{X} - \mathbf{X_i}\|$ gets close to d. We tried several shape functions for the ω_i with no significant impact on the final results. Thus, we set in the following :

$$\omega_i = 1 - \frac{\|\mathbf{X} - \mathbf{X_i}\|^2}{d^2} \tag{6.11}$$

In that case, the optimal translation $\mathbf{T_N}$ and deformation gradient $\mathbf{F_N}$ read :

$$\mathbf{T_N} = \langle \mathbf{\Phi}(\mathbf{X}) \rangle_N - \mathbf{F_N} \cdot \langle \mathbf{X} \rangle_N \tag{6.12}$$

and :

$$\mathbf{F_N} = \left[\sum_{i=1}^{N} \omega_i \left(\mathbf{\Phi}(\mathbf{X_i}) - \langle \mathbf{\Phi}(\mathbf{X}) \rangle_N \right) \otimes \left(\mathbf{X_i} - \langle \mathbf{X} \rangle_N \right) \right] \cdot \left[\sum_{i=1}^{N} \omega_i \left(\mathbf{X_i} - \langle \mathbf{X} \rangle_N \right) \otimes \left(\mathbf{X_i} - \langle \mathbf{X} \rangle_N \right) \right]^{-1} \tag{6.13}$$

where $\langle a \rangle_N = \dfrac{\sum_{i=1}^{N} \omega_i a_i}{\sum_{i=1}^{N} \omega_i}$.

Using this affine local best fit, the dense continuation $\mathbf{\Phi_1}$ of the mechanical transformation can then be defined by :

$$\mathbf{\Phi_1}(\mathbf{X}) = \mathbf{X} + \mathbf{u}(\mathbf{X_0}) + (\mathbf{F_N}(\mathbf{X}) - \mathbf{I}) \cdot (\mathbf{X} - \mathbf{X_0}) \tag{6.14}$$

But, in the following, $\mathbf{\Phi_N}$ is considered as the approximation of the local transformation and the displacement at point $\mathbf{X}$ reads $\mathbf{u}(\mathbf{X}) = \mathbf{\Phi_N}(\mathbf{X}) - \mathbf{X}$. One of the advantage of such an approach is that one can remove automatically the influence of poorly correlated points (for example due to an insufficient local contrast) from the estimation of the local transformation.

6.3.2.b Crack tip detection

As we saw in Chapter 4, two ingredients are essential to characterize the propagation of a crack and the ultimate fracture properties of the material : the position ℓ of the crack front, i.e. crack tip in two-dimensions, and the local ERR G. Let us see first how DIC computations can allow for a precise determination of the crack tip position.

In the adopted experimental conditions, the response of the material is linear elastic so that the displacement field $\mathbf{u}(\mathbf{X}) = u_x + i\,u_y$ can be expanded in William's series. Considering a straight crack located at the origin, it reads Williams [1952] :

$$\mathbf{u}(\mathbf{X}) = \sum_{p=p_{\min}}^{p_{\max}} \frac{\omega_p^{\mathrm{I}}}{2\mu\sqrt{2\pi}} r^{\frac{p}{2}} \psi_p^{\mathrm{I}}(\theta) + \frac{\omega_p^{\mathrm{II}}}{2\mu\sqrt{2\pi}} r^{\frac{p}{2}} \psi_p^{\mathrm{II}}(\theta) \tag{6.15}$$

where μ is the shear modulus of the material, (r,θ) the polar coordinates of points $\mathbf{X}$ and ψ_p^{I} and ψ_p^{II} are the p-terms shape functions in Mode I and II respectively. They reads :

$$\begin{cases} \psi_p^{\mathrm{I}}(\theta) = \kappa e^{i\frac{p}{2}\theta} - \frac{p}{2} e^{i\left(2-\frac{p}{2}\right)\theta} + \left((-1)^p + \frac{p}{2}\right) e^{-i\frac{p}{2}\theta} \\ \psi_p^{\mathrm{II}}(\theta) = \kappa e^{i\frac{p}{2}\theta} + \frac{p}{2} e^{i\left(2-\frac{p}{2}\right)\theta} + \left((-1)^p - \frac{p}{2}\right) e^{-i\frac{p}{2}\theta} \end{cases} \tag{6.16}$$

p is usually taken larger than 1 to ensure that the elastic energy remains finite. Yet, zero-order terms describe rigid translations and super-singular terms can provide useful information as we will see in the following.

In pure Mode I loading, Eq. (6.16) states that the crack opening $[\![u_y]\!](x)$, defined as the jump in vertical displacement between two points located on the crack lips at a distance x of the crack tip, scales as $x^{1/2}$. Consecutively, we place a set of pair correlation points at various positions x on both sides of the crack path with a correlation window 8×14 pixels (see Fig. 6.11) and follow the jump in displacement $[\![u_y]\!](x)$ during the fracture test by DIC [Abanto-Bueno and Lambros, 2002]. As predicted by LEFM, we see in Fig. 6.12.a that $[\![u_y]\!](x)^2$ scales as $\max(x,0)$, which allows for a simple estimation of the crack tip position from a linear fit.

This method is very simple in its implementation but only provides the crack tip position at a precision similar to the size of the correlation window i.e. 8 pixels $\simeq 0.4mm$, which leads to an incertitude of about $\pm 40 - 80 \mathrm{m.s}^{-1}$ on the crack velocity, which is not acceptable. As noted by Henninger et al. [2010], one can estimate the crack tip position as the one which makes super-singular term ω_{-1}^{I} in the William's expansion vanish.

From a linear least square method, we estimate the set of amplitudes $\left(\omega_p^i\right)$ which fits the best the dense estimation of the displacement field $\mathbf{u}$ from the local best-fit transformation

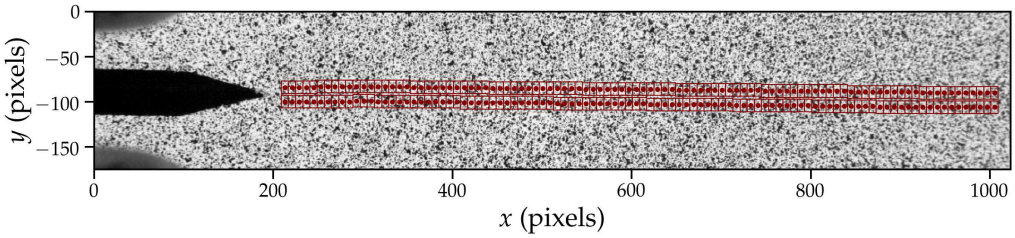

Figure 6.11: Estimation of the crack tip position from the vertical displacement of pairs of correlated points located on both sides of the crack tip.

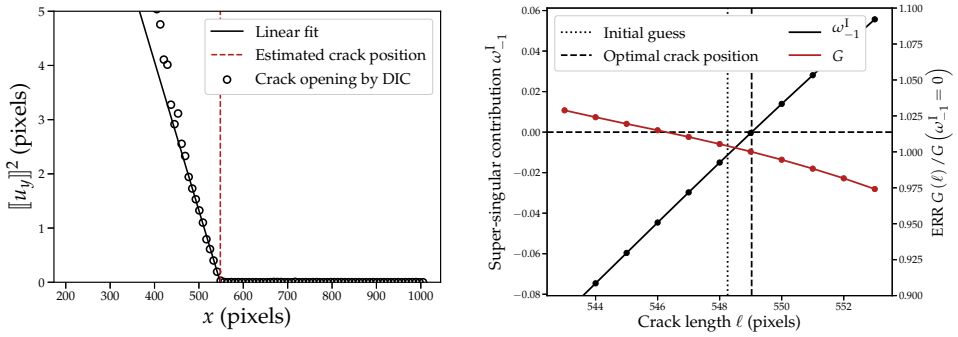

(a) (b)

Figure 6.12: Measurement of the crack tip position : the position of the crack tip is first estimated from the opening displacement method where the vertical displacement of pairs of correlated points located on both sides of the crack tip is tracked during the experiments (a). This initial guess is then refined by determining the position ℓ where the super-singular term in the William's expansion ω^{I}_{-1} vanishes (b).

$\mathbf{\Phi_N}$ by William's expansion of Eq. (6.16) in a defined domain. As proposed by Henninger et al. [2010], one can use a donut of interior radius $R_{\min}$ and exterior radius $R_{\max}$ eroded around the crack path as a proper fitting domain for the linear least square optimization (see Fig. 6.13). As performed by Henninger et al. [2010] and Grabois et al. [2018], we tested various dimensions $(R_{\min}, R_{\max})$ as well as terms numbers in the William's expansion $(p_{\min}, p_{\max})$ (see Eq. (6.15)) with the same conclusions. In the following we set $R_{\min} = 8$ pixels, $R_{\max} = 80$ pixels, $p_{\min} = -3$ and $p_{\max} = 12$.

Several positions for the crack tip are tested along the crack path predicted in Section 6.3.1.c in the vicinity of the position found by the crack opening method, which is used as an initial guess to speed up the computations. The crack position is then measured with a subpixel accuracy as the one where $\omega^{\mathrm{I}}_{-1} = 0$. An example of such a procedure is given in Fig. 6.12.b.

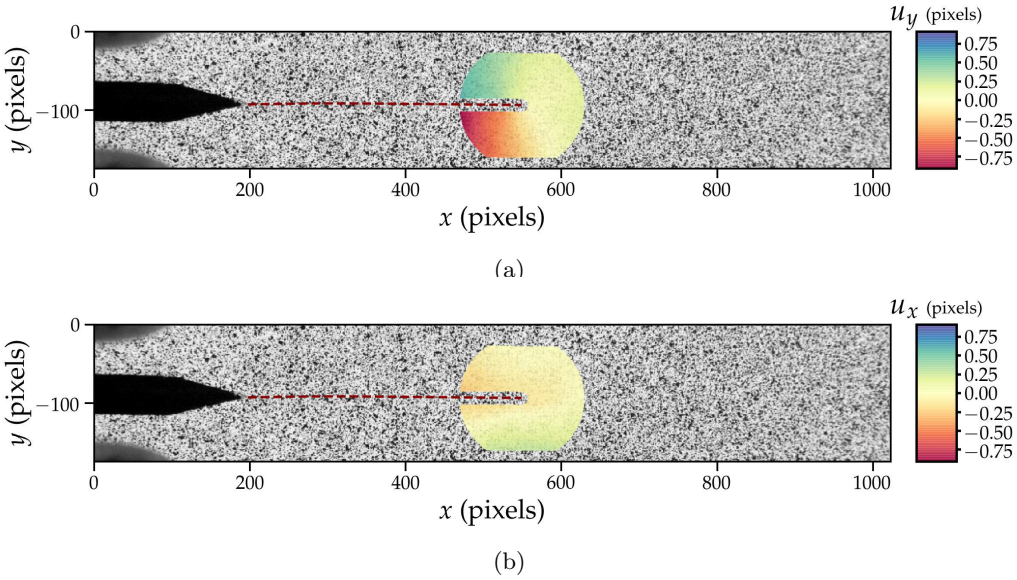

Figure 6.13: Calculation of the local SIF : the vertical u_y (a) and horizontal u_x (b) components of the displacement field $\mathbf{u}$ are approximated by William's expansion series on a circular domain surrounding the crack tip.

6.3.2.c Stress intensity factors measurements

One can finally estimate the stress intensity factors $K_{\mathrm{I}} = \omega_1^{\mathrm{I}}$ and $K_{\mathrm{II}} = \omega_1^{\mathrm{II}}$ from a last linear least square procedure by fitting the dense approximation of the displacement field $\mathbf{u}$ by a William's expansion at the crack tip position [Henninger et al., 2010; Grabois et al., 2018].

6.3.3 Validation of the proposed method on homogeneous materials

We validate the proposed approach with the study of dynamic crack propagation in homogeneous 3D printed specimens. The results presented in this section comes from a fracture test of a DM4310 TDCB sample.

6.3.3.a Crack tip position

First, we need to assess the validity of our method in predicting the position of the crack tip. The fact that the final position for the crack tip is close to the initial guess provided by direct DIC measurements of crack opening already constitutes a validation of the approach.

A second validation is proposed by confronting the estimated position to the results of an image subtraction method [Chateau et al., 2018], which coincides here with the so-called *correlation residuals* of the *global* DIC approach [Besnard et al., 2006]. The deformed image is transformed back to the same frame as the reference image thanks to the estimation $\mathbf{\Phi_N}$ of the local transformation following :

$$\mathbf{r}(\mathbf{X}) = [a_\Omega g(\mathbf{\Phi_N}(\mathbf{X})) + b_\Omega] - f(\mathbf{X}) + k \tag{6.17}$$

where a_Ω and b_Ω are local coefficients computed on subset domains Ω of size 60×60 pixels

to take into account possible variations in image contrast and brightness. They read :

$$a_\Omega = \frac{\sum_{\mathbf{X}\in\Omega}\left(f\left(\mathbf{X}\right) - \bar{f_\Omega}\right)\cdot\left(g\left(\Phi_N\left(\mathbf{X}\right)\right) - \bar{g_\Omega}\right)}{\sum_{\mathbf{X}\in\Omega}\left(g\left(\Phi_N\left(\mathbf{X}\right)\right) - \bar{g_\Omega}\right)^2} \tag{6.18}$$

and :

$$b_\Omega = \bar{f_\Omega} - a_\Omega \bar{g_\Omega} \tag{6.19}$$

The grey values of the points located at $g\left(\Phi_N\left(\mathbf{X}\right)\right)$ are evaluated by a bicubic interpolation of the deformed image.

Results of the subtraction procedure for a given loading state are shown in Fig. 6.14 and confirm the validity of the crack tip detection procedure.

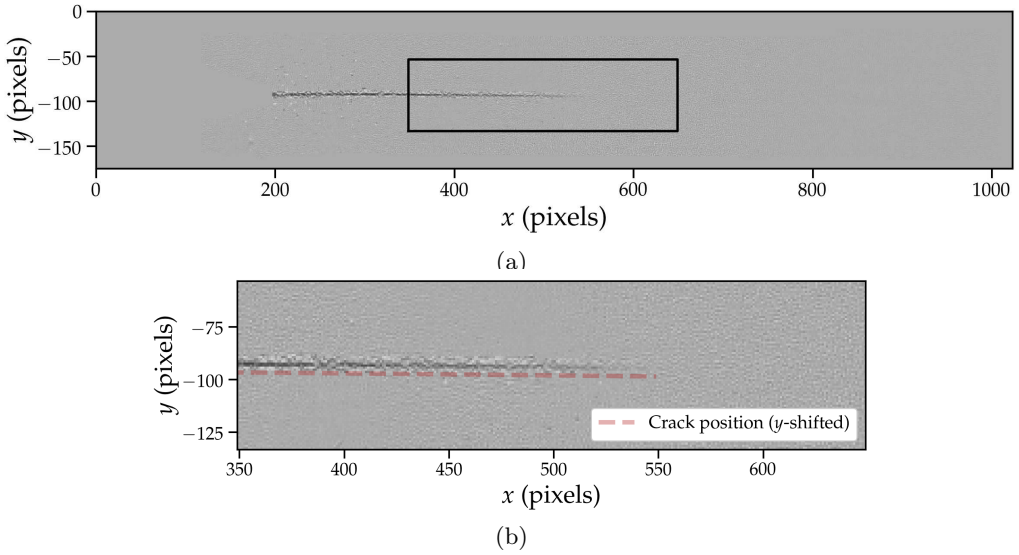

Figure 6.14: Validation of the crack tip position by image subtraction : the deformed image is thus transformed back to the same frame as the reference image to compute the difference between both images, taking into account possible brightness and contrast adjustments. The subtracted image reveals the crack path (a), which is compared to the crack tip position inferred from William's expansion (shifted downwards in the y-direction for clarity) (b).

6.3.3.b SIF estimation

Finally, the estimated values of the stress intensity factors are compared with estimates derived from a DIC-based compliance method. Since the clip-gauge cannot track the crack lips opening during the dynamic fracture test, we replace it by virtual DIC clip-gauges, consisting in a set of 10 pairs of correlation points of correlation window 10x10 pixels, located on both sides of the manufactured notch (see Fig. 6.15).

The opening (δ_i^{DIC}) is computed through a similar DIC procedure as the one described in Section 6.3.1. Since the initial crack length is known from the position of the node, the reduced force $f = F/E$ can be estimated by the FEM-based compliance method described in Section 6.2.1. The Young modulus $E = 2\,\mathrm{GPa}$ of the specimen is then calculated with a least square procedure to match the force data acquired by the load cell during the loading phase up to the peak, characteristic of crack initiation (see Fig. 6.16.a).

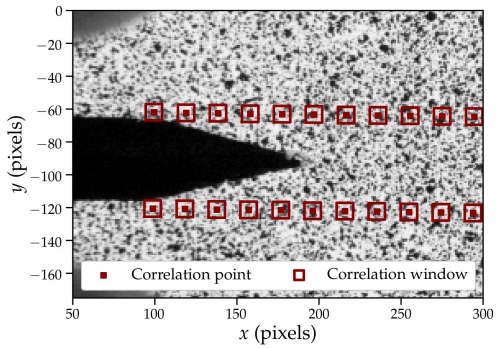

(a)

Figure 6.15: Compliance method coupled with DIC : displacement of virtual DIC clip-gauges (pairs of correlation points located on both sides of the notch) are tracked during the fracture test.

From the data of the crack length ℓ extracted from the DIC procedure and the crack lips opening (δ_i^{DIC}), one can compute the ERR G after Eq. (6.2). The Mode I SIF K_{I} is inferred from G from Irwin's formulae assuming plane stress conditions $K_{\text{I}} = \sqrt{EG}$. Yet these estimates on G and K_{I} correspond to a static case, whereas the crack propagates at a speed $v \simeq 250\,\text{m.s}^{-1} \simeq 0.3c_R$, where $c_R \simeq 770\text{m.s}^{-1}$ is the Rayleigh wave speed of the material. The static Mode I SIF $K_{\text{I}}^{\text{stat}}$ and ERR G^{stat} have to be corrected to take into account inertial effect. Following Freund [1998], one gets in pure Mode I under plane stress conditions :

$$\begin{cases} K_{\text{I}}^{\text{dyn}} = K_{\text{I}}^{\text{stat}} k_{\text{I}}(v) \simeq K_{\text{I}}^{\text{stat}} \dfrac{\left(1-\frac{v}{c_R}\right)}{\sqrt{1-\frac{v}{c_d}}} \\ G^{\text{dyn}} = \dfrac{K_{\text{I}}^{\text{dyn}\,2}}{E} A_{\text{I}}(v) = G^{\text{stat}} g(v) \simeq G^{\text{stat}} \left(1-\frac{v}{c_R}\right) \end{cases} \tag{6.20}$$

where c_d is the dilatational wave speed of the material.

The compliance method only gives an estimate of the static values $K_{\text{I}}^{\text{stat}}$ and G^{stat}, whereas the DIC approach for SIF calculation presented above gives an in-situ measurement of $K_{\text{I}}^{\text{dyn}}$ from which G^{dyn} can be inferred through Eq. (6.20).

The comparison between the dynamic SIF $K_{\text{I}}^{\text{dyn}}$ and ERR G^{dyn} calculated from the DIC and compliance method are plotted in Fig. 6.16.c & d. We see that K_{I} is estimated with a precision of $\pm 0.07\text{MPa}.\sqrt{\text{m}}$, which is consistent with the study of Grabois et al. [2018] based on the global DIC approach. We also notice that the crack is loaded in principal Mode I since Mode II contributions remain small. Such results validate the proposed approach for SIF computation.

Grabois et al. [2018] attributed the discrepancies between the two measurements (DIC and compliance methods) to out-of-plane motions of the TDCB specimen. We propose here a different explanation : material points located at the center of the sample may deform under plane strain conditions whereas material points located near the free surface of the sample are subjected to plane stress conditions. Such an assumption is supported by the fact that the crack front is curved along the width of the sample as we can see in Fig. 6.4.b

and Fig. 6.6.c. The DIC-estimate is essentially local since it relies on the measurement of the displacement field on the free observation surface of the sample. As a result, it may differ from the compliance estimate, which relies on the structural response of the whole specimen.

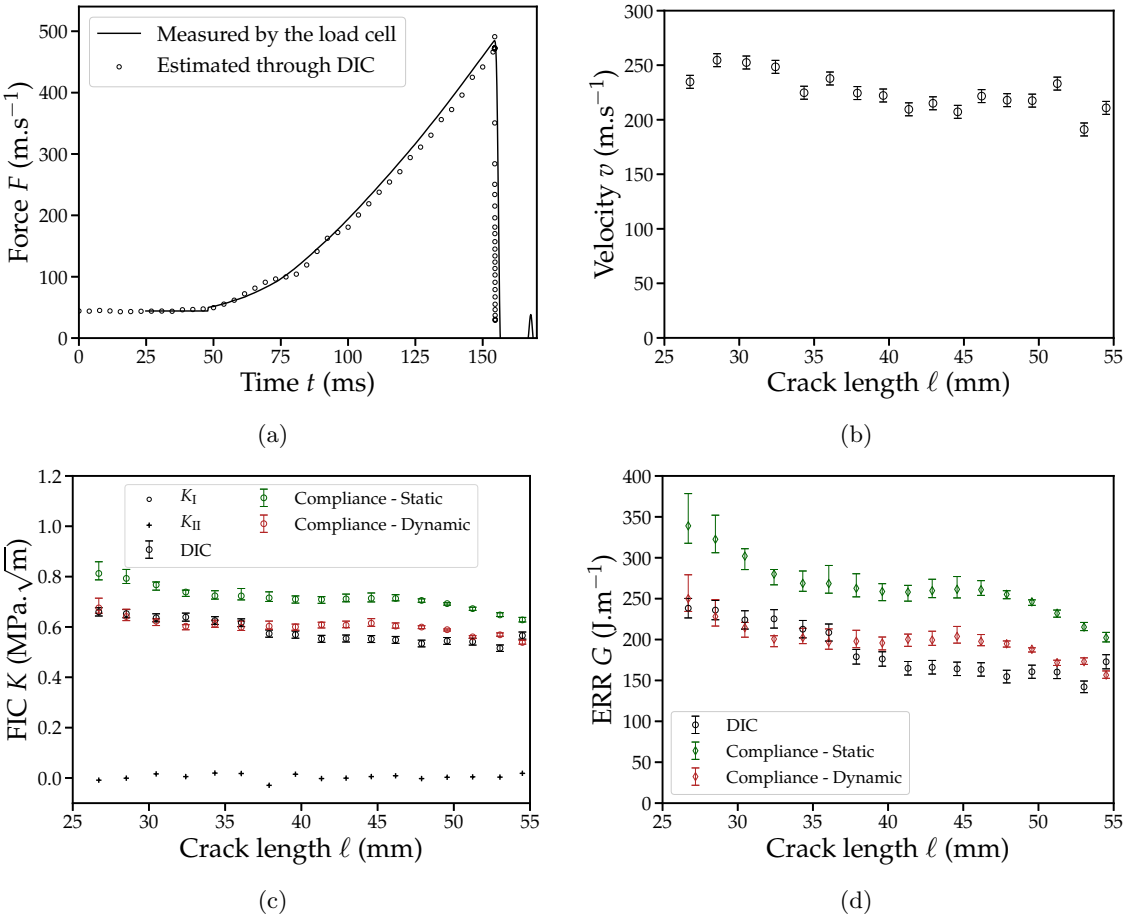

Figure 6.16: Comparison between the compliance and DIC methods : the Young modulus of the material is inferred from the superposition of the force-time curve predicted by DIC and measured by the load cell (a). The position of the crack tip on each frame allows for the computation of the instantaneous crack velocity v during the test (b). Finally, the stress intensity factors (c) and the elastic energy release rate (d), measured by DIC and compliance methods, are compared.

One may finally note that the value of the Young modulus E plays a central role in the estimation of the SIF in both the compliance (see Eq. (6.2)) and the DIC methods (see Eq. (6.15) through the shear modulus μ). Errors in the measurement of E, which fluctuates significantly due to the additive manufacturing process, may overcome the errors due to the DIC analysis.

6.4 Experimental homogenization for striped polymers

In this section, we apply the method developed in Section 6.3 to investigate the homogenization of toughness properties through the experimental fracture of striped polymers (see Fig. 6.16a)[1]. The direct measurement of the crack length ℓ and the local ERR G at a very fine temporal scale offers the unique opportunity to address such a complex problem in the most simple case of one-dimensional heterogeneities. After characterizing the kinetic law of both Veroclear and DM4310 materials in the dynamic regime in Section 6.4.1, we investigate the propagation dynamics of a crack in Section 6.4.2 and their ultimate impact on the homogenization of fracture properties in Section 6.4.3. Some on-going works are finally presented in Section 6.4.4.

6.4.1 Material characterization

Five experiments are conducted on homogeneous samples for each of the two materials. The ERR G and the crack velocity v are measured following the DIC procedure described in Section 6.3 to construct the kinetic law of the rate-dependent fracture energy $G_c(v)$ i.e. the $G_c - v$ curve in the dynamic regime.

The dependence of the material toughness can be grasped within the dynamic LEFM theory by taking into account the contraction of the process zone ℓ_{FPZ} when the crack propagates at high velocity [Barras, 2018]. It reads :

$$\ell_{FPZ}(v) = a\frac{K_I^2(v)}{\sigma_c^2} \tag{6.21}$$

where a is a dimensionless constant and σ_c the material strength.

Scheibert et al. [2010] proposed a way to model the rate-dependent processes occurring within the fracture process zone below the micro-branching instability. As a result, they relate the fracture energy G_c to the material surface energy γ and the process zone size ℓ_{FPZ} through the following equation :

$$G_c(v) = \gamma + 2\epsilon\ell_{FPZ}(v) \tag{6.22}$$

where ϵ is a material dependent parameter.

By combining the evolution of the process zone size with the crack velocity of Eq. (6.21) and its impact on the fracture toughness described in Eq. (6.22) with the expression of the dynamic ERR of Eq. (6.20) into Griffith's criterion, one finally gets :

$$G_c(v) = G_{c,0}\frac{1-\alpha}{1-\frac{\alpha}{A_I(v)}} \tag{6.23}$$

where $\alpha = \frac{2\epsilon E a}{\sigma_c^2}$ is a material dependent parameter.

This kinetic law allows to describe the $G_c - v$ curves of both the matrix material (Veroclear) and the obstacle material (DM4310) for a wide range of velocities (see Fig. 6.17).

[1]This study is the result of a joint work performed during the 4 months visit of Gabriele Albertini, PhD student at Cornell University under the supervision of David Kammer - Contact: ga288@cornell.edu

From this study, we measure $E_{\text{mat}} = 2.9\,\text{GPa}$, $G_{\text{c},0}^{\text{mat}} = 80\,\text{J.m}^{-2}$, $\alpha_{\text{mat}} = 1.15$ and$E_{\text{obs}} = 1.9\,\text{GPa}$, $G_{\text{c},0}^{\text{obs}} = 110\,\text{J.m}^{-2}$, $\alpha_{\text{obs}} = 1.17$. The Poisson ratio of both matrix E_{mat} and obstacle E_{mat} is set to 0.35. Their density is taken equal to $\rho = 1130\,\text{kg.m}^{-3}$ (Stratasys documentation).

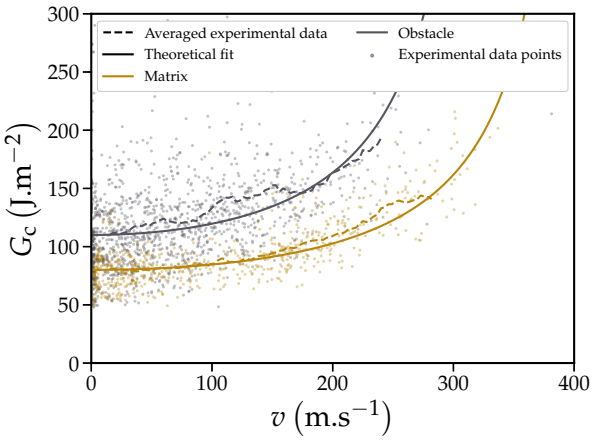

Figure 6.17: Fracture toughness properties of the two materials considered in the study : the evolution of the rate-dependent fracture energy $G_c(v)$ is estimated from fracture tests of homogeneous TDCB specimens of Veroclear (matrix) and DM4310 (obstacle) analyzed with the DIC procedure described in Section 6.3. It is compared to theoretical predictions of Eq. (6.23) in solid lines.

6.4.2 Pinning and depinning dynamics in striped materials

The material being characterized, we consider now heterogeneous samples consisting in alternative stripes of matrix (Veroclear) and tougher obstacles (DM4310) of constant width $w \in \{2.5\text{mm}, 5\text{mm}, 7.5\text{mm}, 10\text{mm}\}$. The first stripe is placed 1cm away from the initial notch. Five to seven experiments are conducted for each considered stripe width.

For each experiment, we measure the Young modulus by comparing the force measurements of the load cell with the DIC-based compliance method performed in Fig. 6.16. This value of the Young modulus is attributed to the matrix material since deformations are concentrated in the vicinity of the notch, which is fully embedded in the matrix, far away from the first stripe (see Fig. 6.18.a). The Young modulus of the obstacle is estimated from the one of the matrix assuming a constant ratio 0.65, observed in the characterization campaign. The crack position ℓ, its velocity v and the local dynamic ERR G are measured by the DIC procedure of Section 6.3. As noted by Wang and Xia [2017] through cohesive-zone simulations of crack propagation in striped composites with dissimilar Young modulus and fracture toughness, the ERR G varies from its homogeneous estimation at the vicinity the interface between the two materials. Thus the value of the dynamic ERR G from the DIC calculation based on William's expansion is adopted here rather than the one resulting from the compliance method. The Young modulus used to estimate the Mode I SIF K_{I} from the DIC method is taken equal as the one of the material the crack is currently propagating into when the fitting domain of the least square procedure (donuts) is lower than the stripe size (stripes of 7.5mm and 10mm). Otherwise one uses the value of the homogenized Young modulus, which is estimated here from the Reuss bound in the case of a striped material

with stripes oriented in the tensile direction.

In contrast with the experiments conducted by Avellar [2018] on the fracture of striped specimens manufactured with the same 3D printer but with different materials, one observes from image subtraction techniques that there is only a single propagating crack in the material whereas Avellar [2018] notices crack nucleation a stripe ahead, leading to crack bridging. Consequently, only one interaction mechanism is involved in our experiments, that is crack pinning.

A typical experiment is illustrated in Fig. 6.18. After crack nucleation, the crack propagates inside the matrix. When it meets the obstacle, it undergoes an abrupt deceleration (Fig. 6.18.b) while its energy release rate remains almost constant (Fig. 6.18.c). The ERR does not see the material transition since G is fixed by the loading (if we neglect the inertial correction). Thus the crack has no other choice than jumping from one $G_c - v$ branch to the other (Fig. 6.18.d).

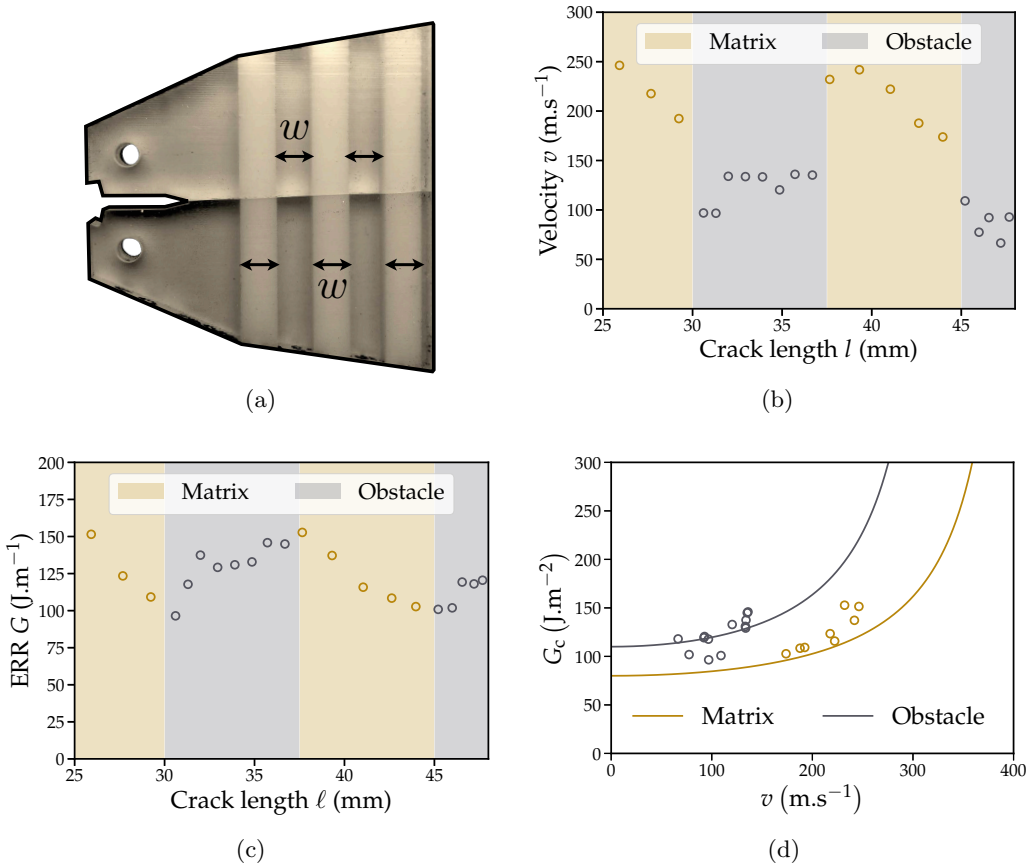

Figure 6.18: Crack propagation in 3D printed striped materials (a) : when the crack goes from one material to another, its velocity changes abruptly (b) while its energy release rate remains almost constant (c). The material jumps from one $G_c - v$ branch to the other (d).

Such intermittent dynamics are characteristic of a strong pinning regime, typically observed in the fracture of strongly heterogeneous materials [Roux et al., 2003; Bonamy,

2009; Ponson, 2009]. The jumps in crack velocity can be rationalized from the continuity of the static ERR G^{stat} at the matrix/obstacle interface. At the position ℓ between the two materials, one gets :

$$\frac{G_{\text{c}}^{\text{mat}}\left(v_{\text{mat}}\right)}{g_{\text{mat}}\left(v_{\text{mat}}\right)} = \frac{G_{\text{c}}^{\text{obs}}\left(v_{\text{obs}}\right)}{g_{\text{obs}}\left(v_{\text{obs}}\right)} \tag{6.24}$$

This equation can be solved numerically, relating the crack velocity after a pinning (matrix to obstacle) or a depinning (obstacle to matrix) event. The LEFM predictions of Eq. (6.24) are successfully compared to the speed jumps observed experimentally in Fig. 6.19.

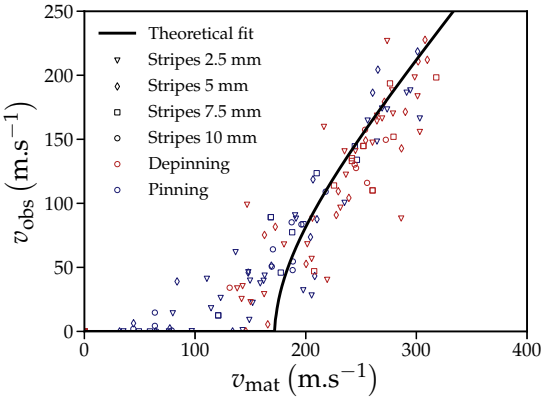

Figure 6.19: Velocity jumps during pinning (matrix to obstacle - in blue markers) and depinning (obstacle to matrix - in red markers) events for various stripe width w : the numerical results in colored markers are compared to LEFM predictions of Eq. (6.24).

6.4.3 Homogenized toughness measurement

One may now wonder how the successive pinning/depinning events impact the effective toughness of the heterogeneous materials. In a quasi-static framework, where the rate-dependency of the fracture toughness G_{c} is neglected, the effective toughness of striped materials is equal to the maximal toughness of its constituents [Hossain et al., 2014]. We prove here that taking into a rate-dependent G_{c} makes the prediction of the effective toughness drift from their quasi-static estimate.

To address this problem, we measure the effective toughness $\overline{G_{\text{c}}}$ of the tested striped composites as the energy dissipated during the fracture of the elementary volume constituted by 2 successive stripes. It reads :

$$\overline{G_{\text{c}}} = \frac{1}{2w}\int_{\ell_{\text{stripe}}}^{\ell_{\text{stripe}}+2w} G\left(\ell\right) d\ell \tag{6.25}$$

This elementary volume is fractured during a time Δt at a mean velocity $\bar{v}$:

$$\bar{v} = \frac{2w}{\Delta t} \tag{6.26}$$

We propose here a theoretical analysis of the homogenization problem in presence of a rate-dependent fracture toughness under the following assumptions : (i) both materials

share the same elastic properties but differ in their rate-dependent fracture energy $G_c(v)$ so that the local static ERR G^{stat} is equal to the ERR imposed by the macroscopic loading G_{loading}; (ii) the structural lengthscale $\mathcal{L} = -G_{\text{loading}}/\frac{\partial G_{\text{loading}}}{\partial \ell} \to +\infty$ so that the static ERR imposed by the loading G_{loading} does not decay with crack advance. Under these assumptions, the crack oscillates between two speeds v_{mat} in the matrix and v_{obs} in the obstacle, related by the equation :

$$G_{\text{loading}} = \frac{G_c^{\text{mat}}(v_{\text{mat}})}{g_{\text{mat}}(v_{\text{mat}})} = \frac{G_c^{\text{obs}}(v_{\text{obs}})}{g_{\text{obs}}(v_{\text{obs}})} \tag{6.27}$$

with a local dynamic ERR :

$$G^{\text{mat}} = G_{\text{loading}} \cdot g_{\text{mat}}(v_{\text{mat}}) \text{ and } G^{\text{obs}} = G_{\text{loading}} \cdot g_{\text{obs}}(v_{\text{obs}}) \tag{6.28}$$

Eq. (6.25) and Eq. (6.26) become :

$$\overline{G_c} = \frac{\left(G_c^{\text{mat}} + G_c^{\text{obs}}\right)}{2} \text{ and } \bar{v} = \frac{2}{\frac{1}{v_{\text{mat}}} + \frac{1}{v_{\text{obs}}}} \tag{6.29}$$

The homogenization procedure is illustrated in Fig. 6.20. We notice that $\overline{G_c}$ corresponds to the arithmetic average of the respective fracture toughness G_c^{mat} and G_c^{obs}, while $\bar{v}$ is the harmonic average of the velocity v_{mat} and v_{obs}, which is dominated by the lower velocity v_{obs}.

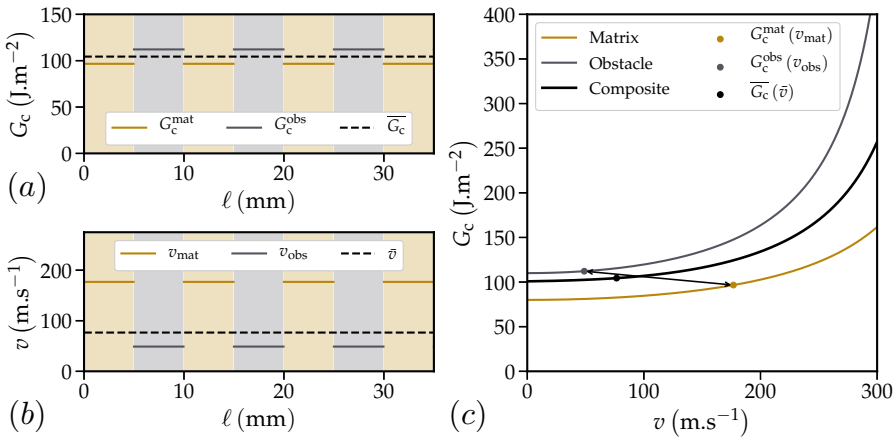

Figure 6.20: Summary of the homogenization scheme for a rate-dependent fracture toughness G_c : (a) the elastic energy release rate imposed by the loading is constant when the crack propagates, (b) making the crack jumps from one $G_c - v$ branch to another at the interface between two materials. (c) The homogenized toughness then is equal to the arithmetic average of the local ERR whereas the homogenized velocity is equal to the harmonic average of the crack velocity, dominated by the lower velocity.

The results of Eq. (6.29) call for some comments. First, the intermittent dynamics, triggered by the rate-dependency of the fracture toughness, strongly modifies the effective toughness from its quasi-static value G_c^{mat} [Hossain et al., 2014]. Second, we find back the property that in the absence of an intermittent dynamic, i.e. in the weak pinning regime, the effective toughness is equal to the spatial average of the local toughness field [Roux et al., 2003; Démery et al., 2014b].

The theoretical predictions of Eq. (6.29) are then compared to experimental measurements of the effective toughness. The effective toughness of Eq. (6.25) and the effective velocity of Eq. (6.26) are computed experimentally from the evolution of $G(\ell)$ and $v(\ell)$ measured by DIC (see Fig. 6.18). We consider here only pairs of successive stripes where no crack arrest occurs due to pinning events. Results are plotted in Fig. 6.21.a.

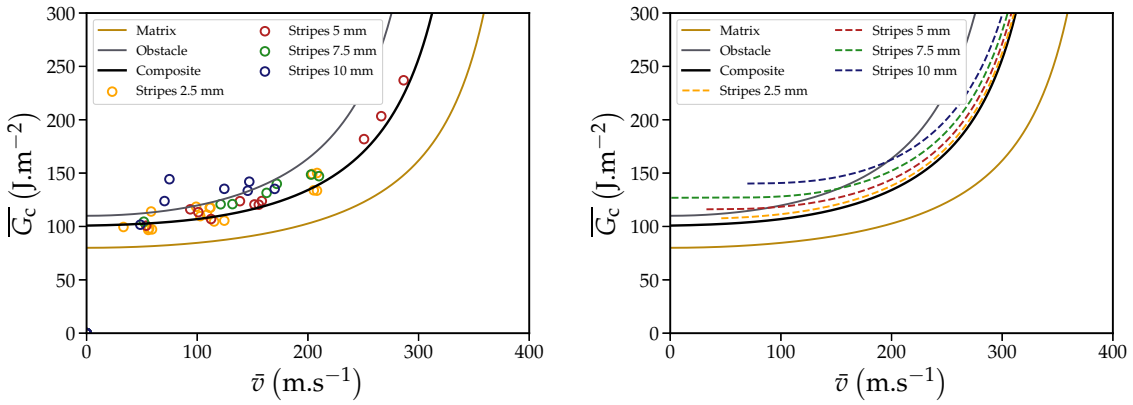

(a) (b)

Figure 6.21: Homogenized $G_c - v$ curves : the effective toughness $\bar{G}_c$ is measured in the experiments as the energy dissipated by the crack when crossing a consecutive pair of matrix/obstacle stripes of length $2\Delta l$ during a time Δt at the effective velocity $\bar{v} = 2\Delta l/\Delta t$ (a). Their are compared to theoretical predictions from the analytical model of dynamic fracture with (dashed colored lines) or without (solid black line) taking into account the influence of the structure (b).

We see that the experimental data are indeed close to the theoretical LEFM predictions. Discrepancies are nonetheless found as the stripe width w grows larger. As stated in Chapter 4, brittle fracture is not only a material problem but a structural one as well. We saw that the influence of the structure can be modeled through the lengthscale $\mathcal{L} = -G_{\text{loading}}/\frac{\partial G_{\text{loading}}}{\partial \ell}$, which is characteristic of the variations of the ERR with the crack advance. Here, we find from the FEM simulations of Section 6.2.1, $\mathcal{L} = 20$mm. The influence of the structural lengthscale $\mathcal{L}$ is computed numerically from Eq. (6.27) assuming an exponential decay of the ERR imposed by the loading $G_{\text{loading}}(\ell) \propto e^{-\ell/\mathcal{L}}$. The results are plotted in Fig. 6.21.b. We see that the influence of $\mathcal{L}$ accounts for the higher effective toughness levels found at large stripe width. It is interesting to note that $\mathcal{L}$ has here a toughening influence on the effective fracture properties whereas it has been proved to weaken the material in a three-dimensional quasi-static setting (see Démery et al. [2014a] and Chapter 4).

6.4.4 From 1D samples to 3D experiments

Veroclear and DM4310 present a toughness ratio around $G_c^{obs}/G_c^{mat} \simeq 1.37$ so that it should be possible to revisit both theoretical predictions and numerical estimates of Chapter 3, Chapter 4 and Chapter 5. Yet as stated in Section 2.2, fracture mechanics is all about lengthscales. In our case, two lengthscales are in competition, the process zone size $\ell_{FPZ} \simeq 20\mu$m and the size ℓ_Δ along which the mechanical properties varies from the one of the matrix to the one of the obstacle (see Fig. 2.4). Due to the manufacturing process, where polymer droplets are successively deposited, cured by UV and flattened by a roller, ℓ_Δ is approximately equal to the 3D printer resolution $\ell_\Delta \simeq 40\mu$m. Thus, no clear separation of length scales can be observed between ℓ_{FPZ} and ℓ_Δ, so that the crack sees a continuous evolution of the material properties rather than a discontinuity. Consequently, out-of-plane deviations of the crack front at the matrix/obstacle interface cannot be observed in this material, as it is proved in Fig. 6.22.

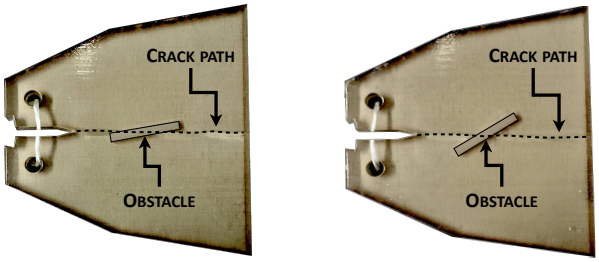

(a) (b)

Figure 6.22: Bi-material TDCB specimen constituted of a Veroclear matrix and a DM4310 obstacle inclined at 5° (a) and 15° (b) : the obstacle are crossed whereas 2D theoretical predictions of Eq. (3.27) based on the GMERR criterion predict a by-pass of the obstacle for a toughness ratio $G_c^{obs}/G_c^{mat} \simeq 1.37$.

Such a behavior is somewhat disappointing since the experimental procedure developed in this chapter does not allow for a direct comparison of experimental results with the theoretical and numerical ones of the previous chapters. Nonetheless, the experimental campaign conducted on striped composites showed than the crack interacted with tougher defects through the sole crossing mechanism. Moreover, the absence of discontinuity between the two materials hinders out-of-plane deviations of the crack along the matrix/obstacle interface due to toughness contrast but also prevent any (de-)nucleation processes from happening due to a contrast in elasticity.

Thus, the experimental set-up developed during the PhD thesis may allow for a quantitative analysis of material toughening by crack trapping in a coplanar situation, which was studied theoretically by Roux et al. [2003], Roux and Hild [2008], Patinet et al. [2013b], Démery et al. [2014a] and Démery et al. [2014b]. Since the choice of the material sets the toughness ratio in our experiments, on-going experiments of coplanar crack propagation are performed by playing on the density of inclusions and also on the correlation length ratio ξ_z/ξ_x, which plays a decisive role in the estimation of the homogenized fracture properties (see Chapter 4). Examples of considered geometries are given in Fig. 6.23.

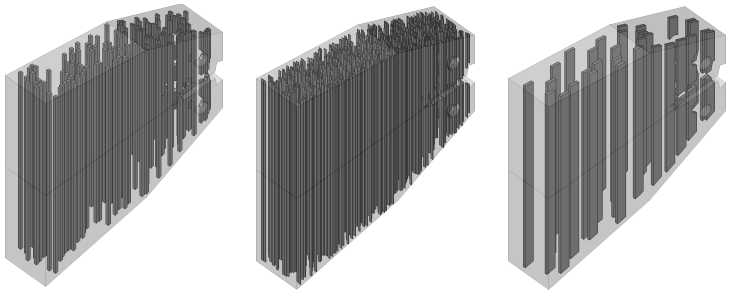

(a) (b) (c)

Figure 6.23: On-going experiments investigating the influence of the correlation length ratio ξ_z/ξ_x on the effective toughness of three-dimensional heterogeneous materials : the ratio ξ_z/ξ_x varies from the reference case $\xi_z/\xi_x = 1$ (a) between $\xi_z/\xi_x = 0.25$ (b) and $\xi_z/\xi_x = 4$ (c).

6.5 Concluding remarks

This chapter was dedicated to the experimental study of the fracture of 3D printed heterogeneous polymers. Specimens are printed with a Tampered Double Cantilever Beam (TDCB) geometry, which allows for stable crack propagation at a prescribed velocity under a constant driving rate. Material properties are then inferred from a compliance method [Vasudevan et al., 2019], giving access to the evolution of their rate-dependent fracture energy $G_c(v)$. Yet crack propagation in homogeneous samples in a quasi-static regime proves to be very difficult to obtain because of the material viscosity and the stick-slip behavior of the photo-polymers selected for the study. To circumvent these issues, one has to work at high driving rates, where the crack propagates in a dynamic regime described by LEFM [Freund, 1998].

Yet standard fracture characterization methods cannot be adapted to the dynamic regime so that one has to call upon more advanced experimental procedures to access relevant information on crack propagation. A DIC-based technique has been developed to track at fine temporal and spatial scales the position and the local elastic energy release rate of a fast propagating crack. Images of the fracture tests are acquired using a high-speed camera at an acquisition rate up to 232,000 Hz. Displacement fields are measured by a local DIC procedure performed by the CMV software [Soppa et al., 2001]. A continuous displacement field is extracted from the local DIC analysis following the work of Chateau et al. [2018]. The crack tip position is then measured using the method proposed by Henninger et al. [2010], based on William's expansion of the displacement fields. It also gives access to the local stress-intensity factors [Roux and Hild, 2006]. This method has been compared to crack opening Abanto-Bueno and Lambros [2002] and subtraction [Chateau et al., 2018] procedures for the crack tip position and the compliance method [Vasudevan et al., 2019] for the SIF estimation. The crack tip position is measured with a precision $\pm 50\mu$m while the SIF are estimated with a ± 0.07MPa.$\sqrt{\text{m}}$. These performances are similar to the one of integrated DIC based on a global approach [Grabois et al., 2018].

The procedure is used to study crack propagation in striped composites. The crack

displays peculiar intermittent dynamics, characteristic of a strong pinning regime, where the crack locally adapts to the change of material by a jump in velocity. These intermittent dynamics ultimately controls the effective toughness of the material in presence of a rate-dependent fracture toughness. As exposed in Chapter 4, the effective fracture energy may be strongly influenced by the structure in which the crack propagates through the lengthscale $\mathcal{L}$, which describes the evolution of the ERR G with crack advance. Intrinsic homogenized fracture properties can only be defined in the limit where the lengthscale $\mathcal{L}$ is far superior to the size of the defects. All these experimental results are successfully captured by theoretical predictions of dynamic LEFM.

Finally, this study does not allow to revisit the theoretical and numerical results of the PhD manuscript because of the absence of toughness discontinuity at the matrix/obstacle interface due to the 3D printing process. Nonetheless, it paves the way for a critical test of Démery et al. [2014a]'s coplanar homogenization theory, on which relies our proposed approach for homogenizing the brittle fracture properties of three-dimensional composites.

7

Conclusions and perspectives

General conclusions

The prediction of the macroscopic response of a material from the knowledge of its constituent at a microscopic or mesoscopic scale has always been the Holy Grail pursued by material science. Yet well-established methods dedicated to the homogenization of conservative and dissipative processes do not currently provide an appropriate framework to predict the effective fracture properties of brittle composite. In the present thesis work, we have proposed to tackle this problem through the combination of an innovative theoretical approach inspired by statistical physics, a new numerical method based on the perturbative approach of the Linear Elastic Fracture Mechanics and advanced fracture experiments of 3D printed heterogeneous polymers. Based on the specificities of brittle fracture, our work provides an original approach to investigate the homogenization of brittle fracture properties.

First, brittle fracture is a *dissipative evolution process*, so that one has to investigate *crack propagation* to measure effective fracture properties. In Chapter 2, we developed a new LEFM-based theoretical framework allowing to model quasi-static crack propagation in three-dimensional heterogeneous brittle materials. The proposed approach predicts the propagation of a semi-infinite crack loaded in tensile Mode I in a composite material constituted of a homogeneous matrix and tough inclusions. It relies on the computation of the stress intensity factors variations from the geometrical perturbations of the crack front within the perturbative LEFM approach developed by Gao and Rice [1986] and Movchan et al. [1998]. A propagation criterion, resulting from the combination of a viscous regularization of Griffith's criterion and the generalized maximum energy release rate (GMERR) criterion [Gurtin and Podio-Guidugli, 1998], describes the interaction between a crack and an inclusion through two mechanisms : inclusion crossing, where the crack penetrates the inclusion, and inclusion by-pass, where the crack goes out-of-plane and propagates along the matrix/inclusion interface. Based on the Fast Fourier Transform algorithm, the numerical implementation of our approach allows to compute the interaction of a crack with millions of tougher inclusions in only a few hours on a laptop computer for a monocore simulation. Such unprecedented performances pave the way for addressing the challenging problem of fracture properties homogenization.

Second, fracture processes are *localized at the crack tip*. The stress singularity at the crack tip enhances the impact of microstructural heterogeneities, so that rare but tough heterogeneities can substantially modify the effective fracture properties. Particular importance is then attached in Chapter 3 to the *mechanisms of interaction* between the crack and tough inclusions. These interaction mechanisms are investigated through numerical simulations of crack growth in periodic arrangements of tough inclusions. We have shown that the mechanical properties of the inclusion, as well as its shape, control the mechanism which is selected by the crack and the resulting propagation dynamics. These features determine in turns the ultimate contribution of this mechanism to material toughening, paving the way to material design aiming at improving fracture properties.

Third, brittle fracture is not only a *material* problem but a *structural* one as well. We take advantage of this coupling in Chapter 4 to measure the effective fracture properties from the crack evolution. We first showed than an *intrinsic* value of the effective toughness can be defined under a *scale separation condition*, which states that the inclusion size d, characteristic of the microstructure, has to be small enough with respect to the structural length $\mathcal{L}$, characteristic of the loading variations. This structural length is related to the structural problem and its boundary conditions and its central role illustrates the specificities of brittle fracture. In a second step, we have conducted numerical simulations on large-scale disordered systems to investigate the impact of microstructural disorder on the effective toughness. Our results illustrate the decisive role of the material disorder in the determination of the effective fracture properties, so that estimating the effective toughness from two-dimensional or three-dimensional periodic situations can produce results which are both quantitatively and qualitatively wrong. Finally, we have compared these results to theoretical predictions derived from a three-step homogenization scheme inspired by micromechanics and statistical physics. First, the full problem of the propagation of a crack in a disordered distribution of inclusions is broken down into multiple simpler problems, considering all the possible ways a crack can interact with a single inclusion and its respective probability. Second, the respective toughening contribution of each cell problem is inferred from the crack front dynamics during its interaction with the tough inclusion. Third, the toughness field actually experienced by the crack during its evolution is reconstructed under the *ergodic assumption*, allowing to predict the effective toughness from the theoretical framework developed by Démery et al. [2014b] for a planar crack problem. This homogenization method has been shown to successfully capture the impact of by-pass mechanism on the effective toughness of heterogeneous brittle materials, as well as the one of various microstructural and geometrical parameters. Our results highlight the substantial impact of a wide range of microstructural parameters on material reinforcement, from which guidelines for microstructural design have been inferred.

Fourth, brittle fracture is an *irreversible* process, whose signature can be ultimately observed on the fracture surfaces. It motivated the study of the statistical properties of fracture surfaces in Chapter 5. First, the roughness of the fracture surfaces has been studied both theoretically within the LEFM framework and numerically via our perturbative model. Our results showed that the surface roughness scaled logarithmically, in coherence with the experimental observations of Dalmas et al. [2008]. Nonetheless, our approach does not explain the emergence of the self-affine roughness observed in porous brittle materials [Ponson et al., 2006a]. Second, the analytical model successfully captures the impact of various microstructural features on the roughness of surfaces produced by brittle fracture simulations. We have shown that quantitative information on the propagation direction and the Poisson ratio could be extracted from the statistical properties of the fracture surfaces. Yet, other quantities of interest, such as the effective toughness, remain out of reach of the fractographic methods developed in this work.

Finally, we revisited the homogenization of brittle fracture properties through an experimental study of the fracture behavior of 3D printed polymers in Chapter 6. The specimens are printed with a Stratasys Objet260 Connex3 printer from photopolymer resins. Quasi-static crack propagation was especially difficult to achieve at low driving rates due to the combination of the visco-elastic and the stick-slip behavior of the material. Thus, experiments were performed at a high driving rates to overcome the material viscosity and prevent stick-slip events, leading to dynamic fracture at velocities reaching $300\,\mathrm{m.s^{-1}}$. At such velocity, standard experimental techniques, such as the compliance method, do not allow for crack propagation to be tracked at the temporal and spatial scales required to investigate effective fracture properties. Consequently, Digital Image Correlations techniques had to be developed to measure accurately the position of the crack tip, the velocity, and the elastic energy release rate. These quantities of interest are inferred from the displacement field [Henninger et al., 2010; Chateau et al., 2018], which is estimated with the local DIC software CMV from the comparison of subsequent images recorded by a high-speed camera, at an acquisition rate up to $230,000\,\mathrm{Hz}$. Our method is applied to investigate the effective toughness of striped polymers constituted of a homogeneous matrix and tougher obstacles. Crack propagation in such materials displays an intermittent dynamic, characteristic of a strong pinning regime, where the crack accommodates to the local property variations through jumps in its velocity. These jumps ultimately control the homogenized fracture properties of the heterogeneous specimen. Experimental results are successfully captured by a dynamic LEFM theoretical model, in which the rate-dependency of the material plays a decisive role.

Future perspectives

This study sets up the foundations for homogenizing brittle fracture properties of three-dimensional composite materials. It leaves naturally several challenging open issues, which it would be interesting to address in the future. They concern every facet of this work and are traced in the following.

First, the pertubative approach could be extended to model more complex situations. Detailed perspectives have been drawn in Section 2.5. The most promising route would consist in extending our approach to mixed mode loading I+III and I+II+III to investigate the influence of material heterogeneities on crack fragmentation, as suggested by the preliminary results of Leblond and Ponson [2016] and of Leblond et al. [2019]. Another route is to model crack propagation in heterogeneous materials with weak elastic heterogeneities, using the formulæ derived by Gao [1991] and Muju [2000]. Despite its significant computational cost, this approach would allow to investigate the homogenization of brittle fracture properties in a much more realistic setting. Additionally, it would provide some valuable insights into the influence of residual stresses and material anisotropy on the effective toughness.

Second, the homogenization method developed for disordered brittle solids could be applied to a much wider range of mechanisms of crack-inclusion interaction. De-nucleation/re-nucleation processes [Leguillon and Martin, 2013], deflection at an elastic interface [He and Hutchinson, 1989] and inclusion debonding [Le et al., 2019] can be grasped within the LEFM framework and thus incorporated in the perturbative approach. Yet, more powerful numerical methods such as phase-field or thick-level-set simulations might prove more appropriate tools to investigate accurately these mechanisms and the conditions (e.g. material properties, inclusion geometry) under which one prevails over the other. As proposed in Section 4.7, these interaction mechanisms could be investigated efficiently in a single inclusion setting, providing valuable insights on their toughening contributions, which could then be embedded in the homogenization scheme proposed in Chapter 4 to predict effective fracture properties in a disordered setting.

Third, the homogenization procedure of Chapter 4, based on the work of Démery et al. [2014b] and Démery et al. [2014a] also need to be refined. One should first revisit the theoretical results of Démery et al. [2014a] within the second-order coplanar perturbative theory of Vasoya et al. [2013], since Démery et al. [2014a]'s formulæ currently predict the effective fracture properties at the second-order in the perturbation from a first-order theory. Then, modeling analytically the cross-over between the collective and the individual regimes as well as the impact of the finite system size would provide *in fine* a better estimate of the effective toughness. Moreover, the non-dilute scheme in a non-coplanar setting should be further improved by taking into account the decisive influence of the out-of-plane perturbations in the prediction of the effective toughness at high toughness contrast. Finally, one could extend the current homogenization framework to estimate *apparent fracture properties*, where the impact of the structural problem and the finite size of the system are predicted quantitatively, similarly to what is performed for linear elastic behaviors [Sab, 1992; Ostoja-Starzewski, 2006; Brisard et al., 2013].

Fourth, significant progress has been achieved in the last decade by describing material failure as a depinning transition. Statistical physics will undoubtedly continue to provide valuable insights on the fracture of heterogeneous materials. Yet, the coexistence of a logarithmic and a self-affine regime of brittle fracture roughness remains puzzling [Ponson et al., 2006a; Dalmas et al., 2008] and the identification of the selection mechanisms between both behaviors is certainly a major lack to be lifted. Accurate information on material properties and its fracture behavior can be extracted from the fracture surfaces only once a deep understanding of the physical mechanisms behind its formation is achieved. Cutting-edge experiments in fracture mechanics coupled with advanced visualization techniques based on X-ray microtomography [Lachambre et al., 2015; Chateau et al., 2018; Renard et al., 2019] could provide the missing elements to understand the origin of the self-affine roughness. Additionally, if we found no relevant information on the effective toughness of brittle materials into the fracture surface morphology and its spatial correlations, the intermittent dynamics of a crack propagating in heterogeneous materials could provide quantitative information on the Larkin length [Laurson et al., 2010] and thus on the effective fracture properties.

Finally, model experimental set-ups in fracture mechanics [Takei et al., 2013; Ibarra et al., 2016; Wang and Xia, 2017] should foster further dialog between experiments, theoretical analysis and simulations before addressing the difficult question of predicting the effective fracture properties of realistic materials [Kataoka et al., 2015; Chandler et al., 2016; Gomez-Monterde et al., 2016]. Experimental techniques for fracture mechanics allow nowadays to investigate crack propagation at unprecedented temporal and spatial scales. One can then apply them to investigate in depth model systems where a limited number of interaction mechanisms is involved. In that sense, additive manufacturing techniques shows promising features by allowing to choose the nature of the crack-inclusion interaction by tuning either the material or the 3D printing technology they use. Namely, the experimental set-up developed in this work may allow to revisit experimentally the work of Démery et al. [2014b], on which is built our proposed approach for homogenizing fracture properties.

Bibliography

Abanto-Bueno, J. and Lambros, J. (2002). Investigation of crack growth in functionally graded materials using digital image correlation. *Engineering Fracture Mechanics*, 69(14).

Agoras, M., Avazmohammadi, R., and Ponte Castañeda, P. (2016). Incremental variational procedure for elasto-viscoplastic composites and application to polymer- and metal-matrix composites reinforced by spheroidal elastic particles. *International Journal of Solids and Structures*, 97-98:668–686.

Albertini, G., Lebihain, M., Hild, F., Ponson, L., and Kammer, D. (2020). Effective toughness of heterogeneous materials: experimental study on pinning and depinning dynamics. *in preparation*.

Alessi, R., Marigo, J., Maurini, C., and Vidoli, S. (2018). Coupling damage and plasticity for a phase-field regularisation of brittle, cohesive and ductile fracture: One-dimensional examples. *International Journal of Mechanical Sciences*, 149:559–576.

Ambrosio, L. and Tortorelli, V. (1990). Approximation of functional depending on jumps by elliptic functional via γ-convergence. *Communications on Pure and Applied Mathematics*, 43(8):999–1036.

Amestoy, M. and Leblond, J. B. (1992). Crack paths in plane situations II. detailed form of the expansion of the stress intensity factors. *International Journal of Solids and Structures*, 29(4):465–501.

Anoukou, K., Brenner, R., Hong, F., Pellerin, M., and Danas, K. (2018). Random distribution of polydisperse ellipsoidal inclusions and homogenization estimates for porous elastic materials. *Computers & Structures*, 210:87–101.

ASTM (2017). Standard test method for measurement of fracture toughness. Standard ASTM E1820-17, ASTM, Geneva, CH.

Avellar, L. (2018). *Observations of Failure Phenomena in Periodic Media*. PhD thesis, California Institute of Technology.

Barak, Y., Srivastava, A., and Osovski, S. (2019). Correlating fracture toughness and fracture surface roughness via correlation length scale. *International Journal of Fracture*.

Barenblatt, G. I. (1962). The mathematical theory of equilibrium cracks in brittle fracture. In Dryden, H. L., von Kármán, T., Kuerti, G., van den Dungen, F. H., and Howarth, L., editors, *Advances in Applied Mechanics*, volume 7, pages 55–129. Elsevier.

Barès, J., Barlet, M., Rountree, C., Barbier, L., and Bonamy, D. (2014). Nominally brittle cracks in inhomogeneous solids: from microstructural disorder to continuum-level scale. *Frontiers in Physics*, 2.

Barras, F. (2018). *When dynamic cracks meet disorder: A journey along the fracture process zone*. PhD thesis, EPFL.

Barthelat, F., Tang, H., Zavattieri, P. D., Li, C. M., and Espinosa, H. D. (2007). On

the mechanics of mother-of-pearl: A key feature in the material hierarchical structure. *Journal of the Mechanics and Physics of Solids*, 55(2):306–337.

Bass, L., Meisel, N., and Williams, C. (2016). Exploring variability of orientation and aging effects in material properties of multi-material jetting parts. *Rapid Prototyping Journal*.

Belytschko, T. and Black, T. (1999). Elastic crack growth in finite elements with minimal remeshing. *International Journal for Numerical Methods in Engineering*, 45(5):601–620.

Besnard, G., Hild, F., and Roux, S. (2006). Finite-element displacement fields analysis from digital images: Application to portevin-le chatelier bands. *Experimental Mechanics*, 46(6):789–803.

Blackman, B. K., Hadavinia, H., Kinloch, A., Paraschi, M., and Williams, J. (2003). The calculation of adhesive fracture energies in mode i: revisiting the tapered double cantilever beam (TDCB) test. *Engineering Fracture Mechanics*, 70(2):233–248.

Bleyer, J. and Alessi, R. (2018). Phase-field modeling of anisotropic brittle fracture including several damage mechanisms. *Computer Methods in Applied Mechanics and Engineering*, 336:213–236.

Boffa, J. M. and Allain, C. (1998). Experimental analysis of fracture rugosity in granular and compact rocks. *The European Physical Journal Applied Physics*, 2(3):281–289.

Bonamy, D. (2009). Intermittency and roughening in the failure of brittle heterogeneous materials. *Journal of Physics D: Applied Physics*, 42(21):214014.

Bonamy, D. and Bouchaud, E. (2011). Failure of heterogeneous materials: A dynamic phase transition? *Physics Reports*, 498(1):1–44.

Bonamy, D., Ponson, L., Prades, S., Bouchaud, E., and Guillot, C. (2006). Scaling exponents for fracture surfaces in homogeneous glass and glassy ceramics. *Physical Review Letters*, 97(13):135504.

Bonamy, D., Santucci, S., and Ponson, L. (2008). Crackling dynamics in material failure as the signature of a self-organized dynamic phase transition. *Physical Review Letters*, 101(4):045501.

Bornert, M., Brémand, F., Doumalin, P., Dupré, J.-C., Fazzini, M., Gréiac, M., Hild, F., Mistou, S., Molimard, J., Orteu, J., Robert, L., Surrel, Y., Vacher, P., and Wattrisse, B. (2009). Assessment of digital image correlation measurement errors: Methodology and results. *Experimental Mechanics*, 49(3):353–370.

Bornert, M., Valès, F., Gharbi, H., and Nguyen Minh, D. (2010). Multiscale full-field strain measurements for micromechanical investigations of the hydromechanical behaviour of clayey rocks. *Strain*, 46(1):33–46.

Bouchaud, E., Lapasset, G., and Plané, J. (1990). Fractal dimension of fractured surfaces: A universal value? *Europhysics Letters (EPL)*, 13(1):73–79.

Bower, A. and Ortiz, M. (1991). A three-dimensional analysis of crack trapping and bridging by tough particles. *Journal of the Mechanics and Physics of Solids*, 39(6):815–858.

Bower, A. F. and Ortiz, M. (1990). Solution of three-dimensional crack problems by a finite perturbation method. *Journal of the Mechanics and Physics of Solids*, 38(4):443–480.

Bower, A. F. and Ortiz, M. (1993). An analysis of crack trapping by residual stresses in brittle solids. *Journal of Applied Mechanics*, 60(1):175–182.

Brach, S., Hossain, M. Z., Bourdin, B., and Bhattacharya, K. (2019a). Anisotropy of the

effective toughness of layered media. *Journal of the Mechanics and Physics of Solids*, 131:96–111.

Brach, S., Tanné, E., Bourdin, B., and Bhattacharya, K. (2019b). Phase-field study of crack nucleation and propagation in elastic - perfectly plastic bodies. *Computer Methods in Applied Mechanics and Engineering*, 353:44–65.

Branco, R., Antunes, F., and Costa, J. (2015). A review on 3d-FE adaptive remeshing techniques for crack growth modeling. *Engineering Fracture Mechanics*, 141:170–195.

Brisard, S., Sab, K., and Dormieux, L. (2013). New boundary conditions for the computation of the apparent stiffness of statistical volume elements. *Journal of the Mechanics and Physics of Solids*, 61(12):2638–2658.

Bueckner, H. (1970). Novel principle for the computation of stress intensity factors. *Zeitschrift fuer Angewandte Mathematik & Mechanik*, 50(9).

Bueckner, H. (1987). Weight functions and fundamental fields for the penny-shaped and the half-plane crack in three-space. *International Journal of Solids and Structures*, 23(1):57–93.

Cagnetti, F., Dal Maso, G., Scardia, L., and Zeppieri, C. I. (2019). Stochastic homogenisation of free-discontinuity problems. *Archive for Rational Mechanics and Analysis*, 233(2):935–974.

Camacho, G. T. and Ortiz, M. (1996). Computational modelling of impact damage in brittle materials. *International Journal of Solids and Structures*, 33(20):2899–2938.

Cambonie, T., Bares, J., Hattali, M. L., Bonamy, D., Lazarus, V., and Auradou, H. (2015). Effect of the porosity on the fracture surface roughness of sintered materials: From anisotropic to isotropic self-affine scaling. *Physical Review E*, 91(1):012406.

Chambolle, A., Francfort, G., and Marigo, J. (2009). When and how do cracks propagate? *Journal of the Mechanics and Physics of Solids*, 57(9):1614–1622.

Chandler, M., Meredith, P., Brantut, N., and Crawford, B. (2016). Fracture toughness anisotropy in shale. *Journal of Geophysical Research: Solid Earth*, 121(3):1706–1729.

Chateau, C., Nguyen, T. T., Bornert, M., and Yvonnet, J. (2018). DVC-based image subtraction to detect microcracking in lightweight concrete. *Strain*, 54(5):e12276.

Chopin, J. (2010). *Statique et dynamique d'un front de fissure en milieu hétégène*. PhD thesis, ENS Paris.

Chopin, J., Bhaskar, A., Jog, A., and Ponson, L. (2018). Depinning dynamics of crack fronts. *Physical Review Letters*, 121(23):235501.

Chopin, J., Prevost, A., Boudaoud, A., and Adda-Bedia, M. (2011). Crack front dynamics across a single heterogeneity. *Physical Review Letters*, 107(14):144301.

Chu, T. C., Ranson, W. F., and Sutton, M. A. (1985). Applications of digital-image-correlation techniques to experimental mechanics. *Experimental Mechanics*, 25(3):232–244.

Clayton, J. D. and Knap, J. (2014). A geometrically nonlinear phase field theory of brittle fracture. *International Journal of Fracture*, 189(2):139–148.

Cotterell, B. and Rice, J. (1980). Slightly curved or kinked cracks. *International Journal of Fracture*, 16(2):155–169.

Da, D., Yvonnet, J., Xia, L., and Li, G. (2018). Topology optimization of particle-matrix

composites for optimal fracture resistance taking into account interfacial damage. *International Journal for Numerical Methods in Engineering*, 115(5):604–626.

Dal Maso, G. and Toader, R. (2002). A model for the quasi-static growth of brittle fractures:existence and approximation results. *Archive for Rational Mechanics and Analysis*, 162(2):101–135.

Dalmas, D., Barthel, E., and Vandembroucq, D. (2009). Crack front pinning by design in planar heterogeneous interfaces. *Journal of the Mechanics and Physics of Solids*, 57(3):446–457.

Dalmas, D., Lelarge, A., and Vandembroucq, D. (2008). Crack propagation through phase-separated glasses: Effect of the characteristic size of disorder. *Physical Review Letters*, 101(25):255501.

Dauskardt, R. H., Haubensak, F., and Ritchie, R. O. (1990). On the interpretation of the fractal character of fracture surfaces. *Acta Metallurgica et Materialia*, 38(2):143–159.

Dautriat, J., Bornert, M., Gland, N., Dimanov, A., and Raphanel, J. (2011). Localized deformation induced by heterogeneities in porous carbonate analysed by multi-scale digital image correlation. *Tectonophysics*, 503(1):100–116.

Davalos, J. F., Madabhusi-Raman, P., Qiao, P. Z., and Wolcott, M. P. (1998). Compliance rate change of tapered double cantilever beam specimen with hybrid interface bonds. *Theoretical and Applied Fracture Mechanics*, 29(2):125–139.

Delaplace, A., Schmittbuhl, J., and Maloy, K. (1999). High resolution description of a crack front in a heterogeneous plexiglas block. *Physical Review E*, 60(2):1337–1343.

Delarue, A. and Jeulin, D. (2011). Multi-scale simulations of spherical aggregates. *Image Analysis & Stereology*, 20(3):181–186.

Démery, V., Lecomte, V., and Rosso, A. (2014a). Effect of disorder geometry on the critical force in disordered elastic systems. *Journal of Statistical Mechanics: Theory and Experiment*, 2014(3):P03009.

Démery, V., Rosso, A., and Ponson, L. (2014b). From microstructural features to effective toughness in disordered brittle solids. *EPL (Europhysics Letters)*, 105(3):34003.

Dimas, L., Bratzel, G., Eylon, I., and Buehler, M. (2013). Tough composites inspired by mineralized natural materials: Computation, 3d printing, and testing. *Advanced Functional Materials*, 23(36):4629–4638.

Dugdale, D. S. (1960). Yielding of steel sheets containing slits. *Journal of the Mechanics and Physics of Solids*, 8(2):100–104.

Ebrahimi, F. and Kalwani, L. (1999). Fracture anisotropy in silicon single crystal. *Materials Science and Engineering: A*, 268(1):116–126.

Engøy, T., Maløy, K., Hansen, A., and Roux, S. (1994). Roughness of two-dimensional cracks in wood. *Physical Review Letters*, 73(6):834–837.

Erdogan, F. and Sih, G. (1963). On the crack extension in plates under plane loading and transverse shear. *Journal of Basic Engineering*, 85(4):519–525.

Evans, A. (1990). Perspective on the development of high-toughness ceramics. *Journal of the American Ceramic Society*, 73(2):187–206.

Evans, A. G. and Cannon, R. M. (1986). Toughening of brittle solids by martensitic transformations. *Acta Metallurgica*, 34(5):761–800.

Evans, A. G. and Faber, K. T. (1981). Toughening of ceramics by circumferential microcracking. *Journal of the American Ceramic Society*, 64(7):394–398.

Evans, A. G., Zok, F. W., and Davis, J. (1991). The role of interfaces in fiber-reinforced brittle matrix composites. *Composites Science and Technology*, 42(1):3–24.

Faber, K. T. and Evans, A. G. (1983a). Crack deflection processes - i. theory. *Acta Metallurgica*, 31(4):565–576.

Faber, K. T. and Evans, A. G. (1983b). Crack deflection processes - II. experiment. *Acta Metallurgica*, 31(4):577–584.

Favier, E., Lazarus, V., and Leblond, J. (2006a). Coplanar propagation paths of 3d cracks in infinite bodies loaded in shear. *International Journal of Solids and Structures*, 43(7):2091–2109.

Favier, E., Lazarus, V., and Leblond, J. (2006b). Statistics of the deformation of the front of a tunnel-crack propagating in some inhomogeneous medium. *Journal of the Mechanics and Physics of Solids*, 54(7):1449–1478.

Forquin, P., Rota, L., Charles, Y., and Hild, F. (2004). A method to determine the macroscopic toughness scatter of brittle materials. *International Journal of Fracture*, 125(1):171–187.

Francfort, G. A. and Marigo, J. J. (1998). Revisiting brittle fracture as an energy minimization problem. *Journal of the Mechanics and Physics of Solids*, 46(8):1319–1342.

Freund, L. B. (1998). *Dynamic Fracture Mechanics*. Cambridge University Press.

Gallagher, J. P. (1971). Experimentally determined stress intensity factors for several contoured double cantilever beam specimens. *Engineering Fracture Mechanics*, 3(1):27–43.

Gao, H. (1991). Fracture analysis of nonhomogeneous materials via a moduli-perturbation approach. *International Journal of Solids and Structures*, 27(13):1663–1682.

Gao, H. and Rice, J. (1986). Shear stress intensity factors for a planar crack with slightly curved front. *Journal of Applied Mechanics*, 53(4):774–778.

Gao, H. and Rice, J. (1987a). Nearly circular connections of elastic half spaces. *Journal of Applied Mechanics*, 54(3):627–634.

Gao, H. and Rice, J. (1987b). Somewhat circular tensile cracks. *International Journal of Fracture*, 33(3):155–174.

Gao, H. and Rice, J. (1989). A first-order perturbation analysis of crack trapping by arrays of obstacles. *Journal of Applied Mechanics*, 56(4):828–836.

Gao, Y., Liu, Z., Wang, T., Zeng, Q., Li, X., and Zhuang, Z. (2018a). Crack forbidden area in the anisotropic fracture toughness medium. *Extreme Mechanics Letters*, 22:172–175.

Gao, Y., Liu, Z., Wang, T., Zeng, Q., Li, X., and Zhuang, Z. (2018b). XFEM modeling for curved fracture in the anisotropic fracture toughness medium. *Computational Mechanics*.

Giacomini, A. and Ponsiglione, M. (2006). A γ-convergence approach to stability of unilateral minimality properties in fracture mechanics and applications. *Archive for Rational Mechanics and Analysis*, 180(3):399–447.

Gol'dstein, R. V. and Salganik, R. L. (1974). Brittle fracture of solids with arbitrary cracks. *International Journal of Fracture*, 10(4):507–523.

Gomez-Monterde, J., Schulte, M., Ilijevic, S., Hain, J., Sanchez-Soto, M., Santana, O., and

Maspoch, M. (2016). Effect of microcellular foaming on the fracture behavior of ABS polymer. *Journal of Applied Polymer Science*, 133(7).

Grabois, T., Neggers, J., Ponson, L., Hild, F., and Toledo Filho, R. (2018). On the validation of integrated DIC with tapered double cantilever beam tests. *Engineering Fracture Mechanics*, 191:311–323.

Gradshteyn, I. S. and Ryzhik, I. M. (2014). *Table of integrals, series, and products*. Elsevier/Academic Press, Amsterdam, seventh edition.

Gravouil, A., Moës, N., and Belytschko, T. (2002). Non-planar 3d crack growth by the extended finite element and level sets - part II: Level set update. *International Journal for Numerical Methods in Engineering*, 53(11):2569–2586.

Griffith, A. (1921). The phenomena of rupture and flow in solids. *Phil. Trans. R. Soc. Lond. A*, 221.

Gu, G., Dimas, L., Qin, Z., and Buehler, M. (2016a). Optimization of composite fracture properties: Method, validation, and applications. *Journal of Applied Mechanics*, 83(7).

Gu, G., Libonati, F., Wettermark, S., and Buehler, M. (2017a). Printing nature: Unraveling the role of nacre's mineral bridges. *Journal of the Mechanical Behavior of Biomedical Materials*, 76:135–144.

Gu, G., Su, I., Sharma, S., Voros, J., Qin, Z., and Buehler, M. (2016b). Three-dimensional-printing of bio-inspired composites. *Journal of Biomechanical Engineering*, 138(2).

Gu, G., Wettermark, S., and Buehler, M. (2017b). Algorithm-driven design of fracture resistant composite materials realized through additive manufacturing. *Additive Manufacturing*, 17:47–54.

Guazzato, M., Albakry, M., Ringer, S. P., and Swain, M. (2004). Strength, fracture toughness and microstructure of a selection of all-ceramic materials. part II. zirconia-based dental ceramics. *Dental Materials*, 20(5):449–456.

Gupta, P. and Duarte, C. (2014). Simulation of non-planar three-dimensional hydraulic fracture propagation. *International Journal for Numerical and Analytical Methods in Geomechanics*, 38(13):1397–1430.

Gurson, A. L. (1977). Continuum theory of ductile rupture by void nucleation and growth: Part i - yield criteria and flow rules for porous ductile media. *Journal of Engineering Materials and Technology*, 99(1):2–15.

Gurtin, M. and Podio-Guidugli, P. (1998). Configurational forces and a constitutive theory for crack propagation that allows for kinking and curving. *Journal of the Mechanics and Physics of Solids*, 46(8):1343–1378.

Hakim, V. and Karma, A. (2005). Crack path prediction in anisotropic brittle materials. *Physical Review Letters*, 95(23):235501.

Hakim, V. and Karma, A. (2009). Laws of crack motion and phase-field models of fracture. *Journal of the Mechanics and Physics of Solids*, 57(2):342–368.

Hannink, R. and Swain, M. (1994). Progress in transformation toughening of ceramics. *Annual Review of Materials Science*, 24(1):359–408.

Hansen, A. and Schmittbuhl, J. (2003). Origin of the universal roughness exponent of brittle fracture surfaces:stress-weighted percolation in the damage zone. *Physical Review Letters*, 90(4):045504.

Hashin, Z. and Shtrikman, S. (1963). A variational approach to the theory of the elastic behaviour of multiphase materials. *Journal of the Mechanics and Physics of Solids*, 11(2):127–140.

He, M. and Hutchinson, J. (1989). Crack deflection at an interface between dissimilar elastic materials. *International Journal of Solids and Structures*, 25(9):1053–1067.

Henninger, C., Roux, S., and Hild, F. (2010). Enriched kinematic fields of cracked structures. *International Journal of Solids and Structures*, 47(24):3305–3316.

Herve, E. and Zaoui, A. (1993). n-layered inclusion-based micromechanical modelling. *International Journal of Engineering Science*, 31(1):1–10.

Hill, R. (1965). A self-consistent mechanics of composite materials. *Journal of the Mechanics and Physics of Solids*, 13(4):213–222.

Hill, R. (1967). The essential structure of constitutive laws for metal composites and polycrystals. *Journal of the Mechanics and Physics of Solids*, 15(2):79–95.

Hossain, M. Z., Hsueh, C. J., Bourdin, B., and Bhattacharya, K. (2014). Effective toughness of heterogeneous media. *Journal of the Mechanics and Physics of Solids*, 71:15–32.

Hsueh, C. and Bhattacharya, K. (2018). Optimizing microstructure for toughness: the model problem of peeling. *Structural and Multidisciplinary Optimization*, 58(3):1067–1080.

Hsueh, C.-J., Avellar, L., Bourdin, B., Ravichandran, G., and Bhattacharya, K. (2018). Stress fluctuation, crack renucleation and toughening in layered materials. *Journal of the Mechanics and Physics of Solids*, 120:68–78.

Hun, D., Guilleminot, J., Y., J., and Bornert, M. (2019). Stochastic multiscale modeling of crack propagation in random heterogeneous media. *International Journal for Numerical Methods in Engineering*, 0(0).

Hussain, M. A., Pu, S., and Underwood, J. (1974). Strain energy release rate for a crack under combined mode i and mode II. *Fracture Analysis: Proceedings of the 1973 National Symposium on Fracture Mechanics, Part II*.

Hutchinson, J. W. and Suo, Z. (1991). Mixed mode cracking in layered materials. In *Advances in Applied Mechanics*, volume 29, pages 63–191. Elsevier.

Huynh, D. B. P. and Belytschko, T. (2009). The extended finite element method for fracture in composite materials. *International Journal for Numerical Methods in Engineering*, 77(2):214–239.

Ibarra, A., Roman, B., and Melo, F. (2016). The tearing path in a thin anisotropic sheet from two pulling points: Wulff"s view. *Soft Matter*, 12(27):5979–5985.

Inglis, C. E. (1913). Stress in a plate due to the presence of cracks and sharp corners. *Transactions of the Institution of Naval Architectures*, 95:219–230.

Ingraffea, A. R. and Saouma, V. (1985). Numerical modeling of discrete crack propagation in reinforced and plain concrete. In Sih, G. C. and DiTommaso, A., editors, *Fracture mechanics of concrete: Structural application and numerical calculation*, Engineering Application of Fracture Mechanics, pages 171–225. Springer Netherlands.

Irwin, G. (1958). Fracture. In Flügge, S., editor, *Elasticity and Plasticity / Elastizität und Plastizittät*, Handbuch der Physik / Encyclopedia of Physics, pages 551–590. Springer Berlin Heidelberg.

Irwin, G. R. (1957). Analysis of stresses and strains near the end of a crack transversing a plate. *Trans. ASME, Ser. E, J. Appl. Mech.*, 24:361–364.

Irwin, G. R. (1962). Crack-extension force for a part-through crack in a plate. *Journal of Applied Mechanics*, 29(4):651–654.

Jo, B., Park, S., and Park, J. (2008). Mechanical properties of polymer concrete made with recycled PET and recycled concrete aggregates. *Construction and Building Materials*, 22(12):2281–2291.

Kataoka, M., Obara, Y., and Kuruppu, M. (2015). Estimation of fracture toughness of anisotropic rocks by semi-circular bend (SCB) tests under water vapor pressure. *Rock Mechanics and Rock Engineering*, 48(4):1353–1367.

Kikuchi, M., Wada, Y., Shintaku, Y., Suga, K., and Li, Y. (2014). Fatigue crack growth simulation in heterogeneous material using s-version FEM. *International Journal of Fatigue*, 58:47–55.

Kolton, A. B., Bustingorry, S., Ferrero, E. E., and Rosso, A. (2013). Uniqueness of the thermodynamic limit for driven disordered elastic interfaces. *Journal of Statistical Mechanics: Theory and Experiment*, 2013(12):P12004.

Kotoul, M., Pokluda, J., Sandera, P., Dlouhý, I., Chlup, Z., and Boccaccini, A. R. (2008). Toughening effects quantification in glass matrix composite reinforced by alumina platelets. *Acta Materialia*, 56(12):2908–2918.

Krstic, V., Nicholson, P., and Hoagland, R. (1981). Toughening of glasses by metallic particles. *Journal of the American Ceramic Society*, 64(9):499–504.

Lachambre, J., Réthoré, J., Weck, A., and Buffière, J. (2015). Extraction of stress intensity factors for 3d small fatigue cracks using digital volume correlation and x-ray tomography. *International Journal of Fatigue*, 71:3–10.

Lacondemine, T. (2019). *Initiation et propagation d'une fissure dans un composite particulaire à matrice verre : expérimentation et analyse numérique*. PhD thesis, Université Rennes I.

Lacondemine, T., Roux-Langlois, C., and Rouxel, T. (2017). Role of poisson's ratio mismatch on the crack path in glass matrix particulate composites. *International Journal of Fracture*, 207(1):73–85.

Lahellec, N. and Suquet, P. (2007). On the effective behavior of nonlinear inelastic composites: I. incremental variational principles. *Journal of the Mechanics and Physics of Solids*, 55(9):1932–1963.

Larkin, A. and Ovchinnikov, Y. (1979). Pinning in type II superconductors. *Journal of Low Temperature Physics*, 34(3):409–428.

Launey, M. and Ritchie, R. (2009). On the fracture toughness of advanced materials. *Advanced Materials*, 21(20):2103–2110.

Laurson, L., Santucci, S., and Zapperi, S. (2010). Avalanches and clusters in planar crack front propagation. *Physical Review E*, 81(4):046116.

Lazarus, V. (2003). Brittle fracture and fatigue propagation paths of 3d plane cracks under uniform remote tensile loading. *International Journal of Fracture*, 122(1):23–46.

Lazarus, V. (2011). Perturbation approaches of a planar crack in linear elastic fracture mechanics: A review. *Journal of the Mechanics and Physics of Solids*, 59(2):121–144.

Lazarus, V. and Leblond, J. (2002a). In-plane perturbation of the tunnel-crack under shear loading i: bifurcation and stability of the straight configuration of the front. *International Journal of Solids and Structures*, 39(17):4421–4436.

Lazarus, V. and Leblond, J. (2002b). In-plane perturbation of the tunnel-crack under shear loading II: Determination of the fundamental kernel. *International Journal of Solids and Structures*, 39(17):4437–4455.

Lé, B., Moës, N., and Legrain, G. (2018). Coupling damage and cohesive zone models with the thick level set approach to fracture. *Engineering Fracture Mechanics*, 193:214–247.

Le, V. H. T., Brisard, S., and Pouya, A. (2019). Debonding of a circular inclusion: Asymmetric propagation of a pair of cracks. *International Journal of Solids and Structures*, 167:71–78.

Lebihain, M., Leblond, J., and Ponson, L. (2020a). Effective toughness of periodic heterogeneous materials: The effect of out-of-plane crack excursions. *submitted to Journal of the Mechanics and Physics of Solids*.

Lebihain, M., Ponson, L., Kondo, D., and Leblond, J. (2020b). Effective toughness of large-scale disordered brittle solids: A homogenization framework. *submitted to Journal of the Mechanics and Physics of Solids*.

Lebihain, M., Ponson, L., and Leblond, J. (2020c). Scaling properties of brittle surface roughness : the impact of microstructal features. *in preparation*.

Lebihain, M., Ponson, L., and Leblond, J. (2020d). Textured brittle metamaterials with anisotropic fracture toughness. *in preparation*.

Leblond, J. (1999). Crack paths in three-dimensional elastic solids. i: two-term expansion of the stress intensity factors : application to crack path stability in hydraulic fracturing. *International Journal of Solids and Structures*, 36(1):79–103.

Leblond, J. (2003). *Mécanique de la rupture fragile et ductile*. Hermes science publications : Lavoisier, DL 2003.

Leblond, J., Karma, A., and Lazarus, V. (2011). Theoretical analysis of crack front instability in mode i+III. *Journal of the Mechanics and Physics of Solids*, 59(9):1872–1887.

Leblond, J., Karma, A., Ponson, L., and Vasudevan, A. (2019). Configurational stability of a crack propagating in a material with mode-dependent fracture energy - part i: Mixed-mode i+III. *Journal of the Mechanics and Physics of Solids*, 126:187–203.

Leblond, J., Lazarus, V., and Mouchrif, S. (1999). Crack paths in three-dimensional elastic solids. ii: three-term expansion of the stress intensity factors - applications and perspectives. *International Journal of Solids and Structures*, 36(1):105–142.

Leblond, J., Mouchrif, S., and Perrin, G. (1996). The tensile tunnel-crack with a slightly wavy front. *International Journal of Solids and Structures*, 33(14):1995–2022.

Leblond, J., Patinet, S., Frelat, J., and Lazarus, V. (2012). Second-order coplanar perturbation of a semi-infinite crack in an infinite body. *Engineering Fracture Mechanics*, 90:129–142.

Leblond, J. and Ponson, L. (2016). Out-of-plane deviation of a mode i+III crack encountering a tougher obstacle. *Comptes Rendus Mécanique*, 344(7):521–531.

Leevers, P. S. (1986). Crack front shape effects on propagation stability in thermosetting polyesters. *Theoretical and Applied Fracture Mechanics*, 6(1):45–55.

Legrand, L. and Leblond, J. B. (2010). In-plane perturbation of a system of two coplanar slit-cracks - ii : Case of close inner crack fronts or distant outer ones. *International Journal of Solids and Structures*, 47(25):3504–3512.

Legrand, L., Patinet, S., Leblond, J., Frelat, J., Lazarus, V., and Vandembroucq, D. (2011). Coplanar perturbation of a crack lying on the mid-plane of a plate. *International Journal of Fracture*, 170(1):67–82.

Leguillon, D. (2002). Strength or toughness? a criterion for crack onset at a notch. *European Journal of Mechanics - A/Solids*, 21(1):61–72.

Leguillon, D. and Martin, E. (2013). The strengthening effect caused by an elastic contrast - part i: the bimaterial case. *International Journal of Fracture*, 179(1):157–167.

Leguillon, D., Quesada, D., Putot, C., and Martin, E. (2007). Prediction of crack initiation at blunt notches and cavities – size effects. *Engineering Fracture Mechanics*, 74(15):2420–2436.

Li, B. and Maurini, C. (2019). Crack kinking in a variational phase-field model of brittle fracture with strongly anisotropic surface energy. *Journal of the Mechanics and Physics of Solids*, 125:502–522.

Li, W., Jin, Z., and Cusatis, G. (2019). Size effect analysis for the characterization of marcellus shale quasi-brittle fracture properties. *Rock Mechanics and Rock Engineering*, 52(1):1–18.

Li, X., Kasai, T., Nakao, S., Tanaka, H., Ando, T., Shikida, M., and Sato, K. (2005). Measurement for fracture toughness of single crystal silicon film with tensile test. *Sensors and Actuators A: Physical*, 119(1):229–235.

Li, Y. and Zhou, M. (2013a). Prediction of fracture toughness of ceramic composites as function of microstructure: I. numerical simulations. *Journal of the Mechanics and Physics of Solids*, 61(2):472–488.

Li, Y. and Zhou, M. (2013b). Prediction of fracturess toughness of ceramic composites as function of microstructure: II. analytical model. *Journal of the Mechanics and Physics of Solids*, 61(2):489–503.

Lôpez, J. and Schmittbuhl, J. (1998). Anomalous scaling of fracture surfaces. *Physical Review E*, 57(6):6405–6408.

Lucchetta, A., Auslender, F., Bornert, M., and Kondo, D. (2019). A double incremental variational procedure for elastoplastic composites with combined isotropic and linear kinematic hardening. *International Journal of Solids and Structures*, 158:243–267.

Ma, J., Wang, H., Weng, L., and Tan, G. E. B. (2004). Effect of porous interlayers on crack deflection in ceramic laminates. *Journal of the European Ceramic Society*, 24(5):825–831.

Madou, K. and Leblond, J. (2012). A gurson-type criterion for porous ductile solids containing arbitrary ellipsoidal voids - i: Limit-analysis of some representative cell. *Journal of the Mechanics and Physics of Solids*, 60(5):1020–1036.

Malik, I. and Barthelat, F. (2016). Toughening of thin ceramic plates using bioinspired surface patterns. *International Journal of Solids and Structures*, 97-98:389–399.

Mandelbrot, B., Passoja, D., and Paullay, A. (1984). Fractal character of fracture surfaces of metals. *Nature*, 308(5961):721–722.

Marcus, H. L. and Sih, G. C. (1971). A crackline-loaded edge-crack stress corrosion speci-

men. *Engineering Fracture Mechanics*, 3(4):453–461.

Marder, M. and Fineberg, J. (1996). How things break. *Physics Today*, 49(9):24.

McMeeking, R. M. and Evans, A. (1982). Mechanics of transformation-toughening in brittle materials. *Journal of the American Ceramic Society*, 65(5):242–246.

McNeill, S. R., Peters, W. H., and Sutton, M. A. (1987). Estimation of stress intensity factor by digital image correlation. *Engineering Fracture Mechanics*, 28(1):101–112.

Mecholsky, J. J., Passoja, D. E., and Feinberg-Ringel, K. S. (1989). Quantitative analysis of brittle fracture surfaces using fractal geometry. *Journal of the American Ceramic Society*, 72(1):60–65.

Mirkhalaf, M., Dastjerdi, A. K., and Barthelat, F. (2014). Overcoming the brittleness of glass through bio-inspiration and micro-architecture. *Nature Communications*, 5:3166.

Moës, N., Dolbow, J., and Belytschko, T. (1999). A finite element method for crack growth without remeshing. *International Journal for Numerical Methods in Engineering*, 46(1):131–150.

Moës, N., Gravouil, A., and Belytschko, T. (2002). Non-planar 3d crack growth by the extended finite element and level sets - part i: Mechanical model. *International Journal for Numerical Methods in Engineering*, 53(11).

Moës, N., Stolz, C., Bernard, P., and Chevaugeon, N. (2011). A level set based model for damage growth: The thick level set approach. *International Journal for Numerical Methods in Engineering*, 86(3):358–380.

Monchiet, V., Cazacu, O., Charkaluk, E., and Kondo, D. (2008). Macroscopic yield criteria for plastic anisotropic materials containing spheroidal voids. *International Journal of Plasticity*, 24(7):1158–1189.

Morel, S., Bonamy, D., Ponson, L., and Bouchaud, E. (2008). Transient damage spreading and anomalous scaling in mortar crack surfaces. *Physical Review E*, 78(1):016112.

Morel, S., Lubet, T., Pouchou, J., and Olive, J. (2004). Roughness analysis of the cracked surfaces of a face centered cubic alloy. *Physical Review Letters*, 93(6):065504.

Morel, S., Mourot, G., and Schmittbuhl, J. (2003). Influence of the specimen geometry on r-curve behavior and roughening of fracture surfaces. *International Journal of Fracture*, 121(1):23–42.

Morel, S., Schmittbuhl, J., Lôpez, J., and Valentin, G. (1998). Anomalous roughening of wood fractured surfaces. *Physical Review E*, 58(6):6999–7005.

Morin, L., Leblond, J., and Kondo, D. (2015). A gurson-type criterion for plastically anisotropic solids containing arbitrary ellipsoidal voids. *International Journal of Solids and Structures*, 77:86–101.

Mourot, G., Morel, S., Bouchaud, E., and Valentin, G. (2005). Anomalous scaling of mortar fracture surfaces. *Physical Review E*, 71(1):016136.

Movchan, A., Gao, H., and Willis, J. (1998). On perturbations of plane cracks. *International Journal of Solids and Structures*, 35(26):3419–3453.

Mueller, J., Raney, J., Shea, K., and Lewis, J. (2018). Architected lattices with high stiffness and toughness via multicore-shell 3d printing. *Advanced Materials*, 30(12):1705001.

Mueller, J., Shea, K., and Daraio, C. (2015). Mechanical properties of parts fabricated with inkjet 3d printing through efficient experimental design. *Materials & Design*, 86:902–912.

Muju, S. (2000). Crack propogation in bimaterial multilayered periodically microcracking composite media. *Composites Science and Technology*, 60(12):2213–2221.

Mumford, D. and Shah, J. (1989). Optimal approximations by piecewise smooth functions and associated variational problems. *Communications on Pure and Applied Mathematics*, 42(5):577–685.

Munch, E., Launey, M. E., Alsem, D. H., Saiz, E., Tomsia, A. P., and Ritchie, R. O. (2008). Tough, bio-inspired hybrid materials. *Science*, 322(5907).

Naslain, R. (1998). The design of the fibre-matrix interfacial zone in ceramic matrix composites. *Composites Part A: Applied Science and Manufacturing*, 29(9):1145–1155.

Nasseri, M. H. B. and Mohanty, B. (2008). Fracture toughness anisotropy in granitic rocks. *International Journal of Rock Mechanics and Mining Sciences*, 45(2):167–193.

Newman, J. C. and Raju, I. S. (1984). Prediction of fatigue crack-growth patterns and lives in three-dimensional crack bodies. In Valluri, S. R., Taplin, D. M. R., Rao, P., Knott, J. F., and Dubey, R., editors, *Fracture 84*, pages 1597–1608. Pergamon.

Nguyen, Q. S. (2000). *Stability and Nonlinear Solid Mechanics*. Wiley.

Nguyen, T. (2015). *Modeling of complex microcracking in cement based materials by combining numerical simulations based on a phase-field method and experimental 3D imaging*. PhD thesis, ENPC.

Nguyen, T., Réthoré, J., Yvonnet, J., and Baietto, M. (2017a). Multi-phase-field modeling of anisotropic crack propagation for polycrystalline materials. *Computational Mechanics*, 60(2):289–314.

Nguyen, T. T., Yvonnet, J., Bornert, M., Chateau, C., Bilteryst, F., and Steib, E. (2017b). Large-scale simulations of quasi-brittle microcracking in realistic highly heterogeneous microstructures obtained from micro CT imaging. *Extreme Mechanics Letters*, 17:50–55.

Nguyen, T. T., Yvonnet, J., Zhu, Q. Z., Bornert, M., and Chateau, C. (2015). A phase field method to simulate crack nucleation and propagation in strongly heterogeneous materials from direct imaging of their microstructure. *Engineering Fracture Mechanics*, 139:18–39.

Nguyen, T. T., Yvonnet, J., Zhu, Q. Z., Bornert, M., and Chateau, C. (2016). A phase-field method for computational modeling of interfacial damage interacting with crack propagation in realistic microstructures obtained by microtomography. *Computer Methods in Applied Mechanics and Engineering*, 312:567–595.

Ortiz, M. (1987). A continuum theory of crack shielding in ceramics. *Journal of Applied Mechanics*, 54(1):54–58.

Ortiz, M. and Pandolfi, A. (1999). Finite-deformation irreversible cohesive elements for three-dimensional crack-propagation analysis. *International Journal for Numerical Methods in Engineering*, 44(9):1267–1282.

Osovski, S., Srivastava, A., Ponson, L., Bouchaud, E., Tvergaard, V., Ravi-Chandar, K., and Needleman, A. (2015). The effect of loading rate on ductile fracture toughness and fracture surface roughness. *Journal of the Mechanics and Physics of Solids*, 76:20–46.

Ostoja-Starzewski, M. (2006). Material spatial randomness: From statistical to representative volume element. *Probabilistic Engineering Mechanics*, 21(2):112–132.

Pallares, G., Lechenault, F., George, M., Bouchaud, E., Ottina, C., Rountree, C., and Ciccotti, M. (2018). Roughness of oxide glass subcritical fracture surfaces. *Journal of*

the American Ceramic Society, 101(3):1279–1288.

Pallares, G., Ponson, L., Grimaldi, A., George, M., Prevot, G., and Ciccotti, M. (2009). Crack opening profile in DCDC specimen. *International Journal of Fracture*, 156(1):11–20.

Paris, P. and Erdogan, F. (1963). A critical analysis of crack propagation laws. *Journal of Basic Engineering*, 85(4):528–533.

Patinet, S., Alzate, L., Barthel, E., Dalmas, D., Vandembroucq, D., and Lazarus, V. (2013a). Finite size effects on crack front pinning at heterogeneous planar interfaces: Experimental, finite elements and perturbation approaches. *Journal of the Mechanics and Physics of Solids*, 61(2):311–324.

Patinet, S., Vandembroucq, D., and Roux, S. (2013b). Quantitative prediction of effective toughness at random heterogeneous interfaces. *Physical Review Letters*, 110(16):165507.

Paul, B., Faivre, M., Massin, P., Giot, R., Colombo, D., Golfier, F., and Martin, A. (2018). 3d coupled HM-XFEM modeling with cohesive zone model and applications to non planar hydraulic fracture propagation and multiple hydraulic fractures interference. *Computer Methods in Applied Mechanics and Engineering*, 342:321–353.

Perales, F., Bourgeois, S., Chrysochoos, A., and Monerie, Y. (2008). Two field multibody method for periodic homogenization in fracture mechanics of nonlinear heterogeneous materials. *Engineering Fracture Mechanics*, 75(11):3378–3398.

Perrin, G. and Rice, J. (1994). Disordering of a dynamic planar crack front in a model elastic medium of randomly variable toughness. *Journal of the Mechanics and Physics of Solids*, 42(6):1047–1064.

Peters, W. H. and Ranson, W. F. (1982). Digital imaging techniques in experimental stress analysis. *Optical Engineering*, 21(3):213427.

Pindra, N., Lazarus, V., and Leblond, J. (2008). The deformation of the front of a 3d interface crack propagating quasistatically in a medium with random fracture properties. *Journal of the Mechanics and Physics of Solids*, 56(4):1269–1295.

Pindra, N., Lazarus, V., and Leblond, J. B. (2010). In-plane perturbation of a system of two coplanar slit-cracks - i: Case of arbitrarily spaced crack fronts. *International Journal of Solids and Structures*, 47(25):3489–3503.

Pisarenko, G. G., Chushko, V. M., and Kovalev, S. P. (1985). Anisotropy of fracture toughness of piezoelectric ceramics. *Journal of the American Ceramic Society*, 68(5):259–265.

Pohanka, R., Freiman, S., and Bender, B. (1978). Effect of the phase transformation on the fracture behavior of BaTiO3. *Journal of the American Ceramic Society*, 61(1):72–75.

Ponson, L. (2007). Crack propagation in disordered materials: how to decipher fracture surfaces. *Annales de Physique*, 32(1):1–120.

Ponson, L. (2009). Depinning transition in the failure of inhomogeneous brittle materials. *Physical Review Letters*, 103(5):055501.

Ponson, L. (2016). Statistical aspects in crack growth phenomena: how the fluctuations reveal the failure mechanisms. *International Journal of Fracture*, 201(1):11–27.

Ponson, L., Auradou, H., Pessel, M., Lazarus, V., and Hulin, J. P. (2007). Failure mechanisms and surface roughness statistics of fractured fontainebleau sandstone. *Physical*

Review E, 76(3):036108.

Ponson, L., Auradou, H., Vié, P., and Hulin, J. (2006a). Low self-affine exponents of fractured glass ceramics surfaces. *Physical Review Letters*, 97(12):125501.

Ponson, L. and Bonamy, D. (2010). Crack propagation in brittle heterogeneous solids: Material disorder and crack dynamics. *International Journal of Fracture*, 162(1):21–31.

Ponson, L., Bonamy, D., and Bouchaud, E. (2006b). Two-dimensional scaling properties of experimental fracture surfaces. *Physical Review Letters*, 96(3):035506.

Ponson, L. and Pindra, N. (2017). Crack propagation through disordered materials as a depining transition: A critical test of the theory. *Physical Review E*, 95(5):053004.

Ponte-Castañeda, P. (1991). The effective mechanical properties of nonlinear isotropic composites. *Journal of the Mechanics and Physics of Solids*, 39(1):45–71.

Ponte-Castañeda, P. and Suquet, P. (1997). Nonlinear composites. In van der Giessen, E. and Wu, T. Y., editors, *Advances in Applied Mechanics*, volume 34, pages 171–302. Elsevier.

Ponte-Castañeda, P. and Willis, J. (1995). The effect of spatial distribution on the effective behavior of composite materials and cracked media. *Journal of the Mechanics and Physics of Solids*, 43(12):1919–1951.

Ramanathan, S., Ertaş, D., and Fisher, D. (1997). Quasistatic crack propagation in heterogeneous media. *Physical Review Letters*, 79(5):873–876.

Raney, J., Compton, B., Mueller, J., Ober, T., Shea, K., and Lewis, J. (2018). Rotational 3d printing of damage-tolerant composites with programmable mechanics. *Proceedings of the National Academy of Sciences*, 115(6):1198–1203.

Raous, M. and Monerie, Y. (2002). Unilateral contact, friction and adhesion: 3d cracks in composite materials. In Martins, J. C. and Marques, M. D. P. M., editors, *Contact Mechanics*, Solid Mechanics and Its Applications, pages 333–346. Springer Netherlands.

Ravi-Chandar, K. and Balzano, M. (1988). On the mechanics and mechanisms of crack growth in polymeric materials. *Engineering Fracture Mechanics*, 30(5):713–727.

Read, B. E. and Duncan, J. C. (1981). Measurement of dynamic properties of polymeric glasses for different modes of deformation. *Polymer Testing*, 2(2):135–150.

Reis, J. M. L. (2006). Fracture and flexural characterization of natural fiber-reinforced polymer concrete. *Construction and Building Materials*, 20(9):673–678.

Renard, F., Cordonnier, B., Kobchenko, M., Kandula, N., Weiss, J., and Zhu, W. (2017). Microscale characterization of rupture nucleation unravels precursors to faulting in rocks. *Earth and Planetary Science Letters*, 476:69–78.

Renard, F., McBeck, J., Cordonnier, B., Zheng, X., Kandula, N., Sanchez, J., Kobchenko, M., Noiriel, C., Zhu, W., Meakin, P., Fusseis, F., and Dysthe, D. (2019). Dynamic in situ three-dimensional imaging and digital volume correlation analysis to quantify strain localization and fracture coalescence in sandstone. *Pure and Applied Geophysics*, 176(3):1083–1115.

Réthoré, J., Gravouil, A., Morestin, F., and Combescure, A. (2005). Estimation of mixed-mode stress intensity factors using digital image correlation and an interaction integral. *International Journal of Fracture*, 132(1):65–79.

Rice, J. (1985). First-order variation in elastic fields due to variation in location of a planar

crack front. *Journal of Applied Mechanics*, 52(3):571–579.

Rice, J. (1987). Tensile crack tip fields in elastic-ideally plastic crystals. *Mechanics of Materials*, 6(4):317–335.

Rice, J., Ben-Zion, Y., and Klm, K. (1994). Three-dimensional perturbation solution for a dynamic planar crack moving unsteadily in a model elastic solid. *Journal of the Mechanics and Physics of Solids*, 42(5):813–843.

Rice, J. R. (1968). A path independent integral and the approximate analysis of strain concentration by notches and cracks. *Journal of Applied Mechanics*, 35(2):379–386.

Rice, J. R. (1989). Weight function theory for three-dimensional elastic crack analysis. *Fracture Mechanics: Perspectives and Directions (Twentieth Symposium)*.

Ritchie, R. O. (1988). Mechanisms of fatigue crack propagation in metals, ceramics and composites: Role of crack tip shielding. *Materials Science and Engineering: A*, 103(1):15–28.

Ritchie, R. O. (2011). The conflicts between strength and toughness. *Nature Materials*, 10(11):817–822.

Rosso, A. and Krauth, W. (2002). Roughness at the depinning threshold for a long-range elastic string. *Physical Review E*, 65(2):025101.

Roux, S. and Hild, F. (2006). Stress intensity factor measurements from digital image correlation: post-processing and integrated approaches. *International Journal of Fracture*, 140(1):141–157.

Roux, S. and Hild, F. (2008). Self-consistent scheme for toughness homogenization. *International Journal of Fracture*, 154(1):159–166.

Roux, S., Vandembroucq, D., and Hild, F. (2003). Effective toughness of heterogeneous brittle materials. *European Journal of Mechanics - A/Solids*, 22(5):743–749.

Roux-Langlois, C., Gravouil, A., Baietto, M. C., Réthoré, J., Mathieu, F., Hild, F., and Roux, S. (2015). DIC identification and x-FEM simulation of fatigue crack growth based on the williams series. *International Journal of Solids and Structures*, 53:38–47.

Sab, K. (1992). On the homogenization and the simulation of random materials. *Eur. J. Mech, . A/Solids*, 1(5):585–607.

Salzman, A., Moës, N., and Chevaugeon, N. (2016). On use of the thick level set method in 3d quasi-static crack simulation of quasi-brittle material. *International Journal of Fracture*, 202(1):21–49.

Scheibert, J., Guerra, C., Célarié, F., Dalmas, D., and Bonamy, D. (2010). Brittle-quasibrittle transition in dynamic fracture: An energetic signature. *Physical Review Letters*, 104(4):045501.

Schmittbuhl, J., Schmitt, F., and Scholz, C. (1995). Scaling invariance of crack surfaces. *Journal of Geophysical Research: Solid Earth*, 100:5953–5973.

Snozzi, L., Gatuingt, F., and Molinari, J. F. (2012). A meso-mechanical model for concrete under dynamic tensile and compressive loading. *International Journal of Fracture*, 178(1):179–194.

Soppa, E., Doumalin, P., Binkele, P., Wiesendanger, T., Bornert, M., and Schmauder, S. (2001). Experimental and numerical characterization of in-plane deformation in two-phase materials. *Computational Materials Science*, 21(3):261–275.

Steinbrech, R. (1992). Toughening mechanisms for ceramic materials. *Journal of the European Ceramic Society*, 10(3):131–142.

Suresh, S. (1985). Fatigue crack deflection and fracture surface contact: Micromechanical models. *Metallurgical Transactions A*, 16(2):249–260.

Sutton, M., Wolters, W., Peters, W., Ranson, W., and McNeill, S. (1983). Determination of displacements using an improved digital correlation method. *Image and Vision Computing*, 1(3):133–139.

Sutton, M. A., McNeill, S. R., Helm, J. D., and Chao, Y. J. (2000). Advances in two-dimensional and three-dimensional computer vision. In Rastogi, P. K., editor, *Photomechanics*, Topics in Applied Physics, pages 323–372. Springer Berlin Heidelberg.

Takei, A., Roman, B., Bico, J., Hamm, E., and Melo, F. (2013). Forbidden directions for the fracture of thin anisotropic sheets: An analogy with the wulff plot. *Physical Review Letters*, 110(14):144301.

Tange, O. (2011). Gnu parallel - the command-line power tool. *;login: The USENIX Magazine*, 36(1):42–47.

Torquato, S. (2002). *Random Heterogeneous Materials: Microstructure and Macroscopic Properties*. Interdisciplinary Applied Mathematics. Springer-Verlag.

Vasoya, M., Lazarus, V., and Ponson, L. (2016a). Bridging micro to macroscale fracture properties in highly heterogeneous brittle solids: weak pinning versus fingering. *Journal of the Mechanics and Physics of Solids*, 95:755–773.

Vasoya, M., Leblond, J., and Ponson, L. (2013). A geometrically nonlinear analysis of coplanar crack propagation in some heterogeneous medium. *International Journal of Solids and Structures*, 50(2):371–378.

Vasoya, M., Unni, A., Leblond, J., Lazarus, V., and Ponson, L. (2016b). Finite size and geometrical non-linear effects during crack pinning by heterogeneities: An analytical and experimental study. *Journal of the Mechanics and Physics of Solids*, 89:211–230.

Vasudevan, A., Grabois, T., Cordeiro, G., Toledo Filho, R., and Ponson, L. (2019). A new fracture test methodology for the accurate characterization of brittle fracture properties. *Submitted for publication*.

Verhoosel, C. and Borst, R. (2013). A phase-field model for cohesive fracture. *International Journal for Numerical Methods in Engineering*, 96(1):43–62.

Vernède, S., Ponson, L., and Bouchaud, J. (2015). Turbulent fracture surfaces: A footprint of damage percolation? *Physical Review Letters*, 114(21):215501.

Vernède, S., Ponson, L., UPMC, and CNRS (International patent WO/2016/050871, 2016). Method for characterizing the cracking mechanism of a material from the fracture surface thereof.

Wang, L., Ju, Y., Xie, H., Ma, G., Mao, L., and He, K. (2017a). The mechanical and photoelastic properties of 3d printable stress-visualized materials. *Scientific Reports*, 7(1):1–9.

Wang, N. and Xia, S. (2017). Cohesive fracture of elastically heterogeneous materials: An integrative modeling and experimental study. *Journal of the Mechanics and Physics of Solids*, 98:87–105.

Wang, X., Jiang, M., Zhou, Z., Gou, J., and Hui, D. (2017b). 3d printing of polymer matrix

composites: A review and prospective. *Composites Part B: Engineering*, 110:442–458.

Wegst, U., Bai, H., Saiz, E., Tomsia, A., and Ritchie, R. (2015). Bioinspired structural materials. *Nature Materials*, 14(1):23–36.

Westergaard, H. (1939). Bearing pressures and cracks. *Journal of Applied Mechanics*, 6:49–53.

Widom, B. (1966). Random sequential addition of hard spheres to a volume. *The Journal of Chemical Physics*, 44(10):3888–3894.

Williams, M. L. (1952). Stress singularities resulting from various boundary conditions in angular corners of plates in extension. *Journal of Applied Mechanics*, 19:526–528.

Willis, J. and Movchan, A. (1995). Dynamic weight functions for a moving crack. i. mode i loading. *Journal of the Mechanics and Physics of Solids*, 43(3):319–341.

Wittbrodt, B. and Pearce, J. M. (2015). The effects of PLA color on material properties of 3-d printed components. *Additive Manufacturing*, 8:110–116.

Xia, L., Da, D., and Yvonnet, J. (2018). Topology optimization for maximizing the fracture resistance of quasi-brittle composites. *Computer Methods in Applied Mechanics and Engineering*, 332:234–254.

Xia, S., Ponson, L., Ravichandran, G., and Bhattacharya, K. (2012). Toughening and asymmetry in peeling of heterogeneous adhesives. *Physical Review Letters*, 108(19):196101.

Xia, S. M., Ponson, L., Ravichandran, G., and Bhattacharya, K. (2013). Adhesion of heterogeneous thin films - i: Elastic heterogeneity. *Journal of the Mechanics and Physics of Solids*, 61(3):838–851.

Xia, S. M., Ponson, L., Ravichandran, G., and Bhattacharya, K. (2015). Adhesion of heterogeneous thin films - ii: Adhesive heterogeneity. *Journal of the Mechanics and Physics of Solids*, 83:88–103.

Xu, G., Bower, A. F., and Ortiz, M. (1998). The influence of crack trapping on the toughness of fiber reinforced composites. *Journal of the Mechanics and Physics of Solids*, 46(10):1815–1833.

Xu, X. P. and Needleman, A. (1994). Numerical simulations of fast crack growth in brittle solids. *Journal of the Mechanics and Physics of Solids*, 42(9):1397–1434.

Yamini, S. and Young, R. J. (1979). Crack propagation in and fractography of epoxy resins. *Journal of Materials Science*, 14(7):1609–1618.

Yilmaz, O. and Molinari, J. (2017). A mesoscale fracture model for concrete. *Cement and Concrete Research*, 97:84–94.

Ylmaz, O., Bleyer, J., and Molinari, J. (2018). Influence of heterogeneities on crack propagation. *International Journal of Fracture*, 209(1):77–90.

8

Appendices

Appendix 8.A Regularization of the perturbative approach for large angle in the propagation direction

8.A.1 Regularization of the perturbated SIF for large X-angles

In our simulations, the local slope of the crack front in the (xOy) plane, $\partial f_y/\partial x$, may be large during the by-pass of inclusions. To deal with this issue, we propose heuristic, approximate expressions of the SIFs and related quantities based on a combination of Eq. (2.14) [Movchan et al., 1998] and Eq. (2.18) [Leblond, 1999].

8.A.2 SIF regularized evaluation

We consider a point P of abscissa z along the crack front $\mathcal{F}$, and note $\theta = \arctan\left(\partial f_y/\partial x\right)$ the angle (which may be arbitrarily large) between with the x-direction and the local direction of crack propagation. Movchan et al. [1998]'s formulæ provide the variations of the SIFs arising from infinitesimal perturbations of the crack front and crack surfaces, to first order in these perturbations, that is for small values of θ. One observes in Eq. (2.14) that the Mode II variation can be split into a local term $\delta K_{\mathrm{II}}^{\mathrm{loc}}$ proportional to the slope $\partial f_y/\partial x$, and a term $\delta K_{\mathrm{II}}^{\mathrm{LR}}$ depicting long-range elastic interactions:

$$\delta K_{\mathrm{II}}\left(z,t\right) = \underbrace{\frac{K_{\mathrm{I}}^{\infty}\left(t\right)}{2}\frac{\partial f_y}{\partial x}\left(z,t\right)}_{\delta K_{\mathrm{II}}^{\mathrm{loc}}} + \underbrace{\frac{2-3\nu}{2-\nu}\frac{K_{\mathrm{I}}^{\infty}\left(t\right)}{2\pi}\,\mathrm{PV}\int_{-\infty}^{+\infty}\frac{f_y\left(z,t\right)-f_y\left(z',t\right)}{\left(z-z'\right)^2}\,dz'}_{\delta K_{\mathrm{II}}^{\mathrm{LR}}} \tag{8.1}$$

Note that the expressions for the Mode I and III variations do not, however, contain any similar term proportional to $\partial f_y/\partial x$.

On the other hand Leblond [1999]'s formulæ relate the values of the SIFs after an abrupt change of the direction of propagation to those of the SIFs before this change, for an extension of vanishingly small length but an arbitrary kink angle.

We therefore propose, for a crack slightly perturbed out of its plane but with a possibly

large slope $\partial f_y/\partial x$, to adopt the following formulæ combining Eq. (2.14) with Eq. (2.18) :

$$\begin{cases} K_{\mathrm{I}}(z,t) = F_{\mathrm{I,I}}(\theta)\left[K_{\mathrm{I}}^{\infty}(t) + \delta K_{\mathrm{I}}(z,t)\right] + F_{\mathrm{I,II}}(\theta)\,\delta K_{\mathrm{II}}^{\mathrm{LR}}(z,t) \\ K_{\mathrm{II}}(z,t) = F_{\mathrm{II,I}}(\theta)\left[K_{\mathrm{I}}^{\infty}(t) + \delta K_{\mathrm{I}}(z,t)\right] + F_{\mathrm{II,II}}(\theta)\,\delta K_{\mathrm{II}}^{\mathrm{LR}}(z,t) \\ K_{\mathrm{III}}(z,t) = F_{\mathrm{III,III}}(\theta)\,\delta K_{\mathrm{III}}(z,t) \end{cases} \tag{8.2}$$

Note that:

- For *small angles* θ, Eq. (8.2) reduces to Eq. (2.14), as desired, by virtue of the following low-order expressions of the functions $F_{\mathrm{i,j}}(\theta)$ [Leblond, 1999]:

$$\begin{cases} \theta = \arctan\left(\dfrac{\partial f_y}{\partial x}\right) = \dfrac{\partial f_y}{\partial x} + O\left[\left(\dfrac{\partial f_y}{\partial x}\right)^3\right] \\ F_{\mathrm{I,I}}(\theta) = 1 + O\left(\theta^2\right) \\ F_{\mathrm{I,II}}(\theta) = -\frac{3}{2}\theta + O\left(\theta^3\right) \\ F_{\mathrm{II,I}}(\theta) = \frac{1}{2}\theta + O\left(\theta^3\right) \\ F_{\mathrm{II,II}}(\theta) = 1 + O\left(\theta^2\right) \end{cases} \tag{8.3}$$

- If the crack lands on an inclusion with a zero angle and subsequently kinks along the interface, at the *very beginning of the by-pass* Eq. (8.2) reduces to Eq. (2.18) and is therefore rigorously correct even for large values of the kink angle.

8.A.3 ERR regularized evaluation

Let us consider, as before, a point M on the perturbed crack front $\mathcal{F}$. The local direction of crack propagation makes an arbitrary angle θ with the x-direction. The elastic ERR rate for a kink angle α is given by:

$$G(\alpha) = \frac{1-\nu^2}{E}\left(K_{\mathrm{I}}^2(\alpha) + K_{\mathrm{II}}^2(\alpha)\right) + \frac{1+\nu}{E}K_{\mathrm{III}}^2(\alpha) \tag{8.4}$$

where $K_{\mathrm{I}}(\alpha)$, $K_{\mathrm{II}}(\alpha)$ and $K_{\mathrm{III}}(\alpha)$ are given by Leblond [1999]'s formulæ :

$$\begin{cases} K_{\mathrm{I}}(\alpha) = F_{\mathrm{I,I}}(\alpha)\,K_{\mathrm{I}}(z,t) + F_{\mathrm{I,II}}(\alpha)\,K_{\mathrm{II}}(z,t) \\ K_{\mathrm{II}}(\alpha) = F_{\mathrm{II,I}}(\alpha)\,K_{\mathrm{I}}(z,t) + F_{\mathrm{II,II}}(\alpha)\,K_{\mathrm{II}}(z,t) \\ K_{\mathrm{III}}(\alpha) = F_{\mathrm{III,III}}(\alpha)\,K_{\mathrm{III}}(z,t) \end{cases} \tag{8.5}$$

where the SIFs $(K_i(z,t))$ are given by Eq. (8.2).

Discarding second-order terms in the crack perturbation, we get :

$$G\left(\alpha,\theta,\frac{\delta K_{\mathrm{I}}}{K_{\mathrm{I}}^{\infty}},\frac{\delta K_{\mathrm{II}}^{\mathrm{LR}}}{K_{\mathrm{I}}^{\infty}}\right) = G^{\infty}\left[g_{\mathrm{I}}(\alpha,\theta)\left(1+2\frac{\delta K_{\mathrm{I}}}{K_{\mathrm{I}}^{\infty}}\right) + g_{\mathrm{II}}(\alpha,\theta)\,\frac{\delta K_{\mathrm{II}}^{\mathrm{LR}}}{K_{\mathrm{I}}^{\infty}}\right] \tag{8.6}$$

where g_{I} and g_{II} are linked to Amestoy-Leblond's functions $(F_{i,j})$ through the following

relation :

$$\begin{cases} g_{\mathrm{I}}(\alpha,\theta) = & \left(F^2_{\mathrm{I,I}}(\alpha)+F^2_{\mathrm{II,I}}(\alpha)\right)F^2_{\mathrm{I,I}}(\theta) \\ & +\left(F^2_{\mathrm{I,II}}(\alpha)+F^2_{\mathrm{II,II}}(\alpha)\right)F^2_{\mathrm{II,I}}(\theta) \\ & +2\left(F_{\mathrm{I,I}}(\alpha)F_{\mathrm{I,II}}(\alpha)+F_{\mathrm{II,I}}(\alpha)F_{\mathrm{II,II}}(\alpha)\right) \\ & \cdot F_{\mathrm{I,I}}(\theta)F_{\mathrm{II,I}}(\theta) \\ g_{\mathrm{II}}(\alpha,\theta) = & 2\left(F^2_{\mathrm{I,I}}(\alpha)+F^2_{\mathrm{II,I}}(\alpha)\right)F_{\mathrm{I,I}}(\theta)F_{\mathrm{I,II}}(\theta) \\ & +\left(F^2_{\mathrm{I,II}}(\alpha)+F^2_{\mathrm{II,II}}(\alpha)\right)F_{\mathrm{II,I}}(\theta)F_{\mathrm{II,II}}(\theta) \\ & +2\left(F_{\mathrm{I,I}}(\alpha)F_{\mathrm{I,II}}(\alpha)+F_{\mathrm{II,I}}(\alpha)F_{\mathrm{II,II}}(\alpha)\right) \\ & \cdot\left(F_{\mathrm{I,I}}(\theta)F_{\mathrm{II,II}}(\theta)+F_{\mathrm{II,I}}(\theta)F_{\mathrm{I,II}}(\theta)\right) \end{cases} \tag{8.7}$$

Appendix 8.B First LEFM perturbative equations for the out-of-plane perturbations of the half-plane crack under mixed mode loading with higher-order terms (T-stresses, A-stresses)

In this appendix, we calculate Movchan et al. [1998]'s (3.36) formulae explicitly, taking into account mixed Mode I+II+II ($K^\infty_{\mathrm{I}}, K^\infty_{\mathrm{II}}, K^\infty_{\mathrm{III}}$) as well as higher-order terms in the asymptotic development of the crack tip stresses, the T-stresses ($T^\infty_{xx}, T^\infty_{zx}$) (constant terms) and A-stresses ($A^\infty_{\mathrm{I}}, A^\infty_{\mathrm{II}}, A^\infty_{\mathrm{III}}$) ($\sqrt{r}$ terms).

Mode I perturbations

$$\begin{aligned} \delta K_{\mathrm{I}}(x,z) = & -\frac{3}{2}K^\infty_{\mathrm{II}}\frac{\partial f_y}{\partial x}(x,z) - 2K^\infty_{\mathrm{III}}\frac{\partial f_y}{\partial z}(x,z) + \left(\sqrt{\frac{\pi}{2}}A^\infty_{\mathrm{II}} + K'^\infty_{\mathrm{II}}\right)f_y(x,z) + \frac{K^\infty_{\mathrm{II}}}{2\pi}\,\mathrm{PV}\int_{-\infty}^{+\infty}\frac{f_y(x,z)-f_y(x,z')}{(z-z')^2}\,dz' \\ & + \frac{\sqrt{2}}{4\pi}\frac{1-2\nu}{1-\nu}\mathrm{Re}\left[\int_{-\infty}^{x}dx'\int_{-\infty}^{+\infty}\frac{K^\infty_{\mathrm{III}}-i(1-\nu)K^\infty_{\mathrm{II}}}{(x-x'+i(z-z'))^{3/2}}\cdot\frac{\frac{\partial f_y}{\partial z'}(x',z')}{\sqrt{x-x'}}\,dz'\right] \\ & - \frac{\sqrt{2}}{4\pi}\frac{1-2\nu}{1-\nu}\mathrm{Re}\left[\int_{-\infty}^{x}dx'\int_{-\infty}^{+\infty}\frac{A^\infty_{\mathrm{III}}-i(1-\nu)A^\infty_{\mathrm{II}}}{(x-x'+i(z-z'))^{3/2}}\cdot\frac{\partial f_y}{\partial z'}(x',z')\sqrt{x-x'}\,dz'\right] \end{aligned} \tag{8.8}$$

Mode II perturbations

$$\begin{aligned} \delta K_{\mathrm{II}}(x,z) = & \frac{K^\infty_{\mathrm{I}}}{2}\frac{\partial f_y}{\partial x}(x,z) + \frac{2-3\nu}{(2-\nu)}\frac{K^\infty_{\mathrm{I}}}{2\pi}\,\mathrm{PV}\int_{-\infty}^{+\infty}\frac{f_y(x,z)-f_y(x,z')}{(z-z')^2}\,dz' + \sqrt{\frac{\pi}{2}}A^\infty_{\mathrm{I}}f_y(x,z) \\ & - \frac{\sqrt{2}}{\pi^{3/2}}\int_{-\infty}^{x}dx'\int_{-\infty}^{+\infty}\frac{\sqrt{x-x'}}{(x-x')^2+(z-z')^2}\left[1+\frac{2\nu}{2-\nu}\cdot\frac{(x-x')^2-(z-z')^2}{x'^2+(z-z')^2}\right]\left[T^\infty_{xx}\frac{\partial f_y}{\partial x'}(x',z')+T^\infty_{xz}\frac{\partial f_y}{\partial z'}(x',z')\right]dz \\ & - \frac{\sqrt{2}}{\pi^{3/2}}\int_{-\infty}^{x}dx'\int_{-\infty}^{+\infty}\frac{\sqrt{x-x'}}{(x-x')^2+(z-z')^2}\left[\frac{2\nu}{2-\nu}\cdot\frac{2(x-x')(z-z')}{(x-x')^2+(z-z')^2}\right]\left[T^\infty_{xz}\frac{\partial f_y}{\partial x'}(x',z')+T^\infty_{zz}\frac{\partial f_y}{\partial z'}(x',z')\right]dz' \end{aligned} \tag{8.9}$$

Mode III perturbations

$$\begin{aligned}\delta K_{\mathrm{III}}(x,z) =& \frac{2(1-\nu)^2}{2-\nu} K_{\mathrm{I}}^{\infty} \frac{\partial f_y}{\partial z}(x,z) + K'^{\infty}_{\mathrm{I}} f_y(x,z) \\ &- \frac{\sqrt{2}}{\pi^{3/2}} \int_{-\infty}^{x} dx' \int_{-\infty}^{+\infty} \frac{\sqrt{x-x'}}{(x-x')^2+(z-z')^2} \left[1 - \frac{2\nu}{2-\nu} \cdot \frac{(x-x')^2-(z-z')^2}{(x-x')^2+(z-z')^2}\right] \left[T_{xz}^{\infty} \frac{\partial f_y}{\partial x'}(x',z') + T_{zz}^{\infty} \frac{\partial f_y}{\partial z'}(x',z')\right] dz \\ &- \frac{\sqrt{2}}{\pi^{3/2}} \int_{-\infty}^{x} dx' \int_{-\infty}^{+\infty} \frac{\sqrt{x-x'}}{(x-x')^2+(z-z')^2} \left[\frac{2\nu}{2-\nu} \cdot \frac{2(x-x')(z-z')}{(x-x')^2+(z-z')^2}\right] \left[T_{xx}^{\infty} \frac{\partial f_y}{\partial x'}(x',z') + T_{xz}^{\infty} \frac{\partial f_y}{\partial z'}(x',z')\right] dz'\end{aligned} \tag{8.10}$$

Appendix 8.C Performances of the computational model

8.C.1 Software versus hardware acceleration

The acceleration procedure presented in Section 2.3.3 is a way to speed up the procedure by working on the software part of the computational method. Efforts have been made to speed up simulations through hardware-oriented methods. The C language, a low level one, has been chosen to make the simulations as fast as possible on a single core. Local (OpenMP) and distributed (MPI) CPU parallelisms have been investigated. In the case of OpenMP, it often appears to be more interesting to run n simulations on 1 core than 1 simulation on n cores even for $n = 2$, due to the small computational time required by a single simulation and the global number of simulations required for parametric studies. Distributed parallelism on MPI appears to be even more detrimental to computational performances. Indeed the computation time of a single step is small and data needs to be merged at the end of each step for the computation of the SIF perturbations, which involve the position of the whole crack front. The time required to exchange data between distributed stations slows down the computation dramatically. GPU parallelism on Cuda has also been investigated but the fact that points in different interaction states (Section 2.2.3.a) behave differently does not allow to take fully advantage of the GPU parallelism, where all cores need to execute the same algorithm to make the most of GPU specificities. We thus stick to monocore simulations in all studies presented in this manuscript. Individual simulations are launched in parallel thanks to GNU Parallel [Tange, 2011].

8.C.2 Algorithm complexity

8.C.2.a Problem statement

We finally conduct a study where we define the algorithmic complexity of our numerical method (computational time, computational step count) regarding the various convergence parameters.

Our numerical method contains four convergence parameters :

1. Δz, the spatial discretization of the crack front. It dictates the total number of crack front points N for a given system size L_z ;

2. $\Delta G_{\max}$, the loading increment during pinning configurations. This parameter also corresponds to the upper bound of the errors made on Griffith's criterion $G = G_{\mathrm{c}}$

during the pinning events. It ultimately controls the error made on the macroscopic loading required to make the crack propagate ;

3. $\Delta x_{\max}$, the maximum crack advance during a propagation step. Many variables are saved locally on a spatial grid. A finner $\Delta x_{\max}$ allows a better description of crack propagation. In contrast to previous numerical methods [Bower and Ortiz, 1990; Lazarus, 2003; Favier et al., 2006a; Vasoya et al., 2016a], it does not have any major impact on the numerical convergence of our simulations given that we adopted a time-based convergence criterion;

4. p_v corresponds to the threshold on crack velocity variations below which the propagation can be fastened considerably. It only plays a significant role in the case of very low inclusion density.

L_z/d	64
L_x/d	64
L_y/d	10
ρ_{inc}	0.25
σ_d/d	0

(a) Geometrical properties of the domain

Geometry	Spherical
ν	0.3
$G_c^{\text{inc}}/G_c^{\text{mat}}$	1.75
$\tilde{\sigma}$	0
$G_c^{\text{int}}/G_c^{\text{mat}}$	1

(b) Mechanical properties of the composite

v_m/v_0	10^{-4}
$\mathcal{L}/d$	10^3
G_0/G_c^{mat}	1

(c) Loading parameters

$\Delta z/d$	$[1/64, 1/32, \mathbf{1/16}, 1/8, 1/4]$
$\Delta x_{\max}/d$	$[1/100, 1/50, \mathbf{1/25}, 1/10, 1/5, 1/2]$
$\Delta G_{\max}/G_c^{\text{mat}}$	$[10^{-6}, 10^{-5}, 10^{-4}, \mathbf{10^{-3}}, 10^{-2}, 10^{-1}]$
p_v	$[10^{-6}, 10^{-4}, \mathbf{10^{-2}}, 10^{-1}]$

(d) Numerical parameters

Table 8.1: Numerical parameters used in the performance study.

We define a reference case where the numerical convergence parameters meet their lowest value :

$$\Delta z = \frac{1}{64}\, d;\ \Delta G_{\max} = 10^{-6}\, G_c^{\text{mat}};\ \Delta x_{\max} = \frac{1}{100}\, d;\ p_v = 10^{-6} \tag{8.11}$$

The following study consists in quantifying the impact of such parameters on three different indicators :

1. the overall simulation time Δt_{simu};

2. the precision on the macroscopic loading $\Delta G_{\text{error}} = \langle |G^{\infty}(x) - G^{\infty}_{\text{ref}}(x)| \rangle_x$ with regard to the reference configuration ;

3. the precision on crack trajectory $\Delta h_{\text{error}} \langle |h(z,x) - h_{\text{ref}}(z,x)| \rangle_x$, where h denotes the height profile of the resulting fracture surface.

8.C.2.b Overall performances

We thus compute the propagation of a crack interacting with a medium-scaled disordered distribution $L_z = L_x = 64\, d$ of tougher spherical inclusions $G_c^{\text{inc}} = 1.75\, G_c^{\text{mat}}$ and $G_c^{\text{int}} = G_c^{\text{mat}}$ for various convergence parameters. The simulation parameters are summarized in

Table 8.1

For each of the four convergence parameters considered, we make it vary, letting the other fixed (to the values in bold in Table 8.1). The numerical errors on the macroscopic loading ΔG_{error} and the crack trajectory Δh_{error} are estimated in comparison to the stricter case. The results are averaged on five different distributions. Final results are plotted in Fig. 8.1-Fig. 8.3. From those curves, we can establish that :

- $\Delta G_{\max}$ essentially controls the precision of the algorithm as depicted in Fig. 8.1. It effectively ensures a precision at the order of $\Delta G_{\max}$ on the macroscopic loading. The macroscopic loading impact local SIF, which controls the crack trajectory through the GMERR criterion. Thus it is normal that such parameter also gives us a better precision on the height profiles of the crack surface. Yet the lower it gets, the longer the simulations become : the pinned configurations are not accelerated enough and a lot of time is lost thereby ;
- the spatial discretization Δz is the second most important parameter on the macroscopic indicators ΔG_{error} and Δh_{error}. As depicted in Fig. 8.2, the finer the mesh, the better the precision since more points of the crack front contribute to the interaction with the inclusions and the pinned configurations are better modeled ;
- the maximal advance criterion $\Delta x_{\max}$ can bring better simulations results at a small computational cost but have little impact on the convergence of our algorithm (Fig. 8.3) ;
- results for p_v are not plotted since it has a very small impact on numerical precision even if it allows significant computation acceleration in very restricted cases.

Finally, we can extract from those results the impact of various parameters on the duration of our simulations as :

$$\Delta t_{\text{simu}} \propto \Delta z^{-2} \Delta G_{\max}^{-0.8} \Delta x_{\max}^{-0.5} \tag{8.12}$$

The final procedure is at the end in $O\left(N^2\right)$ and not $O\left(N\ln(N)\right)$ as allowed by the FFT algorithm. It is explained by the fact that the number of points does increase the computation time of each step in $O\left(N\ln(N)\right)$. It also increases in $O\left(N\right)$ the total number of steps computed for a simulation since the time step Δt_{conv} depends on Δz (Eq. (2.29)). It results in a complexity in $O\left(N^2\ln(N)\right)$. The $\ln(N)$ dependence cannot be highlighted on such small variations of N.

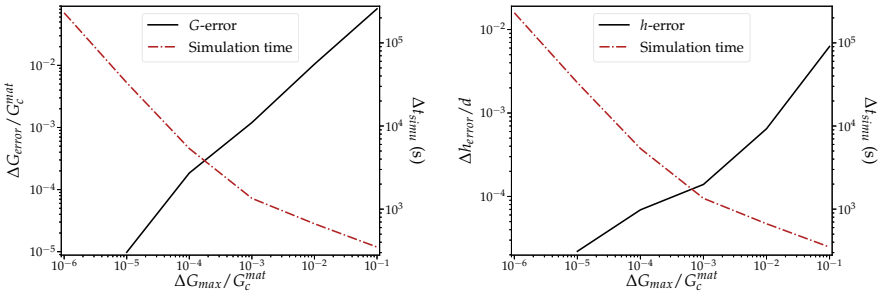

(a) Loading errors (b) Height errors

Figure 8.1: Impact of the loading increment parameter $\Delta G_{\max}$ on numerical precision on the macroscopic loading (a) or fracture surface (b) and the simulation time Δt_{simu}

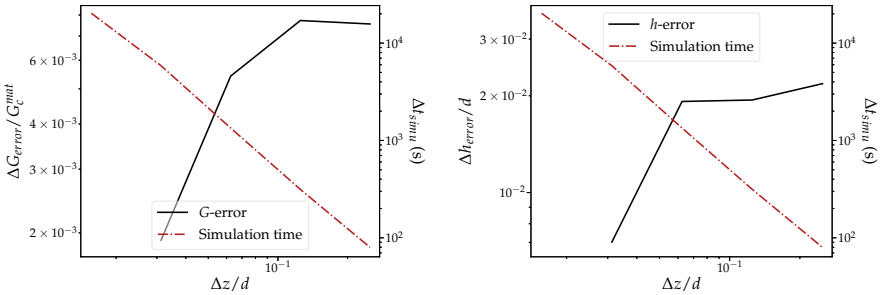

(a) Loading errors (b) Height errors

Figure 8.2: Impact of the spatial step Δz on numerical precision on the macroscopic loading (a) or fracture surface (b) and the simulation time Δt_{simu}

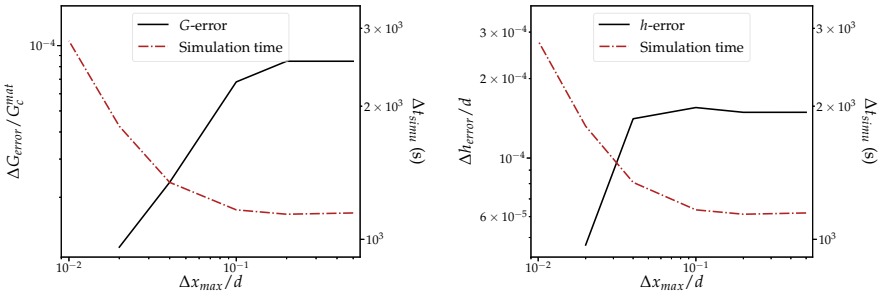

(a) Loading errors (b) Height errors

Figure 8.3: Impact of the maximal advance parameter $\Delta x_{\max}$ on numerical precision on the macroscopic loading (a) or fracture surface (b) and the simulation time Δt_{simu}

Appendix 8.D Homogenization of brittle fracture properties : towards a non-dilute scheme for the out-of-plane interactions.

8.D.1 How does the interaction of a crack with an inclusion impact consecutive interactions ?

During a by-pass event, the crack front deforms out of the mean crack plane. When the crack leaves the interface and goes back in the matrix, the out-of-plane perturbation is relaxed toward a flat configuration due to the long-range elastic interactions of Eq. (2.14). However, the crack may land on an inclusion before this relaxation phase is over. It then lands on this inclusion with a non-zero angle θ_{ini}. Moreover, when pinned by an inclusion, the crack front cannot adapt to local variations of Mode II contributions δK_{II} resulting from the out-of-place excursions of other regions of the crack front. It may thus be loaded under a mixed Mode I+II. Those perturbations can change the nature of the interaction mechanism selected by the crack.

Impact of the initial angle on crack-inclusion interaction

The impact of landing with an initial angle θ_{ini} on the inclusion on the crossing to by-pass transition can be analyzed within the two-dimensional framework developed in Section 3.3.1.a. Consider again the two-dimensional case where a crack is landing on a cylindrical inclusion invariant along the front direction (Oz). The crack lands with an initial angle θ_{ini} on the inclusion at a height y_{landing}, imposing an angle $\theta_{\tan}$ for the by-pass direction. Since it is initially propagating in the homogeneous matrix, its out-of-plane relaxation follows the principle of local symmetry so that the mode mixity ratio is null, $\rho_{\text{II}} = K_{\text{II}}/K_{\text{I}} = 0$.

We consider the situation where a crack lands with an angle $\theta_{\text{ini}} = \frac{\pi}{18}$ $(10°)$ at a height $y_{\text{landing}}/d = -0.3$ on a inclusion of toughness $G_{inc}/G_{\text{c}}^{\text{mat}} = 1.8$. We see in Fig. 8.4 that the initial angle increases the kink the crack has to make to by-pass the inclusion downwards. The ERR the crack can develop in the tangent direction $G\left(\theta_{\tan}\right)$ is thus reduced (Fig. 8.4.a). It can lead the crack to cross the inclusion where it would have by-passed it otherwise (Fig. 8.4.c).

If the crack had landed on the upper part of the inclusion, a positive landing angle θ_{ini} would have decreased the kink required to by-pass the inclusion and thus favor the by-pass mechanism over inclusion crossing. The impact of the initial angle can be rationalized from Eq. (3.26) and translated in a new interaction diagram, plotted in Fig. 8.5. Landing on an inclusion with an angle can thus modify the crack-inclusion interaction mechanism by reducing/increasing the kink angle the crack has to make to by-pass the inclusion and thus favors/penalizes the related interaction mode.

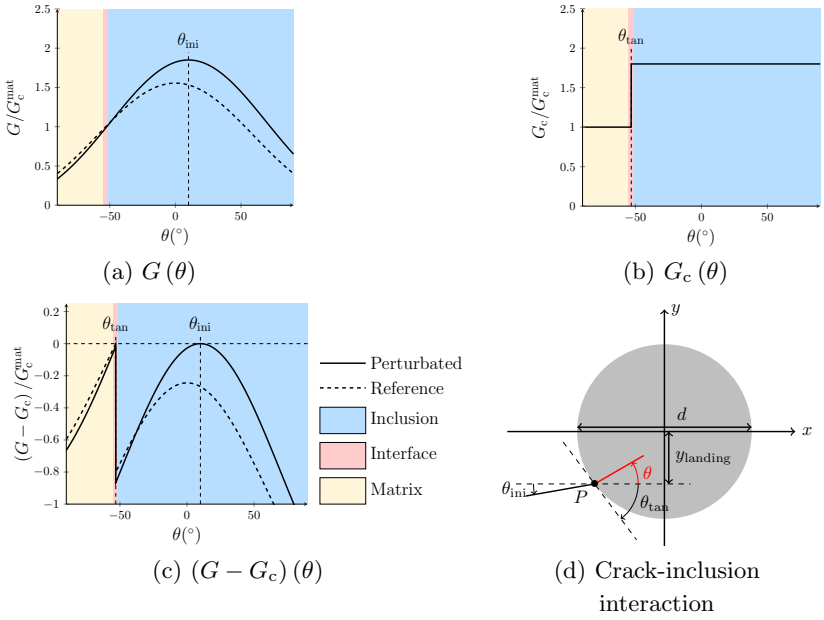

(a) $G(\theta)$ (b) $G_c(\theta)$

(c) $(G - G_c)(\theta)$ (d) Crack-inclusion interaction

Figure 8.4: Generalized Maximum Energy Release Rate criterion for a non-zero initial angle : angle distribution of G (a), G_c (b) and $(G - G_c)$ (c) for a crack landing with an angle $\theta_{ini} = \frac{\pi}{18}$ (10°) at a height $y_{landing}/d = -0.3$ on a inclusion of toughness $G_{inc}/G_c^{mat} = 1.8$ (d) at the onset of depinning

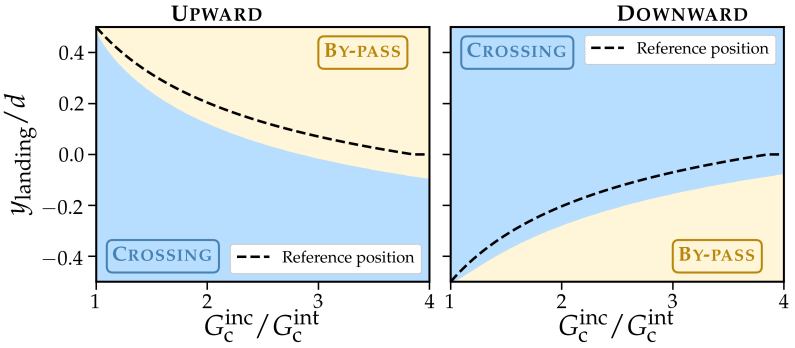

Figure 8.5: Two-dimensional analysis of the impact of an initial angle θ_{ini} on the by-pass to crossing transition: the crack lands a height $y_{landing}$ with an angle $\theta_{ini} = \frac{\pi}{18}$ on a cylindrical inclusion characterized by the toughness ratio G_c^{inc}/G_c^{int}. The reference transition limit for a zero angle is plotted from Fig. 3.16 in black dashed line.

Impact of the long-range interactions on crack-inclusion interaction

We saw in Section 3.4.1 that a local Mode I+II mixity triggered by long-range elastic interactions (see Eq. (2.14)) can also change the way the crack interacts with an inclusion. A positive mode mixity ratio $\rho_{II} = K_{II}/K_I$ will favor inclusion crossing over inclusion by-pass if the crack lands on the upper part of the spherical inclusion and promote inclusion by-pass over inclusion crossing if the crack lands on the lower part of the inclusion. As before, the impact of the long-rate interactions on the crossing to by-pass transition can be taken into account through Eq. (3.26).

The relative impact of those mechanisms in our simulations : the bi-inclusion case

Both mechanisms (non-zero initial angle and local mode mixity triggered by long-range elastic interactions) are likely to occur when a crack interacts with a disordered distribution of inclusions. The question is to know how often such perturbations are likely to affect the crossing to by-pass transition. To address this problem, we consider the bi-inclusion problem, where two spherical inclusions of diameter d are located nearby. We explore how the interaction of the crack with the first inclusion modifies the interaction mechanism triggered on the second one. If the first inclusion is crossed, it does not modify the landing angle on the second inclusion or the long-range perturbations in Mode II. We thus consider the case where the first inclusion is by-passed. To trigger as many interactions as possible, we assume that the crack lands on the equatorial plane of the first inclusion, giving rise to large out-of-plane perturbations

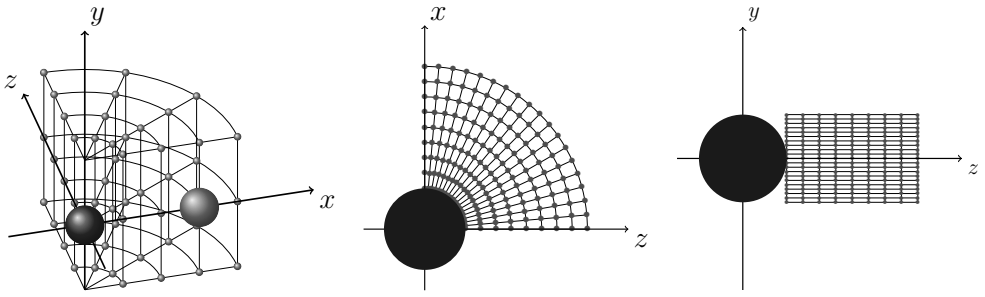

(a) 3D view (b) $(x0z)$ plane (c) $(y0z)$ plane

Figure 8.6: Array of position for the second inclusion (light grey) in the vicinity of the first one (dark grey) : three-dimensional simplified representation (a) and real discretization in the $(x0z)$ plane (b) and $(y0z)$ plane (c)

We place the second particle in the vicinity of the first one, at most at a distance $2\,d$ as depicted in Fig. 8.6. We choose a coarse radial disposition of the second inclusion in the $(x0z)$ plane and a much finer disposition in the y-direction, since the landing height is a decisive parameter for crack-inclusion interaction (see Section 3.3.1). Finally, for each second inclusion position, we vary the inclusion toughness from $G_{\mathrm{c}}^{\mathrm{inc}} = G_{\mathrm{c}}^{\mathrm{mat}}$ to $G_{\mathrm{c}}^{\mathrm{inc}} = 3\,G_{\mathrm{c}}^{\mathrm{mat}}$. We end up with 75,241 possible configurations, which are computed within a day thanks to the computational performances offered by the perturbative approach. Simulation parameters are summarized in Table 8.14.

From those simulations, we extract the geometrical configuration (x, y, z, θ) and the local loading $(K_{\mathrm{I}}, K_{\mathrm{II}})$ at each point of the crack front interacting with the second inclusion. We predict analytically from Eq. (3.26) the interaction mechanism that would have been selected instead in the absence of a neighboring inclusion. We compare these theoretical predictions to the mechanism actually observed in numerical simulations. Fig. 8.7 shows the positions of the second particle that have been significantly impacted by the by-pass of the first one. We conclude from Fig. 8.7 that the interaction between inclusions is limited and very local : if two inclusions are positioned far away, their interaction with the crack

can be considered independent of each other. However, the landing angle θ_{ini} seems to play a dominant role on crack-inclusion interaction and has thus to be considered in the homogenization framework.

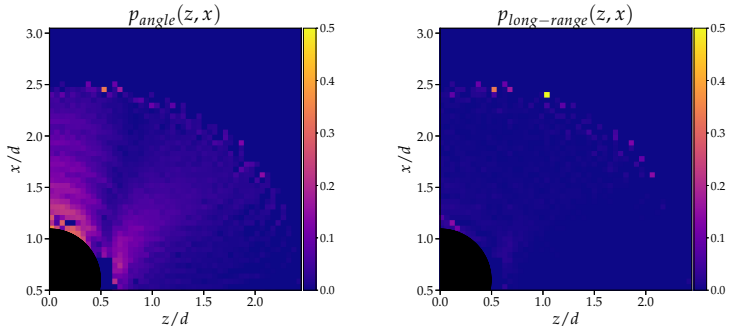

(a) Angle (b) Long-range perturbations

Figure 8.7: Impact of a non-zero initial angle θ_{ini} (a) and mode mixity (b) triggered by the by-pass of the first inclusion on the interaction mechanism happening on second one. The colormap represents the probability of interaction shift (crossing to by-pass or by-pass to crossing) at a given position. Abnormally high values located far away from the first inclusion can be attributed to lack of statistics.

8.D.2 Incorporation of the interaction angle in the model

In the proposed non-dilute model, the crack is allowed to land on the inclusion with a non-zero angle θ_{ini}. The probability density function for a realization $\omega_{\text{F}} \in \Omega_{\text{F}}$ thus reads :

$$p_{\text{FRVE}}\left(\omega_{\text{F}}\right) = p_y\left(y\right) \cdot p_\theta\left(\theta_{\text{ini}}\right) \cdot p_d\left(d_{\text{inc}}\right) \cdot p_{\text{inc}}\left(G_{\text{c}}^{\text{inc}}\right) \cdot p_{\text{int}}\left(G_{\text{c}}^{\text{int}}\right) \tag{8.13}$$

where p_θ is the probability density function associated with the landing angle θ_{ini}. The impact of θ_{ini} on the interaction mechanism is well understood from Eq. (3.26) so that the main challenge of the non-dilute model consists in estimating the probability density function p_θ.

A theoretical model for the relaxation of a perturbation in a homogeneous phase

To take up this challenge, we first have to understand the relaxation dynamics of the crack front after a by-pass event. We consider the theoretical problem where the crack front is only perturbed out-of-plane, so that $f_x\left(z, t=0\right) = 0$ and $f_y\left(z, t=0\right) = h_0\left(z\right)$. It is propagating in a homogeneous phase, namely the matrix.

Under the hypothesis where crack angle $\theta = \arctan\left(\frac{\partial f_y}{\partial x}\right)$ remains small during crack propagation, Mode II perturbed SIF writes as in Eq. (2.14). These Mode II contribution being small in regards to Mode I, the Generalized Maximum Energy Release Rate (GMERR) criterion reads at first order :

$$\frac{\partial f_y}{\partial x}\left(z,t\right) \sim \theta\left(z,t\right) = -2\frac{K_{\text{II}}\left(z,t\right)}{K_{\text{I}}\left(z,t\right)} = -2\frac{\delta K_{\text{II}}\left(z,t\right)}{K_{\text{I}}^{\infty}\left(t\right) + \delta K_{\text{I}}\left(z,t\right)} = -2\frac{\delta K_{\text{II}}}{K_{\text{I}}^{\infty}}\left(z,t\right) \tag{8.14}$$

Under the small-angle assumption $\theta \ll 1$, the out-of-plane perturbation contributions in

G are second-order terms. The in-plane perturbation evolution then reads Eq. (3.2) :

$$\frac{1}{v_0}\frac{\partial f_x}{\partial t}(z,t) = \frac{v_\mathrm{m}}{v_0} + \frac{G^\infty}{G_\mathrm{c}^\mathrm{mat}}\left(1 - \frac{f_x(z,t)}{\mathcal{L}} - \frac{1}{\pi}\,\mathrm{PV}\int_{-\infty}^{+\infty}\frac{f_x(z,t) - f_x(z',t)}{(z-z')^2}\,dz'\right) - 1 \quad (8.15)$$

If we suppose that $\mathcal{L} \to +\infty$, given that $f_x(z,0) = 0$, we get :

$$f_x(z,t) = \left[v_\mathrm{m} + v_0\left(\frac{G^\infty}{G_\mathrm{c}^\mathrm{mat}} - 1\right)\right] t \quad (8.16)$$

In that case, the time t can be replaced by the position x and the out-of-plane perturbation $f_y(z,t)$ becomes the height profile of the fracture surface $h(z,x)$. The out-of-plane relaxation equation finally reads :

$$\frac{\partial h}{\partial x}(z,x) = -\frac{A(\nu)}{\pi}\,\mathrm{PV}\int_{-\infty}^{+\infty}\frac{h(z,x) - h(z',x)}{(z-z')^2}\,dz' \quad (8.17)$$

where $A(\nu) = \dfrac{2-3\nu}{2-\nu}$ is varying between $\frac{1}{3}$ and 1.

In order to model out-of-plane relaxation from a by-pass event, we consider that the crack is initially perturbed out-of-plane by a box-car function perturbation characterized by its width d in the z-direction and its height Δh in the y-direction as illustrated in Fig. 8.8.a. We thus have :

$$h(z,0) = \Delta h\mathcal{H}(z) \quad (8.18)$$

where $\mathcal{H}$ is the indicator function of the interval $\left[-\frac{D}{2}, \frac{D}{2}\right]$.

By working in the Fourier space and using Gradshteyn and Ryzhik [2014] formula (3.893.1) to come back in the real space, one gets :

$$\frac{\partial h}{\partial x}(z,x) = -\frac{A(\nu)\,\Delta h}{\pi}\left[\frac{D/2+z}{(A(\nu)\,x)^2 + (D/2+z)^2} - \frac{-D/2+z}{(A(\nu)\,x)^2 + (-D/2+z)^2}\right] \quad (8.19)$$

Or alternatively :

$$h(z,x) = \Delta h\mathcal{H}(z) - \frac{\Delta h}{\pi}\left[\arctan\left(\frac{A(\nu)\,x}{D/2+z}\right) - \arctan\left(\frac{A(\nu)\,x}{-D/2+z}\right)\right] \quad (8.20)$$

Such relaxation is plotted in Fig. 8.8.b.

Theoretical estimations of the landing angle probability density function

This simple model allows us to estimate the probability density function p_θ associated with the landing angle θ_ini from the following procedure :

1. for each FRVE $\omega_\mathrm{F} \in \Omega_\mathrm{F}$, we can predict under the dilute hypothesis if the inclusion of diameter d is crossed or by-passed for a given landing height y. If the inclusion is by-passed, the crack front it deformed out-of-plane. The out-of-plane perturbation can be approximated as a box-car function of width $D\sqrt{1 - \left(\frac{y}{d}\right)^2}$ and height $\Delta h = \frac{d}{2} - y$. The angle spatial distribution $\theta(z,x) = \arctan\left(\frac{\partial h}{\partial x}(z,x)\right)$ during the subsequent relaxation can be inferred from Eq. (8.19). If the inclusion is crossed, $\theta(z,x) = 0$;

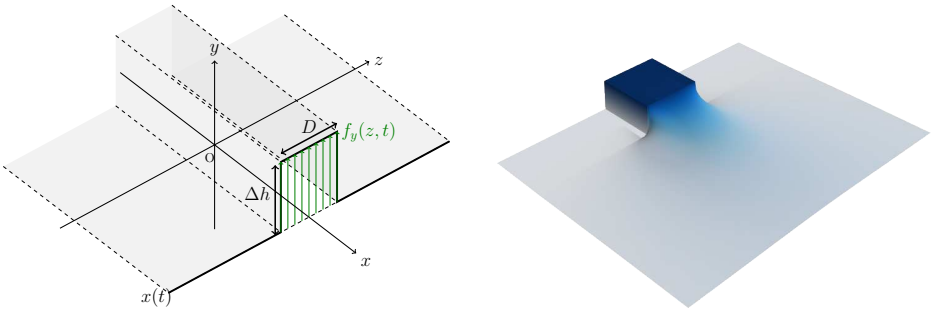

(a) (b)

Figure 8.8: Out-of-plane box-car perturbation of height Δh and size D (a) and its relaxation (b)

2. the bi-inclusion study makes us understand that an inclusion has to be placed in the vicinity of a by-passed defect to trigger a shift in the interaction mechanism happening on this inclusion. Thus we can assume that the angle at which the crack impacts the inclusion is caused by the relaxation from the by-pass of the nearest neighbor inclusion. We assume that the point 1 from which the crack leaves the first inclusion to relax in the matrix and the point 2 on which the crack lands on the second inclusion with an angle both follow a Poisson planar distribution. Then the probability $p_{1\to 2}\left(\Delta z, \Delta x\right)$ that those two points are separated by a distance Δz in the z-direction and Δx in the x-direction reads [Torquato, 2002] :

$$p_{1\to 2}\left(\Delta z, \Delta x\right) = 2\pi\rho_{\text{inc}}\sqrt{\Delta z^2 + \Delta x^2}\exp\left[-\pi\rho_{\text{inc}}\left(\Delta z^2 + \Delta x^2\right)\right] \tag{8.21}$$

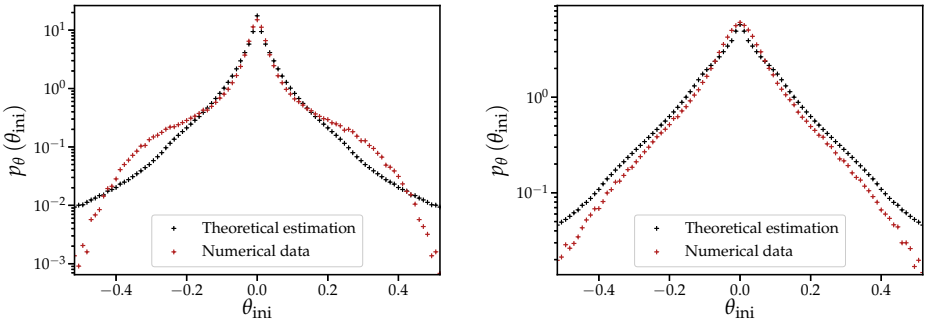

(a) $G_{\text{c}}^{\text{inc}} = 2\,G_{\text{c}}^{\text{mat}}$ (b) $G_{\text{c}}^{\text{inc}} = 4\,G_{\text{c}}^{\text{mat}}$

Figure 8.9: Probability density function of landing angles $p_\theta\left(\theta_{\text{ini}}\right)$ for the interaction between a crack and an inclusion distribution of density $\rho_{\text{inc}} = 25\%$ and toughness $G_{\text{c}}^{\text{inc}} = 2\,G_{\text{c}}^{\text{mat}}$ (a) and $G_{\text{c}}^{\text{inc}} = 4\,G_{\text{c}}^{\text{mat}}$ (b). The angle at which points of the crack front land on a inclusion are recorded during numerical simulation (in red cross markers) and compared to the probability density function reconstructed analytically (in black cross markers).

The superposition of the angle spatial distribution $\theta\left(z, x\right)$ for each FRVE $\omega_{\text{F}} \in \Omega_{\text{F}}$, with the associated weight function $p_{1\to 2}\left(z, x\right)$ allows to construct numerically the probability density function of landing angles $p_\theta\left(\theta_{\text{ini}}\right)$ required by the non-dilute model. Examples

of constructed $p_\theta(\theta_{\text{ini}})$ are given in Fig. 8.9 and compared to probability density function of landing angles extracted from numerical simulations. We see that the comparison between the theoretical and the numerical estimation of the probability density function p_θ is satisfactory despite the crudeness of the analytical model.

The homogenization procedure is now conducted considering FRVEs with a crack landing with an angle θ_{ini} on the inclusion. The interaction mechanism is inferred from Eq. (3.26). The CRVE is then constructed as in Section 4.4.3. $\langle G_{\text{c}} \rangle$, $\sigma(G_{\text{c}})$, ξ_z, ξ_x are estimated from the non-dilute probability density function p_{FRVE} of Eq. (8.13) under the *ergodic assumption*. They are finally injected in Eq. (4.31) to predict the effective toughness of large-scale disordered systems from Section 4.3.2 under a non-dilute hypothesis.

Appendix 8.E Numerical parameters used in crack propagation simulations

8.E.1 Chapter 3

L_x/d	$[2, 4, 8, 16, 32]$
L_x/d	4

(a) Geometrical properties of the domain

$G_c^{\text{inc}}/G_c^{\text{mat}}$	$[1 : 0.1 : 4]$

(b) Mechanical properties of the composite

v_m/v_0	10^{-8}
$\mathcal{L}/d$	10^6
G_0/G_c^{mat}	1

(c) Loading parameters

$\Delta z/d$	1/32
$\Delta x_{\max}/d$	1/25
$\Delta G_{\max}/G_c^{\text{mat}}$	10^{-4}

(d) Numerical parameters

Table 8.2: Parameters used in Section 3.2.2 for the determination of the effective toughness of periodic arrangements of circular/square/elliptic inclusions with varying parameters in beige

L_z/d	4
L_x/d	4
L_y/d	4

(a) Geometrical properties of the domain

ν	0.3
$G_c^{\text{inc}}/G_c^{\text{mat}}$	$[1 : 0.1 : 4]$
$G_c^{\text{inc}}/G_c^{\text{mat}}$	1
y_{landing}/d	$[0 : 0.0125 : 0.5]$

(b) Mechanical properties of the composite

v_m/v_0	10^{-8}
$\mathcal{L}/d$	10^6
G_0/G_c^{mat}	1

(c) Loading parameters

$\Delta z/d$	1/32
$\Delta x_{\max}/d$	1/25
$\Delta G_{\max}/G_c^{\text{mat}}$	$\min\left(10^{-2}c_{inc}, 10^{-3}\right)$

(d) Numerical parameters

Table 8.3: Parameters used in Section 3.3 for the interaction of a crack with periodic arrangements of spherical inclusions with varying parameters in beige

L_z/d	4
L_x/d	4
L_y/d	4
d_z/d_x	$\}1, 2, 4\}$

(a) Geometrical properties of the domain

ν	0.3
$G_c^{\text{inc}}/G_c^{\text{mat}}$	$[1 : 0.1 : 4]$
$G_c^{\text{inc}}/G_c^{\text{mat}}$	1
y_{landing}/d	$[0 : 0.0125 : 0.5]$

(b) Mechanical properties of the composite

v_m/v_0	10^{-8}
$\mathcal{L}/d$	10^6
G_0/G_c^{mat}	1

(c) Loading parameters

$\Delta z/d$	1/64
$\Delta x_{\max}/d$	1/25
$\Delta G_{\max}/G_c^{\text{mat}}$	$\min\left(10^{-2}c_{inc}, 10^{-3}\right)$

(d) Numerical parameters

Table 8.4: Parameters used in Section 3.4 for the interaction of a crack with periodic arrangements of ellipsoidal inclusions with varying parameters in beige

L_z/d	4
L_x/d	4
L_y/d	4

(a) Geometrical properties of the domain

ν	0.3
$G_c^{\text{inc}}/G_c^{\text{mat}}$	$[1 : 0.025 : 4]$
$G_c^{\text{inc}}/G_c^{\text{mat}}$	1
β_{inc}	$\left[0 : \frac{\pi}{18} : \frac{\pi}{2}\right]$
$y_{\text{landing}}/h_{\text{up}}$	$[0 : 0.1 : 1]$

(b) Mechanical properties of the composite

v_m/v_0	10^{-8}
$\mathcal{L}/d$	10^6
G_0/G_c^{mat}	1

(c) Loading parameters

$\Delta z/d$	1/64
$\Delta x_{\max}/d$	1/25
$\Delta G_{\max}/G_c^{\text{mat}}$	$\min\left(10^{-2}c_{inc}, 10^{-3}\right)$

(d) Numerical parameters

Table 8.5: Parameters used in Section 3.5 for the interaction of a crack with periodic arrangements of cubical inclusions with varying parameters in beige

L_z/d	4
L_x/d	4
L_y/d	4

(a) Geometrical properties of the domain

ν	0.3
$G_c^{\text{inc}}/G_c^{\text{mat}}$	$[1 : 0.05 : 4]$
$G_c^{\text{inc}}/G_c^{\text{mat}}$	$[0.6 : 0.1 : 1]$
y_{landing}/d	$[0 : 0.05 : 0.5]$

(b) Mechanical properties of the composite

v_m/v_0	10^{-8}
$\mathcal{L}/d$	10^6
G_0/G_c^{mat}	1

(c) Loading parameters

$\Delta z/d$	1/64
$\Delta x_{\max}/d$	1/25
$\Delta G_{\max}/G_c^{\text{mat}}$	$\min\left(10^{-2}c_{inc}, 10^{-3}\right)$

(d) Numerical parameters

Table 8.6: Parameters used in Section 3.7 for the interaction of a crack with periodic arrangements of spherical inclusions with varying parameters in beige

8.E.2 Chapter 4

L_z/d	256
L_x/d	256
ρ_{inc}	0.25

(a) Geometrical properties of the domain

Geometry	Circular
$G_c^{\text{inc}}/G_c^{\text{mat}}$	$[1, 4]$
$\tilde{\sigma}$	0

(b) Properties of the composite

v_m/v_0	10^{-8}
$\mathcal{L}/d$	10^6
G_0/G_c^{mat}	1

(c) Loading parameters

$\Delta z/d$	$\left[\frac{1}{32}, \frac{1}{8}\right]$
$\Delta x_{\max}/d$	1/50
$\Delta G_{\max}/G_c^{\text{mat}}$	$\min\left(10^{-2}c_{inc}, 10^{-3}\right)$

(d) Numerical parameters

Table 8.7: Parameters used in Section 4.2.2.a to study the impact of the inclusion toughness G_c^{inc} and mesh size Δz on the effective toughness for coplanar propagation.

L_z/d	$[8, 4096]$
L_x/d	384
ρ_{inc}	0.25

(a) Geometrical properties of the domain

Geometry	Circular
$G_c^{\text{inc}}/G_c^{\text{mat}}$	1.5
$\tilde{\sigma}$	0

(b) Properties of the composite

v_m/v_0	10^{-8}
$\mathcal{L}/d$	10^6
G_0/G_c^{mat}	1

(c) Loading parameters

$\Delta z/d$	1/16
$\Delta x_{\max}/d$	1/50
$\Delta G_{\max}/G_c^{\text{mat}}$	$\min\left(10^{-2}c_{inc}, 10^{-3}\right)$

(d) Numerical parameters

Table 8.8: Parameters used in Section 4.2.2.a to study the impact of the system size L_z on the effective toughness for coplanar propagation.

L_z/d	256
L_x/d	256
ρ_{inc}	$[0.1, 0.4]$

(a) Geometrical properties of the domain

Geometry	Circular or squared
$G_c^{\text{inc}}/G_c^{\text{mat}}$	$[1, 4]$
$\tilde{\sigma}$	0

(b) Properties of the composite

v_m/v_0	10^{-8}
$\mathcal{L}/d$	10^6
G_0/G_c^{mat}	1

(c) Loading parameters

$\Delta z/d$	1/16
$\Delta x_{\max}/d$	1/50
$\Delta G_{\max}/G_c^{\text{mat}}$	$\min\left(10^{-2}c_{inc}, 10^{-3}\right)$

(d) Numerical parameters

Table 8.9: Parameters used in Section 4.2.2.a to study the impact of the inclusion density ρ_{inc} on the effective toughness for coplanar propagation.

L_z/d	256
L_x/d	256
ρ_{inc}	0.25

(a) Geometrical properties of the domain

Geometry	Circular
$G_c^{\text{inc}}/G_c^{\text{mat}}$	$[1, 4]$
$\tilde{\sigma}$	$[0, 5]$

(b) Properties of the composite

v_m/v_0	10^{-8}
$\mathcal{L}/d$	10^6
G_0/G_c^{mat}	1

(c) Loading parameters

$\Delta z/d$	1/16
$\Delta x_{\max}/d$	1/50
$\Delta G_{\max}/G_c^{\text{mat}}$	$\min\left(10^{-2}c_{inc}, 10^{-3}\right)$

(d) Numerical parameters

Table 8.10: Parameters used in Section 4.2.2.a to study the impact of the contrast disorder $\tilde{\sigma}$ on the effective toughness for coplanar propagation.

L_z/d	256
L_x/d	256
ρ_{inc}	0.25

(a) Geometrical properties of the domain

Geometry	Elliptic
$G_c^{\text{inc}}/G_c^{\text{mat}}$	$[1, 4]$
d_z/d_x	$\|brace1, 2, 4, 8\}$

(b) Properties of the composite

v_m/v_0	10^{-8}
$\mathcal{L}/d$	10^6
G_0/G_c^{mat}	1

(c) Loading parameters

$\Delta z/d$	1/16
$\Delta x_{\max}/d$	1/50
$\Delta G_{\max}/G_c^{\text{mat}}$	$\min\left(10^{-2}c_{inc}, 10^{-3}\right)$

(d) Numerical parameters

Table 8.11: Parameters used in Section 4.2.2.a to study the impact of the inclusion elongation d_z/d_x on the effective toughness for coplanar propagation.

L_z/d	256
L_x/d	288
L_y/d	16
ρ_{inc}	0.25
σ_d/d	0

(a) Geometrical properties of the domain

Geometry	Spherical
ν	0.3
$G_c^{\text{inc}}/G_c^{\text{mat}}$	$\{1.5, 2, 3\}$
$\tilde{\sigma}$	0
$G_c^{\text{int}}/G_c^{\text{mat}}$	1

(b) Mechanical properties of the composite

v_m/v_0	10^{-8}
$\mathcal{L}/d$	$\left[10^{-1} : 10^6\right]$
G_0/G_c^{mat}	1

(c) Loading parameters

$\Delta z/d$	1/16
$\Delta x_{\max}/d$	1/25
$\Delta G_{\max}/G_c^{\text{mat}}$	$\min\left(10^{-2}c_{inc}, 10^{-3}\right)$

(d) Numerical parameters

Table 8.12: Parameters used in Section 4.3.1 to study the impact of the structural length $\mathcal{L}$ on the effective toughness.

L_z/d	256
L_x/d	288
L_y/d	16
ρ_{inc}	0.25
σ_d/d	0

(a) Geometrical properties of the domain

Geometry	Spherical
ν	0.3
$G_c^{\text{inc}}/G_c^{\text{mat}}$	$[1, 4.5]$
$\tilde{\sigma}$	0
$G_c^{\text{int}}/G_c^{\text{mat}}$	1

(b) Mechanical properties of the composite

v_m/v_0	10^{-8}
$\mathcal{L}/d$	10^6
G_0/G_c^{mat}	1

(c) Loading parameters

$\Delta z/d$	$[\frac{1}{32}, \frac{1}{8}]$
$\Delta x_{\max}/d$	1/25
$\Delta G_{\max}/G_c^{\text{mat}}$	$\min\left(10^{-2}c_{inc}, 10^{-3}\right)$

(d) Numerical parameters

Table 8.13: Parameters used in Section 4.3.2 to study the impact of the inclusion toughness G_c^{inc} and mesh size Δz on the effective toughness

ν	0.3
$G_c^{\text{inc}}/G_c^{\text{mat}}$	4
$G_c^{\text{inc}}/G_c^{\text{mat}}$	1
z/d	0
x/d	0.6
y/d	0

(a) Properties of the first inclusion

ν	0.3
$G_c^{\text{inc}}/G_c^{\text{mat}}$	$[1 : 0.05 : 3]$
$G_c^{\text{inc}}/G_c^{\text{mat}}$	1
z/d	$[0.5, 2.5]$
x/d	$[0.5, 2.5]$
z/d	$[-0.5, 0.5]$

(b) Properties of the second inclusion

L_z/d	8
L_x/d	4
L_y/d	8

(c) Geometrical properties of the domain

v_m/v_0	10^{-8}
$\mathcal{L}/d$	10^6
G_0/G_c^{mat}	1

(d) Loading parameters

$\Delta z/d$	1/32
$\Delta x_{\max}/d$	1/25
$\Delta G_{\max}/G_c^{\text{mat}}$	10^{-3}

(e) Numerical parameters

Table 8.14: Parameters used in Section 8.D.1 for the simulations of the bi-inclusion problem with varying parameters in beige

L_z/d	$[16, 512]$
L_x/d	588
L_y/d	16
ρ_{inc}	0.25
σ_d/d	0

(a) Geometrical properties of the domain

Geometry	Spherical
ν	0.3
$G_c^{\text{inc}}/G_c^{\text{mat}}$	$\{1.5, 2, 3\}$
$\tilde{\sigma}$	0
$G_c^{\text{int}}/G_c^{\text{mat}}$	1

(b) Mechanical properties of the composite

v_m/v_0	10^{-8}
$\mathcal{L}/d$	10^6
G_0/G_c^{mat}	1

(c) Loading parameters

$\Delta z/d$	1/16
$\Delta x_{\max}/d$	1/25
$\Delta G_{\max}/G_c^{\text{mat}}$	$\min\left(10^{-2}c_{inc}, 10^{-3}\right)$

(d) Numerical parameters

Table 8.15: Parameters used in Section 4.5.1 to study the impact of the system size L_z on the effective toughness

L_z/d	256
L_x/d	288
L_y/d	16
ρ_{inc}	$[0.1, 0.5]$
σ_d/d	0

(a) Geometrical properties of the domain

Geometry	Spherical
ν	0.3
$G_c^{\text{inc}}/G_c^{\text{mat}}$	$[1, 4.5]$
$\tilde{\sigma}$	0
$G_c^{\text{int}}/G_c^{\text{mat}}$	1

(b) Mechanical properties of the composite

v_m/v_0	10^{-8}
$\mathcal{L}/d$	10^6
G_0/G_c^{mat}	1

(c) Loading parameters

$\Delta z/d$	1/16
$\Delta x_{\max}/d$	1/25
$\Delta G_{\max}/G_c^{\text{mat}}$	$\min\left(10^{-2}c_{inc}, 10^{-3}\right)$

(d) Numerical parameters

Table 8.16: Parameters used in Section 4.5.2 to study the impact of the inclusion density ρ_{inc} on the effective toughness

L_z/d	256
L_x/d	288
L_y/d	16
ρ_{inc}	0.25
σ_d/d	0

(a) Geometrical properties of the domain

Geometry	Spherical
ν	0.3
$G_c^{\text{inc}}/G_c^{\text{mat}}$	$[1, 4.5]$
$\tilde{\sigma}$	$[0, 5]$
$G_c^{\text{int}}/G_c^{\text{mat}}$	1

(b) Mechanical properties of the composite

v_m/v_0	10^{-8}
$\mathcal{L}/d$	10^6
G_0/G_c^{mat}	1

(c) Loading parameters

$\Delta z/d$	1/16
$\Delta x_{\max}/d$	1/25
$\Delta G_{\max}/G_c^{\text{mat}}$	$\min\left(10^{-2}c_{inc}, 10^{-3}\right)$

(d) Numerical parameters

Table 8.17: Parameters used in Section 4.5.3 to study the impact of the contrast disorder $\tilde{\sigma}$ on the effective toughness

L_z/d	256
L_x/d	288
L_y/d	16
ρ_{inc}	0.25
σ_d/d	0

(a) Geometrical properties of the domain

Geometry	Spherical
ν	0.3
$G_c^{\text{inc}}/G_c^{\text{mat}}$	$[1, 4.5]$
$\tilde{\sigma}$	0
$G_c^{\text{int}}/G_c^{\text{mat}}$	$[0.6, 1]$

(b) Mechanical properties of the composite

v_m/v_0	10^{-8}
$\mathcal{L}/d$	10^6
G_0/G_c^{mat}	1

(c) Loading parameters

$\Delta z/d$	1/16
$\Delta x_{\max}/d$	1/25
$\Delta G_{\max}/G_c^{\text{mat}}$	$\min\left(10^{-2}c_{inc}, 10^{-3}\right)$

(d) Numerical parameters

Table 8.18: Parameters used in Section 4.5.4 to study the impact of the interface toughness $G_{\text{c}}^{\text{int}}$ on the effective toughness

L_z/d	256
L_x/d	288
L_y/d	16
ρ_{inc}	0.25
σ_d/d	0

(a) Geometrical properties of the domain

Geometry	Spherical
ν	0.3
$G_c^{\text{inc}}/G_c^{\text{mat}}$	$[1, 4.5]$
$\tilde{\sigma}$	0
$G_c^{\text{int}}/G_c^{\text{mat}}$	1

(b) Mechanical properties of the composite

v_m/v_0	10^{-8}
$\mathcal{L}/d$	10^6
G_0/G_c^{mat}	1

(c) Loading parameters

$\Delta z/d$	1/16
$\Delta x_{\max}/d$	1/25
$\Delta G_{\max}/G_c^{\text{mat}}$	$\min\left(10^{-2}c_{inc}, 10^{-3}\right)$

(d) Numerical parameters

Table 8.19: Parameters used in Section 4.6.1 to study the impact of the size disorder σ_d on the effective toughness

L_z/d	256
L_x/d	288
L_y/d	16
ρ_{inc}	$[0.1, 0.3]$
σ_d/d	0

(a) Geometrical properties of the domain

Geometry	Cubical
ν	0.3
$G_c^{\text{inc}}/G_c^{\text{mat}}$	$[1, 4.5]$
$\tilde{\sigma}$	0
$G_c^{\text{int}}/G_c^{\text{mat}}$	1

(b) Mechanical properties of the composite

v_m/v_0	10^{-8}
$\mathcal{L}/d$	10^6
G_0/G_c^{mat}	1

(c) Loading parameters

$\Delta z/d$	1/16
$\Delta x_{\max}/d$	1/25
$\Delta G_{\max}/G_c^{\text{mat}}$	$\min\left(10^{-2}c_{inc}, 10^{-3}\right)$

(d) Numerical parameters

Table 8.20: Parameters used in Section 4.6.2 to study the impact of the inclusion shape on the effective toughness

L_z/d	256
L_x/d	288
L_y/d	16
ρ_{inc}	0.25
$d_{\max}/d_{\min}$	$\{1, 2, 4\}$

(a) Geometrical properties of the domain

Geometry	Ellipsoidal
ν	0.3
$G_c^{\text{inc}}/G_c^{\text{mat}}$	$[1, 4.5]$
$\tilde{\sigma}$	0
$G_c^{\text{int}}/G_c^{\text{mat}}$	1

(b) Mechanical properties of the composite

v_m/v_0	10^{-8}
$\mathcal{L}/d$	10^6
G_0/G_c^{mat}	1

(c) Loading parameters

$\Delta z/d$	1/16
$\Delta x_{\max}/d$	1/25
$\Delta G_{\max}/G_c^{\text{mat}}$	$\min\left(10^{-2}c_{inc}, 10^{-3}\right)$

(d) Numerical parameters

Table 8.21: Parameters used in Section 4.6.3 to study the impact of the material texture on the effective toughness